Effects of mining subsidence observed by time-lapse seismic reflection profiling

Salim Y.S. Al-Rawahy

How to cite:

Al-Rawahy, Salim Y.S. (1995) Effects of mining subsidence observed by time-lapse seismic reflection profiling. Doctoral thesis, Durham University.

Effects of Mining Subsidence Observed by Time-Lapse Seismic Reflection Profiling

by

Salim Y.S. Al-Rawahy

A thesis submitted in partial fulfilment of the requirements for the degree of Doctor of Philosophy

Department of Geological Sciences

University of Durham
1995

Declaration

The contents of this thesis is the original work of the author and has not previously been submitted for a degree at this or any other university. The work of other people is acknowledged by reference.

Salim Y.S. Al-Rawahy
University of Durham.

Abstract

Effects of Mining Subsidence Observed by Time-Lapse Seismic Reflection Profiling

by

Salim Y.S. Al-Rawahy.

Extracting coal from underground mineworkings causes the overlying rocks to subside with associated changes in the stress regime. The aim of the study reported here was to apply the surface seismic reflection method to study the effect of subsidence on seismic velocity.

Two sets of time-lapse surveys were carried out over two longwall mining panels in the Selby Coalfield. Seismic lines were profiled parallel and perpendicular to adjacent panels H45 and H46, respectively. A total of twenty-one repeated surveys were carried out along the two lines over a period of three years. The effect monitored was due to mining in the Barnsley Seam, at 550 m depth. As mining progressed, the traveltime of a strong reflection event from an anhydrite bed at 150 m depth was measured after processing the data with standard techniques. An overall increase in traveltime of about 4 % was observed.

The progressive increase in traveltime over panel H45 correlated well with empirical calculations of differential subsidence between the surface and the anhydrite. However, the magnitude of the change must principally be accounted for by a decrease in seismic velocity, associated with a reduction in the vertical effective stress. Although the traveltime over panel H46 was also found to increase, and to correlate quite well with the expected differential subsidence, the agreement was less good along this transverse profile. This is attributed to asymmetric subsidence effects because the ground on the SW side of the panel had already been worked by panel H45, but the ground on the NE side was unworked.

At the time of each seismic survey across panel H46, the profile was also levelled, and it was found that surface subsidence values along the profile increased towards panel H45. As most of the subsidence caused by mining panel H45 would have been completed by the time the H46 profile was surveyed, the effect must be at least partly attributed to asymmetric subsidence due to panel H46. Where the ground had been weakened by subsidence due to mining H45, near-total subsidence from mining H46 took place rapidly; but in the previously unworked ground on the NE side of panel H46, the residual subsidence was presumably delayed by competent strata in the overburden. Further work is needed to confirm whether this explanation is correct.

Acknowledgement

Firstly, I would like to thank my supervisor Dr. Neil Goulty not only for devising this exciting project but also for helping out with most of the field work.

Secondly, I must thank Petroleum Development of Oman (PDO) for financial support during my study.

Thirdly, I would like to express my cordial gratitude to Peter Rowbotham, Tian Gang, Ibrahim Said, Miles Legget, Khalid Ahmed and Paul Field for their help in acquiring the data.

Last, but not least, I would like to thank my wife Asma Al-Abdulsalaam and my daughter Azza for their understanding and for making my stay in Durham a bit more interesting.

Contents

Chapter 1

Introduction

1.1 Synopsis

The main task of the research reported in this thesis was to use the surface seismic reflection technique to study the effect of deep coal mining on seismic velocity. The seismic velocity in the rockmass affected by subsidence was monitored before, during and after mining had taken place.

Chapter 1 summarises the relationships between the physical properties of rocks and seismic parameters. Also discussed in this chapter are some of the factors that can cause these properties to change over a short time scale, the seismic methods for measuring their effects and the seismic method used in this project. In Chapter 2, the methods of deep coal mining are explained and different modelling and methods of determining the amount of subsidence caused by mining are examined. In Chapter 3, the general data acquisition and processing techniques for shallow seismic reflection surveys are reviewed and the results of a pilot survey carried out in Selby are presented. The acquisition of the datasets used in this study and the data processing scheme are described in Chapter 4. The final results are presented in Chapter 5, their interpretation in Chapter 6 and the conclusions reached and suggestions for further work are given in Chapter 7.

1.2 Seismic parameters and physical properties of rocks

The method of using seismic parameters to assess the rockmass condition can be a very useful tool in the oil industry and in mining. In the oil industry, seismic velocity and the amplitude of reflected seismic signals can be used to infer the porosity and type of pore fluids in reservoir rocks at the exploration stage (e.g. Brown *et al.* 1986), and to assess the hydrocarbon recovery processes during production (e.g. Greaves and Fulp 1987). In mining, the method can be used to monitor the deformation processes as stress builds up and relaxes during the extraction of ore (e.g. Gladwin 1982).

The basic principle of the method is that the physical properties or physical state of rocks affect the seismic velocity within rocks and the reflection coefficients at interfaces. To implement this method, therefore, the relationship between changes in rock properties and variations in acoustic properties must be established and well understood. For example, the velocity at which a seismic signal travels in a rock is a function of the elastic moduli and rock density. Hence changes in either the elastic moduli or density will contribute to variations in velocity. A number of physical properties and state, such as porosity, temperature, pore fluid, fluid saturation, pore pressure and confining pressure, affect rock elastic moduli and/or rock density. Changes in any of these rock parameters may also affect the seismic reflection amplitude because the amplitude depends on contrast in acoustic impedance, which is the product of velocity and density. The seismic quality factor, Q, which is a measure of the rate of anelastic attenuation as a seismic wave propagates through a rockmass, will also change.

To quantify the contribution of each rock physical property to the acoustic measurements, theories of the propagation of elastic waves through porous media and empirical relationships, derived from laboratory experiments or from well log data and core measurements, are often used. Laboratory experiments involve transmitting a seismic pulse through a rock sample of known physical properties and measuring the traveltimes and amplitudes of the direct arrivals. Velocities can also be calculated from sonic logs and be related to rock properties, such as porosity measured directly from core samples. In the following sub-sections, the effect of some of the main rock properties and physical states on seismic parameters are reviewed. Although these properties will be discussed individually, it is important to bear in mind that some of them are not independent. For example changes in confining pressure may also cause porosity to vary.

1.2.1 Porosity, pore shapes and clay content

Porosity is the rock property that most strongly affects observed seismic parameters. Its effect on P-wave velocity was first examined by Wood (1941) in a suspension of solid particles in fluid. With the assumption that the solid and fluid components react independently to the propagation of the wave, the bulk modulus K of the suspension can be written:

$$\frac{1}{K} = \frac{\phi}{K_f} + \frac{(1-\phi)}{K_m} \qquad (1.1)$$

where ϕ is the porosity, and K_m and K_f are the bulk moduli of the solid particles and the pore fluid, respectively. The P-wave velocity V_p is then:

$$V_p = \left(\frac{K}{\rho_b}\right)^{\frac{1}{2}} \tag{1.2}$$

where ρ_b is the bulk density and given by

$$\rho_b = \phi\rho_f + (1 - \phi)\rho_m \tag{1.3}$$

where ρ_m and ρ_f are densities of the solid particles and the pore fluid, respectively. The shear rigidity does not appear in equation (1.2) because a suspension of solid particles in fluid does not have any rigidity. The equations above were verified experimentally by measurements of P-wave velocity in kaolin-water and xylene-water emulsions (Urick 1947). These equations, however, have limited application in sedimentary rocks because most rocks, even highly porous unconsolidated marine sediments, have shear rigidity and frame modulus (Hamilton 1971).

A more robust equation was developed by Wyllie *et al.* (1956). In this equation, also known as the time-average equation, the slowness (reciprocal of the P-wave velocity) in a saturated rock is the weighted-by-volume average of the slownesses in pore fluid and rock matrix:

$$\frac{1}{V_p} = \frac{1-\phi}{V_m} + \frac{\phi}{V_f} \tag{1.4}$$

where V_m and V_f are P-wave velocities of the rock matrix and fluid, respectively. This equation is widely used to determine porosities from velocities in water-saturated sand and sandstone measured by sonic logs. However, the equation seems to work relatively well only in consolidated sandstone with a high velocity fluid at high differential pressure (Wyllie *et al.* 1958). Furthermore, the sandstone must be clean with porosity between 10 and 25 percent (Han *et al.* 1986).

Pickett (1963) modified the time-average equation to take into account other rock properties such as pore geometry and differential pressure. His equation took the form of

$$\frac{1}{V} = A + B\phi \tag{1.5}$$

where V is either P-wave or S-wave velocity, and A and B are constants. Domenico (1984) performed a regression analysis fit of equation (1.5) to the observed data, and he found that the value of A for V_p was approximately equal to the reciprocal of matrix velocity, as in Wyllie's time-average equation, and the value of B was a function of pressure. This relationship can be used for different rock types so long as B is adjusted empirically for each. The drawback of equation (1.5), as with the time-average equation (1.4), is that it fits the observed measurements satisfactorily only at high effective pressure.

In recent studies, other more complicated equations which take the shape of the pores into account have been developed theoretically and tested by laboratory measurements (e.g. Kuster and Toksoz 1974a, b; Toksoz *et al.* 1976; Cheng and Toksoz 1979; Burns *et al.* 1990). If the pore spaces in rocks are assumed to be represented by small oblate spheroids, then their effect on velocity is a function of their aspect ratios (Toksoz *et al.* 1976). The aspect ratio is the ratio of minor to major axes for an oblate spheroid; perfect spheres have an aspect ratio of 1.0 and flat penny-shaped pores have an aspect ratio of 0.1 or less. For a given porosity and concentration of pores, the pores with smaller aspect ratio affect both V_p and V_s much more than those with greater aspect ratios. Theoretically, less than 1 percent of pores with aspect ratios of 0.01 or less can decrease the velocities by 20 percent (Toksoz *et al.* 1976).

It is well known that a seismic velocity in shaly sandstone is lower than that in a clean sand of the same porosity. The effect of clay on velocity was examined in laboratory experiments by Tosaya and Nur (1982), Kowallis *et al.* (1984) and Han *et al.* (1986). The results showed that velocity varies linearly with clay content in the rock. Tosaya and Nur (1982) and Han *et al.* (1986) demonstrated that velocity V in shaly sandstone is related to porosity ϕ and the volume fraction of clay C by

$$V = A_0 - A_1\phi - A_2C \tag{1.6}$$

where A_0, A_1 and A_2 are constants. At an effective pressure of 39 MPa, the values of A_0, A_1 and A_2 given by Han *et al.* (1986) are 5.59, 6.93 and 2.18 km/s, respectively for the V_p, and 3.52, 4.91, and 1.89 km/s, respectively for V_s. At almost the same effective pressure, Tosaya and Nur (1982) suggested the values of these constants for V_p as 5.8, 8.6 and 2.4 km/s, respectively. In both studies the reduction in V_p caused by an increase in clay content was about 30 percent of that caused by an increase in porosity. The results of Han *et al.* (1986) also showed that the effect of porosity and clay content on velocity are fairly independent of differential pressure above 10 MPa.

One of the most important conclusions which can be drawn from the above equations and experimental studies is that, for a given rock with all other parameters fixed, an increase in porosity over the range of from about 3 to 30 percent can reduce the velocity by up to 60 percent (Hicks and Berry 1956).

1.2.2 Pore fluid type and fluid saturation

The increase in seismic reflection amplitude caused by change in fluid type in a reservoir rock, known as a bright spot, is widely used as a hydrocarbon indicator in oil exploration. Bright spots occur mainly in young unconsolidated rocks where a water-saturated reservoir has lower acoustic impedance than surrounding rock, and therefore the presence of gas decreases the impedance even further. The change in acoustic impedance is principally due to change in V_p, as V_p is lower in gas than in water. Although this velocity relationship is always true for fully saturated gas reservoir rocks, it may not necessarily be applied to oil or partially saturated gas rocks as will be apparent by the results discussed below.

Gassmann (1951) investigated theoretically the effects of pore fluid on elastic properties of a porous medium in a 'closed system' (pore fluid is not allowed to flow in or out of a porous medium as stresses vary during the propagation of waves). He derived an equation which allows the bulk modulus of a porous medium saturated with fluid to be calculated from the bulk modulus of the same medium without fluid and the bulk modulus of the fluid. At any given pressure, the bulk modulus K of a saturated medium is given by

$$K = K_m \frac{K_d + Q}{K_m + Q}, \quad \text{where } Q = \frac{K_f(K_m - K_d)}{\phi(K_m - K_f)} \qquad (1.7)$$

and K_m, K_d and K_f are the bulk moduli of the mineral grains, the granular frame (dry medium) and the pore fluid, respectively. When the frame modulus is equal to zero, the Gassmann equation reduces to the Wood equation (1.1).

The Gassmann equation has been extended by different authors to account for other factors which influence velocity in saturated rocks. These factors include the effect of the relative motion between the fluid and the frame considered by Biot (1956), the dependency of the velocity on frequency accounted for by Geertsma (1961), the microheterogeneity of the sediments (Brown and Korringa 1975) and the coupling of the fluid to the grain (Domenico 1977).

The P-wave velocities calculated using the above equations, sometimes referred to as Biot-Gassmann (BG) equations, are always higher in saturated rocks in which the pore fluids also have higher velocity. However, it has been shown experimentally that this is not always the case (King 1966; Wang and Nur 1988). King (1966) found that P-wave velocities in some brine-saturated rocks were lower than those in the same rocks saturated with kerosene, although V_p in brine solution is higher than in kerosene. He attributed this effect to the presence of detrital minerals in sandstone which react with the sodium chloride solution and reduce the rock's rigidity. For rocks which did not have detrital minerals, the velocity behaviour was found to approach that predicted by the Biot-Gassmann equations at high confining pressure. Wang *et al.* (1988) showed that V_p was much higher when a sandstone was saturated with heavy oil than when saturated with water. These results also contradict the Biot-Gassmann equations because the velocity and density of the heavy oil are very close to those of water. They attributed this to the high viscosity of the heavy oil. When a pore is filled with viscous oil, the oil is physically or/and chemically bound to the grain so that both the bulk and shear moduli are high.

Experimental studies on S-velocity have shown that at high pressure the velocity is lower when a consolidated rock is saturated with water than when saturated with air (King 1966; Gregory 1976). This is caused by a reduction in density of a rock while there is no change in rigidity when water is replaced by air. The same results can be found at low pressure if a saturated rock has a porosity of more than about 18 percent (Gregory 1976). These results, therefore, agree with the BG equations.

Domenico (1974, 1977) extended the BG equations to include the effects of partial water saturation. By assuming that the water and gas are mixed in the same proportions throughout the pore space, the compressibility (inverse of bulk modulus) of the mixture can be given by the weighted-by-volume average of the compressibilities of water and gas. The bulk modulus of the mixture, K_f, is therefore given by

$$\frac{1}{K_f} = \frac{1 - S_w}{K_g} + \frac{S_w}{K_w} \tag{1.8}$$

If the water and gas are not mixed in the same proportions throughout the pore space, then Dominico (1977) suggests that

$$K_f = (1 - S_w)K_g + S_w K_w \tag{1.9}$$

where K_w and K_g are the bulk moduli of water and gas, respectively; and in both cases the bulk density ρ_b of a partially saturated rock is given by

$$\rho_b = (1 - \phi)\rho_m + \phi S_w \rho_w + \phi(1 - S_w)\rho_g \tag{1.10}$$

where S_w is the water saturation, and ρ_m, ρ_w and ρ_g are the densities of matrix, water and gas, respectively. Domenico (1974) suggested that the actual value of K_f is expected to lie between the values given by equations (1.8) and (1.9). Due the large contrast between the bulk moduli of liquid and gas, (bulk moduli of brine, oil and gas are 0.022 Mbar, 0.002 to 0.02 Mbar and 1 to 100 bar, respectively (Yale 1985), the equations above suggest that a small percentage of gas in water or oil saturated rock can cause the fluid modulus to decrease significantly. The effect of this on V_p will depend on the bulk modulus of the solid material (equation 1.7).

Measurements of V_p at low (seismic) frequencies (Murphy 1982, 1984) and in unconsolidated sands (Elliot and Wiley 1975; Domenico 1977) have shown that a small amount of gas, about 5 percent or less, in a water-saturated rock causes the V_p to decrease significantly. A subsequent increase in gas saturation, up to about 90 percent, causes the velocity to stay constant or increase only slightly, due to a decrease in the bulk density, which compensates for the further reduction in modulus. This trend of velocity correlates well, at least qualitatively, with that predicted by the BG equations. However, in most cases, as gas saturation approaches 100 percent, velocity has been observed to increase significantly. Murphy (1982) observed an increase of about 60 percent between 98.5 and 100 percent gas saturation. As such an increase cannot be accounted for by a decrease in density alone, as suggested by the BG equations, bulk modulus must increase greatly. Murphy (1982) and others (e.g. Bulau *et al.* 1984; Murphy *et al.* 1984) have attributed this increase to chemical and capillary forces which hold a thin film of water around the grains and therefore stiffen them.

Unlike consolidated rocks at low frequencies, the effect of partial saturation on V_p in consolidated rocks at ultrasonic frequencies is more complicated and difficult to predict (Gregory 1976). This is due to the fact that at high frequencies, the distribution of gas in the pore space is very crucial. However, most measurements show that the velocity in low porosity rocks decreases gradually with an increase in gas saturation (Gregory 1976; Murphy 1984). In medium and high porosity rocks (Gregory 1976), the measurements show that the velocity trends resemble those in an unconsolidated sand, with the exception that when a small amount of gas is added to a fully water-saturated rock, the decrease is more gradual than in unconsolidated sands.

1.2.3 Confining and pore pressures

Confining, or overburden, pressure is a pressure exerted on the rock matrix due to the weight of the overburden, and pore pressure is the pressure in the pore fluid. In a normally pressured formation, the pore pressure is hydrostatic. The main effect of increasing confining pressure on a sedimentary rock during burial is to deform most of the pore spaces and to compress the rock matrix, and thus to increase the effective bulk and shear moduli. If the pore fluid is not allowed to escape, then overpressure will develop. The pore pressure counteracts the tendency of the confining pressure to reduce porosity. Consequently, the change in elastic moduli and therefore velocity, depends on the differential pressure: the difference between the confining and pore pressures (Brandt 1955; Hicks and Berry 1956; Wyllie *et al.* 1958; Banthia *et al.* 1965; Christensen and Wang 1985).

Brandt (1955) developed a theory to describe the effect of pressure on P-wave velocity. For a medium with non-spherical particles, the velocity was found to be dependent on an effective pressure, P_e, which is given by

$$P_e = P_c - nP_p \qquad (1.11)$$

where P_c and P_p are confining and pore pressure, respectively, and *n* is a constant at a given differential pressure being in the range of 0 to 1. He showed that theoretical velocities agreed closely with velocities measured in a liquid-saturated sandstone under differential pressure of 1500 to 9000 psi, with *n* averaged at 0.87. For a pore pressure of less than half of the confining pressure, he suggested that *n* can be taken as 1.

A number of different values of *n* have been indicated by several workers. These values are either given by the authors or can be inferred from their graphs of velocity against differential pressure and confining or pore pressure. P-wave velocity measurements by Willie *et al.* (1958) in water-saturated Berea sandstone suggested a value of 1. This implies that the effect on V_p of an increase in confining pressure is cancelled by an equal increase in pore pressure, and therefore the velocity at a given differential pressure is constant. Experimental data by Banthia *et al.* (1965) of S-wave velocities in three different sandstones and a chalk showed that *n* is a function of pressure and is less than 1. Their results suggest, therefore, that at a given differential pressure V_s increases with an increase in confining and pore pressure. Similar results were observed by Christensen and Wang (1985) for V_p in water-saturated Berea sandstone. However, their S-wave velocities indicated a value of *n* of greater than 1, which suggests that at a given differential pressure, V_s decreases with increasing confining and pore pressure.

Different causes of the discrepancies in the values of *n* observed in different experiments for the same rock type and wave modes have been suggested. Banthia *et al.* (1965) pointed out that at high pressure the value of *n* is very sensitive and therefore small experimental errors can effect its value significantly. Gardner *et al.* (1965) showed that the value of *n* is determined not only by the present values of pressures, but also by the past pressure history. They found that if differential pressure follows a pressure cycle previously imposed on the rock, then the value of *n* will be equal to 1. Christensen and Wang (1985) suggested that the high precision measurements of velocities made their results more accurate and reliable. However, it is important to note that although the precise value of *n* may be crucial from a theoretical point of view, it does not have the same importance in practice (Gardner *et al.* 1965).

Apart from the disagreement as to whether the value of *n* is less than, equal to or greater than 1, all the experimental studies discussed above showed that the velocity increases with increasing effective pressure, at first rapidly and then more gradually until a constant velocity is attained. This is due to the presence of pores and cracks in rocks at low differential pressure. As differential pressure increases, more cracks are closed and therefore the signal travels primarily through the high velocity rock matrix. A decrease in seismic velocity of up to 20 percent was observed by Christensen and Wang (1985) in water-saturated sandstone when the pore pressure approached the confining pressure (differential pressure approaches zero). Similar percentages can be deduced from graphs plotted by others (e.g. Domenico 1977; King 1966).

1.2.4 Temperature

Increase in temperature affects the rockmass in a number of different ways, such as softening the rock matrix, lowering the rock density, and increasing the porosity and the pore pressure. Increase in temperature also causes the bulk modulus of the pore fluid to increase or decrease depending on the temperature range and the type of fluid. For example, the bulk modulus of oil decreases with an increase in temperature whilst the bulk modulus of water at atmospheric pressure increases as temperature increases to about 73°C and then decreases as temperature increases further. At higher pressures, the maximum bulk modulus of water occurs at higher temperatures.

The effect of temperature on P-wave velocities in water-saturated unconsolidated rocks was demonstrated by Shumway (1958). It was shown that the variation in velocity in saturated sediment with small changes in temperature was approximately the same as that of water alone. This was due to the relatively high temperature sensitivity of the bulk modulus of water to that of the rock matrix at low temperature. Similar results were observed by Bell and Shirley (1980). They also showed that the S-wave velocity and attenuation of P and S amplitudes were independent of a change in temperature.

In contrast to the results for unconsolidated sediments discussed above, the measurements of V_p and V_s in brine-saturated consolidated rocks by Timur (1977) showed that at a given pressure the velocity decreased linearly with increase in temperature. Two sandstone and seven carbonate rocks were studied, and average decreases in V_p and V_s of 1.7 and 0.9 % per 100°C, respectively, were reported. In general, for a given consolidated rock and pressure, the velocity reduction caused by an increase in temperature is minimum when the rock is dry or gas-saturated, and maximum when the rock is saturated with heavy hydrocarbons (Wang and Nur 1988).

1.3 Short time-scale sources of change in rock properties

Although the physical properties and states of sedimentary rocks are mainly determined by long-term geological factors, such as the environment in which the rock was deposited, the processes of deposition and diagenesis and the tectonic history, there are other processes which operate over a shorter time scale and which are equally effective. In this section some of these processes will be discussed.

In oil production, when the primary energy (initial pore pressure) which drives hydrocarbons towards production wells declines, artificial methods known as secondary recovery and enhanced oil recovery (EOR) processes are used. Secondary recovery processes are processes whereby water or gas such as nitrogen is injected into the reservoir to displace the hydrocarbon towards the production well. EOR processes involve setting fire to the hydrocarbon in the reservoir, or injecting carbon dioxide, hydrocarbon solvent or foam into the reservoir to displace the hydrocarbon. Inevitably, all recovery processes cause the physical states and properties of the rock and the pore fluid to change. Fire or steam modifies the hydrocarbon saturation and increases the temperature in the reservoir, and thus decreases the bulk moduli and the densities of the fluid and the rock matrix. Injection of gas, foam or hydrocarbon solvents increases the pore fluid pressure and changes the hydrocarbon saturation, and therefore causes the bulk modulus of the pore fluid to change.

In underground mining, extraction of ore can cause the overlying rocks to subside into the cavities opened up by mining. As rocks above the mined horizon subside, they expand and therefore the subsidence decreases progressively in magnitude towards the surface, whilst also spreading outwards. Accompanying the subsidence is a change in the stress regime above the workings. The change in vertical stress vertically above the mine working is tensile, with a small increase in compressive stress above the edges of the working and over the unworked seam. Tensile stress indicates that there is a decrease in confining pressure, whilst compressive stress indicates an increase.

The same stress distribution as observed in mining can form above underground tunnels and buried pipes. In some mining (especially coal mining), the extraction is often accompanied by pumping of water from underground, and this can cause a change in water saturation.

1.4 Seismic methods in assessing the change in rock properties

Nearly all seismic methods have been used in the field to monitor changes in physical properties of rocks. The changes are usually inferred from repeated seismic measurements, of velocities or amplitudes, made at the same location before and after the expected change had taken place. This technique of carrying out repeated surveys at the same location is known as time-lapse seismology, and can be used with any seismic method.

Greaves and Fulp (1987) used 3D seismic surveys to monitor the propagation of a fire front in the fire-flood EOR process. Bright spots in post-burn sections were attributed to the decrease in density and velocity in the reservoir caused by the combustion process. A velocity decrease of about 25 percent was observed on the sonic log. This decrease was mainly due to the decrease in the bulk modulus of the rock matrix caused by an increase in temperature. The 3D seismic method was also successful in locating the heated zone in Athabasca tar sands in Canada following steam injection (Matthews 1992). Here the zone was detected by the pushdown effect on reflectors below the reservoir (caused by a decrease in velocity in the reservoir) and change in seismic amplitude within the reservoir.

Macrides *et al.* (1988), Justice *et al.* (1989) and Justice *et al.* (1993) reported the applications of crosshole tomography in monitoring enhanced oil recovery processes, such as steam and carbon dioxide flooding. Low velocity anomalies observed correlated well with the carbon dioxide or steam fronts. The crosshole method was also used by Spathis *et al.* (1985) to assess the effect of the change in rock mass conditions induced by mining and by controlled blasts. The change was inferred from the change in traveltime and in rock attenuation calculated from the rise time.

Kormendi *et al.* (1986) used a modified in-seam seismic method to monitor stresses in a coal seam when the seam was extracted. Seismic sources were placed in the coal seam in one underground road and receivers were fixed in the same seam in the other road. The measurements were repeated and changes in velocity calculated from the traveltimes were related to the stresses caused by mining activities.

1.5 Seismic method used in this project

Previous surface seismic surveys over coal workings by Goulty and Ziolkowski (1985), Pietsch and Slusarczyk (1992) and the National Coal Board (C. M. Fairbairn, personal communication) have revealed an increase in traveltimes to the reflectors above an extracted coal seam. The only survey which was set up with the aim of investigating the effect of deep coal mining on seismic was that carried out by the National Coal Board. Even in this survey, the profile was surveyed only twice: before and after mining.

Goulty and Ziolkowski (1985) carried out only one survey, and the increase in traveltime was deduced from the fact that the reflectors could be traced smoothly across the section except where the seismic line passed over the old workings, and it was known from the old workings that no structures were present in these reflectors. This has subsequently been confirmed by pairs of surveys, before and after longwall mining, in the UK and in Poland. At Cotgrave, Nottinghamshire, increases in traveltimes of several milliseconds were observed for reflectors at depths of several hundred metres (C. M. Fairbairn, personal communication). Pietsch and Slusarczyk (1992) used data from intersecting profiles, acquired before and after mining a longwall panel in the Lublin Coal Basin, to determine the height of a caved roof zone. They showed that after mining the smooth reflectors above the coal seam became discontinuous. Although they did not specifically attribute this effect to change in seismic velocity, it may be inferred that velocity change is the principal factor causing the observed effect.

In this project, the effects of deep coal mining on seismic P-wave velocity are studied by repeatedly surveying two short seismic reflection profiles in the Selby coalfield before, during and after mining two longwall panels. One profile was laid out parallel to the direction of mining advance of panel H45, whereas the second profile was perpendicular to the direction of mining of panel H46. The profiles have been surveyed ten and eleven times, respectively, over a period of more than 16 months. Both panels were 220 m wide and the coal seam extracted was at a depth of 550 m.

For reasons of economy and repeatability, the source used was a sledgehammer, and strong reflections were obtained from an anhydrite bed in the Upper Permian Marl at a depth of 150 m. The effect of mining subsidence on seismic velocity can clearly be seen in the increased traveltimes to this reflector as the faces advanced. The increases in traveltimes are compared with the differential subsidence between the surface and the anhydrite, calculated from empirical curves published by the National Coal Board (1975). Surface subsidence values over panel H46 are also calculated from levelling results obtained along the seismic profile. The observations show that the surface subsidence above the side of panel H46 adjacent to H45 was as expected, but less subsidence than expected had taken place above the side of H46 adjacent to unworked ground.

Chapter 2

Deep coal mining

2.1 Introduction

Extracting ore from underground causes the physical properties of the rockmass around, and particularly above, the extracted horizon to change. These changes are mainly due to the strains in the subsurface rockmass and the associated change in the stress field induced by mining. The bulk of this chapter is concerned with subsidence caused by deep coal mining, including the models which are used to describe the distribution of the mining induced stresses and the displacement fields in the rockmass. The chapter ends with a discussion of subsidence effects on hydrogeology and permeability. Firstly, however, the methods employed in deep coal mining will be described.

2.2 Mining methods

There are two main methods for underground mining of coal: the bord and pillar method and the caved method. In the bord and pillar, or partial extraction, method only a fraction of coal is mined out, leaving pillars of coal to support the roof. The percentage of coal extracted by this method depends on its depth and the strength of the rockmass above the seam. The deeper the seam is, the larger the fraction of coal is left in the ground. In the caved, or total extraction, method the roof is systematically allowed to collapse behind the coal face. At present, the depth to which the coal can be extracted by this method is limited by the induced stresses and by the underground temperature. In the UK this depth is about 1300 m (Ziolkowski 1979).

Most underground coal mining in the UK uses a state-of-the-art caved method known as the 'caved longwall retreat'. In this technique (Fig. 2.1), two parallel underground roads about 200m apart are driven within the seam on either side of the panel of coal to be extracted. The roads are joined at the far end to form the coal face and the coal-cutting equipment is installed. The panel is then extracted by retreating the coal face between the underground roads. Hydraulic jacks are used to support the roof above the coal face. As mining progresses, they are moved forward, allowing the roof behind to cave in. The layers in the immediate roof collapse by breaking off into large lumps of rock to fill in the mine cavity. The rock mass overlying the immediate roof deforms elastically by expanding and subsiding almost unbroken on to the caved waste. The surficial layer of glacial drift, loose sand or clay subsides in a plastic manner by following the bedrock below.

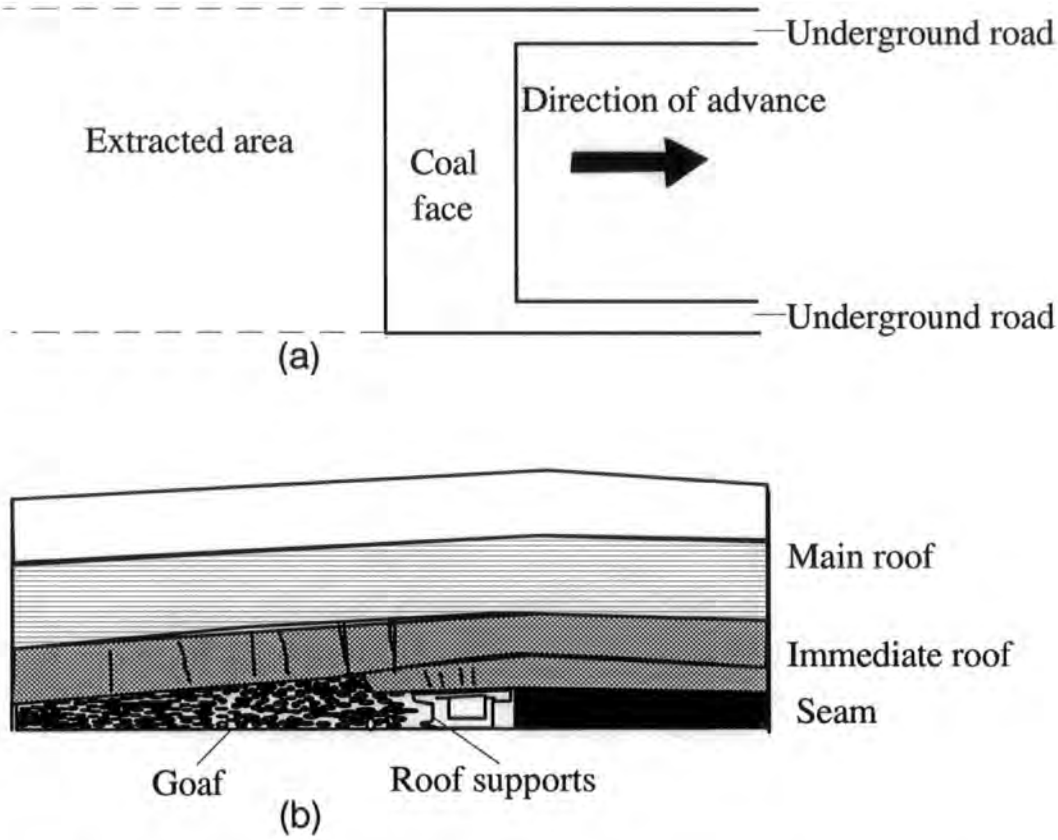

Fig 2.1. Longwall retreat coal face: (a) a plan view, and (b) a cross section through the centre of the panel along the direction of face advance.

The magnitude of vertical displacement attained by individual strata above the mining horizon decreases progressively towards the surface whilst the surface area affected increases. The overlying rockmass affected by subsidence can be defined within planar surfaces extending from the edges of the excavation to the ground surface, sloping away from the panel (Fig. 2.2). The angle these surfaces make with the vertical is termed the 'angle of draw' and is about 25-35° for most of the UK coalfields.

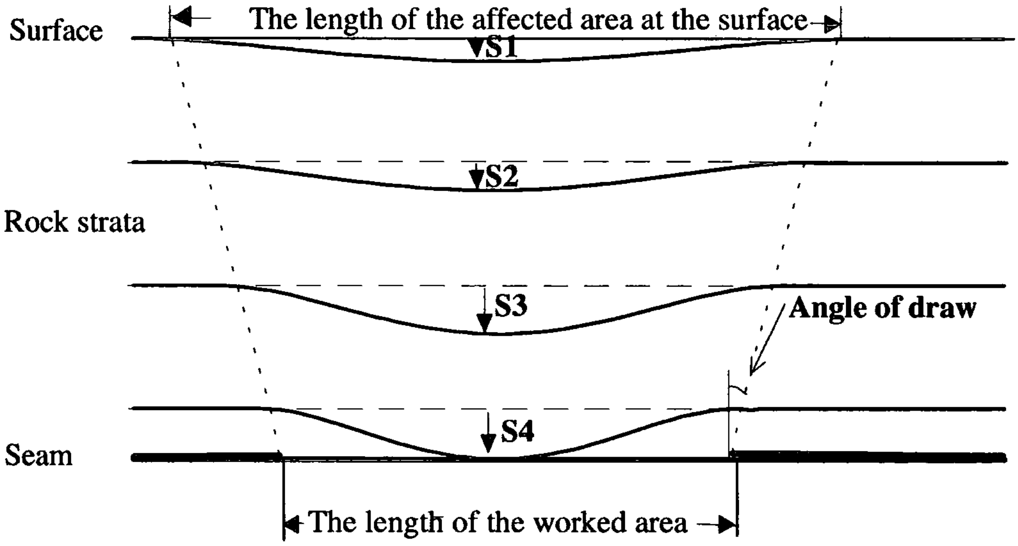

Fig. 2.2 Vertical movements of rock strata above a coal mining panel. S1 to S4 are values of maximum subsidence at corresponding depths as shown, such that S4 > S3 > S2 > S1.

The magnitude and the shape of the subsidence profile observed at the ground surface depend not only on the physical properties of the overburden strata, but also on the geometry of the workings and the rate at which the coal seam is extracted. Field measurements have shown that for given physical properties of the overlying rocks, the subsidence increases with the thickness and the width of the coal seam extracted (National Coal Board 1975).

2.3 Initial stresses

Initial stresses are natural stresses that exist in underground rock before mining. The state of stress at a point in a rock is a function of both the current loading conditions and other effects due to the geological history of the rockmass. The latter include temperature change, tectonics, erosion, and re-crystallisation of minerals. Unless stated otherwise, the horizontal and vertical stresses discussed below are assumed to be the principal stresses.

2.3.1 Stresses due to gravity

The vertical normal stress component σ_z due to loading (gravity) in a rock at depth z, overlain by material whose density $\rho(z)$ varies with depth, is given by

$$\sigma_z = \int_0^z \rho(z)\, g\, dz \qquad (2.1)$$

where g is the acceleration due to gravity. Most field measurements in sedimentary rocks have shown that vertical stress varies linearly with depth at a rate of about 25 kN/m (Gay 1975; Haimson 1978). Using equation (2.1), this corresponds to an overburden density of about 2.55 g/cm^3. Since this value is similar to the average density of most rocks, it would appear that the vertical component of initial stress is due to loading, and therefore can be calculated using equation (2.1). However, special care must be exercised when analysing highly deformed rocks. For example, the vertical stress measured in the axial plane of a syncline fold in a rigid rock can be significantly higher by an order of magnitude, than that predicted by equation (2.1) (Goodman 1980).

The initial horizontal stress components are also found to be dependent on depth. By assuming that an elastic rockmass is restricted from deforming laterally (zero horizontal strains) during the gravitational loading, the principles of elasticity can be used to calculate the horizontal normal stress components. If ν is Poisson's ratio of the rock and σ_x and σ_y are the horizontal normal stress components then

$$\sigma_x = \sigma_y = \left(\frac{\nu}{1-\nu}\right)\sigma_z \qquad (2.2a)$$

Equation (2.2a) is often given in the form

$$\sigma_x = \sigma_y = K\sigma_z \qquad (2.2b)$$

where K is constant. For most rocks ν ranges from 0.2 to 0.33 and hence the value of K lies between 0.25 and 0.5. This therefore suggests that the horizontal components of initial stress will always be less than the vertical component. However, K has been observed to take values of greater than 1 at shallow depths, decreasing non-linearly with depth to values close to 1 (Gay 1975; Haimson 1978). Brown and Hoek (1978) determined the value of K by plotting the ratios of horizontal to vertical stresses against depth using measurements observed in different studies around the world. They found that, although the measurements scattered widely especially at low depths due to measurement error, the trend was such that K decreases from values of more than 2.5 at shallow depths to the approximately constant value of 1 at depths greater than 1500 m. The state of stress when the vertical component is equal to the horizontal components ($K = 1$) is referred to as lithostatic. According to Heim's rule, this is attributed to the viscoelastic (creep) behaviour of the rock (Jaeger and Cook 1969). The value of $K = 1$ also coincides with the value of $\nu = 0.5$, which is Poisson's ratio for a fluid.

Values of K greater than 1 suggest that there are other stresses apart from the gravitational loading that exist in rocks prior to mining. These are mainly tectonic and residual stresses. Unlike the stress due to gravity, tectonic and residual stresses (discussed below) are complex and are impossible to predict without in situ measurements. Hence the state of the initial stress in a highly disturbed rockmass, which is the resultant stress formed by the superposition of these stresses on the stress due to gravity, cannot easily be predicted even qualitatively without knowledge of the geological history of the rockmass.

2.3.2 Tectonic stresses

Tectonic activity, such as uplift, folding and faulting, induces stresses by straining rocks on a regional scale. Stress anomalies induced by this activity disrupt the continuity of the pre-tectonic stress field both in magnitude and in its state (compressive and tensile). Uplift, for example, can perturb the state of initial stress by inducing tensile stresses in rocks, and this in turn may cause fractures to develop and split up the rockmass. The existence of tectonic stresses is often characterised by an increase in one of the horizontal normal stress components relative to the other.

A number of field measurements have been carried out around the globe to determine the magnitude and direction of the present state of tectonic stresses (e.g. Gay 1975; Ranalli 1975; Greiner 1975; Haimson 1978). Zoback (1992) compiled more than 7000 in situ stress measurements around the globe, and showed that the midplate stress fields in the regional scale can be explained in terms of plate tectonic (i.e. the stresses are the results of forces acting at the plate boundaries). Locally, however, other sources of stress, such as erosion, can have a significant effect on stress fields, especially at shallow depths, as discussed below.

2.3.3 Stresses due to erosion and isostasy

Erosion and isostasy reduce the vertical stress and the horizontal stresses according to equations (2.1) and (2.2), respectively. If an overburden of Δz thickness is removed by erosion, then the decrease in vertical stress is equal to $\rho g \Delta z$ and the decrease in horizontal stresses is equal to $\rho g \Delta z \left(\frac{\nu}{1-\nu} \right)$. Since ν in rocks is always less than 0.5, the decrease in horizontal stresses is less than that in the vertical stress. Thus if rocks respond in elastic manner during erosion, then the effect of erosion on initial stress is to increase the horizontal/vertical ratios, and therefore the value of K becomes greater 1.

2.3.4 Residual stresses

These stresses are mainly due to volume changes caused by thermal or chemical processes operating non-homogeneously in restricted parts of a rockmass. For example, differential cooling of a uniform rock, or uniform cooling of a rock with lithological units of different coefficients of thermal expansion, can induce stresses locally. Crystallisation or change in the water content of some minerals can also result in non-uniform volumetric strain.

2.3.5 Resultant initial stress

A number of empirical formulae have been proposed for calculating the initial stresses without trying to separate the effect of the factors detailed above. An example of these formulae is that of Brown and Hoek (1978) which relates the value of K to the depth z expressed in metres:

$$\frac{100}{z} + 0.3 < K < \frac{1500}{z} + 0.5 \tag{2.3a}$$

Equation (2.3a) was derived from a number of observations around the globe. The wide range of values of K predicted by equation (2.3a) for a given depth shows how variable the state of initial horizontal stress is, from place to place. However, the range is reduced significantly if the observations considered are from the same region or geological environment. In South Africa, for example, Brown and Hoek (1978) used Gay results by (1975) to obtain K as

$$K = \frac{248}{z} + 0.45 \tag{2.3b}$$

There is general agreement that in most cases the vertical component of the stress can be calculated using equation (2.1).

2.4 Displacements and stresses induced by mining

Once a coal seam is extracted, the normal stresses on the surface of the cavity are reduced to zero, and the original equilibrium under the action of the initial stress is destroyed. To re-establish the equilibrium, the stresses and rock displacements induced by mining are distributed around the cavity. The extent to which the stresses affect the surrounding rocks is a function of the size of the excavation and the physical properties of the rocks. Different mathematical models based on the theory of elasticity have been developed to study the distribution of stresses and the displacement field in underground rockmass (Berry 1960, 1963a, b, 1964; Berry and Sales 1961, 1962; Salamon 1968, 1974).

2.4.1 Beam model

One of the simplest models is that based on the theory of uniformly loaded beams. In this model the cohesion between successive strata in the rockmass above an extracted horizon is assumed to be so poor that each stratum acts like an individual elastic beam on the removal of the coal seam. The beams are considered to be uniformly loaded with their ends built into abutments at either side of the excavation. If the length of the excavation is long compared with the width, then the deformation is often assumed to be two-dimensional.

The vertical deflection w in the z direction of a uniformly loaded long beam lying along the x-axis, with unit width in the y-direction, can be calculated using the beam theory (given in any text book on rock mechanics, e.g. Jaeger and Cook 1969 pg 123) by

$$EI_y \frac{d^4w}{dx^4} = P \qquad (2.4)$$

where I_y is the moment of inertia in the x-y plane, E is the Young's modulus and P is the uniform distributed force per unit area applied in the z direction. The quantity EI_y is known as the flexural rigidity of the beam. If the length of the beam, also known as the span, is equal to l and one of its ends is at $x=0$, then, with the boundary conditions that w and $\frac{dw}{dx}$ equal zero at the ends of the beam ($x=0$ and $x = l$), equation (2.4) can be integrated to give

$$w = \frac{Px^2(l-x)^2}{24EI_y}. \tag{2.5}$$

Equation (2.5) shows that the vertical deflection is maximum at the centre of the beam, and that the points of inflection, which can be found by differentiating w twice with respect to x, are at a distance $\pm\sqrt{\frac{1}{12}}\,l$ from the centre of the beam. The points of inflection are where the change in stress regime takes place. The middle part of the bottom surface of the beam, between the points of inflection, is subjected to tension while the outer portions are in compression, and vice versa in the upper surface of the beam, i.e. there is compression in the middle and tension at the sides.

The bending moment M at any point in the beam, the stress σ tangential to the beam surfaces and shear stress τ can also be calculated from the equations above by

$$M = -EI_y\frac{d^2w}{dx^2} = -\frac{p}{12}(l^2 - 6lx + 6x^2) \tag{2.6}$$

$$\sigma = -\frac{Mt}{2I} = \frac{Pt}{24I}(l^2 - 6lx + 6x^2) \tag{2.7}$$

$$\tau = t\frac{dM}{dx} = -\frac{P}{2t}(2x - l) \tag{2.8}$$

where t is the thickness of the beam. It is possible to show from these equations that the maximum tensile stress occurs on the upper surface at both ends of the beam, and that the shear stress is zero at the centre of the beam and maximum at the ends of the beam.

The following conclusions can be drawn if the deflection and stresses in the strata of the overlying rockmass are calculated using the above equations. The closure of the opening due to elastic deflection, at the centre of the immediate roof above the mining, varies as the fourth power of the span: by doubling the span, the deflection increases sixteen fold. The maximum tensile stress occurs at the ends of the strata on the top surface, and at the centre on the bottom surface. It is on these parts of the rock strata that first cracks often appear (Goodman 1980). For a given force, the vertical deflection and shear and tensile stresses are higher in thin strata than in thicker strata. Consequently, an immediate roof composed of thin strata tends to break more easily than a roof composed of thick strata of the same rock type.

In practice, however, the manner in which the load is distributed between successive strata, and the upward force exerted by fill in the cavities must be considered. The distribution of load in two successive strata can be examined by studying their relative deflections calculated from equation (2.5). There are three different cases of relative deflections between two successive strata: the deflections of the lower stratum are greater, equal, or greater in some values of x and equal in others to those of the overlying stratum (Fig. 2.3).

It is obvious that if the deflections of the lower stratum for all values of x are greater than the upper stratum, a gap known as the Weber cavity (Roberts 1981) develops between the strata, and the distributed load, P, along the lower stratum is only due to its own weight. According to equation (2.5), this happens when the ratio of the load per unit length to the flexural rigidity for the lower stratum is greater than that for the overlying stratum. If the Weber cavity is occupied by water of pressure p then equation (2.5) becomes

$$w = (P + p)\frac{x^2(l - x)^2}{24EI_y} \tag{2.9}$$

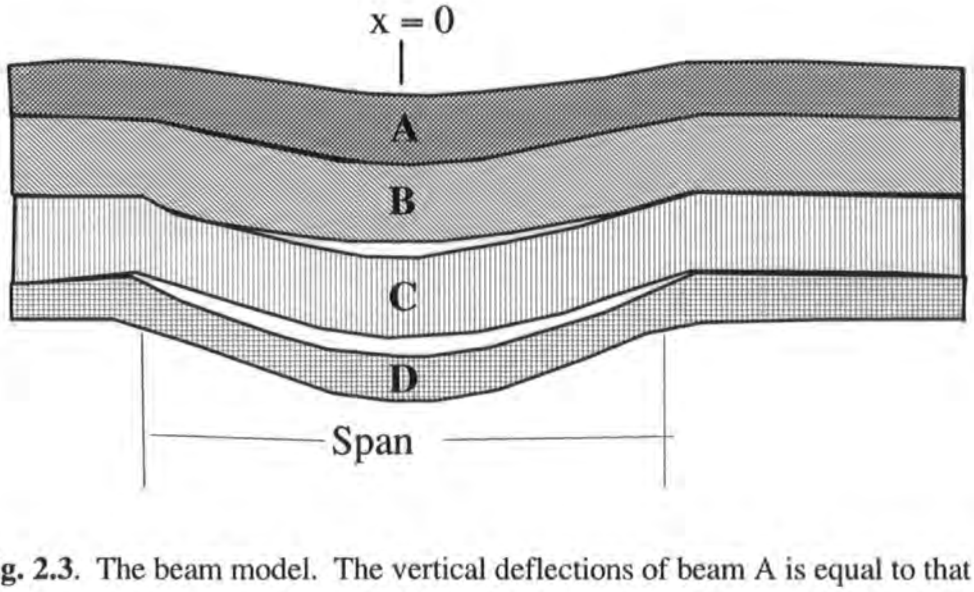

Fig. 2.3. The beam model. The vertical deflections of beam A is equal to that of B for all values of x. Beam B is separated from C only at the centre and therefore its vertical deflection is less than that of C for some values of x and equal for others. The vertical deflection of beam D are greater than that of C for the whole span.

If the deflections of the lower stratum for all values of x are less than the upper stratum, then the overlying stratum will load the lower stratum. The deflection for either stratum can easily be calculated by manipulating equation (2.5) (Obert and Duvall 1967) to get

$$w_1 = w_2 = \frac{(P_1 + P_2)x^2}{24(EI_1 + EI_2)}(l - x)^2 \tag{2.10}$$

where the subscripts 1 and 2 refer to the lower and the upper stratum, respectively. For n layers the above equation can be written as

$$w_n = w_{n-1} = \ldots\ldots = w_1 = \frac{(P_1 + P_2 + \ldots\ldots + P_n)x^2}{24(E_1I_1 + E_2I_2 \ldots\ldots + E_nI_n)}(l - x)^2. \tag{2.11}$$

In most cases, the relative deflection between two successive strata varies with position x along the span. The lower stratum deflects more than the upper stratum at the centre of the panel and the difference decreases to zero near the abutments. Hence, the Weber cavities tend to occur only around the centre of the panel and their effective lengths decrease progressively towards the surface. The load in these cases will no longer be evenly distributed along the stratum but will decrease in the centre and increases toward the abutment. At the centre of the panel, the load on the lower stratum is only due to its own weight and therefore can be determined using equation (2.9). As the value of x approaches 0 or l, the load on the stratum approaches the value given in equation (2.10).

The deflection pattern of the immediate roof, and therefore of the overlying strata, is complicated further by the existence of an upward force exerted by fill in the excavation. As soon as the immediate roof above the mining has collapsed, the rubble from the broken rock starts to provide a cushion for the higher strata and therefore reduces their deflections The stratum immediately above the broken rubble will continue to deflect, however, until the packing material in the cavity is completely compacted.

The potential of using the theory of elastic beams to determine the displacement field and the stress in the main roof (the rockmass between the immediate roof and the ground surface) is impeded by the number of unknowns involved. Although the Young's modulus and the thicknesses of the strata can be estimated fairly accurately from the well log data, the load distribution, the span of the beams and the length of the Weber cavities can only be assumed. Despite all these draw-backs, Obert and Duvall (1967) and Hoek and Brown (1980) have used the form of the equations (2.10) and (2.11) to calculate the strength of the bolts required to support the strata in the immediate roof from collapsing. The theory of elastic beams also provides a background for other methods of analysing stresses and displacement fields in a rockmass.

2.4.2 The whole rockmass as an elastic body

This model is based on the assumption that the rock strata above a coal seam are homogeneous and behave as linear elastic media, and therefore the extraction of the seam causes the overlying rockmass to deform coherently as a single elastic body. Furthermore, the deformation is assumed to be two-dimensional with the long mining axis parallel to a pre-mining principal stress axis. The displacement field and the stress induced by mining are thus calculated by solving the two-dimensional plane strain equations. For isotropic elasticity, these equations are

$$\begin{aligned}
\varepsilon_{xx} &= \frac{1}{E}((1-\nu^2)\sigma_{xx} - (1+\nu)\sigma_{zz}) \\
\varepsilon_{zz} &= \frac{1}{E}((1-\nu^2)\sigma_{zz} - \nu(1+\nu\sigma_{xx})) \\
\varepsilon_{yy} &= \nu(\sigma_{zz} + \sigma_{xx}) \\
\gamma_{xy} &= \frac{1}{G}\sigma_{xy} = \frac{2(1+\nu)}{E}\sigma_{xy}
\end{aligned} \tag{2.12}$$

where ε is normal strain, γ is shear strain, σ is stress, E is Young's modulus, ν is the Poisson's ratio and G is the modulus of rigidity. The only known quantities in the above equations are the elastic constants of the rockmass, which can either be inferred from laboratory measurements or the well log.

Several methods can be used to obtain solutions of the plane strain equations by imposing appropriate boundary conditions. Berry (1960) and Salamon (1968, 1974) obtained the solutions of the two-dimensional stress and displacement in isotropic elastic media in terms of complex potential (the method is outlined in appendix 1). The induced stresses and displacements are determined from the distribution of the convergence and ride components obtained on the basis of the elastic model. The convergence and ride are the vertical and horizontal movements of the roof relative to the floor in the extraction plane. As mining progresses, the convergence, and so the induced stresses, varies until the roof comes into contact with the floor. There are three different solutions from which the induced stresses and displacements are calculated, dependent on the state of the excavation: the non-closure, partial closure and full closure states.

The total vertical and horizontal stresses in homogeneous isotropic media will now be considered for all these states. The total stresses are the result of adding the initial stresses, which are assumed to be lithostatic, and the induced stresses. The extraction is horizontal and advances in the x-direction with its plane perpendicular to the z-axis. The origin of the coordinate system is located at the centre of the panel.

Non-closure state: If the span of the panel $2a$ is less than the length on which the contact between the roof and the floor starts, then the convergence s_z along the excavation at the mining horizon is given by

$$s_z = \frac{2\rho g H(1-\nu)}{G}\sqrt{(a^2 - x^2)} \tag{2.13}$$

where x is the distance along the x-axis, H is the depth to the mining horizon and other variables have been defined elsewhere. From equation (2.13) it can be seen that the maximum convergence occurs at the centre of the panel, and is a function of the vertical initial stress, the span, Poisson's ratio and the modulus of rigidity. The resultant vertical and horizontal stresses on the unworked seam along the x-axis, $|x| > a$, are obtained from

$$\sigma_{zz}(x) = \sigma_{xx}(x) = \frac{q|x|}{\sqrt{x^2 - a^2}} \tag{2.14}$$

where $q=\rho g H$. The equation shows that as $|x|$ approaches a, the end of the panel at the coal face, the stresses increase abruptly. This is in agreement with the field results which tend to show that the maximum stress occurs near the face (e.g. Wilson 1981). Since $|x| = a$ causes the stresses in equation (2.14) to approach infinity, the stresses at the face are assumed to be equal to the root-mean-square stress given by

$$\sigma_{rms} = 2.51\rho g H\sqrt{a/t} \tag{2.15}$$

where t is the thickness of the workings. Since the length of extraction is generally hundreds of times greater than the thickness of the workings, equation

(2.15) suggests that the stress at the face can be as much as 20 times greater than the initial stress.

The distribution of stresses above and below the extraction at the centre of the panel may be calculated from the following formulae:

$$\sigma_{xx}(z) = \frac{qz}{H} + \frac{q|z|(2a^2 + z^2)}{\sqrt{(a^2 + z^2)^3}}$$

$$\sigma_{zz}(z) = \frac{qz}{H} + \frac{q|z^3|}{\sqrt{(a^2 + z^2)^3}} \tag{2.16}$$

where $z = 0$ at the mining horizon and is positive below the horizon. The total stresses calculated using the above equations are demonstrated in Fig. 2.4. The following parameters for a typical coal mining were used in calculations: depth $H = 1200$ m, density $\rho = 2500$ kg/m^3, Poisson's ratio $\nu = 0.25$ and the advance $a = 150$ m. The figure shows that the stresses are dominantly compressive and therefore, as noted by Salamon (1974), this will ensure that the rockmass behaves as a continuum after the extraction. The figure also shows that the total vertical stress after mining is always less than the initial stress.

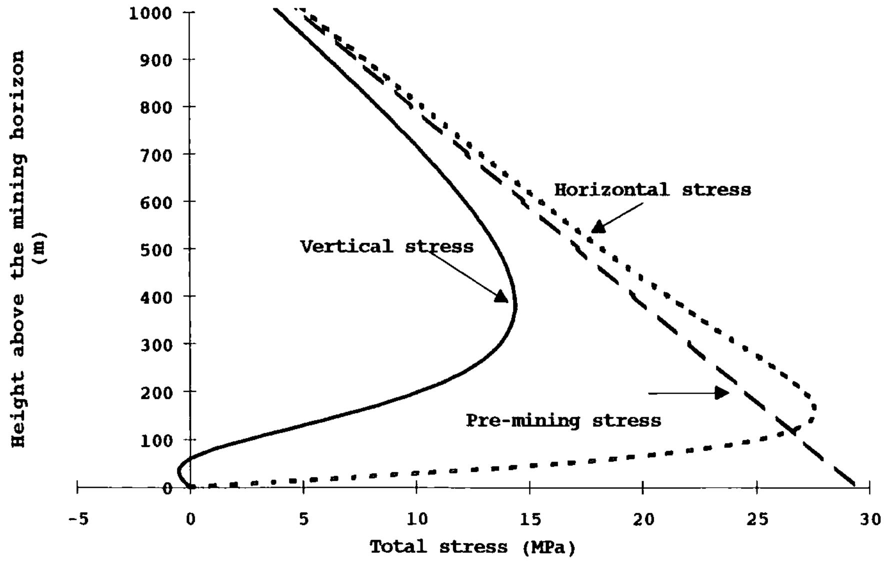

Fig. 2.4. The total stress distribution above the excavation on the centre line of the panel. Negative stress is tensile.

Partial closure state: The closure starts to take place at the centre of the panel, $x=0$, when the convergence is equal to the thickness of the working, s_m. The half span of the panel at this stage, a_c, can be calculated using equation (2.13)

$$a_c = \frac{s_m G}{2(1-\nu)\rho g H} \tag{2.17}$$

As expected, the equation shows that the distance the extraction has to advance before the closure starts decreases with increasing mining depth. For a mine with the parameters given in Fig. 2 4, with a modulus of rigidity G = 5 MPa and a seam thickness of 2 m, the panel length ($2a$) would have to be more than 453 m before the closure starts.

If b is the half length of the contact zone, the total stresses vertically above the centre of the mining are given by

$$\sigma_{zz} = \frac{qz}{H} + \frac{q(z^4 + 2z^2b^2 + a^2b^2)}{\sqrt{(z^2+a^2)^3}\sqrt{z^2+b^2}}$$

and (2.18)

$$\sigma_{xx} = \frac{qz}{H} + \frac{q(z^4 + 2z^2a^2 + a^2b^2)}{\sqrt{(z^2+a^2)^3}\sqrt{z^2+b^2}}$$

The value of b however cannot be determined accurately. If it is assumed that when a is 600 m b is 90% of the length of the panel, then the results of applying the equations above to the parameters defined earlier will be as shown in Fig. 2.5.

Full closure state: For complete closure, the induced stresses vertically above the centre of the panel are given by

$$\sigma_{zz} = \frac{Gta(a^2+2z^2)}{\pi(1-\nu)(a^2+z^2)^2}$$

$$\text{and} \quad \sigma_{xx} = \frac{Gta^3}{\pi(1-\nu)(a^2+z^2)^2}. \tag{2.19}$$

The initial stress does not appear in the above equations which suggests that once complete closure occurs, stresses depend only on the geometry of the working and the elastic constants. The stresses calculated using the above equations and the parameters given for Fig. 2.4 with $a = 900$ m are shown in Fig. 2.6.

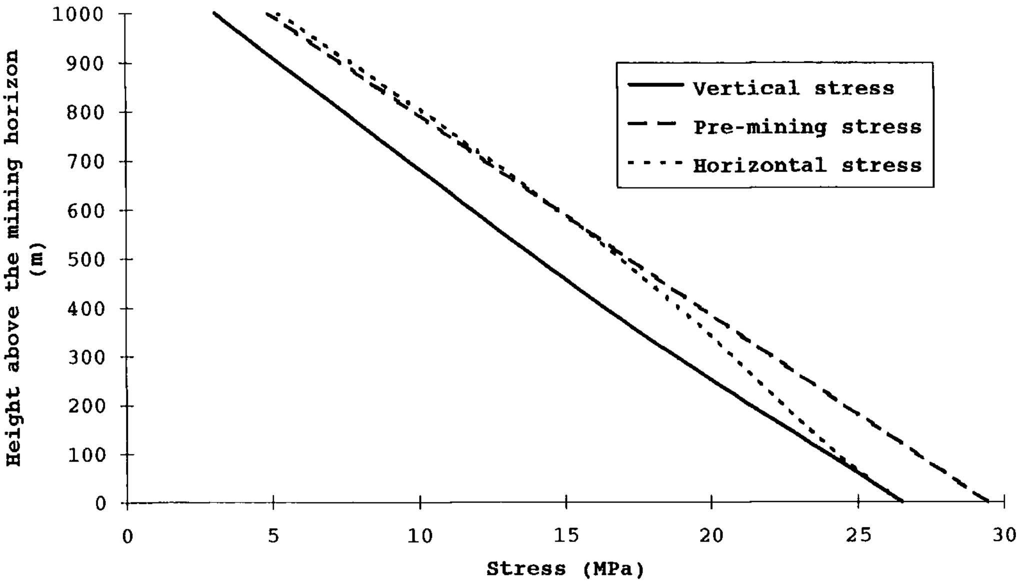

Fig. 2.5. Total stresses for the partial closure state.

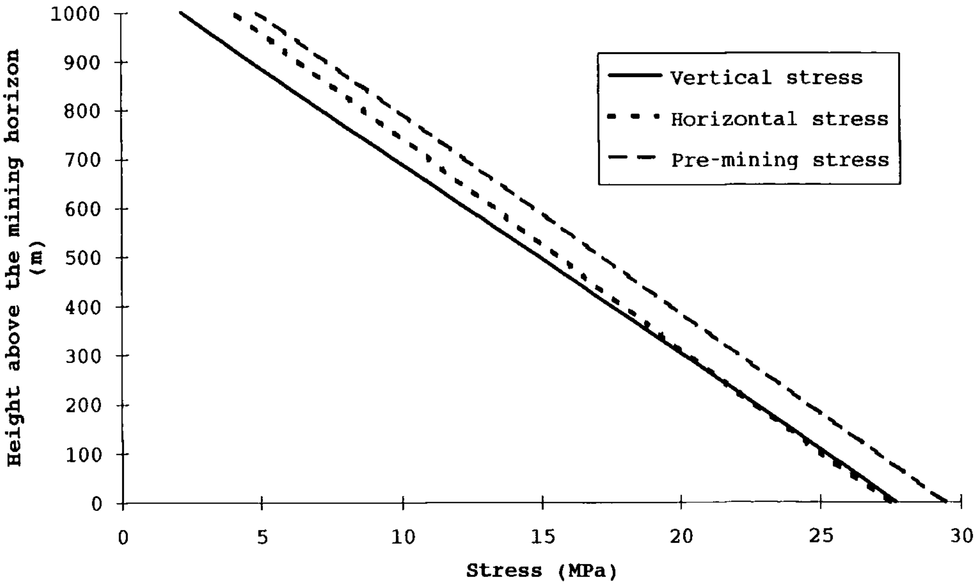

Fig 2.6. Total stress for the full closure state.

2.4.3 In situ measurements

In situ stresses can be inferred from a number of physical quantities measured in the field. Such measurements include strain, acoustic velocity and pressure. Of these the simplest and the most used is strain. The stress, strain and displacements at the ground surface are determined from measurements carried out at the surface whilst the subsurface deformations are obtained from measurements made in boreholes.

Strain in the rockmass can be measured using various gauges, ranging from those based on mechanical systems to those using electrical and photoelastic properties. The simplest and the most reliable measuring techniques use mechanical systems for detection and reading (Franklin 1977). For example, mechanical extensometers, which are used to measure subsurface strains, may consist of a series of anchors positioned at various depths in a borehole and connected to the surface using rods or wires from which the displacement of each anchor relative to the surface is measured. Another example of an extensometer is the magnet extensometer described by Burland *et al.* (1974). It consists of a number of magnetic rings fixed to the wall of a borehole at different depths, and their relative movements are detected by means of reed switches moving in the centre of the borehole. Strain derived from the relative displacement measurements can be used to calculate the corresponding change in stress, using an assumed or measured set of elastic constants for the rockmass.

The change in stress can also be measured 'directly' by using a variety of hydraulic pressure cells. The most widely used hydraulic pressure cell is probably the Glötzl cell, and has been described by Haws *et al.* (1974), Franklin (1977) and Sauer and Sharma (1977). The Glotzl cell is composed of a flatjack filled with mercury connected to a hydraulic diaphragm transducer, which in turn is connected to a read-out unit by two flexible tubes. A flatjack is installed in a slot cut in the rock at the location where pressure is to be measured and embedded by cement mortar. The measurements are taken by applying a pressure from the read-out unit through one of the tubes to the diaphragm transducer. When the applied pressure balances the pressure of the fluid in the cell a valve in the second tube opens and the pressure, which then equals the normal stress in the surrounding rock, is displayed on the read-out unit.

2.4.4 Finite element method

In recent years, the finite element method has become one of the most popular numerical methods for solving the equations of elasticity. This is because the method is capable of handling anisotropic, inhomogeneous and non-linear materials of different shapes while all the operations, which are carried out in terms of matrices, can be performed by digital computers very easily.

Essentially, the method involves dividing the region of interest into a number of small elements, usually triangles and/or rectangles for 2D problems and tetrahedra and/or hexahedra for 3D problems, over which the dependent variables are interpolated. The elements are connected only at ***nodal points*** where the continuity of displacements between adjacent elements is preserved. The displacement over an element is assumed to vary in a systematic manner and therefore can be modelled by a displacement function. The most commonly used displacement functions are polynomials of the first order, i.e. displacements varying linearly, and second order, i.e. displacements varying in quadratic form over an element. As strains are derivatives of displacements, the strains and stresses in an element are constant or vary linearly depending on whether the displacements vary linearly or quadratically over the element, respectively.

A number of text books have been written on the procedures for formulating and applying the finite element method (e.g. Desai and Abel 1972; Zienkiewicz 1977). A constant strain triangle (CST) element will be used here to illustrate how the analysis of the finite element method in plane strain is carried out. As the name implies, the strain, and therefore the stress, in a CST element is assumed constant, and therefore the displacements vary linearly over the element. Fig. 2.7 shows a typical CST. If u_i and v_i are the displacements of node point i in the x and y directions, respectively, then the linear displacement functions are

$$\begin{aligned} u_i &= \alpha_1 + \alpha_2 x_i + \alpha_3 y_i \\ v_i &= \alpha_4 + \alpha_5 x_i + \alpha_6 y_i \end{aligned} \tag{2.20}$$

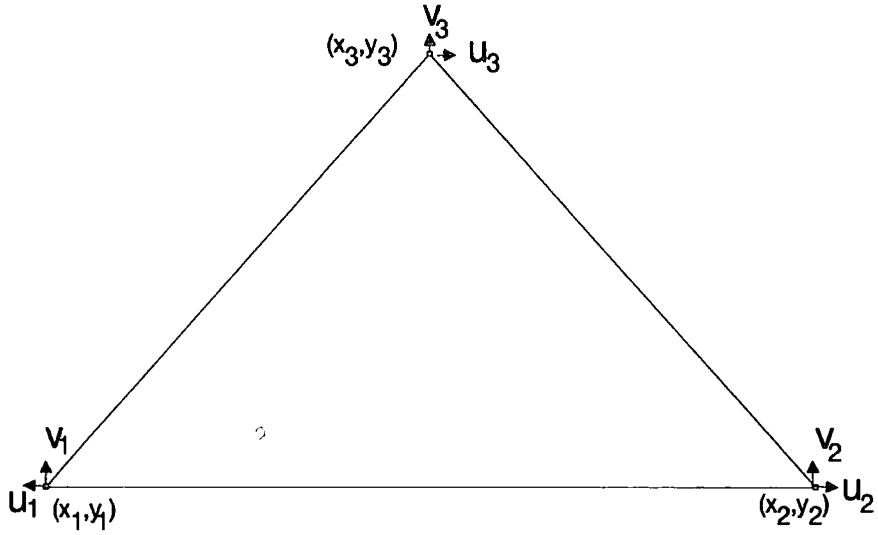

Fig. 2.7. Triangle finite element with three nodal points and six values of displacement.

There are six values of displacement at three nodal points, so equation (2.20) can be written in matrix form as:

$$\{\delta\} = [A]\{\alpha\} \quad \text{or} \quad \{\alpha\} = [A]^{-1}\{\delta\} \tag{2.21}$$

where [A] is a 6 x 6 matrix, and $\{\delta\}$ and $\{\alpha\}$ are column vectors. The normal and shear strain components ε_{xx}, ε_{yy} and ε_{xy} are determined by differentiating equation (2.20) and can be simplified by substituting equation (2.21) as follows:

$$\{\varepsilon\} = \begin{Bmatrix} \varepsilon_{xx} \\ \varepsilon_{yy} \\ \varepsilon_{xy} \end{Bmatrix} = \begin{bmatrix} \frac{\partial}{\partial x} & 0 \\ 0 & \frac{\partial}{\partial y} \\ \frac{\partial}{\partial y} & \frac{\partial}{\partial x} \end{bmatrix} \begin{Bmatrix} u \\ v \end{Bmatrix} = [\psi]\{\alpha\} = [B]\{\delta\} \tag{2.22}$$

where $[\psi] = \begin{bmatrix} 010000 \\ 000001 \\ 001010 \end{bmatrix}$ and strain matrix $[B] = [\psi]^{-1}[A]$.

The stresses are calculated using the plane strain equations, the inverse of equations (2.12), to yield

$$\{\sigma\} = [C]\{\varepsilon\} = [C][B]\{\delta\} \tag{2.23}$$

where [C] is the elastic constant matrix.

In order to determine the displacements of the nodal points of other elements, the nodal point forces have to be obtained. The relationship between the magnitude of the force acting at the nodal points and the nodal point displacement, known as stiffness, is established using the principle of minimum energy of an elastic body. The total potential energy in a strained elastic body is the sum of the energy due to internal stresses and the external forces. For most mining engineering purposes the only external forces acting at the nodal points are gravity (initial force) and surface tractions (imposed boundary conditions). If {F} is the column matrix of the net external force per unit thickness and the thickness of the element is equal to one, then

$$\{F\}\{\delta\}^T = \int\int \{\varepsilon\}^T\{\sigma\}dxdy = \int\int \{\delta\}^T[B]^T[C][B]\{\delta\}dxdy$$

$$\therefore \quad \{F\} = \int\int [B]^T[C][B]\{\delta\}dxdy = [K]\{\delta\} \tag{2.24}$$

The stiffness matrix [K] gives the nodal points forces-displacements relationship.

The above description of how the nodal points forces relate to the displacements for a single element can be extended to any number of elements by using computer programs. A number of finite elements computer programs have been written for commercial use (e.g. PEFEC software) and for academic purposes (e.g. Desai and Abel 1972; Bott, personal communication (see chapter V)). Once the region of interest has been divided up into finite elements (Fig. 2.8), a computer program uses the following steps to solve the linear elastic equations (some programs can automatically divide up the domain into small elements, known as mesh, by specifying the beginning and the end of each grid row and column).

1) For each element, the stiffness matrix [K] and the nodal points load vector {F} are computed.
2) The global stiffness matrix and load vector representing the whole system are assembled by adding the submatrices of [K] and subvectors of {F} into the appropriate locations.

3) Imposed displacement boundary conditions are applied at the appropriate nodal points.
4) The nodal points displacements are computed by solving equation 2.24, using Gaussian elimination or otherwise.
5) Strain and stresses are computed from the nodal points displacements.

To decrease the time and space required by a computer program to process the data, the nodal points are closely spaced only in places where the displacements between adjacent nodal points are expected to vary rapidly. This is demonstrated by the elements in region ABCD of Fig. 2.8, where the removal of the hatched material is expected to cause the greatest variation in displacements. Substantially larger elements can be used if linear rather than constant strain is used, but require six rather than three nodes for triangle elements and eight in place of four for quadrilateral elements.

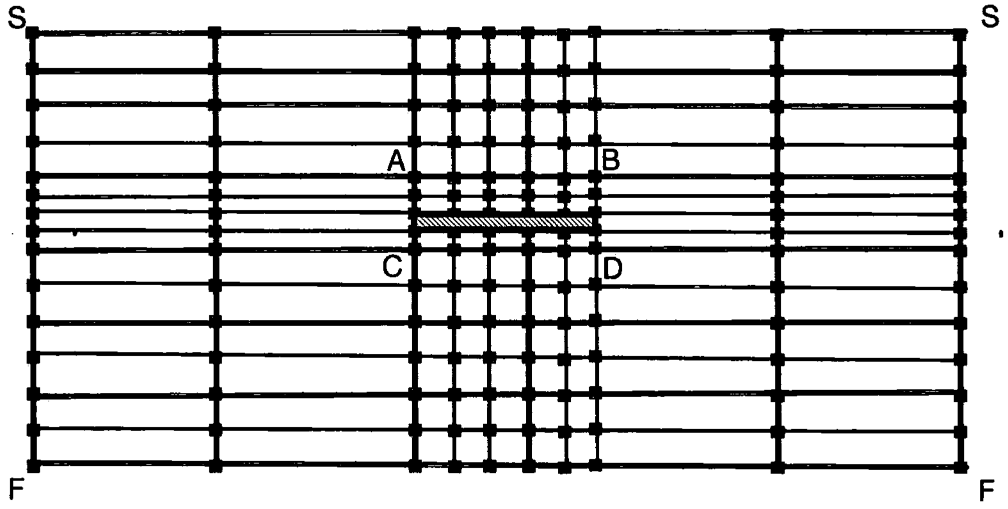

Fig. 2.8. Example of mesh with rectangle finite elements.

In the mining environment, the finite element method has been used to predict the displacements and stresses away from the mining panel (e.g. Diering 1982; Kratzsch 1983). Two different approaches regarding the boundary conditions at the excavation can be used to compute the displacements following mining, fixed tractions and fixed displacements. In both approaches, either the vertical and horizontal displacements of the lower and lateral boundaries (surfaces FF and SF in Fig. 2.8) are fixed at zero, or their tractions are fixed to stresses equal to the pressure. It is important that these boundaries are remote from the excavation, as the effect of mining on displacement extends very far from the mining panel. With these boundary conditions applied, the initial states of the displacements and stresses before the excavation are first calculated. The effect of mining is then determined by either applying forces at the mining panel equal in magnitude and opposite in direction to the initial forces, or by moving the nodal points immediately above and below the panel such that the sum of their vertical displacements equal the thickness of the coal seam extracted.

A section perpendicular to the direction of mining can be treated as a 2-D problem only if the length of the panel is much greater than the width, and the section considered is almost at the middle of the panel. Where this is the case, it is usually for a completed panel with most of the void closed - plane strain can be assumed, with zero strain in the direction along the length of the panel.

2.5 Time dependent effects

The analysis methods discussed in section 2.4 are based on the assumption that the rockmass above the mining panel deforms in a linearly elastic manner. This suggests that removal of coal from underground leads immediately to the change in stresses and displacements in all rock strata up to the ground surface, and that the displacements and the change in stresses cease immediately when the excavation stops. However, observations of ground surface movements have shown that although some of the displacements take place instantaneously (i.e. within the sampling interval of the observation) after the extraction, there is often an increase in displacement after the mining has been halted. The time taken for the displacement to complete can vary from a few months to 5 years after the working has been stopped (Kratzsch 1983).

The most observed and reported time dependent effect of coal mining is the ground surface subsidence. This is the vertical component of displacement of the ground surface. Thus it is easiest to discuss the time dependent phenomenon in terms of surface subsidence.

2.5.1 Active and residual subsidence

To understand the time dependent effects, the distinction must be made between the subsidence which takes place while extraction proceeds, and the subsidence which takes place after the face has come to a halt. The subsidence that takes place as mining progresses is known as the active (or dynamic) subsidence. For a given point on the ground surface, most of the active subsidence occurs when the distance between that point and the coal face is less than a certain distance, known as the 'critical distance' or 'radius of the critical area'. For the coalfields in the UK, where the angle of draw is about 35º, the critical distance for a coal seam at depth *h* is 0.7*h* (NCB 1975). This, however, does not coincide with the distance from the coal face where a point attains its maximum possible subsidence (Fig 2.9). This, as pointed out by Goulty and Al-Rawahy (1995), is due to the fact that as the coal face advances beyond this distance, the increase in subsidence is too small to be detected accurately. The active subsidence curve in Fig 2.9, also known as subsidence development curve after Wardell (1954), shows that the subsidence at an observation point P is 97.5% of maximum when the distance from the coal face is equal to the critical distance. The curve in Fig 2.9 is the NCB development curve (see §2.6.2.1) and is applicable only if the start of the panel is at least 0.7*h* to the left of point P.

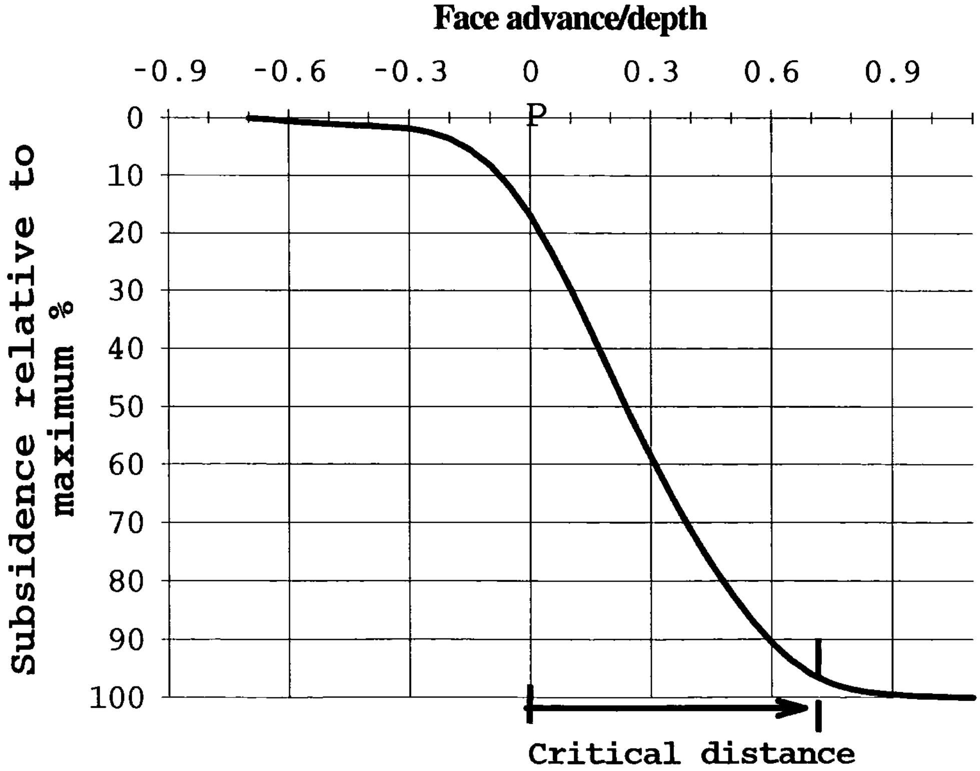

Fig 2.9. Active subsidence of a point P relative to the position of the coal face.

Thus, the active subsidence may be attributed to the elastic behaviour of rockmass and time dependent effects, such as the propagation of subsidence upwards from the mining horizon and the compaction of the broken rubble which forms the goaf. This has been demonstrated by the detailed measurements of active surface movements over underground faces of cyclic type, i.e. mining carried out by cutting, coaling and preparation shifts, reported by Corden and King (1966) and Orchard and Allen (1975). Among them a total of five different cases were reported and almost similar trend of observations was noted. The cutting operation had an immediate effect and produced the highest and approximately constant rate of movement over the period of cutting shift, while a lesser rate of movement which decreased with time was observed during the other two shifts. Orchard and Allen (1975) named these two types of movements as 'the active subsidence element' for the former and 'the time dependent element' for the latter. The latter was attributed solely to the time-dependent effect because no cutting was carried out during coaling and preparation shifts. Although these observations will be discussed again in the next section, it is worthwhile pointing out that most of the active subsidence element may also be a time dependent (viscoelastic) phenomenon.

When the mining has terminated any further subsidence observed is only due to time-dependent effects. This phase of subsidence will be referred to here as the 'residual subsidence'. Depending on its position relative to the coal face when the working stops, the residual subsidence of a given point can be up to 10% of the final value. Orchard and Allen (1975) and Yao and Reddish (1994) defined residual subsidence as the time dependent movement that takes place when the coal face has stopped or has passed beyond the limit of lateral draw. The limit of lateral draw is equivalent to the radius of the critical area and as noted above it does not represent the limit of active subsidence; accordingly the definition of the residual subsidence as the time dependent movement that takes place after the face has stopped is to be preferred (Goulty and Al-Rawahy 1995).

2.5.2 Time dependent models

The time dependent effects in both stages of subsidence, active and residual subsidence, can be attributed to two main factors: the compaction of fragmented roof rock as the overlying rockmass sags on top of it, and the creep of the intact rockmass due to its rheological properties.

The creep phenomenon of rock has been examined by a number of researchers using laboratory measurements (e.g. Afrouz and Harley 1974) and in-situ measurements (e.g. Salem *et al.* 1987). In laboratory measurements, the creep is determined either by measuring the variation of strain with time at constant stress, or the strain is held constant and the variation of stress with time is measured. Times involved range from hours (e.g. Afrouz and Harley 1974) to years (e.g. Ito and Sasajima 1987). In general, if a laboratory test lasts for a long time and the applied stress is well controlled, four stages of deformation depicted in Fig. 2.10 are identified: the instantaneous elastic strain, primary creep, secondary creep and tertiary creep. If the applied stress is suddenly removed during the primary creep stage, the strain decreases, at first rapidly, and then gradually, to zero. However, if the applied stress is suddenly removed during the secondary creep stage, the strain decreases first rapidly and then gradually to a permanent deformation.

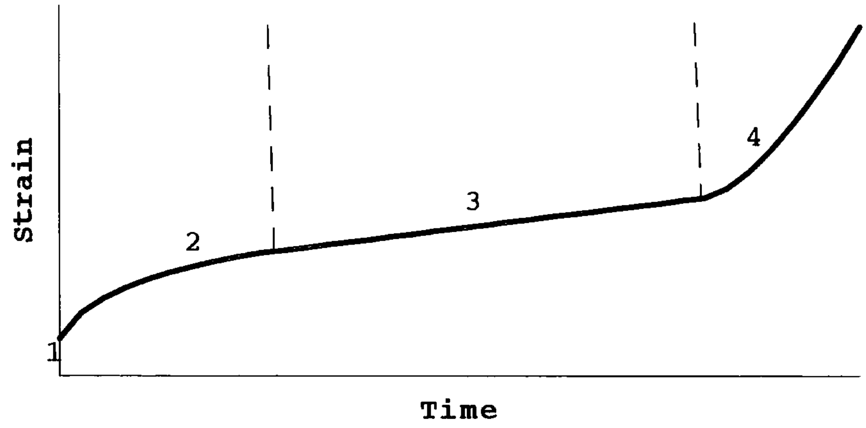

Fig. 2.10. Creep deformation at constant stress. Region 1 is the instantaneous elastic strain, 2 is the primary creep region, 3 is the secondary creep region and region 4 is the tertiary creep.

Most in-situ creep measurements have been carried out in salt mines to study the effect of creep in pillars, and over tunnels to study the mechanism of tunnel convergence for support design purposes. The cavities in salt mines have been observed to close themselves by creep many years after excavation (Kratzsch 1983). In tunnel-support analysis, Salem *et al.* (1987) were able to separate and predict the amount of tunnel convergence caused by the instantaneous movement as the face advances and that due to creep. They also showed that the latter is dominant.

Some authors have attempted to match observed results with empirical functions or with functions derived from simple rheological models. Most of these functions are in logarithmic or exponential form. For given pressure and temperature conditions, the displacement or strain at time t, $D(t)$, can be determined by

$$D(t) = D^f(1 - exp(-t / T)) \tag{2.25a}$$

or

$$D(t) = C + B\log t \tag{2.25b}$$

where D^f is the final displacement when $t \rightarrow \infty$, T is a time constant also known as the relaxation time, C is an instantaneous displacement and B is constant. Equation (2.25a), which can be derived from linear rheological theory using the Kelvin or Voigt model for a viscoelastic substance, gives the displacement that occurs only in the primary creep region. The Kelvin model is composed of a spring and dash-pot connected in parallel. The spring represents a linearly elastic element and the dash pot represents a perfectly viscous element. When a force is applied to such a model, the elastic response of the spring is delayed by the viscous response of the dash pot.

Jarosz *et al.* (1990) summarised a number of empirical and theoretical based functions which relate mining subsidence with time. Most of these are identical to equation (2.25a). They also showed that the subsidence calculated using a slightly modified version of this equation (including a time lag to allow for the 'edge effect') correlated well with most of the active surface subsidence and 'the residual subsidence' observed over three different coal mines in the Appalachian Coalfield. Most of their observations lasted for up to five months, and the residual subsidence in all cases reported was due to coal face advanced beyond the critical distance (the definition of the residual subsidence being the latter one given by Orchard and Allen (1975)). It is important to note that the calculated value of T of about 15 days may not necessarily be appropriate for modelling the actual residual subsidence defined above as that which takes place after mining has stopped, as will be apparent on the next sections.

The variation of the value of D^f with the position of mining face can be taken into account by writing equation (2.25a) as

$$D(t) = D^f(t) - e^{-\frac{t}{T}}) \int_0^t \left(\frac{dD^f(u)}{du} \right) e^{\frac{u}{T}} du$$

or in discrete form (Goulty and Al-Rawahy 1995)

$$D_t = D^f{}_t - e^{\frac{-t\Delta t}{T}} \sum_{i=1}^{t} \Delta D^f{}_i e^{\frac{i\Delta t}{T}} \qquad (2.26)$$

where $D^f(t)$ or $D^f{}_i$ is the final subsidence due to excavation up to time t, $\Delta D^f{}_i$ is the increment in final subsidence due to extraction at time step i, and Δt is the magnitude of the time step.

2.5.3 Factors governing the time dependent effects

Only a limited number of observations of residual subsidence under different conditions that could affect its magnitude and duration have been reported in the literature. Such conditions include the rate of face advance, the position of the surface point relative to the coal face and the lithology of the overlying rockmass.

The rate at which the coal face advances affects the magnitude of residual subsidence by controlling the amount of active subsidence: the higher the rate of face advance the less time is available for active subsidence to take place and therefore the greater the residual subsidence. This, however, may not necessarily imply that the duration of residual subsidence will also increase.

The magnitude of the residual subsidence also depends on the position of the observation point relative to the coal face, when mining stopped. Maximum residual subsidence has been observed to occur at the point of half maximum active subsidence (NCB 1975) (see Fig. 2.12(b)). This is the point where the rate of active subsidence would have been greatest just before the mining stopped.

The lithology of the overburden was found by Orchard and Allen (1975) to be the most important factor in influencing the duration of residual subsidence. They reported two cases in the Durham coalfield where subsidence continued for several years after the working had ceased. One was in North Durham where the existence of a 23 m thick Carboniferous sandstone above the Harvey seam at 105 m depth delayed the beginning of the residual subsidence for four years and extended its duration for a further four years. Yao and Reddish (1994a) also claimed to have found empirically from other observations, that the duration of residual subsidence depends on the percentage of hard rock in the overburden. However, after the correction of an error (Goulty 1994; Yao and Reddish 1994b), their conclusion was that the duration of residual subsidence increases with decreasing percentage of hard rock, in contradiction to the findings of Orchard and Allen (1975). This may be due to insufficient number of data points used by Yao and Reddish (1994a) (Goulty and Al-Rawahy 1995).

2.5.4 Relaxation time

In the viscoelastic model, the relaxation time represents the viscoelastic response of the ground and is defined as the ratio of the viscosity to the modulus of elasticity (Young's modulus in case of uniaxial compression) of the rock. For given physical properties of the rock, the relaxation time is constant and so would be expected to be independent of the rate of face advance and the geometry of the workings. The credibility of this statement will now be examined.

The measurements of active subsidence in cyclical longwall mining at 74 m depth reported by Orchard and Allen (1975) suggested that the rate of time dependent subsidence, following a single cutting shift, had decreased from 0.33 mm/h to 0.17 mm/h over a period of one day. Using the derivative of equation (2.25a), this decay implies that the relaxation time following a single cutting shift is about 1.5 days. However, the complete plot of time-subsidence curve of the same results suggests the relaxation time of about 10 to 12 days. A relaxation time close to this was also reported by Jarosz *et al.* (1990) when they fitted equation (2.25a) to composite subsidence development curves of three different cases. The depths to the workings in these cases range from 90 to 245 m. Goulty and Al-Rawahy (1995) agreed that a similar value for the relaxation time, in the range of 10-15 days, would have been found by using equation (2.26).

A significantly longer relaxation time can be inferred from the delayed residual subsidence in the Durham Coalfield reported by Orchard and Allen (1975) and in the South Wales Coalfield reported by Collins (1978). Although subsidence in these observations did not occur continuously, the relaxation time can be approximated to be in the order of a year.

It is evident from the discussion above that different types of observation in different circumstances are giving widely different values of the relaxation time. Due to a limited number of observations involved, the following two conclusions can only be inferred with caution. Firstly, there is a fundamental difference in the mechanics of deformation between the phases of active and residual subsidence, and therefore they cannot be described by the same simple viscoelastic model with the same relaxation time. Thus, secondly, the duration of residual subsidence cannot be predicted, empirically or otherwise, even when the magnitudes of active and residual subsidence are known.

The mechanics of deformation during the active and residual subsidence deduced from the observations discussed above can be summarised as follows. During active subsidence, the immediate effect of mining seen at the ground surface is due to a viscoelastic deformation response with a short relaxation time due to compaction of goaf material as the overlying rockmass, which has detached from the main roof, subsides on it. The main roof itself reacts by settling down in a gentle curve with elasto-plastic deformation: the curvature is convex upwards over the face and concave upwards behind it (Kratzsch 1983). It is at the inflection points where the stress is highly concentrated and where bed separation tends to occur. As the coal face moves forwards, the region of deformation moves with it and the deformed rocks relax behind.

During residual subsidence, no stress changes are induced by mining advance and therefore the region of high deformation is stationary. The stresses in this zone dissipate in situ as the strata relax viscoelastically or elastoplastically and the gaps between bedding planes close. Depending on lithology and thickness of the overburden, the relaxation time at this stage appears to be much greater than that observed during active subsidence. If the overburden predominantly consists of thick beds of competent rocks, e.g. massive sandstone, higher stresses will be required to overcome their static friction or inertia force before the movement can take place (Orchard and Allen 1975). Such deformations are characterised by longer relaxation times.

2.6 Subsidence

Ground surface subsidence is the most widely observed and discussed effect of underground mining. This is not only because subsidence data can be collected cheaply and processed quickly, but also the subsidence can be used to determine the ground horizontal strains (National Coal Board 1975), which are the major cause of damage to structures following mining. The factors influencing the surface subsidence and the methods of predicting its magnitude have been studied and reported widely in the literature.

2.6.1 Factors influencing the subsidence

•Thickness of the coal seam extracted. It is obvious that the magnitude of displacement experienced by the rock strata above the mining horizon will increase in direct proportion to the thickness of the coal seam extracted. Depending on other factors, the maximum subsidence at the ground surface can reach up to 90% of the thickness of the seam extracted.

•Face advance. It was stated in §2.4.1 that most of the effects of the face advance on the subsidence stop when the distance between the face and the observation point is more than the critical distance. By neglecting the time dependent effect, within the critical distance the subsidence is a function of the face advance, and outside it the face advance has no effect on the subsidence.

•Rock properties. The lithology of the rockmass above the panel influences the magnitude of the surface subsidence in a number of different ways. The physical properties of the rock strata in the vicinity of the working may determine the extent of the immediate roof that deforms plastically, which in turn influences the movement of the overlying rockmass. In the main roof, the existence of a competent rock, such as thick beds of sandstone, may cause bed separation to occur, in which case the active subsidence at the surface would be less than otherwise.

•Width and depth of the panel. According to beam theory (§2.4.1), an increase in the span of the beam increases its deflection; thus the wider the panel the greater the surface subsidence. An increase in the depth of the working, on the other hand, causes a decrease in subsidence observed at the surface. This is due to the reduction in displacement with distance from the mining horizon. Examples of maximum surface subsidence caused by mining at different depths and of different panel widths are shown in Fig. 2.11. The values are taken from the empirical curves of the National Coal Board (see §2.6.2.1).

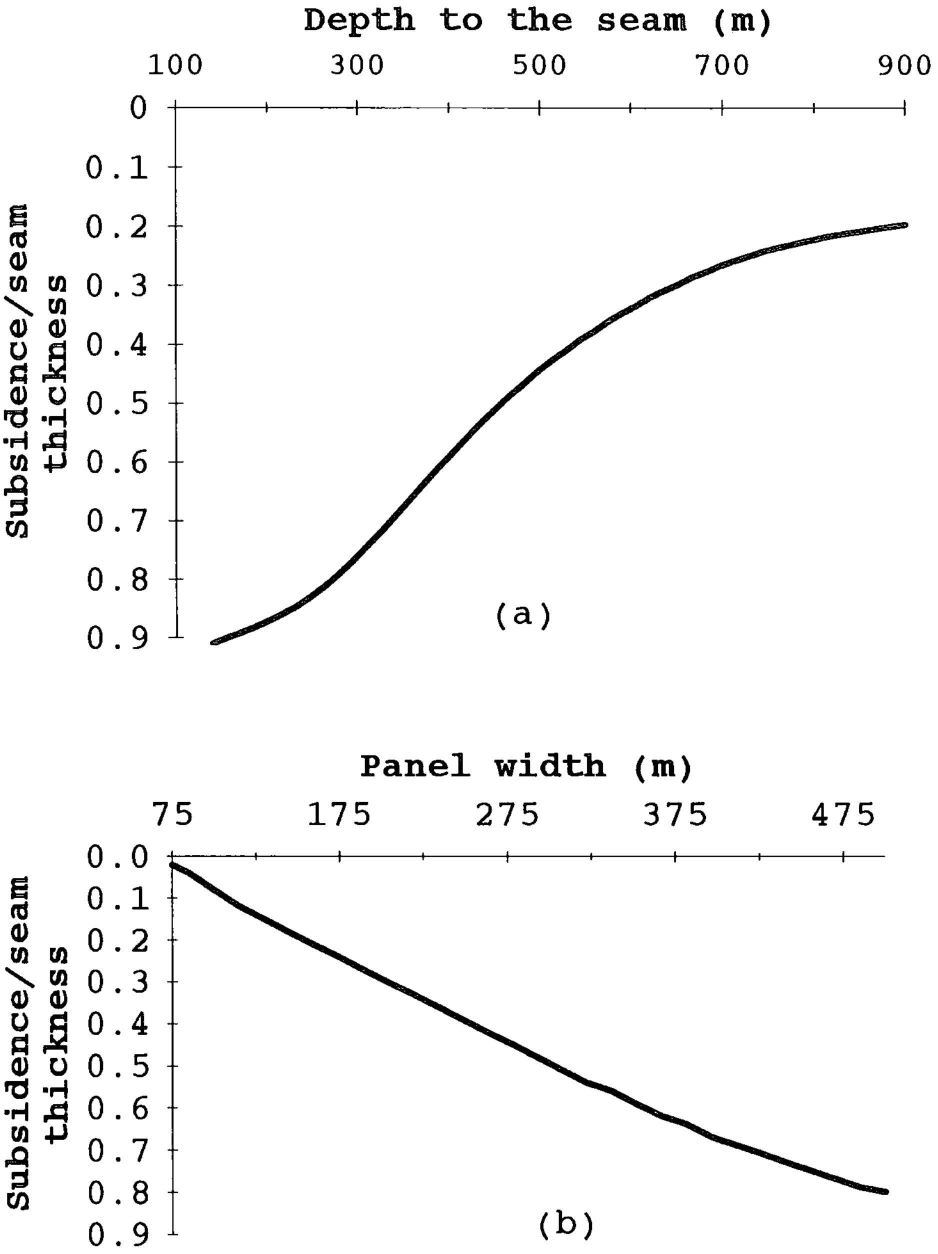

Fig. 2.11. Relationship of maximum subsidence to depth and width: (a) width equal to 250m and (b) depth equal to 550m.

•Geological faults. Lee (1966) compiled a number of surface subsidence observations made near surface faults. Most of the results showed that faults modify the normal smooth subsidence profile by creating steps. In virgin workings, the movements of the subsidence steps tend to be towards the panel, regardless of the direction of the throw of the fault. However, at present the influence of faults on subsidence cannot be quantified accurately because their exact positions at the surface are not always easy to determine, and if they are known the surface observation lines are often set out to avoid them.

2.6.2 Methods of predicting subsidence profiles

2.6.2.1 Empirical prediction methods

The amplitude and shape of the subsidence profile can be predicted by a number of empirical methods. One method is to use the empirical graphs published by the National Coal Board (NCB) (1975), which were obtained by averaging observations of surface subsidence in UK coalfields. They give the amount of subsidence, per unit thickness extracted, in terms of the depth to the seam, the width and the length of the panel, and the distance from the observation point to the face. Essentially, three different sets of graphs are used to predict the amplitude and the shape of the complete subsidence profile. The maximum subsidence per unit thickness of the coal seam extracted is first read off from the graphs which relate the subsidence to the width and the depth of the panel. When the length of the panel is not enough to cause the maximum subsidence, the ratio predicted is adjusted by using the second set of graphs, which relates the length extracted, as a fraction of the depth, to the actual subsidence-maximum subsidence ratio. The third set of graphs is used to obtain the shape of the subsidence profile, as subsidence decreases from the centre of the panel towards the edges. Most subsidence values estimated by these graphs are within ±10% of the actual values.

The subsidence profiles constructed from the NCB graphs show that for a given depth h, and a total panel length of $1.4h$, the maximum subsidence occurs when the coal face has advanced $0.7h$ from the observation point. The radius of the critical area is therefore equal to $0.7h$. The profiles also show that the subsidence extends outwards beyond the edges of the panel with an angle of draw in the range of 25 to 35°. It is important to note that the observations used to construct these graphs were made after settlement had finished, and therefore they show the total subsidence including the time-dependent contribution. To take the time factor into account, the National Coal Board (1975, pp 38-39) has also published a typical subsidence development curve. This predicts the active subsidence at a point as a coal face passes below and beyond it as a percentage of the maximum subsidence over the centre of the panel. It may be deduced from the NCB's development curve that the active subsidence at a point equals the total subsidence when the face has passed beyond the point by a distance of 1.1*h* (i.e. the residual subsidence will be zero for such a point). The NCB's typical subsidence development curve, the final subsidence profile and the difference between the two are shown in Fig 2.12. The figure shows that the maximum residual subsidence occurs at about 0.23*h* where the active subsidence is 50% of the maximum subsidence.

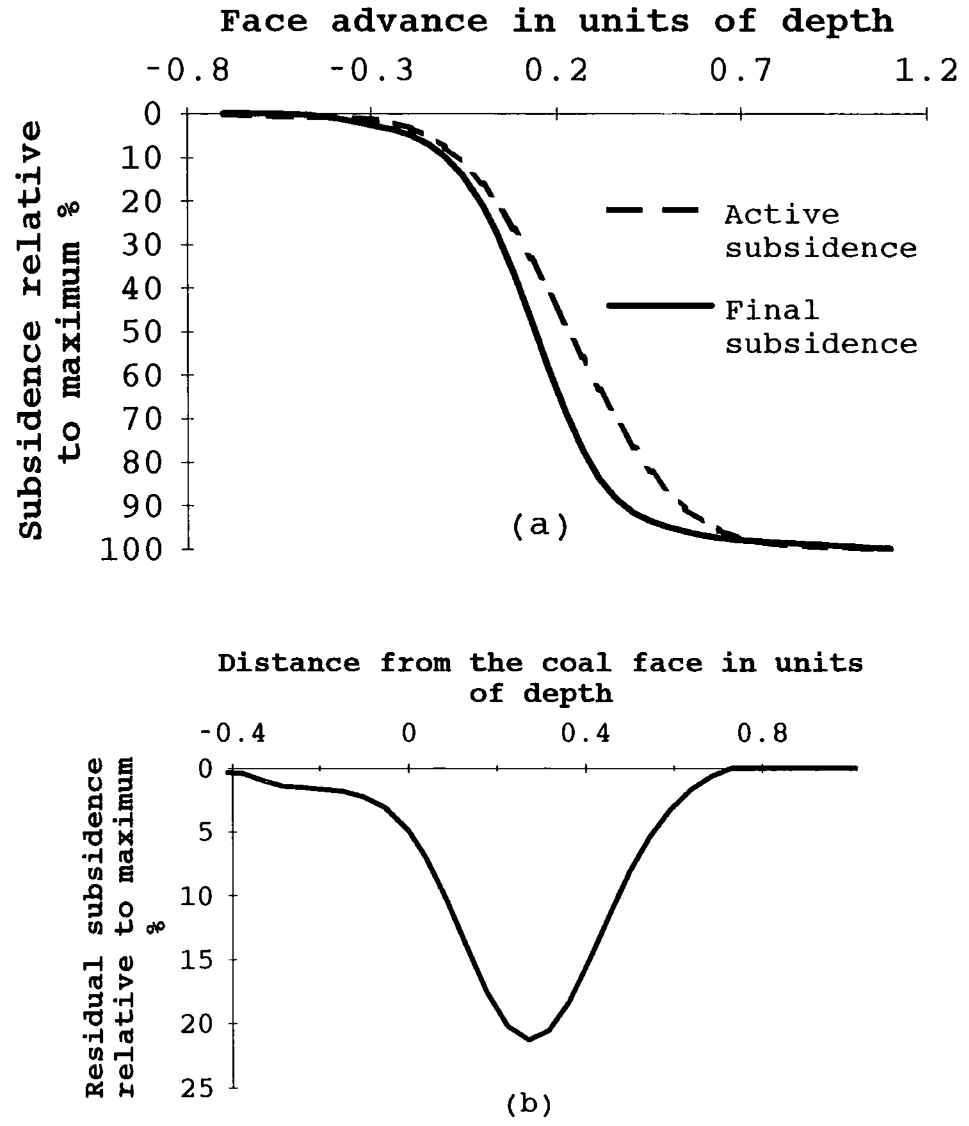

Fig 2.12. (a) The National Coal Board's (1975) active and final subsidence profiles and (b) the residual subsidence, the difference between the final and active subsidence.

Some authors have attempted to describe the shape of the subsidence profile using mathematical functions (e.g. King et al. 1975). An example of such a function is the hyperbolic tangent function, where the active subsidence $s(x)$ is given by

$$s(x) = \frac{S}{2}\left(1 - tanh(\tfrac{bx}{h})\right) \qquad (2.27)$$

where x is the distance from the point of half maximum subsidence measured away from the centre of the panel, h is the depth of the seam, S is the maximum subsidence and b is constant. For UK coalfields a value of b = 5 has been suggested (King *et al.* 1975). The profiles calculated from the hyperbolic tangent functions with b=5 and 3.25 are compared with the profile obtained from the NCB development curve in Fig. 2.13. The hyperbolic function with b = 3.25 seems to fit the empirical curve better than that of b = 5.

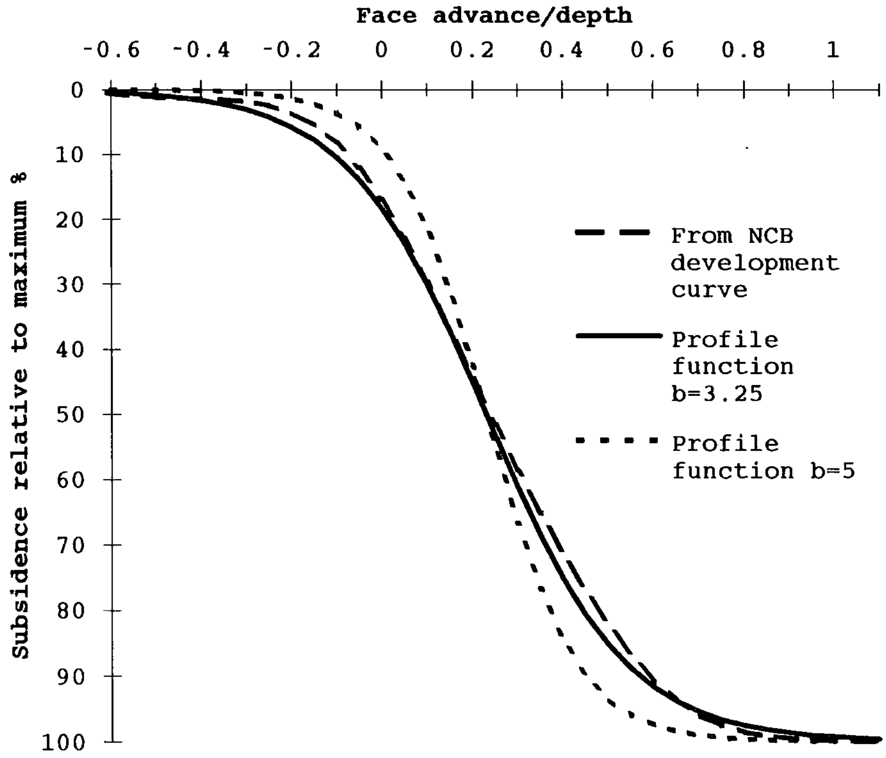

Fig. 2.13. Surface subsidence profile predicted by the NCB development curve and hyperbolic tangent functions.

Another empirical method of predicting subsidence is the zone area method, which has been used to predict surface subsidence in many coalfields of western Europe. Marr (1975) suggested that the method can be adopted for British mining conditions and used to predict subsidence in British coalfields. Basically, subsidence of a surface point in this method is estimated first by constructing a number of concentric rings around the point, the radius of the outer ring being equal to the critical distance. The magnitude of the subsidence contributed by each ring is then obtained by multiplying the proportion of the area extracted by its subsidence factor. The summation of the subsidence contributed by each ring gives the subsidence at the surface point. Marr (1975) found that three, five or seven rings are suitable for most cases and that the proportion of the area extracted of each ring has to be raised by 2.296 before being multiplied by its subsidence factor. The subsidence factors are derived from the known values of subsidence, obtained from empirical curves or observed data, and the proportion of each ring extracted. The major problem with this method is that it predicts final subsidence of 0.5 S_{max} above the position of the coal face, but observations (such those in NCB curves) show only around 0.2 S_{max}.

2.6.2.2 Numerical methods

Various numerical methods have been formulated for predicting surface subsidence. Hackett (1959) used a two-dimensional plane strain solution for a crack in an isotropic homogeneous rock at infinite depth, similar to that outlined in section (2.4.2), to calculate displacements at large distances from the excavation. However, Hackett showed that the displacements calculated at the ground surface were similar to the observed data only qualitatively. This is because rocks are rarely homogeneous and isotropic, and the depth/width ratios of most workings are not large enough for the depth to be assumed infinite.

Berry and Sales (1961) and Berry (1963a, b, 1964) suggested elastic models based on a transversely isotropic rockmass. The elastic moduli in x and z directions (planes along and perpendicular to the mining panel) were assumed to be different, and the functions of their ratios were deduced from graphs of measured subsidence. Approximate solutions for non-closure and partial closure and the exact solution for complete closure in a semi-infinite medium were obtained. The solution for complete closure appeared to correlate well with the observed data. However, the similarity was made possible only when the thickness of the coal seam extracted was assumed to be a third of the actual extracted thickness. Moreover, the Young's modulus in the vertical direction was assumed to be twice that in the horizontal direction, even though the direction of the smallest Young's modulus in sedimentary rocks tends usually to be perpendicular to the bedding. The unrealistic values of the physical parameters required by the model, to force agreement between the calculated and observed data, can be attributed to the fact that the strata above the panel do not deform elastically as a homogeneous entity as assumed in the model. Dahl and Choi (1973), for example, found that strains in rock strata far from the mining horizon frequently exceed the elastic limit.

Another numerical method that can be used to predict surface subsidence is the finite element method discussed in the previous section. In this method, the heterogeneity due to the presence of different rock units in the overlying rockmass and the existence of a plastic zone above the mining horizon can be handled easily. The influence of the plastic zone on subsidence can be taken into account by assigning the values of Young's modulus and Poisson's ratio less than their actual values.

2.7 Differential subsidence

It has already been stated that the magnitude of subsidence decreases away from the centre of the panel and away from the mining horizon. Thus, if the subsidence profile is taken along a line parallel or perpendicular to the plane of the excavation, it is possible to determine the differential subsidence along the line by subtracting the values of subsidence of adjacent points. In mining subsidence engineering, the differential subsidence along a line at the ground surface can be used for calculating the horizontal strain (NCB 1975). As the main interest of the subject reported here is the change that takes place underground, only the subsurface subsidence and therefore the differential subsidence along a (vertical) line perpendicular to the mining horizon, will be considered.

Apart from direct measurements in boreholes using extensometers, subsurface subsidence can also be obtained using empirical and finite element methods. The empirical curves of the NCB, for example, can be used to determine subsurface subsidence of a given stratum by taking that stratum as datum, i.e. as the ground surface, from which the depth to the mining horizon is measured. The subsurface subsidence can also be computed by finite element methods by resolving the displacement field at a given horizon into its vertical components.

Shu and Bhattacharyya (1990) devised a simple technique of calculating subsurface subsidence from surface subsidence using a mathematical model. The model is based on the assumption that a cross-sectional area subsided at any horizon between the workings and the ground surface is constant and equal to the subsided area at the ground surface. The model is depicted in Fig. 2.14, and shows two elements, element ABCD at the surface and element abcd at a horizon at depth *h* below the ground surface. According to the model, the elemental area ABCDA equals area abcda and therefore the relative lengths from the centre of the panel, AB and ab, as well as the relative values of ground and subsurface subsidence, AC and ac, can be derived.

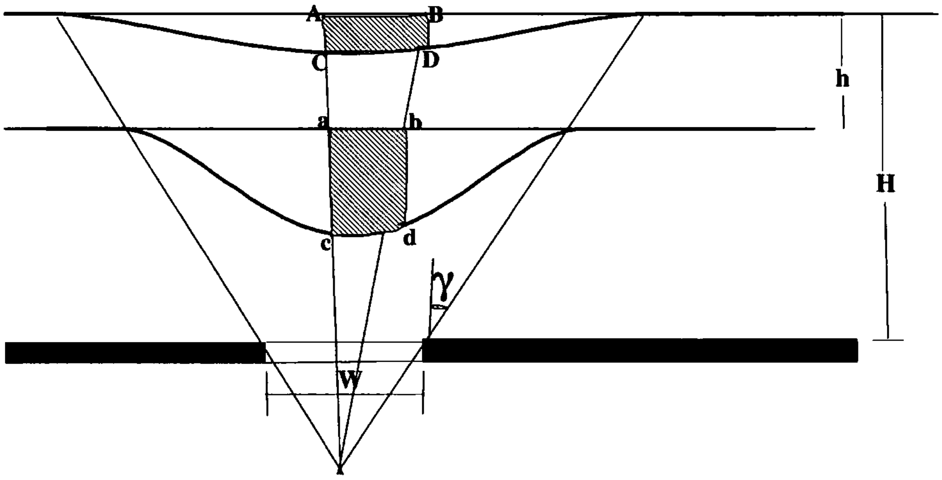

Fig. 2.14. A model used to derive the relationship between the subsurface and ground surface subsidence.

If the lengths AB and ab are equal to x_o and x_s, respectively, then it can easily be shown that

$$\frac{x_s}{x_o} = \frac{H - h + \frac{W}{2}\cot\gamma}{H + \frac{W}{2}\cot\gamma} \tag{2.28}$$

where γ is the angle of draw and other variables are defined in Fig. 2.14. The relationship between subsidence at these points, $s(x_s)$ and $s(x_o)$ is derived by assuming that x_o and x_s are infinitesimal distances such that the subsided areas can be approximated by $x_s s(x_s)$ and $x_o s(x_o)$. Hence, using the relationship above gives

$$s(x_s) = \frac{H + \frac{W}{2}\cot\gamma}{H - h + \frac{W}{2}\cot\gamma}\, s(x_o) \tag{2.29}$$

A subsurface subsidence profile calculated using the above technique is compared with that obtained from empirical curves of NCB in Fig. 2.15. The surface subsidence was determined using the NCB empirical curves. The parameters used were H= 500 m, h=100 m, W = 200 m, γ=35º, the thickness of the coal seam extracted equals 2 m and the face advance was more than 700m, so that maximum subsidence at the ground surface has developed.

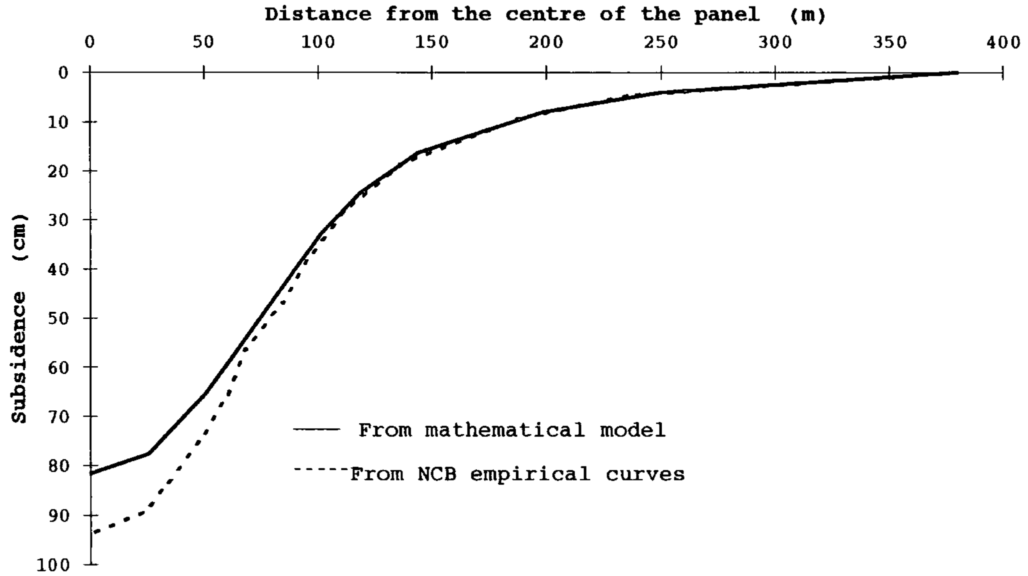

Fig. 2.15. Subsurface subsidence at a horizon 100 m below the ground surface calculated from the mathematical model and from the empirical curve of the National Coal Board.

Figure 2.15 shows that away from the centre of the panel, from about 50 m, there is a good agreement between the subsurface subsidence calculated using the mathematical model and that obtained from the empirical curves of the NCB. Towards the centre of the panel, however, the results deviate gradually from each other with a maximum discrepancy of about 13% at the centre. The discrepancy suggests that the assumption of the constancy of the area subsided between horizons is violated, especially at the centre of the panel where bed separation is more likely to occur.

2.7 Hydrogeology and permeability effects

2.7.1 Change in water table

Hydrogeology can be affected by mining subsidence in a number of different ways. Subsidence in an embankment that separates a low-lying area from a body of standing water can cause flooding to occur. In an area which has water that is interconnected throughout the near-surface layer, surface subsidence can cause the depth to the water table measured from the ground surface in the subsidence trough to decrease as shown in Fig. 2.16. Often, however, water in surficial clay layers, in particular for parts of the UK where the near-surface is glacial drift, tends to exist in isolated patches with perched water tables, and the situation depicted in Fig. 2.16 would be a simplification.

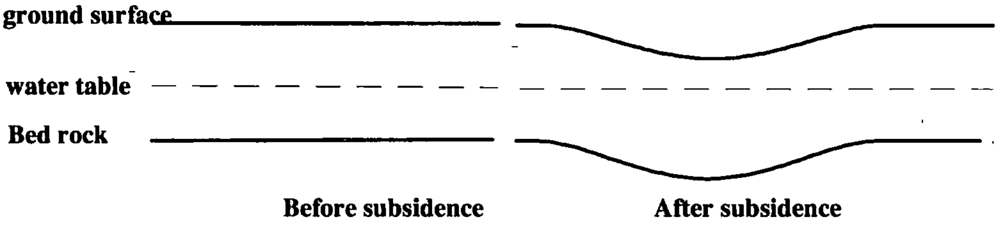

Fig. 2.16. The effect of subsidence on depth to the water table. .

2.8.2 Change in porosity and permeability

One of the most significant effects of subsidence on geohydrology was that attributed to the cause of the disaster at Aberfan village in South Wales in 1966, where colliery spoil moving as a flow-slide down the side of a hill was deposited in the village. The mining subsidence was said to have contributed to the disaster by influencing the movement of water in the thick massive sandstone of the Pennant Measures, which forms the hillside and extends down the hill to the area where the tip complex was situated (Mather *et al.* 1969). Mather *et al.* (1969) analysed data from this area and found that there was an increase in underground fissure sizes and development of surface fissures in areas which have been subjected to tensile horizontal strain due to mining. These effects, in turn, increased the reservoir capacity of the sandstone and the speed with which the water was transmitted, i.e. increased the permeability.

The change in permeability due to mining was also studied by Holla and Buizen (1991). Their in-situ measurements were performed by first sealing a portion of a borehole to be tested, the length varying between 12 and 15 m. With the drill string filled with water and pressure stabilised at a fixed value, the water flow rate was then monitored for 10 minutes. As water loss is a function of permeability and pressure, the permeability was determined by plotting water loss against pressure and measuring the slope of the straight line obtained.

Chapter 3

Shallow seismic reflection technique and test profile results

3.1 Introduction

In this chapter, the surface seismic reflection method is briefly outlined, and the acquisition, processing and results of a test profile at Bishopwood, Selby, site where the time-lapse surveys were carried out, are described.

It is not intended here to review all the applications and developments of the shallow seismic reflection method, but only to discuss the relevant aspects of the method to the time-lapse surveys, which are presented in the following chapters. For further discussions of the method, the reader is referred to the references cited in the text.

3.2 Shallow seismic reflection technique

Shallow seismic reflection surveys on land are surveys carried out for the purpose of investigating targets at shallower depths than are typical for hydrocarbon exploration: a maximum of 1 s two-way traveltime, although in some cases the target may lie in the uppermost 100 ms. Reflections from such shallow targets can provide valuable information for engineering, mining and groundwater applications. However, it is only in recent years that a significant number of case studies on the applications of land shallow reflection seismics have started to appear in the literature (e.g. Singh 1986; Knapp and Steeples 1986). This can primarily be attributed to the availability of powerful computers, which has helped to cut the cost of processing, whilst improving the data quality and increasing the capability of interpretation. Secondary factors have been the development of suitable recording systems and of a variety sources, which are cheap and safe yet produce short seismic wavelets to yield good resolution.

The feasibility of using the shallow seismic reflection technique to image structures in the coal mining environment has been well documented in the literature (e.g. Ziolkowski and Lerwill 1979; Fairbairn *et al.* 1986; Gochioco and Cotten 1989; Pietsch and Slusarczyk 1992; Miller *et al.* 1992). Seismic data can be used to determine the location of geological faults in the coal seam prior to mining, and therefore appropriate measures can be taken to avoid unnecessary costs. One of the first successful shallow reflection surveys in coal exploration was reported by Ziolkowski and Lerwill (1979). They demonstrated that faults with a small vertical throw of about 5 m at 800 m depth could be resolved by using the right size of explosive charge and appropriate acquisition parameters.

In groundwater exploration, even if the water table does not coincide with a change in lithology, the seismic reflection technique can still be used to determine its depth if the presence of water in the rock has caused a significant change in acoustic impedance. This is often the case where the water table is very shallow or the formation is very porous. In some rocks, however, a water table may represent a change which is not only small but also a gradational one (e.g. in chalk) and therefore no strong acoustic impedance contrast may be expected (Davies *et al.* 1992). In cases where no stratigraphic information is available to distinguish the reflections from the water table from those due to lithological changes, shear wave reflection data may be used to constrain the interpretation. Shear waves are not affected by the presence of water in sediments and therefore cannot be reflected off the water table.

For site investigation, seismic reflections from the bedrock may be used to infer the bedrock structure and its depth. Although the depth to the bedrock can commonly be determined quite easily using the seismic refraction method, the reflection method can be equally successful (Hunter *et al.* 1984; Singh 1986; Miller *et al.* 1989; Meekes *et al.* 1990) with the extra advantage that a shorter profile can be used.

3.2.1 Factors influencing the data quality

Most studies of the applications of shallow seismic reflection surveys have shown that the quality of data relies heavily on how and where the data are acquired. For example, incorrect acquisition parameters may result in interference from surface waves and refracted arrivals to such an extent that all the reflection arrivals in a record are completely masked even after processing. The data quality is also very dependent on the near surface geology. The choice of field acquisition parameters and instrumentation for shallow seismic reflection surveys has been fully discussed by Ziolkowski and Lerwill (1979), Knapp and Steeples (1986a and b) and Hill (1992).

3.2.1.1 Seismic sources

Depending on the environmental conditions at and just below the ground surface, the choice of seismic source can be a major factor influencing data quality (Bredewout and Goulty 1986). It is for this reason that many researchers have embarked on projects to compare seismic sources (notably McCann *et al.* 1985; Miller *et al.* 1986; Pullan and MacAulay 1987). An ideal seismic source would be one that is cheap, safe, efficient to operate, and produces a repeatable spike-like wavelet (i.e. a Dirac delta pulse). However, the Dirac delta pulse, which has a zero-phase spectrum and a flat amplitude spectrum for all frequencies, cannot be reproduced in the field. Since the ground is a very effective high cut filter, a desirable seismic source is often considered to be the one that generates and directs into the ground as much high frequency energy as possible (Hill 1992). A wavelet produced by such a source will have short duration and therefore increases the resolution, provided also that it has broad bandwidth.

Seismic sources used on land can be divided into two types: surface sources, such as sledge hammer, weight drop and vibrator; and subsurface sources, such as detonator, dynamite, sparker and buffalo gun. Comparisons between the two types have shown that subsurface sources usually produce higher frequency signals, and (apart from the sparker source) often have higher total energy than the surface ones. The compacted materials at depth ensure good source coupling and most of the energy generated by the subsurface source is directed into the ground, whereas a significant proportion of the energy is converted into airwaves or ground roll for surface sources. The signals produced below the surface are also less affected by anelastic attenuation, which is greater at higher frequencies due to transmission through the weathered layer compared with the signals generated at the surface.

3.2.1.2. Ground condition

The quality of signal generated by any type of seismic source is highly influenced by the near surface geology. Pullan and MacAulay (1987) showed that the quality of signals generated by subsurface sources deteriorated systematically as the surface changed from water-saturated fine-grained material to drier, coarser material. Subsurface sources used in these experiments were 8- and 12- gauge buffalo guns. A similar deterioration trend was also noted for surface seismic sources (sledge hammer and weight drop), with the exception of dry fine-grained materials where a weight drop produced excellent results.

The effect of near surface material on seismic signals can also be seen in Fig 3.1. The figure shows four different field records along the same seismic profile, in Bishopwood (see §3.3), obtained using a sledge hammer as a seismic source. The poor quality of records (c) and (d) in Fig. 3.1 is due to poor source coupling caused by dry ground near a farm track.

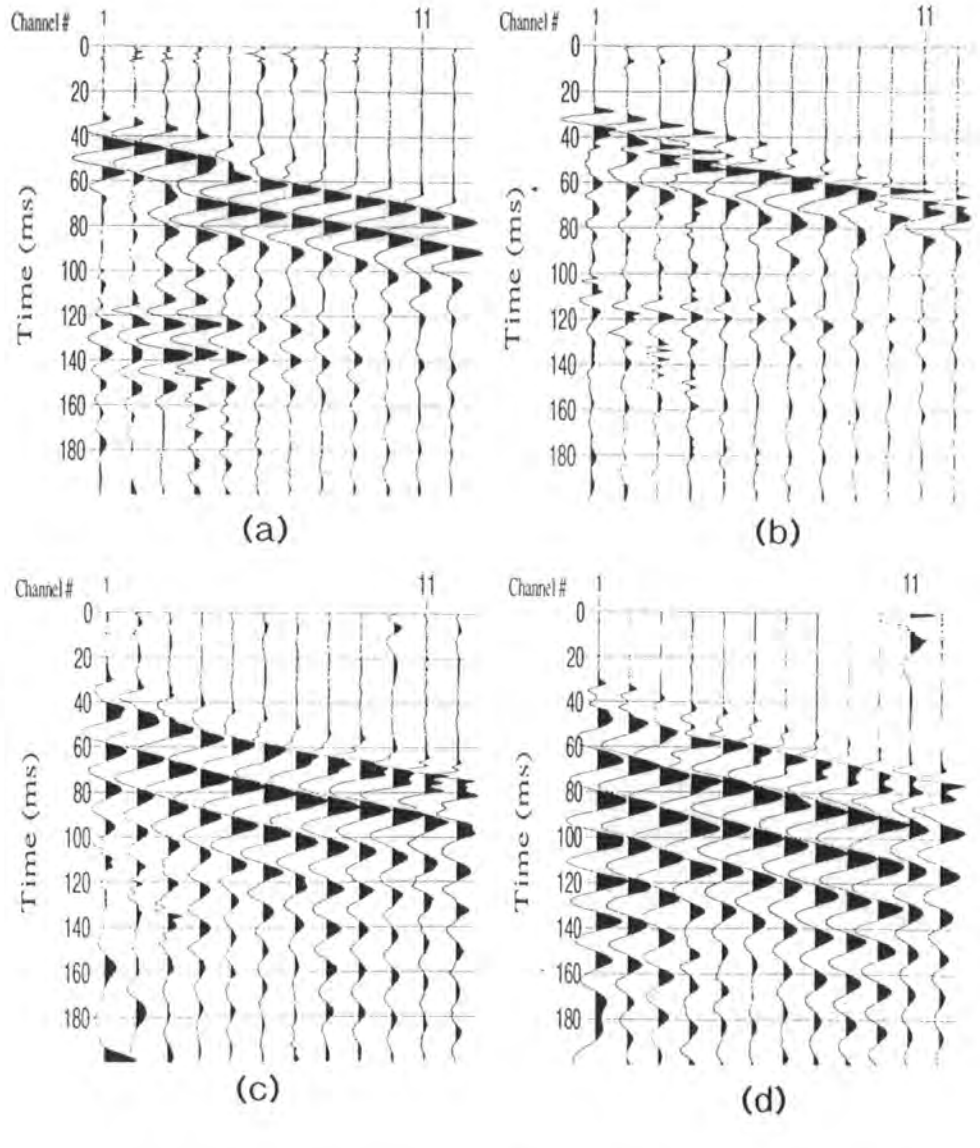

(a)

(b)

(c)

(d)

Fig 3.1. Field records as the near surface ground changes from wet (a) and (b) to dry (c) and (d). Channel 1 is at 35 m offset and the trace spacing is 5 m. Note the reflected arrivals around 120 ms in (a) and (b).

3.2.1.3 Acquisition parameters

Field acquisition parameters can be designed by modelling expected arrivals and by conducting a walkaway test. The acquisition parameters to be considered include the type of geophones to be used, near-trace offset, geophone spacing, spread type, temporal sampling rate and the record time length.

In a walkaway test, the optimum parameters are obtained by varying the source offset from an array of closely spaced geophones, and examining the results. The optimum layout is the one that produces high signal- to -noise ratio reflections with the least contamination from refracted, ground roll and airwave arrivals. In some cases, however, a field record may not display reflection events unless the records are filtered. Minor processing in the field is necessary therefore before the data are condemned as useless.

For an area where the interval velocity profile and target depth are known, simple modelling may be used to work out the appropriate layout. A sketch showing the various arrivals expected on a field record for a surface source are shown in Fig 3.2. A wavelet with a finite width in the figure serves the purpose of illustrating how different arrivals interfere with each other (its shape is not significant). The ground roll, airwave, multiples (not shown on Fig. 3.2), refracted and direct arrivals are referred to as coherent noise to distinguish them from random noise which occurs in non-systematic patterns.

Figure 3.2 shows that if the reflections that are swamped with ground roll cannot be retrieved during processing (if the ground roll is aliased, for example), then the reflection arrivals available will only be those in a window between the ground roll and refracted arrivals (to the right of the shaded zone in Fig 3.2). This window is known as an optimum window (Hunter *et al.* 1984) or reflection window (Singh 1986), and its size is a function of a number of factors including the ground roll, refraction and reflection velocities and the signal bandwidth, which affects the wavelet duration. To increase the optimum window, the acquisition parameters must be designed to minimise the interference of the ground roll with refractions, and the reflections, or the geophone spacing must be chosen to ensure that the ground roll is not spatially aliased. The ground roll that is not aliased can be eliminated in the processing stage.

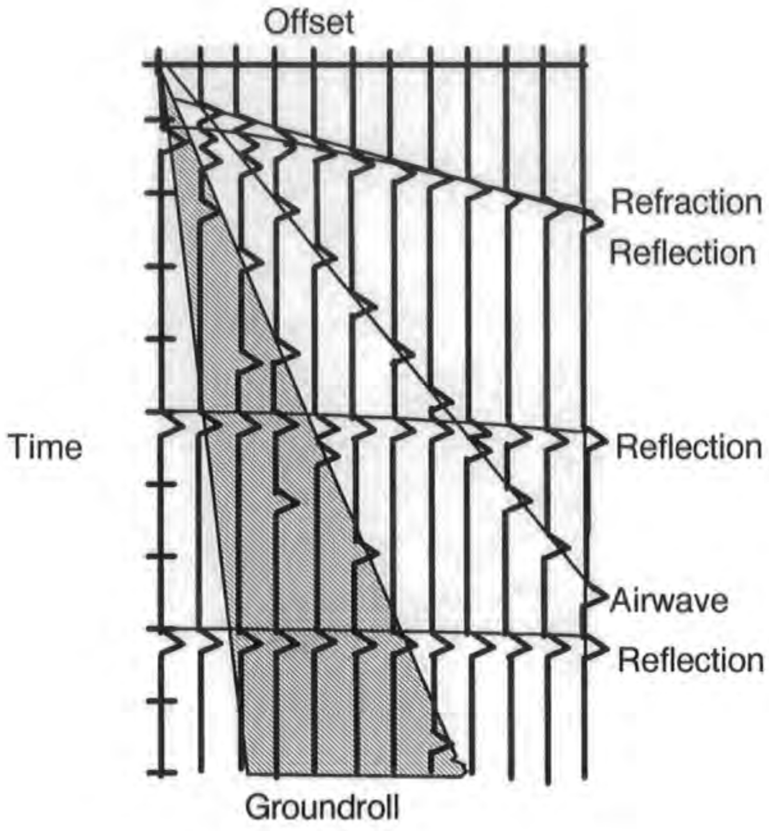

Fig. 3.2. A simple diagram to illustrate different arrivals in a shot record. The shaded region indicates the extent of the ground roll.

Ground roll generally has the largest amplitudes in field records for surface sources. It consists of dispersed Rayleigh waves, with velocities close to shear-wave velocities in the near surface, and it is possible for more than one ground wave-train to exist in a record with different velocities. If the ground roll frequency is lower than the reflection frequency, it can be suppressed by applying a bandpass filter during acquisition or in the processing stage. The ground roll can also be suppressed during processing by velocity filtering in the f-k domain if the geophone spacing used is less than half the shortest wavelength in the ground roll. This and other methods of suppressing ground roll are discussed in §4.5.2 and §4.6.1.

Two important characteristics of the airwave are its almost constant velocity of 330 m/s and its high frequency content. In most cases, the frequency spectrum of the airwave tends to be wider than that of the reflected arrivals, although the majority of the airwave energy concentrates at the higher frequency end. Thus, the airwave usually cannot be entirely eliminated by applying a low pass filter. To suppress the airwave during acquisition, the geophones have to be buried or arrays of geophones have to be used (see §4.5.2). If the geophone spacing is less than half the shortest wavelength in the airwave, then the airwave can also be suppressed during processing by velocity filtering in the f-k domain.

Refractions, or headwaves, are arrivals that usually have linear moveout. For horizontal interfaces, refractions are made up of segments of straight lines with each segment represents a refracting horizon, and its slope, dx/dt, is the refraction velocity of that horizon. As shown in Fig 3.2, for a given depth h and stacking velocity V of a very shallow reflector, there is an offset x where the refraction and reflection will arrive at the same time t. If V, h, and direct and refraction velocities are known, then the maximum useable offset for a particular reflection horizon, can be determined using a simple relationship. For a 2-layer model, (e.g. a weathered layer and bedrock), and reflection horizon at the base of the second layer, the maximum offset x is given approximately by

$$\frac{2h}{V}+\frac{x^2}{4Vh}=\frac{x}{v_2}+2d\frac{\sqrt{v_2^2-v_1^2}}{v_1v_2} \qquad (3.1)$$

where d is the depth to the refracted horizon, v_1 is the velocity in the upper layer and v_2 is the refraction velocity. For example, if we were to image a reflector at h = 20 m (the top of the Bunter in some parts of Selby for instance, see §4.2.2) with d (the depth to the water table) equal to 2 m, and V, v_1 and v_2 equal to 2000, 500, 1500 m/s, respectively, then the maximum offset x should be 24 m, which is about 1.2h. Usually, the maximum offset is taken to lie between 0.7 and 1.5 times the depth (Knapp and Steeples 1986b).

3.3 The pilot survey

Before the government's tighter legal regulations on acquiring and storing explosives came into effect, explosives were the main source of seismic energy used by researchers in applied geophysics at Durham University.

Consequently, at the time of this research the only available seismic source in the University was a sledge hammer, since then the department has acquired a buffalo gun. It was therefore decided to acquire a preliminary profile to test the feasibility of using a sledge hammer as a seismic source in the Selby area, prior to the main surveys undertaken in this study.

The test was performed in 1992 at Bishopwood in the Selby district. This area was chosen so that the data quality could be compared with data obtained the previous year on the same profile using explosives as the seismic source. The explosive data, which will be referred to hereafter simply as that, were collected in 1991 as part of an MSc project, and the details regarding their acquisition and processing are given by Douglas (1991).

The target horizon for both surveys was an anhydrite bed in the Upper Permian Marl at 100 m depth. The contrast in acoustic impedance between the anhydrite and the marl gives a large reflection coefficient. The near-surface is composed of Quaternary deposits of about 20 m thickness and which are comprised of silt and clay with sand lenses (see also § 4.2.2). The Quaternary deposits overlie the Triassic Bunter (Sherwood) Sandstone, which is conformable with the Permian strata beneath.

3.3.1 Data acquisition

A spread of 12 single geophones at a spacing of 5 m was used. The source was moved at 5 m intervals with the nearest geophone at 35 m offset (Fig 3.3), yielding 6-fold data with a CMP interval of 2.5 m. At each shot point, 10 hammer blows were stacked to increase the signal-to-noise ratio, and the data were recorded using a sampling interval of 0.2 ms. Although a 24-channel ES2401 EG&G Geometrics seismograph was used for recording, only 12 channels were activated at a time due to the lack of a roll-along switch. A total of 35 shot points were recorded, only a part of the profile being shown in Fig 3.3.

As acquisition details of the explosive data are given elsewhere (Douglas 1991), only relevant points will be reproduced here. Twenty-four single geophones spaced at 5 m intervals were deployed for recording. Shots, which each consisted of 50 g of gelomex explosive, were fired every 10 m between the geophones at a depth of about 1 m. Six shots were fired into each spread before the spread was moved 60 m as shown in fig 3.4; three additional shots were fired into the spread at each end of the profile. Across the middle of the profile, the coverage varied between 6-fold and 10-fold at the same CMP spacing of 2.5 m. The same seismograph was used with the sampling interval set at 1 ms.

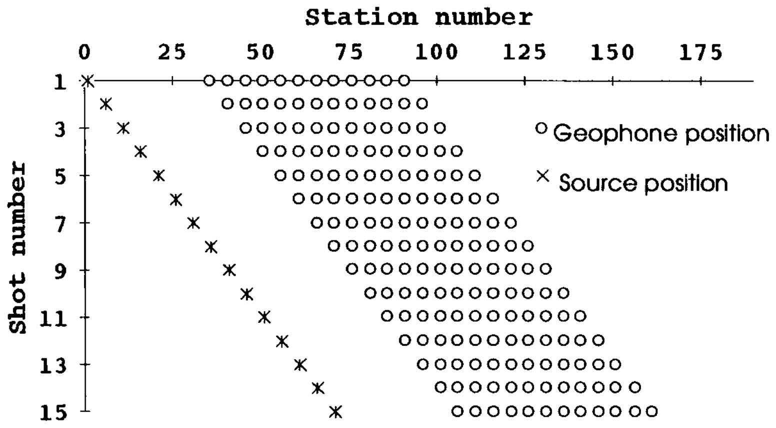

Fig 3.3. Part of the hammer data acquisition geometry showing the positions of the spreads relative to the shot points. A total of 35 shot points were recorded

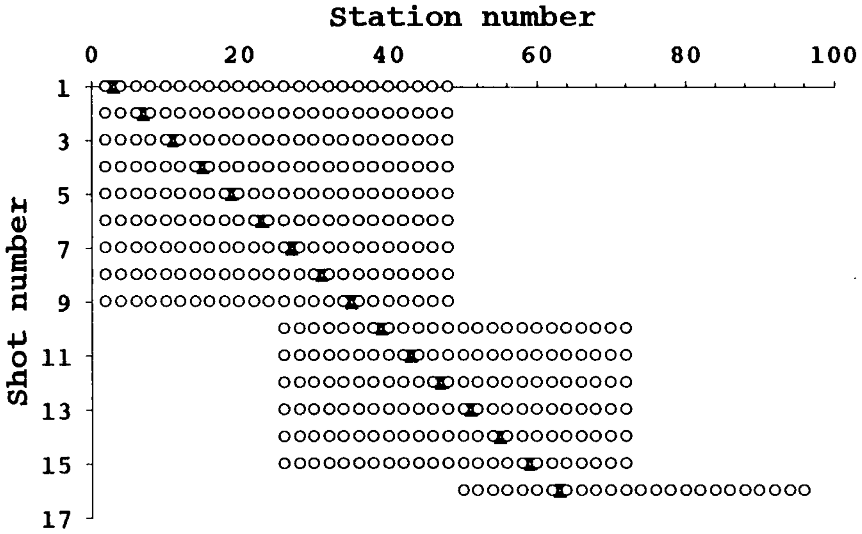

Fig. 3.4. Part of the acquisition geometry of the explosive data. A total of 30 shots were carried out and 4 geophone spreads were deployed.

3.3.2 Data quality

Two field records from the two surveys taken almost at the same location are shown in Fig 3.5. Weak reflection arrivals from the target can be seen at about 110 ms on both records. The explosive shot record shows that geophones close to the source are dominated by large-amplitude ground roll, which has masked most of the reflected arrivals. The amplitude spectra shown in the figure are for the traces at an offset of 65 m for the hammer record (trace 7) and 67.5 m for the explosive record (trace 21). The spectra were calculated first for the whole traces and then for 80 ms windows centred at the reflection arrivals.

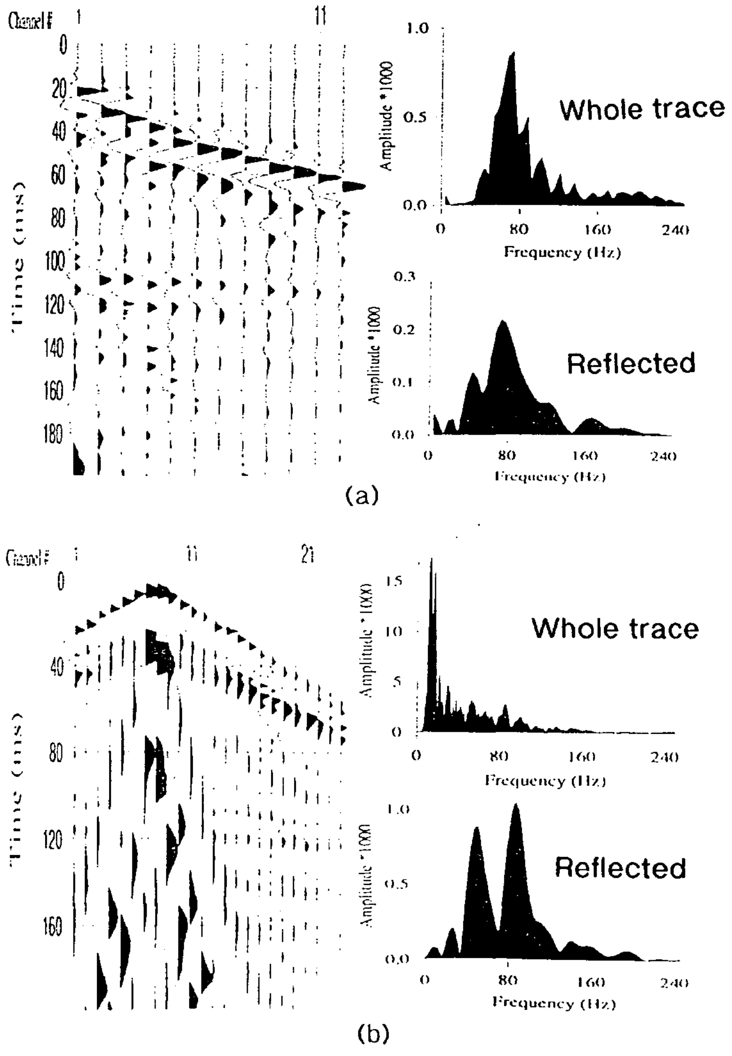

Fig 3.5. Typical field records obtained using (a) hammer blows and (b) explosives as the seismic source. The amplitude spectra are for trace 7 of the hammer record and trace 21 of explosive record.

.The amplitude spectra of the hammer data (Fig 3.5a) show that the dominant frequency of the reflected signals is about 70-90 Hz, whilst those of the explosives (Fig 3.5b) show the dominant frequency in the range 80-100 Hz. In both datasets, however, the significant reflected signal can be seen to extend up to just over 140 Hz. Apart from having higher dominant frequency, the reflected signals in the explosive data are also about 5 times greater in amplitude than those in the hammer data.

The two records shown in Fig. 3.5 are representative of the quality of most shot records collected in both surveys. In some places, however, field records were dominated by low frequency reverberations following the first arrivals, as shown in Fig 3.1c and d. It was not until bandpass filters were applied that the reflections started to appear. A sudden deterioration of the data quality, as noted in § 3.1.2.2, is due to the change in source coupling caused by the change in the characteristics of the weathered layer. The reverberations appeared where the ground surface was harder and drier.

3.3.3 Data processing

Three different seismic data processing packages are available in the department: ProMAX, EAVESDROPPER and FORTRAN programs written in-house. ProMAX is a state-of-the-art 2D commercial software package with a number of interactive processing flows. EAVESDROPPER is PC-based software which, although slow, can do most of the main processing sequences effectively provided that the data are only 16-bit. The in-house software is a collection of FORTRAN programs with UNIRAS plotting subroutines written by a number of Durham researchers, notably Kragh (1990), Findlay (1991), Leggett (1992) and Rowbotham (1993). In most cases a combination of these three packages were used to process the datasets used in this project.

3.3.3.1 Prestack processing

The hammer dataset was processed by applying a conventional surface seismic processing sequence. The refracted first arrivals were muted, and a surgical taper was applied to remove the airwave arrivals. The data were then bandpass filtered and sorted into CMP gathers before the field statics were applied.

Field statics were determined using the first breaks, which were head waves refracted from the water table as implied from its velocity of 1500 m/s. The statics were calculated by assigning the first shot with a fixed static value s_1. The receiver statics s_g of the first 12 geophone stations were then calculated from the traveltimes t_{sg} using the refractor velocity V, the first shot static and the shot-receiver distance X_{sg} (Fig. 3.7) by

$$s_{g_n} = t_{sg_n} - \frac{X_{sg_n}}{V} - s_1 \qquad (3.1)$$

where n =1, 2,. . . ., 12. Using the receiver statics obtained from the first shot, the static for the second shot s_2 was then calculated, and in turn its value was used to determine the static of the new station of the geophone 12, as illustrated in Fig 3.6. The statics of other receiver and shot positions were obtained following the same procedure.

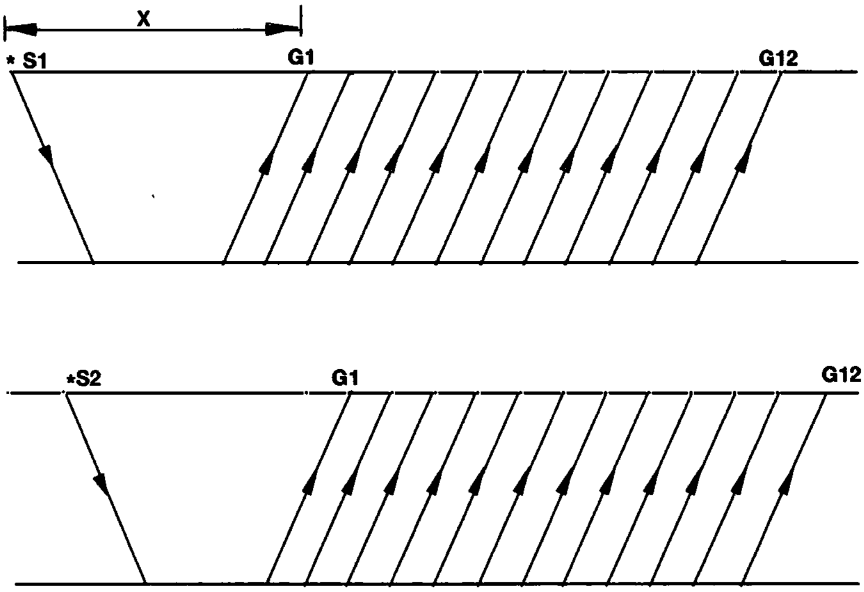

Fig 3.6. A diagram showing the first 13 geophones positions and the first two shots.

The explosive data were reprocessed using a similar sequence except that the traces dominated by ground roll to the two-way-time of the target reflector were edited out. Since both forward and reverse shots were available, the receiver statics were determined using the plus-minus method, and the shot statics were calculated from the receiver statics using the method described above.

After static corrections, both datasets were normal moveout corrected using a constant velocity of 2000 m/s and stacked. Figures 3.7 and 3.8 show stacked sections from both surveys before and after field static corrections. There is a clear improvement in reflector coherency after static corrections have been applied. The disturbance of the reflection in the explosive data (Fig 3.7b) between CMP 64 and 84 has been interpreted as a pair of faults forming a graben (Douglas 1991). As the first geophones in both surveys were approximately at the same location, CMP 1 in the explosive data corresponds to CMP 9 in hammer data, and therefore the faults observed in the explosive section appear just at the end of the hammer section.

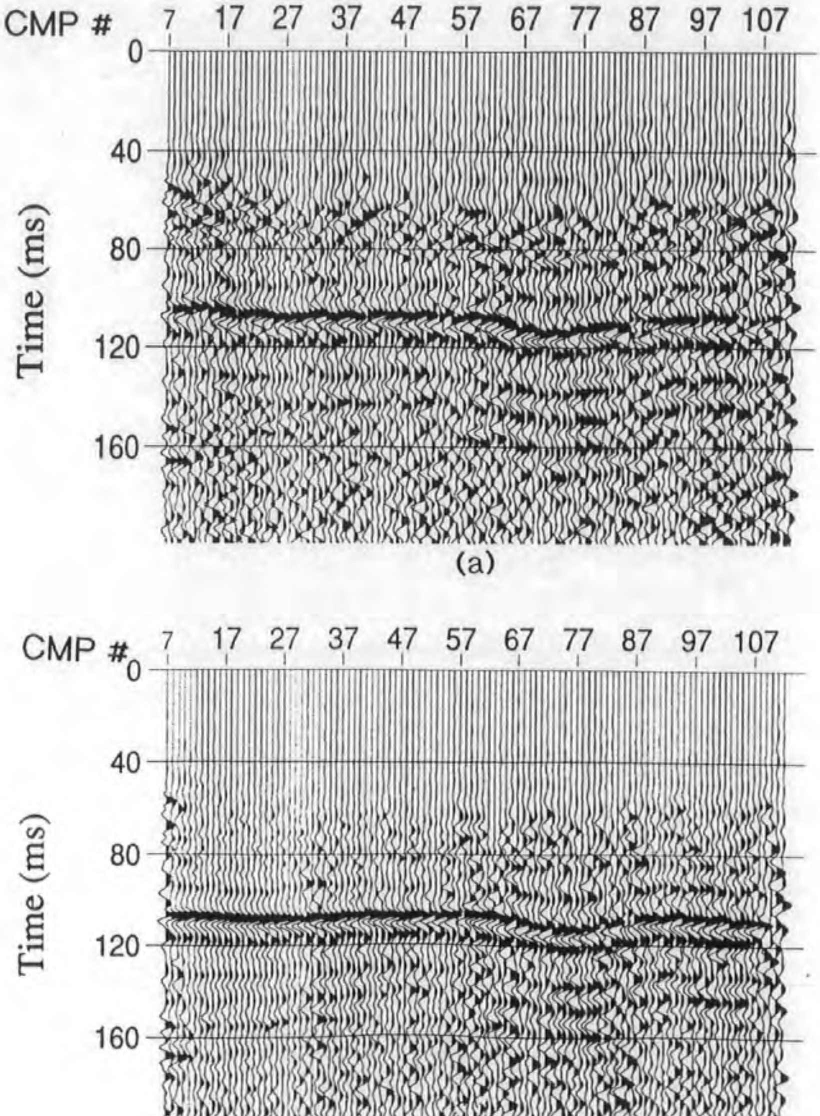

Fig 3.7. Stacked section of the explosive data (a) without and (b) with static corrections.

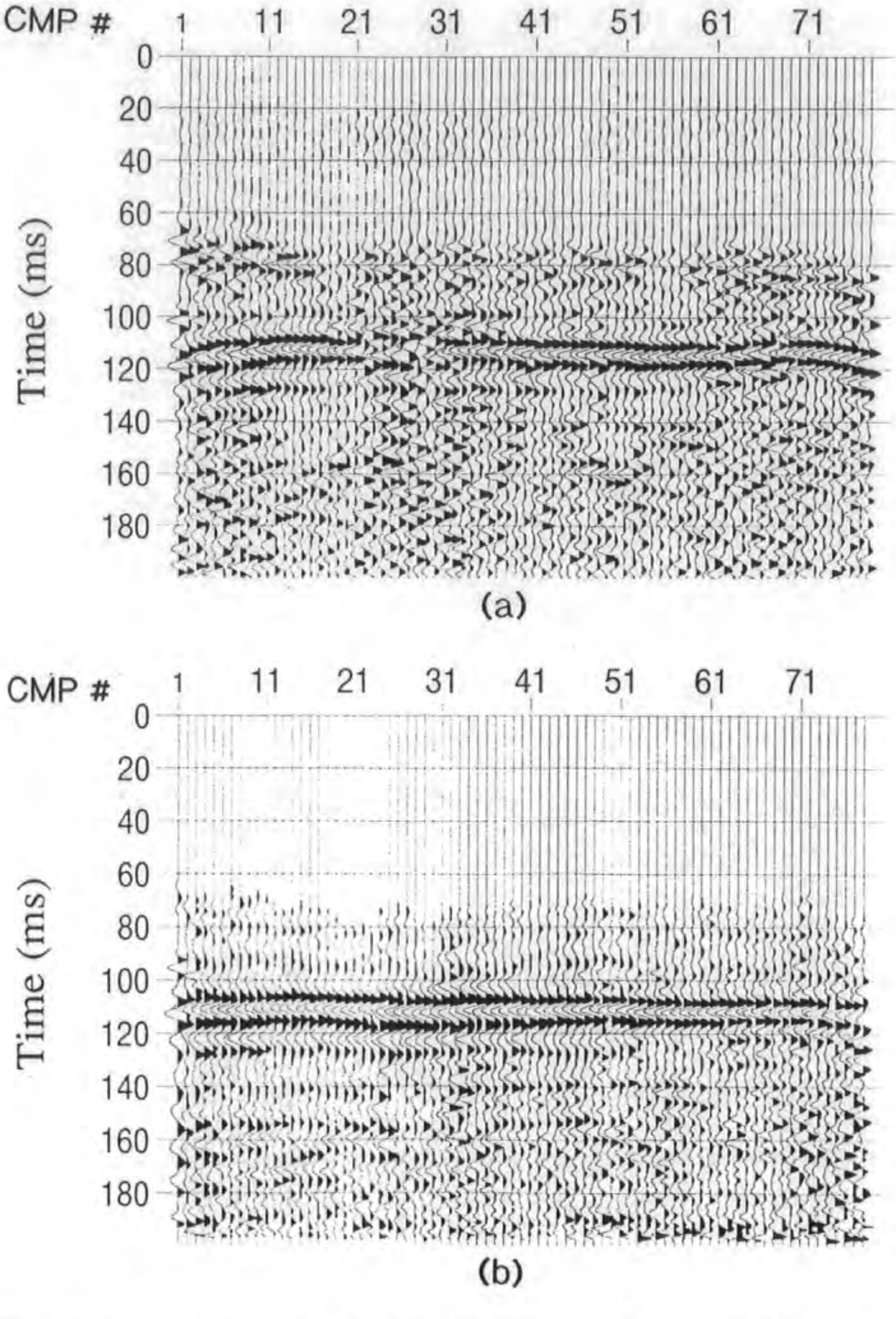

Fig 3.8. Stacked section of the hammer data (a) without and (b) with static corrections.

3.3.3.2 Post stack processing

Different post stack processes were applied to the hammer data to find the optimum data enhancement technique. These processes included spiking deconvolution, spectral balancing, velocity filtering and time migration.

Spiking deconvolution As seismic wavelets propagate into the ground, they preferentially lose high frequency content, thus broadening in time, and therefore arrivals from different reflectors tend to overlap with each other. The main objective of spiking deconvolution is to counteract this effect by 'compressing' the wavelets in the data and placing their onsets at the traveltimes of the corresponding reflectors. Usually, spiking deconvolution is followed by a zero-phase bandpass filter to produce a band-limited zero-phase wavelet, the peak or trough of the wavelet being at the arrival time. In time-lapse surveys, such wavelets not only improve the resolution, but also make the correlation between different surveys easier.

In order to apply spiking deconvolution, or any predictive deconvolution filter for that matter, it is implicit that the trace can be treated as the convolution of a white noise reflectivity with an effective wavelet which is minimum-phase. In most shallow reflection datasets this assumption is rarely fulfilled; in our data, for example, there is only one pair of strongly reflecting interfaces bounding the anhydrite bed. However, although it is not possible to quantify the effectiveness of deconvolution in the data (Hatton *et al* 1986), Fig 3.9 shows that a spiking deconvolution followed by a bandpass filter applied to the hammer data has yielded a section with a short wavelet at the anhydrite horizon. The effectiveness of the spiking deconvolution can also be seen by comparing the amplitude spectra of a seismic trace before and after deconvolution, depicted in Fig 3.9b and c. The amplitude spectrum of the trace after deconvolution has more energy around 200 Hz than that of the trace before deconvolution. The parameters used were a filter length of 3 ms and design gate of 80 ms.

Spectral balancing The coherency of a reflector can also be improved by making the amplitude spectra of all the traces in the section the same. One way of doing this is to replace the amplitude spectra of all traces with a more desirable spectrum but without changing their phase spectra. The effect of applying spectral balancing is shown in Fig 3.10.

Velocity filtering The reflector's continuity in Figs 3.9 and 3.10, which has been improved by single trace processes only, can be improved even further by applying a velocity, or *f-k* filter. Velocity filtering involves both axes, the temporal axis and spatial axis (multiple trace process), and can be used to limit the apparent angle of any coherent event by applying an appropriate filter in the *f-k* domain. The optimum filter is that which rejects most of the coherent noise without over-smoothing the reflection data. The section in Fig 3.11 has been filtered by a velocity fan filter with the parameters -2000 m/s, -3000 m/s, 3000 m/s, 2000 m/s after spiking deconvolution (i.e. velocities below 2000 m/s rejected, velocities above 3000 m/s passed, with linear tapers between).

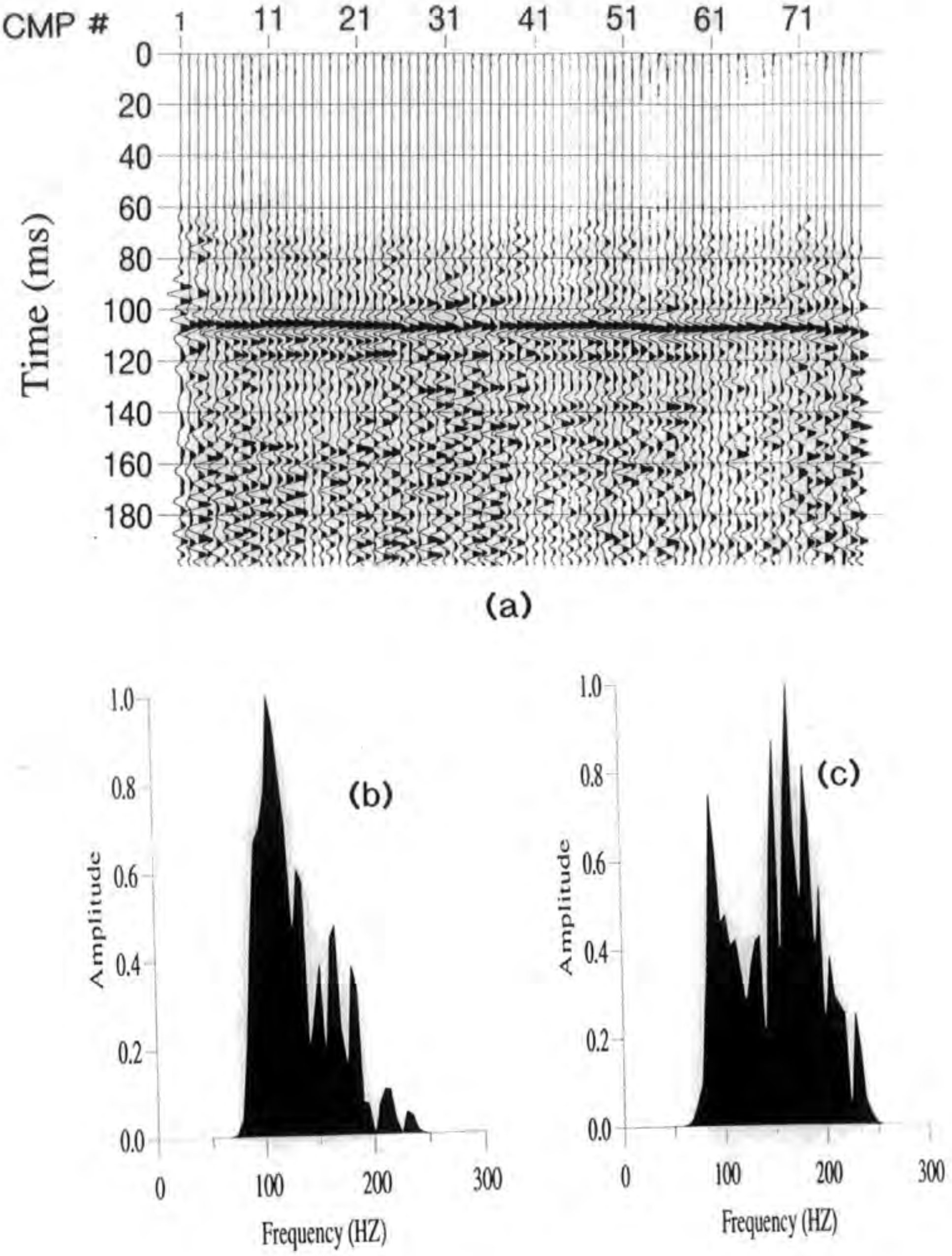

Fig 3.9. (a) Stacked section shows the effect of applying spiking deconvolution followed by a zero-phase bandpass filter. The amplitude spectrum of a trace (b) before and (c) after spiking deconvolution and bandpass filter.

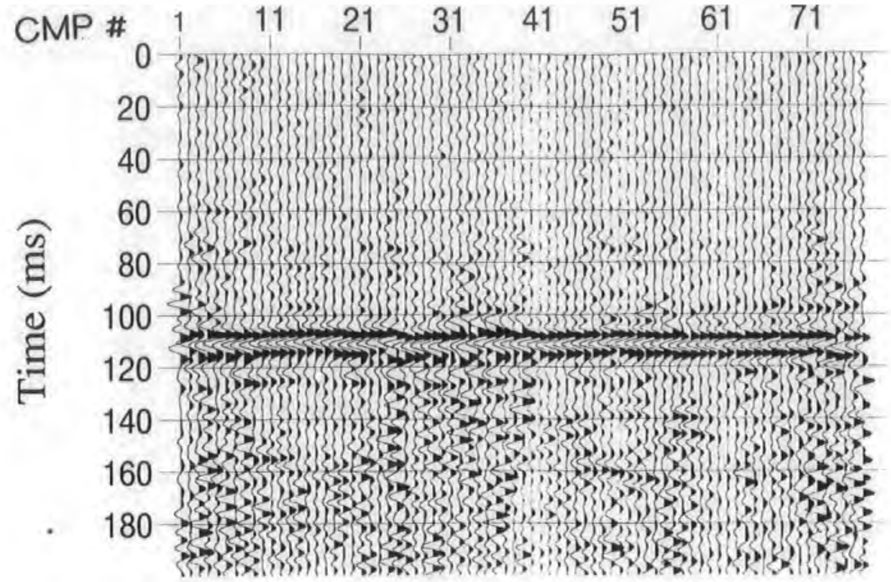

Fig. 3.10. Stacked section after spectral balancing.

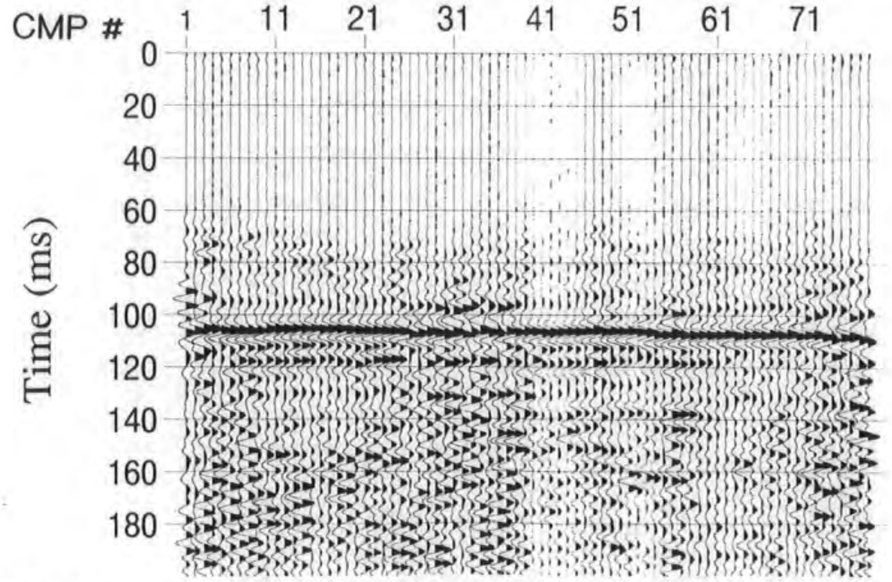

Fig 3.11. Section with spiking deconvolution followed by velocity filtering.

Time migration In unmigrated stacked sections, the reflection point is normally considered to be at a point vertically below the source - receiver midpoint. In reality, however, this is the case only if the velocity field is laterally invariant. For a dipping interface, this point is at a down-dip location compared with the actual reflection point. To correct for this, a migration process is carried out. Migration also increases horizontal resolution by downward-continuing the wavefields to the reflector depth. Figure 3.12 shows a time migrated section after deconvolution. The time migration was carried out in the f-k domain.

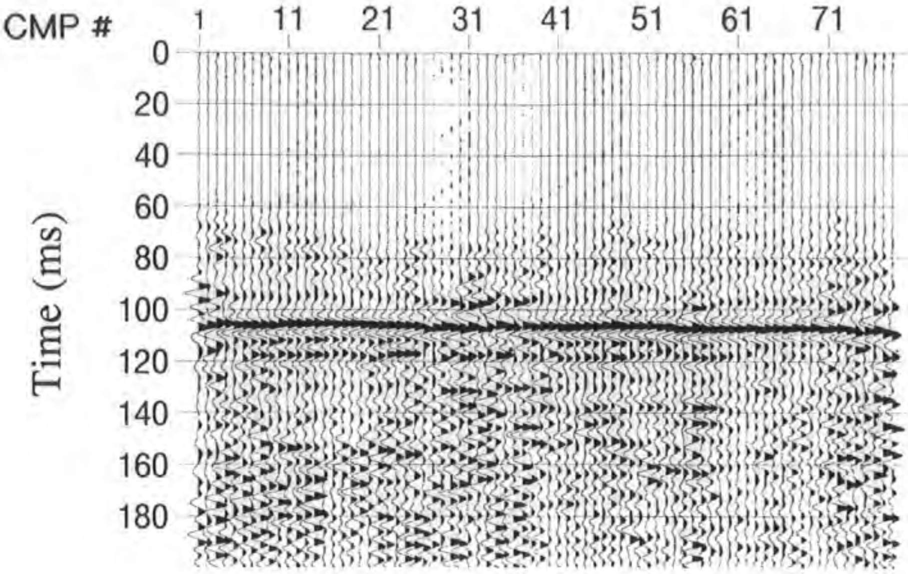

Fig 3.12. Spiking deconvolution followed by time migration.

3.4 Concluding remarks

The test profile has shown that a sledge hammer, with about 10 hammer blows stacked at each shot point, can be used in Selby to produce enough reflection energy to image the anhydrite reflector at a depth of more than 100 m. Due to the ground roll on the near offset traces in the explosive data, the top of the Bunter Sandstone could not be imaged properly. The same would have been observed if the near offset in the hammer data was reduced. Spiking deconvolution after stack followed by time migration or velocity filtering have been shown to enhance the data quality.

Chapter 4

Acquisition and processing of the Selby time-lapse surveys

4.1 Introduction

A total of twenty one time-lapse surveys were acquired on two profiles over different coal panels. The acquisition and data processing of these surveys, including the geology of the area and the layout of the coal panels, are described in this chapter. The results of an experiment carried out using a stack-array approach to suppress ground roll are also presented.

"Time-lapse surveys" is a term used to describe surveys that are acquired repeatedly on the same profile(s) to monitor the change in seismic parameters over time. The seismic parameters often studied are seismic velocity and the amplitude of the reflected energy. To avoid repetition, the causes of change in these parameters will not be explained here but can be found in §1.2.

In this study, time-lapse surveys were conducted along two profiles over adjacent coal mining longwall panels to study the effect of subsidence on seismic velocity. The longwall panels studied are at the Wistow Mine in the Selby coalfield and will be identified using the names given to them by the National Coal Board: H45 and H46. For clarity, the seismic data acquisition, the data quality and the geometry of each panel will be described separately. As a means of ground roll attenuation, a survey using arrays of geophones rather than single geophones was also performed over panel H46. The acquisition and results of this survey will be described separately from the rest of the H46 surveys.

The data in all surveys were recorded on 3.5 inch floppy discs using an EG&G Geometrics ES2401 24-channel seismograph. A total of 1024 samples were recorded at each geophone station. The data were transferred to a PC and to the UNIX system, where the processing was carried out using EAVESDROPPER and ProMAX software, respectively. As the data processing was similar in both profiles, the processing will be combined here and presented in one section.

4.2 Site location and geological setting

4.2.1 Site location

The site studied is about 4 km east of Wistow, which is to the north of Selby town (Fig 4.1a). The detailed map of the site is shown in Fig 4.1b. The site, as with most of the Selby district, is situated in a low lying area, about 2 m above mean sea level. A predominant feature near the site, as can be seen in Fig 4.1, is the river Ouse, which is a tidal river and flows over most of the mining panels in the area. The existence of a river in these low-lying areas made the National Coal Board take appropriate measures to reduce the magnitude of surface subsidence to avoid flooding. For this reason, only the Barnsley Seam is being worked in the Selby coalfield, although there are about five other seams of suitable thickness. The measures taken may also include the reduction in width of the coal seam extracted and leaving pillars of coal in densely populated areas (Pyne and Randon 1986).

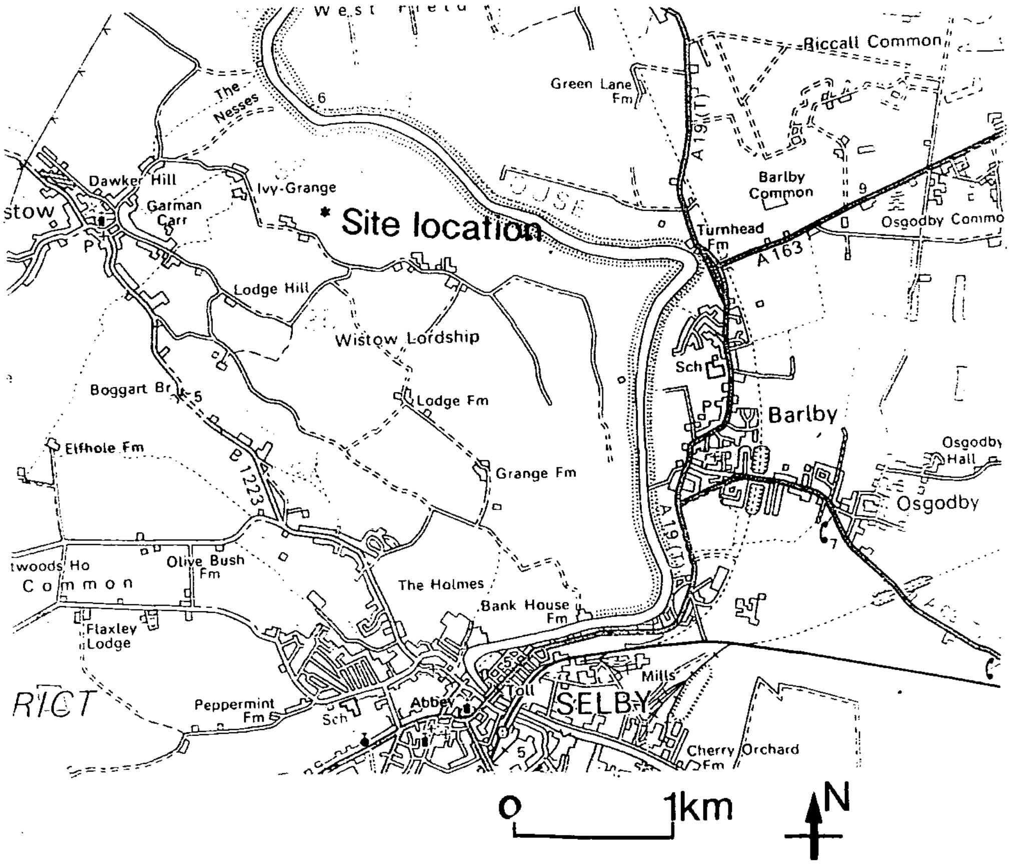

Fig 4.1a. The map showing the location of the site investigated in this study.

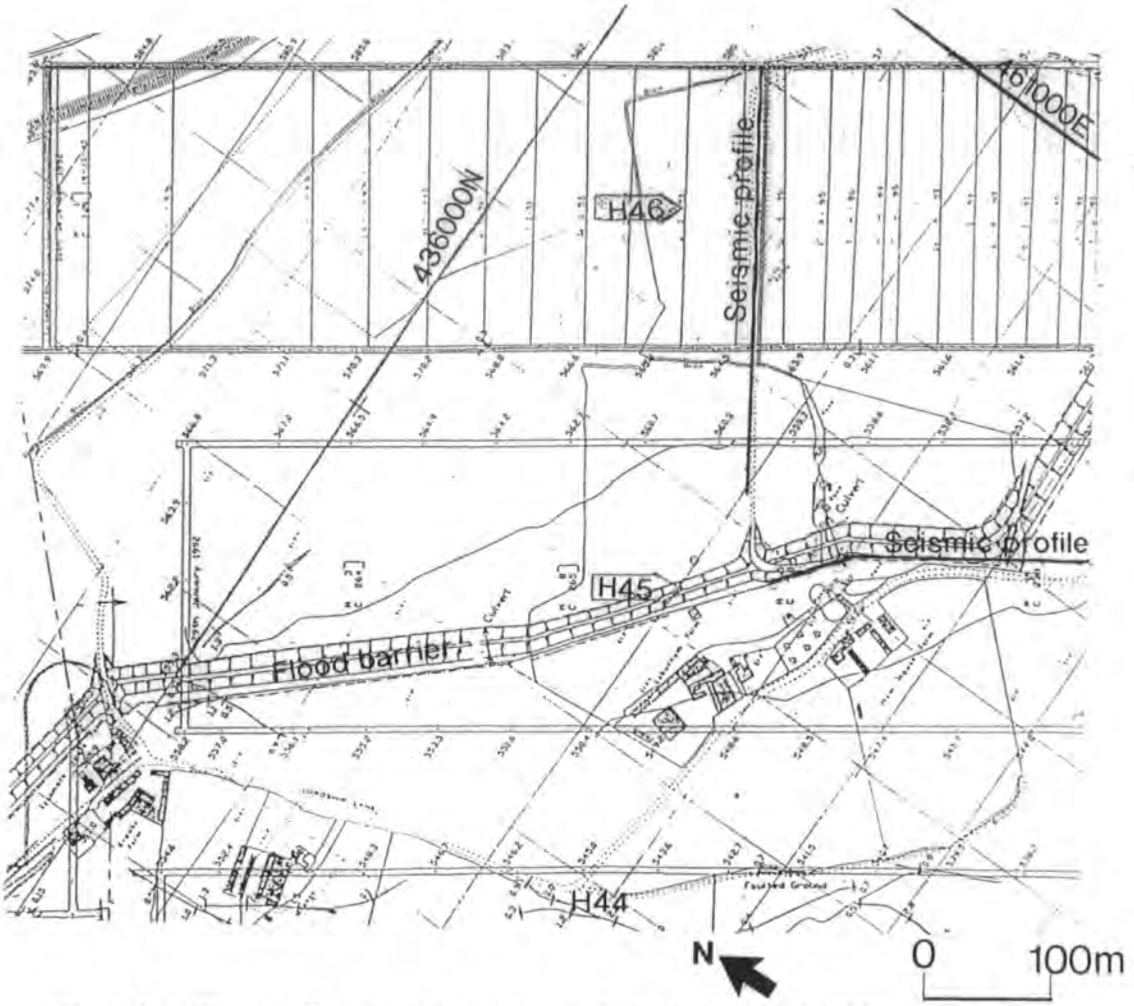

Fig 4.1b. The detailed map showing panels H44, H45 and H46. Also shown are the positions of the seismic profiles.

4.2.2 Geology

The Wistow Mine is part of the Selby Mines Complex in the Selby coalfield. The first coal extraction in this mine was carried out in 1983 (Pyne and Randon 1986). A number of longwall panels in the Barnsley Seam, in the Coal Measures, have been mined since then. The geology of this area is such that the Coal Measures are overlain by Permo-Triassic strata (Fig. 4.2). The Carboniferous Coal Measures are composed of sandstone interbedded with shale and coal seams. The Manor Field House borehole, about 1000 m south west of the panel H45, shows that the Barnsley Seam is at 504 m depth. The seam at panel H45 was found at about 550 m depth, dipping approximately northeastwards at a slope of 1 in 22 (3°). At H46 the depth to the seam was 570 m with almost the same angle of dip.

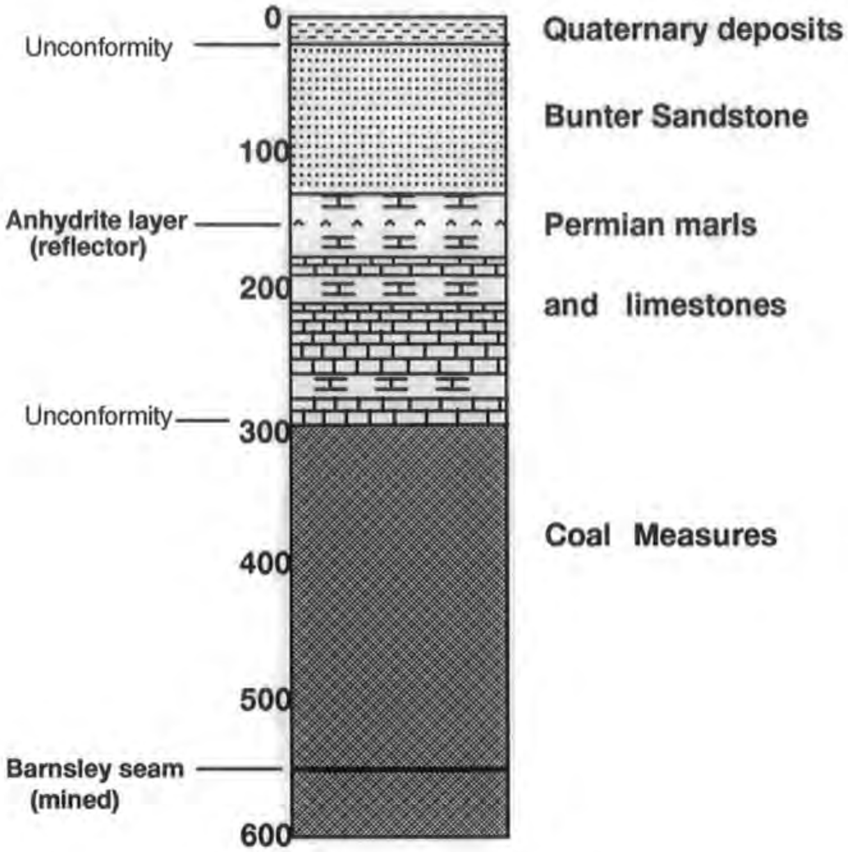

Fig 4.2. Stratigraphic column down to the Barnsley seam.

The Permian strata consist mainly of marl and magnesian limestone with some anhydrite bands. At the borehole the base of Permian is at 292 m. With reference to another borehole at Bishopwood, the top Permian at the panels H45 and H46 can be inferred to be at 130 m. Overlying the Permian strata is the Triassic Bunter Sandstone, which is very porous and an excellent aquifer. The near surface is composed of the surficial Quaternary deposits of about 20 m thickness, which are comprised of silt and clay with sand lenses. The target horizon for the survey was an anhydrite bed in the Upper Permian marl at about 150 m depth. Thus, the reflected seismic energy travelled mainly through the Bunter Sandstone.

4.3 Data acquisition over panel H45

4.3.1 Mining

Mining of panel H45 at an almost constant rate of extraction took place over the period of January - September 1992. The panel was 220 m wide and 935 m long when the extraction was completed, and the thickness of coal extracted was 2.6 m. A number of mining panels were extracted in this area before H45. The nearest parallel panel to H45 is H44 whose edge is just over 100 m away as shown in Fig 4.3. Mining at this panel finished in November 1991, when the panel was 875 m long with width and thickness of coal seam extracted similar to that of H45.

4.3.2 Data acquisition

The seismic profile was laid out above the middle of the panel, parallel to the direction of mining (Fig 4.3). A 6.3 kg hammer was used as the seismic source, with 10 blows stacked at each source point, and a spread of 24 single geophones at 5 m spacing was deployed for recording. Source points were spaced 5 m apart over a total distance of 265 m, and were located between the geophones over the central part of the profile (Fig 4.4). A fixed, rather than a moving, spread of geophones was used in order to minimise labour for the three-person crew. This layout gave a maximum coverage of 24-fold, a total subsurface coverage of 190 m and a common depth point interval of 2.5 m. The temporal sampling interval was set at 0.5 ms.

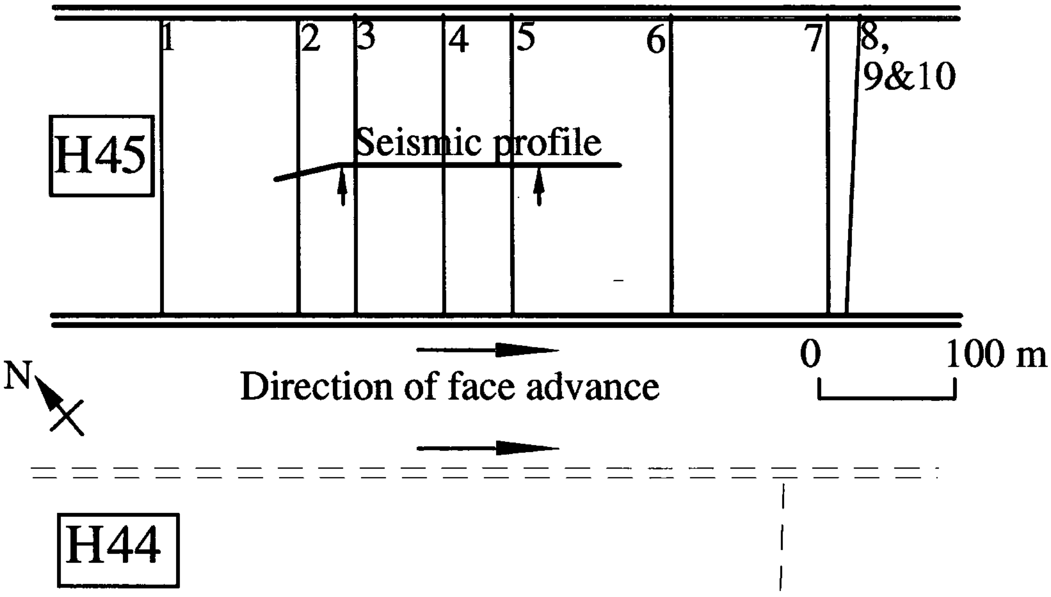

Fig 4.3. Plan of the longwall panel H45 showing the position of the coal face for surveys 1-10 and the location of the seismic profile. Arrows on the seismic profile mark the segment of the profile interpreted. Also shown is the location of panel H44.

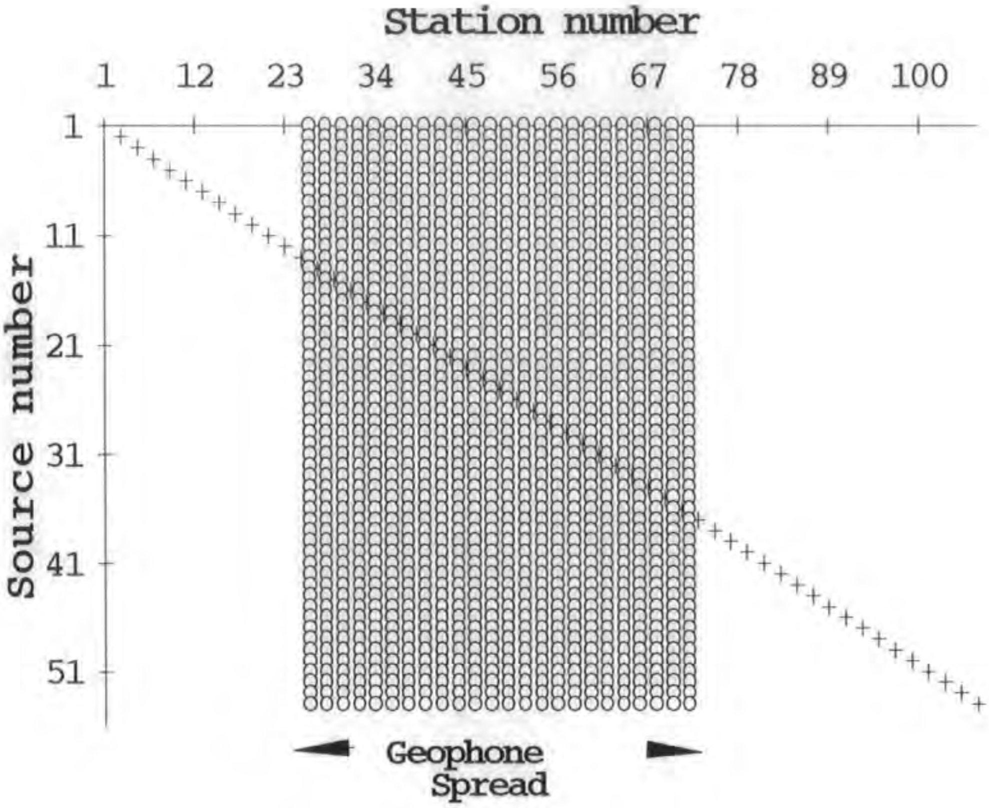

Fig. 4.4. Data acquisition geometry of the seismic profile over the longwall panel H45. Station interval equal to 2.5 m.

The first survey, H45/1, was carried out in April 1992 when the coal face was about 100 m short of the first source point. At this stage, the effect of subsidence on the ground beneath the central segment of the seismic profile would have been negligible. Subsequent surveys, H45/2 to H45/10, were carried out at intervals of 2-5 weeks until mining was completed, with a final survey in September 1993, almost a year after mining had finished. The complete dates of each survey and the position of the coal face, relative to the first common midpoint (CMP), at these dates are given on the table below. The negative distances indicate that the coal face is short of the first CMP. The positions of the coal face are also shown on the map in Fig. 4.3.

Table 4.1. The dates and location of the coal face when the profile over the panel H45 was surveyed.

Survey	Date	Distance from coal face to first CMP in metres
H45/1	10/04/92	-116
H45/2	02/05/92	-18
H45/3	14/05/92	35
H45/4	27/05/92	100
H45/5	09/06/92	150
H45/6	09/07/92	270
H45/7	13/08/92	395
H45/8	26/10/92	415
H45/9	15/04/93	415
H4510	10/09/93	415

4.3.3 Data quality

The data were of similar quality for all surveys. As observed in Bishopwood, the shot records in this area are also dominated by low frequency reverberations following the first arrivals (Fig 4.5a). In some records this source-generated noise masks the reflected arrivals from our target horizon (170-200 ms) as shown in Fig 4.5a. Figure 4.5b shows the effect of applying a bandpass filter of 60-100-160-240 Hz to the record to remove the low frequency arrivals; there is now a clear reflection event between 170 and 200 ms. The dominant reflection frequency is in the range of 100-150 Hz. An AGC of 100 ms has been applied to the shot record of Fig 4.5b for display. Unless stated otherwise, traces shown in all figures are normalised to their maximum values.

Geophones close to the source also recorded large-amplitude ground roll as shown in Fig 4.6a. Although the dominant frequency of the ground roll is 50 Hz (Fig 4.6), some of the ground roll energy has the same frequency as the reflection and therefore cannot be eliminated by applying a low cut frequency filter (Fig 4.6b).

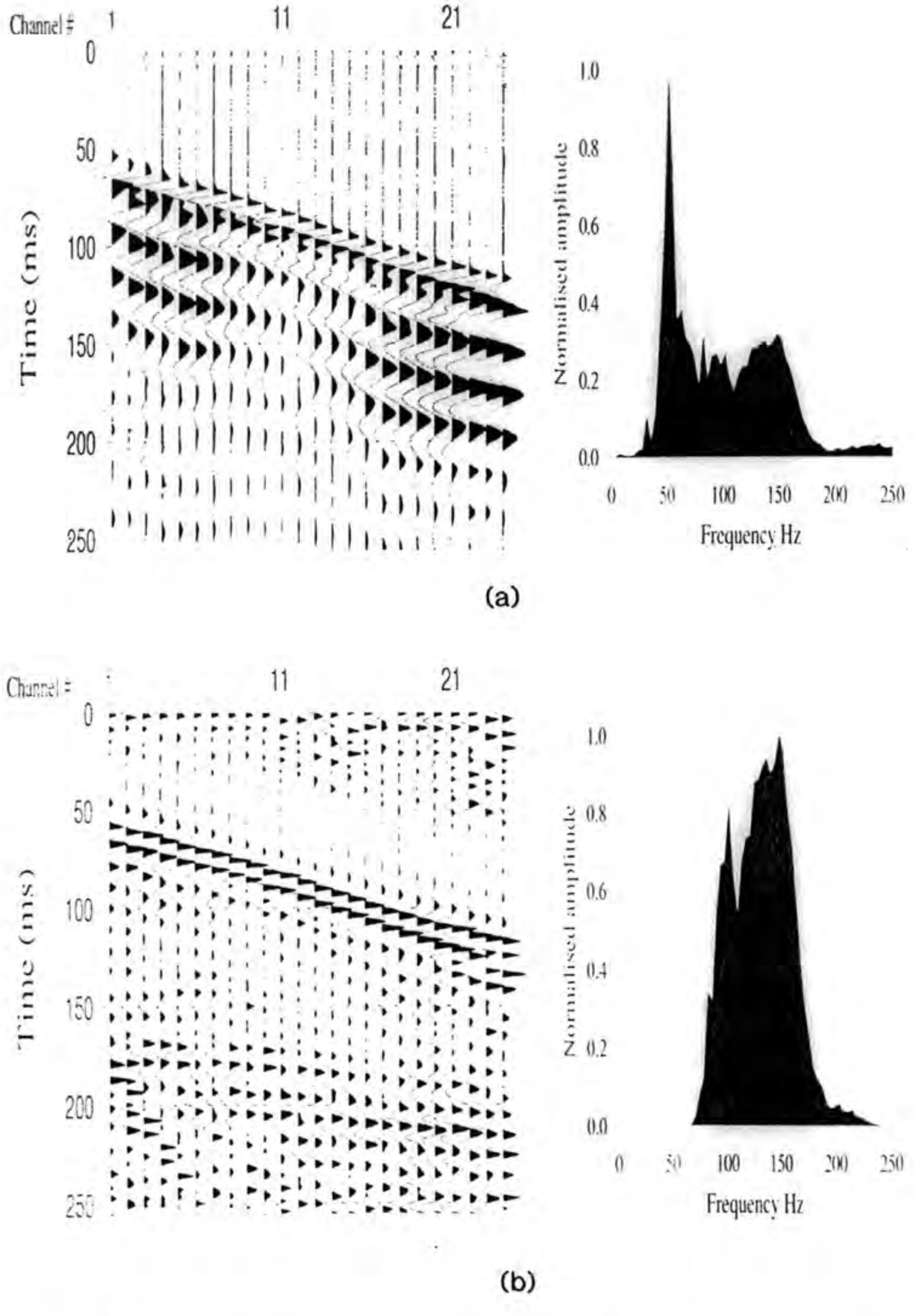

Fig. 4.5. (a) Typical shot record with a near offset of 62.5 m, showing low frequency reverberation following the first arrivals, and the amplitude spectrum of trace of channel 10. (b) Same gather after applying a bandpass filter to the record, and the amplitude spectrum of the same trace as in (a).

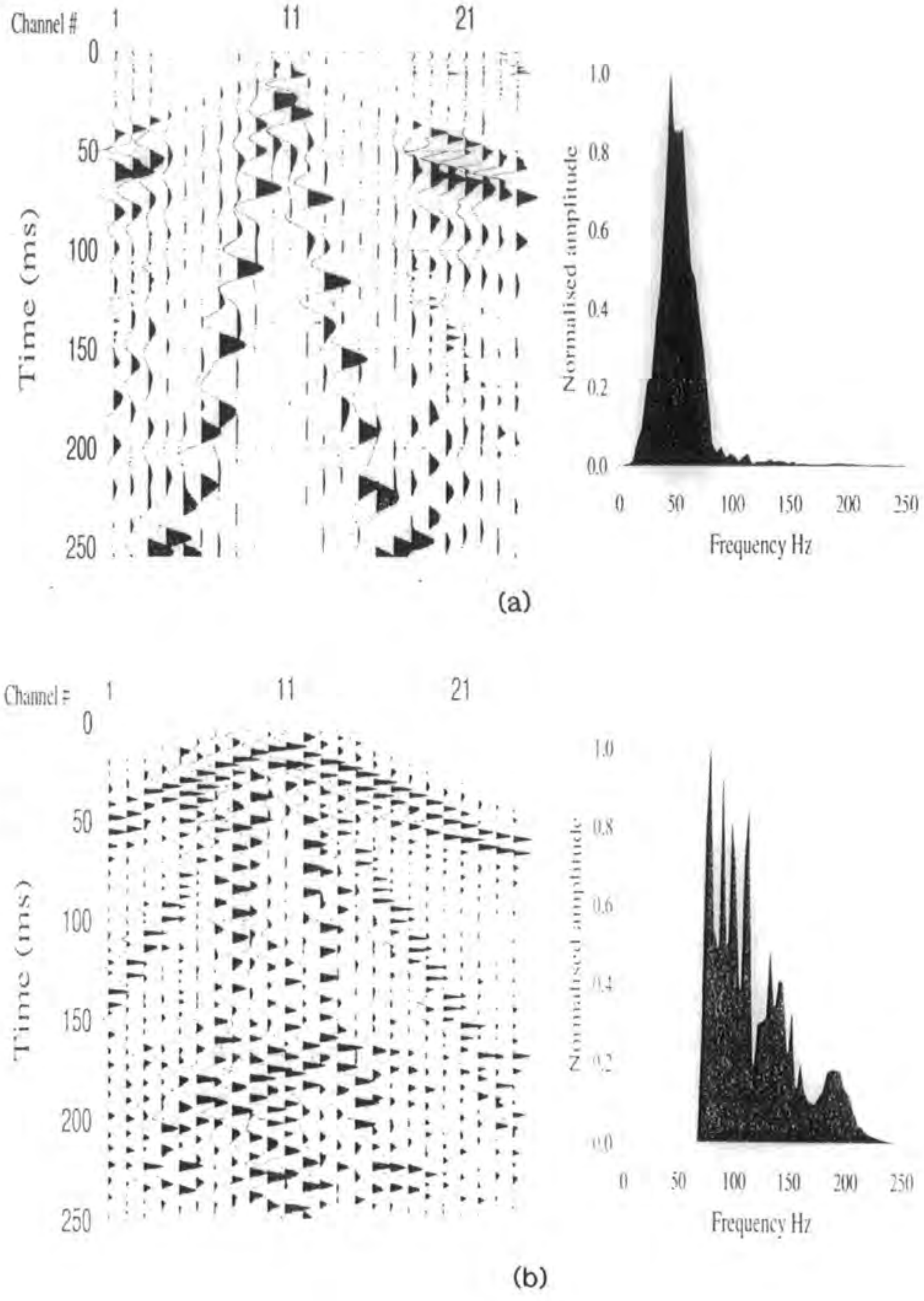

Fig 4.6. Typical field record with source between geophones on channels 10 and 11 showing high amplitude ground roll (a) before and (b) after applying a bandpass filter. The amplitude spectra are of channel 13.

Far offset shot records from four different surveys are shown in Fig 4.7 for comparison. The source position is the same as that of the record shown in Fig

4.5, and the same bandpass filter and the length of the AGC window were used as in Fig 4.5. The reflection from our target at about 170 ms to 200 ms and with almost the same frequency content can be traced in all shot records.

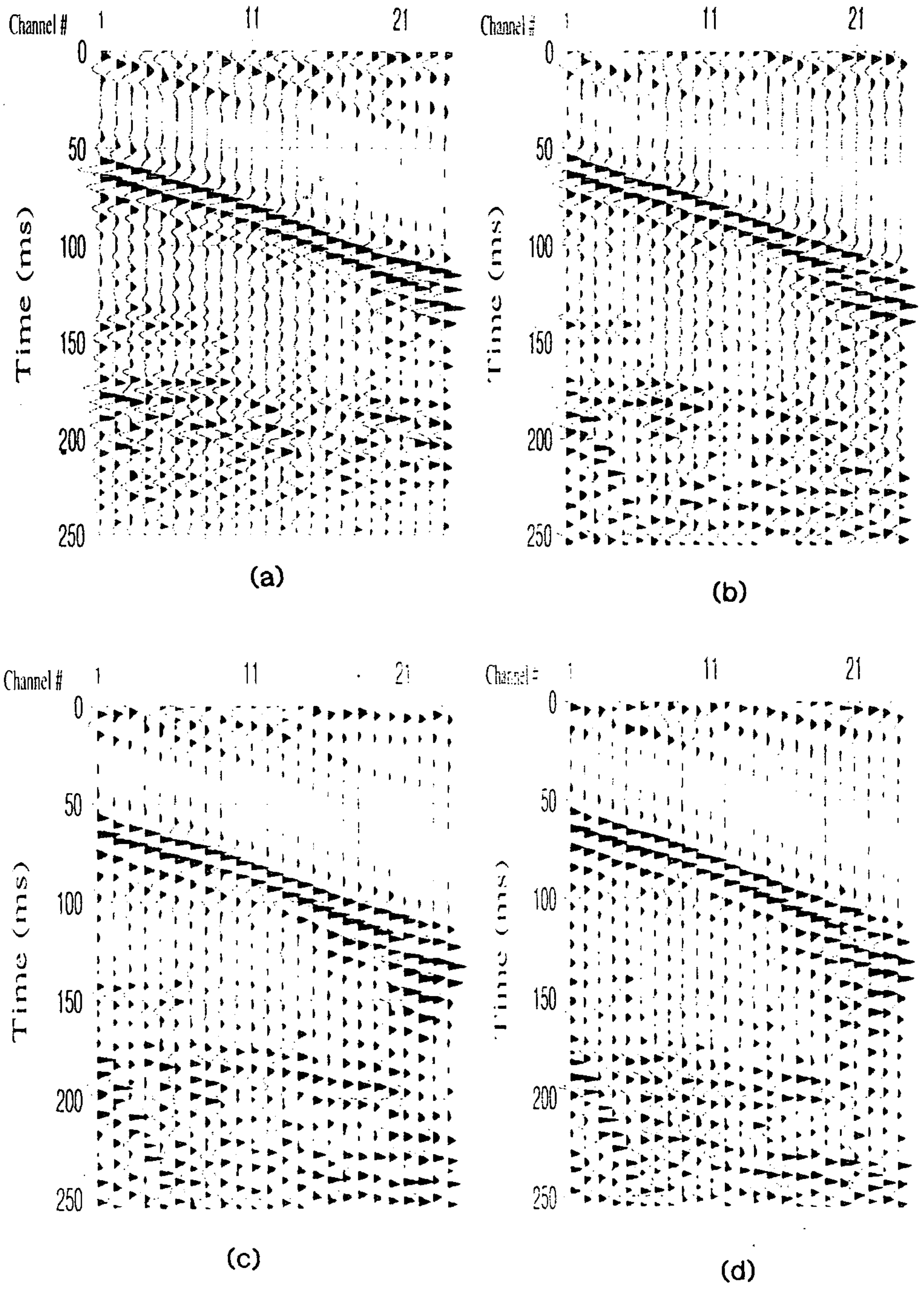

Fig 4.7. Filtered shot records from the same shot point (a) H45/4, (b) H45/6, (c) H45/8 and (d) H45/10. The bandpass filter of 60-100-180-250 Hz was used and an AGC window of 100 ms was applied for the display.

4.4 Data acquisition over panel H46

4.4.1 Mining

Panel H46 is located 70 m North East of panel H45 as shown in Fig 4.8. The mining in this panel was carried out from December 1992 to October 1993. The extraction rate varied almost gradually from 16 metres per day, at the beginning of the panel, to just less than 1 metre per day, when a disturbance in the seam was encountered towards the end of the panel. The average rate was about 5.5 metres per day in the fast region and about 2.5 metres per day in the slow region. When mining was completed, the panel was 1100 m long and 220 m wide, and the thickness of coal extracted was 2.6 m.

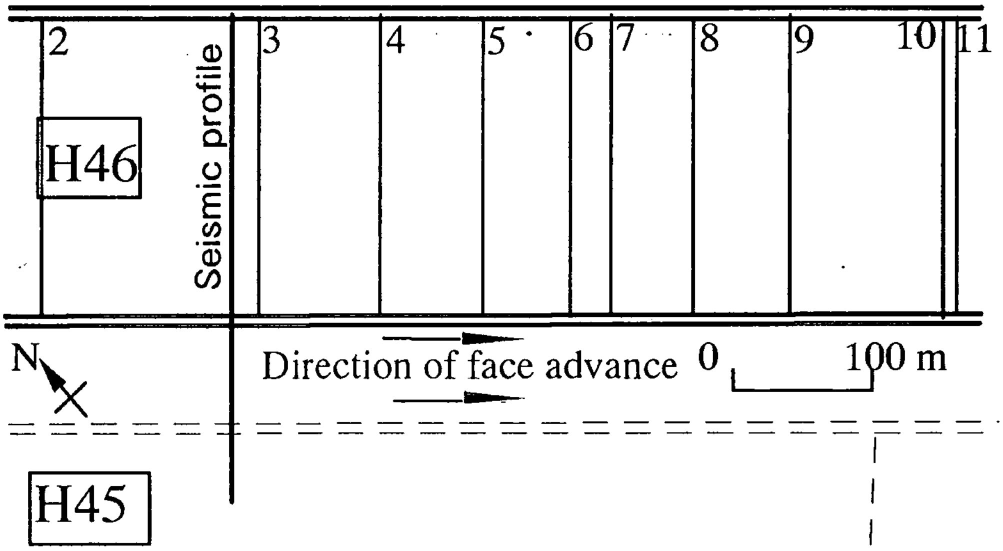

Fig 4.8. The layout of panel H46 showing the location of the seismic profile and the positions of the coal face when the profile was surveyed.

4.4.2 Data acquisition

The seismic profile was laid out approximately above the middle of the panel, perpendicular to the direction of mining (Fig 4.8). A sledge hammer was used as seismic source, and a total of sixty shot points at a 10 m interval, with 10 hammer blows stacked at each shot point, were carried out. Two spreads were used for recording, each consisting of 24 geophones at 5 m spacing. The first spread was used to record the first thirty shots, with the first shot point located at 57.5 m offset. The whole geophone spread was then moved 120 m such that the first geophone of the second spread was 5 m from the position of the last geophone of the first spread. The position of the first shot into the second spread was at 117.5 m offset. The acquisition geometry is shown in Fig. 4.9. This layout gave a total subsurface coverage of 292.5 m with the coverage varying between 12-fold and 24-fold across the middle of the profile.

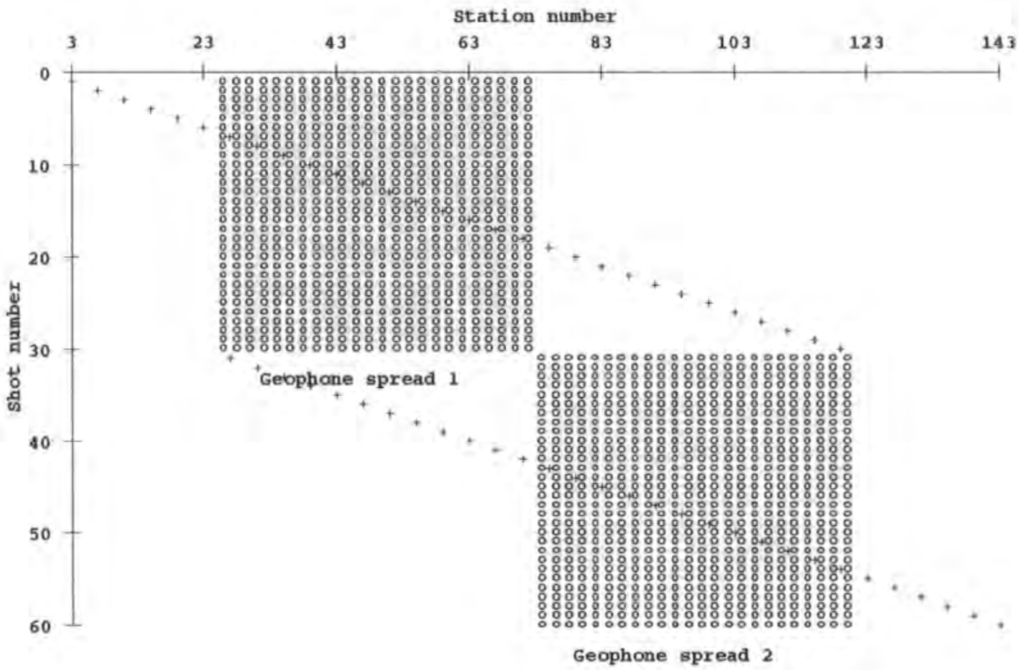

Fig 4.9. Seismic data acquisition geometry of the profile over panel H46.

The dates and position of the coal face when the profile over panel H46 was surveyed are tabulated in table 4.2. The negative distances given on the table indicate that the coal face had not passed the profile.

Levelling was also carried out along the seismic profile at 30 m intervals, with the first station at the far end of the profile, to determine surface subsidence. A point more than 200 m from the panel towards panel H45 was taken as a fixed station and all the levelling measurements were tied to this point. The levelling was done on the same days as seismic surveys with an extra levelling survey on 20.12.94.

Table 4.2. The dates and location of the coal face when the profile over panel H46 was surveyed

Survey	Date	Distance from the coal face to the seismic profile in metres
H46/1	13/01/93	-400
H46/2	18/02/93	-150
H46/3	19/03/93	15
H46/4	15/04/93	110
H46/5	05/05/93	180
H46/6	26/05/93	250
H46/7	16/06/93	280
H46/8	12/07/93	340
H46/9	30/07/93	410
H46/10	10/09/93	525
H46/11	25/05/94	535 (7 months after extraction complete)

4.4.3 Data quality

Similar interference from the ground roll and the first arrivals reverberation observed in H45 were also observed in shot records of this profile. The frequency content of the reflected arrivals and the noise for most of the surveys were also similar to those of H45. However, some shot records of certain surveys in this profile displayed poor signal-to-noise ratios, in particular those of survey H46/7. For comparison, Fig 4.10 shows four bandpassed shot records of different surveys from the same source point. The same filter and AGC window parameters as in Fig 4.7 were applied. Although some records of H46/7 were of better quality, the record shown in Fig 4.10(c) is typical of the poor quality records in this survey. The poor quality data was due to a crew who were less skilled in hitting the plate with the sledge hammer during the H46/7 survey.

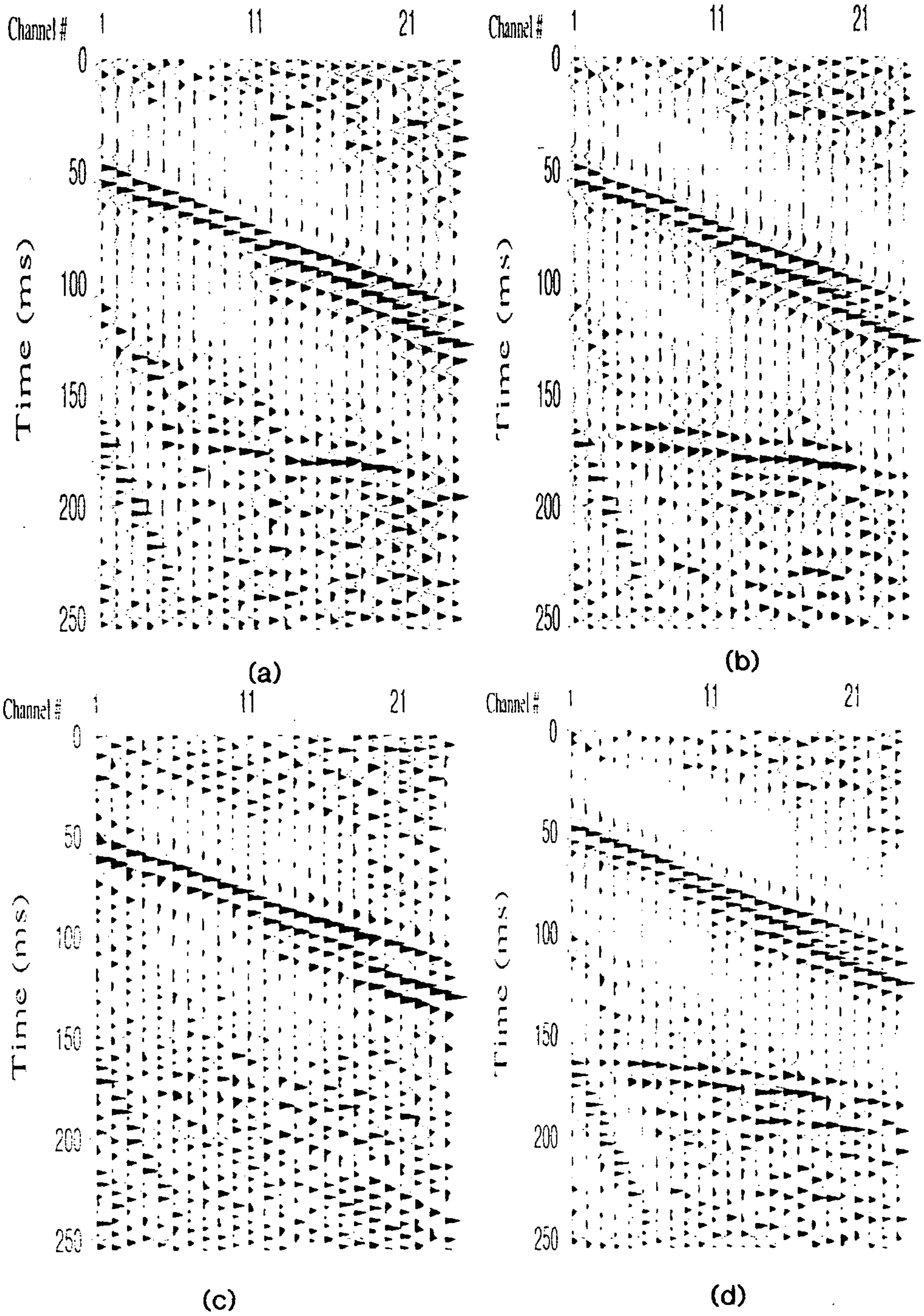

Fig 4.10. Filtered shot records from the same shot point of surveys (a) H46/1, (b) H46/4, (c) H46/7 and (d) H46/10.

4.5 Ground roll suppression using the stack array

4.5.1 Introduction

It was shown in § 4.4.3 and Fig 4.6 that for field records with geophones close to the source, most of the noise that interferes severely with reflected arrivals was due to ground roll. In some records the ground roll plagued more than 30 percent of the traces in a shot record. It is obvious therefore that the data quality can be improved significantly by eliminating or suppressing the ground roll. For unaliased data this can be achieved at the processing stage as described in §4.6.1. In conventional seismic surveys, however, most of the ground roll is suppressed during data acquisition by using arrays of geophones or sources. If the geophones (or sources) in an array are spaced evenly, then maximum suppression of ground roll with wavelength equal to the array length is achieved. The wavelength, and therefore the length of the array, can vary from a few tens of metres to just over one hundred metres, depending upon the frequency content of the noise and the weathered layer condition. For shallow seismic surveys, with a geophone group spacing of less than 10 m, such array sizes are impractical.

It was not until fairly recently that an approach using geophones or sources arrays that are shorter than the apparent wavelength of the ground roll was discussed in the literature. Anstey (1986) named this approach 'stack-array' and gave a comprehensive description of the method. Basically, the field geometry is laid out such that each CMP gather has the same even, continuous range of offsets.

The stack-array criterion in an end-on spread configuration is fulfilled by using a group length equal to the group interval, and the source interval equal to half the group interval. In a split-spread layout the stack-array criterion is met by setting the group length, group interval and source interval to be the same, with the source point located between geophone groups. The groups in both layouts can be either source arrays or geophone arrays.

4.5.2 Data acquisition

To test the data quality obtainable using the stack-array approach at the study site, a split spread with geophone arrays was shot on the seismic profile above the panel H46. The survey was carried out on the same day as H46/5 (see table 4.2), with group length, group interval and source interval all equal to 10 m (Fig 4.11). Source points were located between geophone groups, and 24 groups, each consisting of 12 evenly spaced geophones, were used for recording. At each source point ten hammer blows were stacked to increase the signal to noise ratio and the data were recorded using a sampling rate of 0.5 ms.

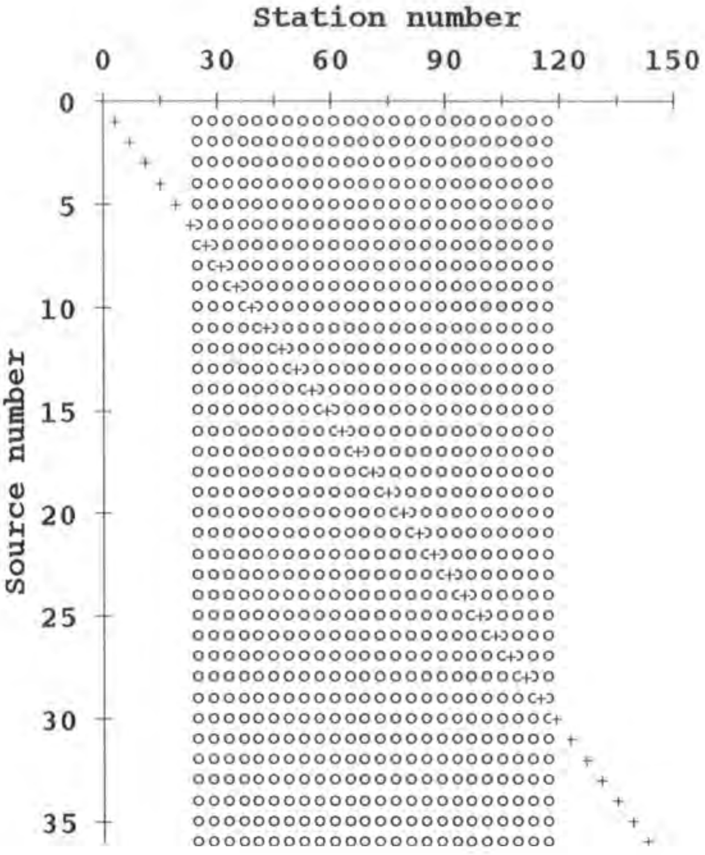

Fig 4.11. Stack-array acquisition geometry.

4.5.3 Field records

Figure 4.12a shows a typical field record obtained using a stack-array approach, and Fig 4.12b shows the same record after applying a bandpass filter. The reflected arrivals from our target can be seen at about 180 ms zero offset. As expected the record displays higher reflection energy than that observed when using a single geophone. Statistically, for a given offset and the same input energy, the signal-to-noise ratio in the stack-array is $\sqrt{12}$ times greater than the signal-to-noise ratio obtained using a single geophone pattern. The polarity of the record in Fig 4.12 is opposite to that of single geophone pattern as the clips were connected with the opposite polarity.

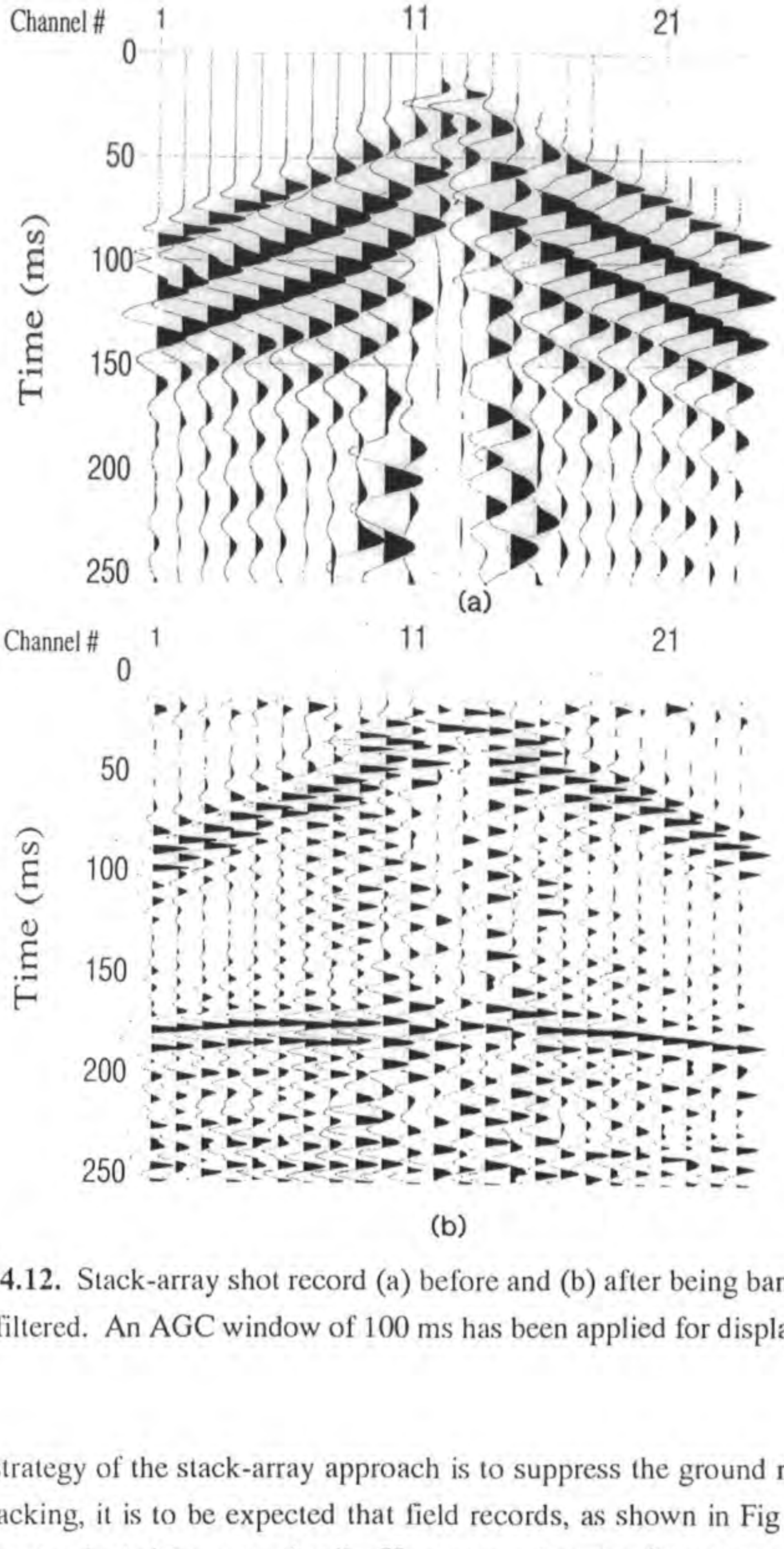

Fig 4.12. Stack-array shot record (a) before and (b) after being bandpass filtered. An AGC window of 100 ms has been applied for display.

As the strategy of the stack-array approach is to suppress the ground roll during CMP stacking, it is to be expected that field records, as shown in Fig 4.12, will still be contaminated by ground roll. However, when the filtered record in Fig 4.12 is compared with that of single geophones (Fig 4.5), it can be seen that in the stack array record the airwaves have been suppressed to an insignificant level. Figure 4.13 illustrates how this has been achieved. The first 12 traces in the figure represent the outputs from individual geophones in an array, and the last trace is the actual output recorded from the group, which is the summation of all the geophones in an array. The wavelet used to model the airwaves in Fig 4.13 is an actual airwave wavelet from one of a single geophone record. Since the dominant frequency of the airwave is about 200 Hz and its apparent velocity is equal to 330 m/s, the geophone spacing of 83 cm has caused the airwaves in two adjacent traces to arrive at times which differ by half the period of the airwaves.

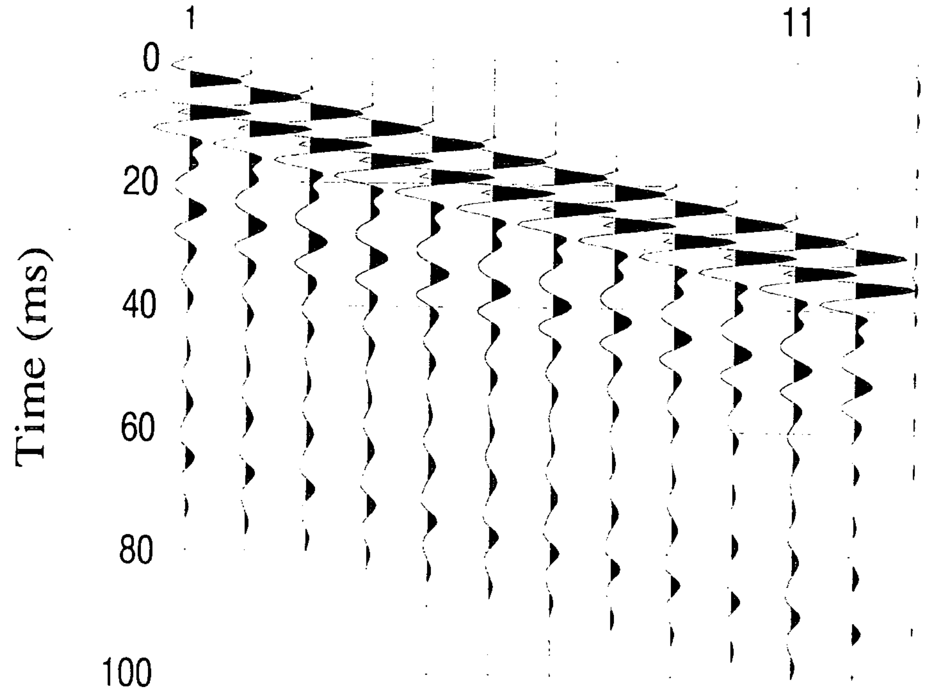

Fig 4.13. Diagram to illustrate the effect of stack array on the airwaves. Traces 1 to 12 are from individual geophones in the array, and trace 13 is the sum of traces 1 to 12.

4.5.4 Results

To find out how successful the stack-array has been in suppressing the ground roll, three stacked sections obtained using different offsets are compared in Fig. 4.14. In all sections, first arrival muting, a bandpass filter and an AGC of 100 ms were applied to the data before sorting into CMP gathers. All traces, including those which have ground roll, were used to obtain the top section of Fig 4.14. The middle section was formed by stacking only the far offset traces, i.e. the traces which are free from the ground roll to the reflected arrival times, whilst the near offset traces, 5 to 25 m, were stacked to form the bottom section. The polarity was reversed during processing of these sections so that they can be compared with those of single geophones.

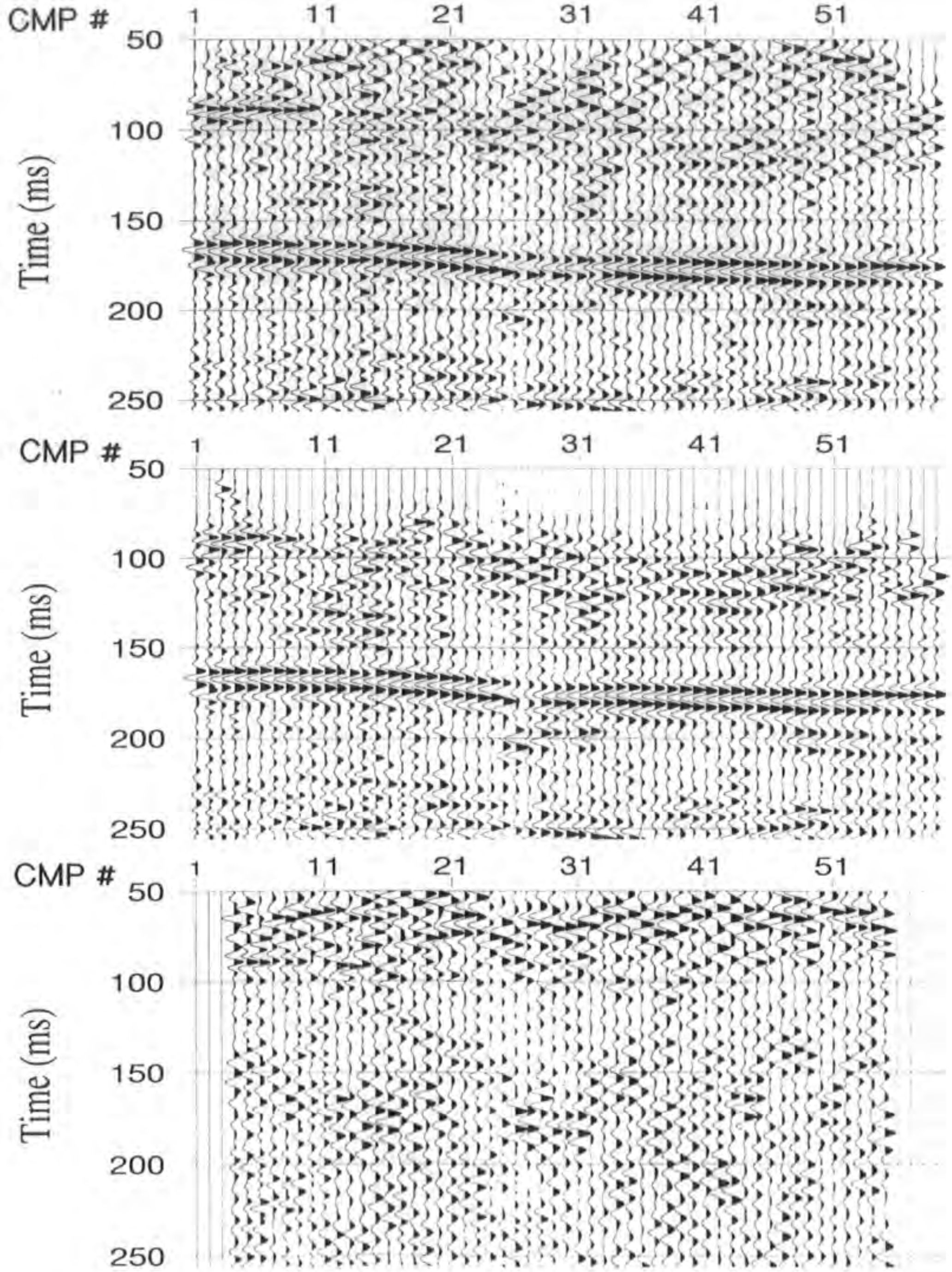

Fig 4.14. Stack-array stacked sections: the top section was formed using all the offsets, while only the far and near offset traces were used to form the middle and the bottom sections, respectively.

It is evident from Fig 4.14 that it is only at the middle of the section (CMP 21-31) that significant suppression of ground roll has been achieved. The unsatisfactory results of the stack-array methodology in this area is principally due to inconsistency between the ground roll wave trains generated at successive source points. It is possible, however, that for deeper surveys, and therefore longer spreads, the effect of the near surface on the ground roll wave train would be averaged out and therefore the stack array would be more appropriate.

4.6 Processing of the single-geophone data

4.6.1 Rejection of coherent noise

First arrivals As first arrivals (direct and head waves) did not interfere with the reflected arrivals from our target, it was possible to eliminate them by applying a top mute. In very shallow reflection data, headwaves tend to interfere with the reflections and in such cases *f-k* filtering is sometimes effective for suppressing the headwaves.

Airwaves The airwave is a broad-band noise phase with an apparent velocity of about 330 m/s, and its amplitude depends on the weather condition (the state of the wind and temperature stratification) and to some extent on the ground surface conditions. In this work, the airwaves were removed by applying surgical muting. In surgical muting, the location of the noise window is identified either by editing individual traces or, as in ProMAX, by indicating its velocity and the duration of the airwave wavelets.

Ground roll Apart from a stack-array survey (see §4.5), two different processing approaches for suppressing ground roll were attempted: *f-k* or velocity filtering and matched filtering.

Generally, ground roll tends to have much lower velocity than the apparent velocities of the reflections, and therefore plots in the higher wavenumbers segments of an *f-k* plot. Thus, appropriate velocity filtering can be used to reject the ground roll by filtering out all the events which have low apparent velocity. However, as shown in Fig 4.15, when a shot record from one of the surveys in this study is transformed into the *f-k* domain, the ground roll is severely spatially aliassed or 'wrapped round'. The frequency at which spatial aliasing of ground roll occurs is governed by its velocity and the geophone spacing. For ground roll with velocity V and a geophone spacing x, the frequency f_a at which spatial aliasing occurs is given by

$$f_a = \frac{V}{2x}. \tag{4.1}$$

The velocity of the ground roll in the Selby area is about 100 to 120 m/s and its maximum frequency is more than 125 Hz. With a geophone spacing of 5 m, the aliasing starts at 10 Hz, and wraps round more than six times before its energy content becomes insignificant. It is obvious, therefore, that velocity filtering could not be used to filter out the ground roll, even after applying a low cut filter as in Fig 4.15.

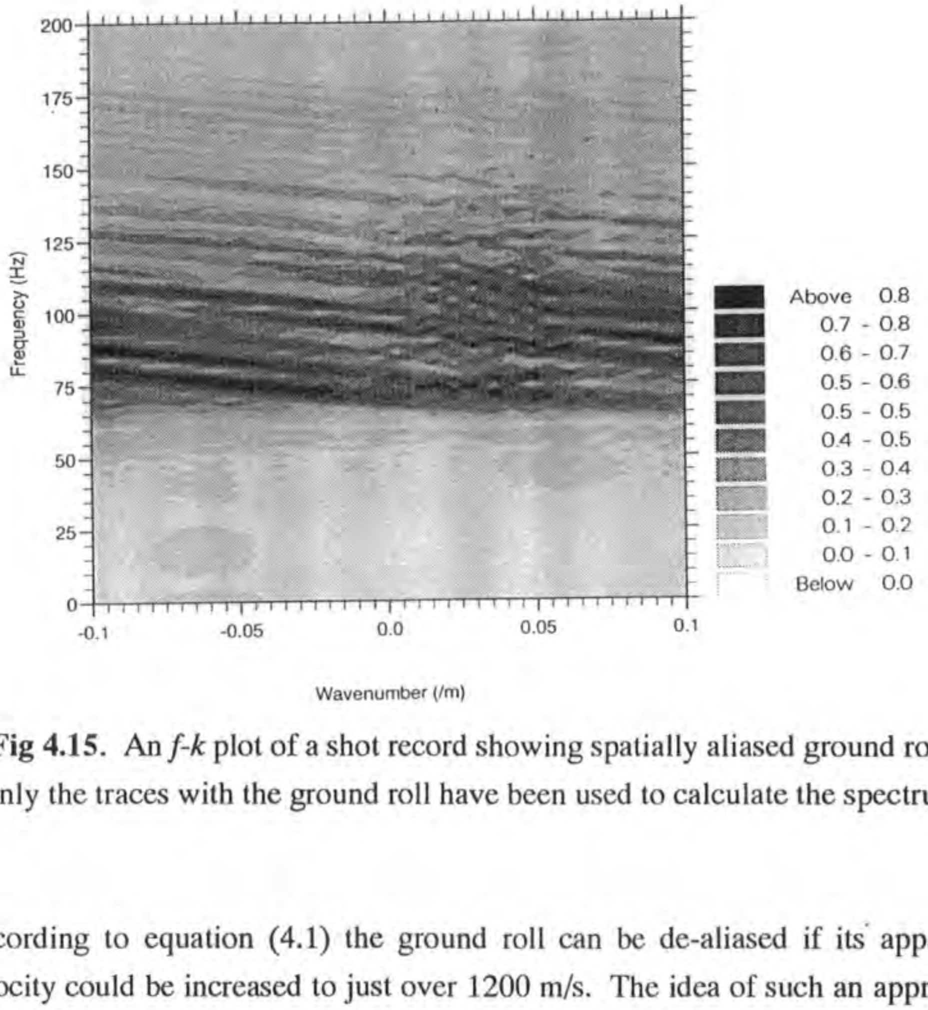

Fig 4.15. An *f-k* plot of a shot record showing spatially aliased ground roll. Only the traces with the ground roll have been used to calculate the spectrum.

According to equation (4.1) the ground roll can be de-aliased if its apparent velocity could be increased to just over 1200 m/s. The idea of such an approach would be to increase the velocity by linearly normal moveout correcting the traces, transforming to the f-k domain, applying the appropriate velocity filtering, transforming back to t-x and then removing the linear normal moveout correction. However, to increase the velocity from 120 to 1200 m/s, the ground roll traveltimes at each trace have to be decreased by 90 percent. For example, at an offset of 30 m, the ground roll traveltime is approximately 250 ms, and therefore the trace would have to be shifted 225 ms upwards. Although this may de-alias the ground roll, it will instead cause the reflection arrivals to be aliassed.

The second method of removing the ground roll considered was linear frequency modulated matched filtering. In contrast to f-k filtering, this is a single-channel filtering and therefore is not affected by spatial alias. The theory of the method is given by Blinchikoff and Zverev (1976) and has been used by Saatçilar and Canitez (1988) to eliminate ground roll in synthetic and real data.

Matched filters are commonly used in radar systems to detect the presence of the signal and increase the signal-to-noise ratio. Basically, if the shape of a signal that is embedded in noise is known, a matched filter can be designed to retrieve it, even though the frequency of the signal is the same as that of the noise. For a signal *v(t)*, the impulse response of the matched filter is defined as

$$h(t) = kv(\Gamma - t) \tag{4.2}$$

where k is a scale factor and Γ is the time delay. The transfer function of the matched filter, which is the Fourier transform of equation (4.2) is

$$H(\omega) = ke^{-j\omega\Gamma}V^*(\omega) \tag{4.3}$$

where $V^*(\omega)$ is the complex conjugate of the Fourier transform of *v(t)*.

If *v(t)* is a linear frequency modulated (LFM) signal (the frequency increases or decreases linearly with time), then it can be modelled by

$$v(t) = \cos(\omega_c t + \frac{\Delta\omega}{2T}t^2) \text{ for } \frac{T}{2} \leq t \leq \frac{T}{2} \tag{4.4}$$

where ω_c is a carrier angular frequency in rad/s, T is the length of the LFM signal and $\Delta\omega$ is its bandwidth. The derivation of the transformation of *v(t)* to the frequency domain is given by Blinchikoff and Zverev (1976). Approximately $V(\omega)$ is given by

$$V(\omega) = |V(\omega)|e^{j(\theta_0+\theta_1(\omega))} \tag{4.5}$$

where $\theta_1(\omega) = -\pi D(\frac{\omega_c-\omega}{\Delta\omega})^2$, $|V(\omega)|$ is the amplitude spectrum, θ_0 is the initial phase and D=ΔfT. D is also known as the time-bandwidth product or compression factor. Substituting equation (4.5) in (4.3), the transfer function of the filter to be matched to the LFM signal is

$$H(\omega) = k|V(\omega)|e^{-j(\omega\Gamma+\theta_0+\theta_1)}. \tag{4.6}$$

The matched filter, however, is often approximated to

$$H(\omega) = \exp\left\{ j\left(\pi D\left(\frac{\omega_c-\omega}{\Delta\omega}\right)^2 - \omega\Gamma - \theta_0 \right)\right\}. \tag{4.7}$$

If the filter of equation (4.7) is applied to a sequence that contains the signal of equation (4.5), all frequency components of the signal will be shifted by time Γ and therefore the signal will be compressed.

Since ground roll is composed of frequency modulated wave trains, it implies that the matched filter for the LFM signal described above can be used to compress the ground roll and move it out of the reflection window. However, before the filter was applied to eliminate the ground roll in the real data, it was decided to test its applicability to synthetic data of different ground roll frequency and signal-to-noise ratio. The results showed that the method works better in data with a higher reflection amplitude than the ground roll, and with less frequency overlap between the two. This is demonstrated in Fig 4.16 where the ratio of the reflected to ground roll amplitude was changed from 0.5 (Fig 4.16c) to 2.0 (Fig 4.16d). Although not stated in their paper, I would suspect that the good results obtained by Saatçilar and Canitez (1988), when they applied a matched filter to synthetic and real data, was due to the high reflected amplitude and low frequency ground roll involved.

It was obvious from the synthetic data results (Fig 4.16) that no significant improvement, if any, was to be expected by applying matched filter to the real data from our surveys. This is because the ground roll in these data have extremely high amplitude and high frequency. The effect of applying a matched filter in one of the shot gathers is shown in Fig 4.17. The matched filter was applied after the record had been bandpass filtered to reduce the amplitude of the ground roll. The same shot record before the matched filter had been applied is shown in Fig 4.6b.

Thus, it was decided that the only way of removing the ground roll without creating artefacts detrimental to the reflected arrivals was to apply a surgical mute in the far offset traces, and to kill the traces that are severely dominated by the ground roll.

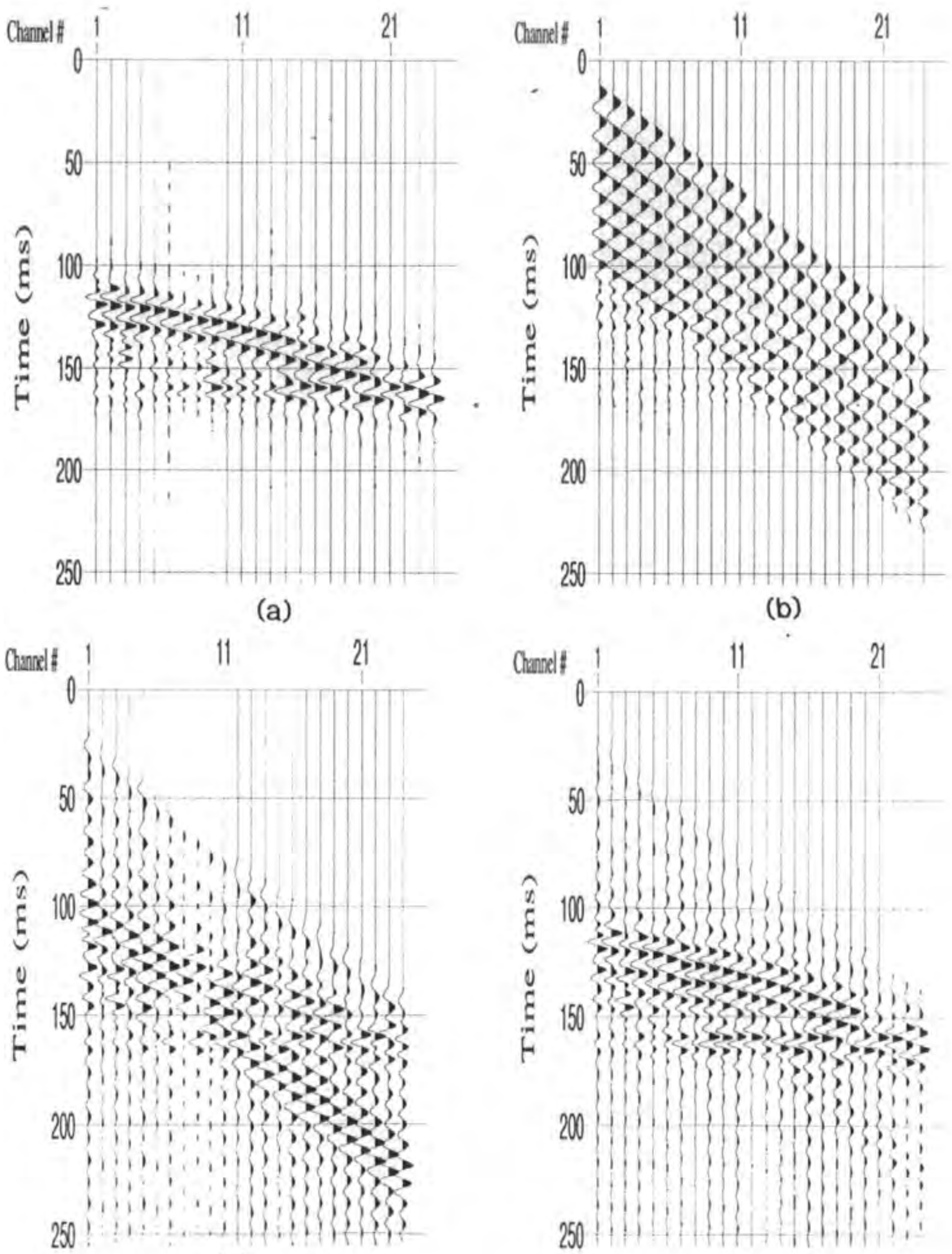

Fig 4.16. Synthetic data showing the effect of applying matched filter to a LFM signal: (a) reflected arrivals, (b) reflected and ground roll arrivals, and (c) and (d) are the matched filtered version of (b) with reflected amplitude half and twice that of the ground roll, respectively.

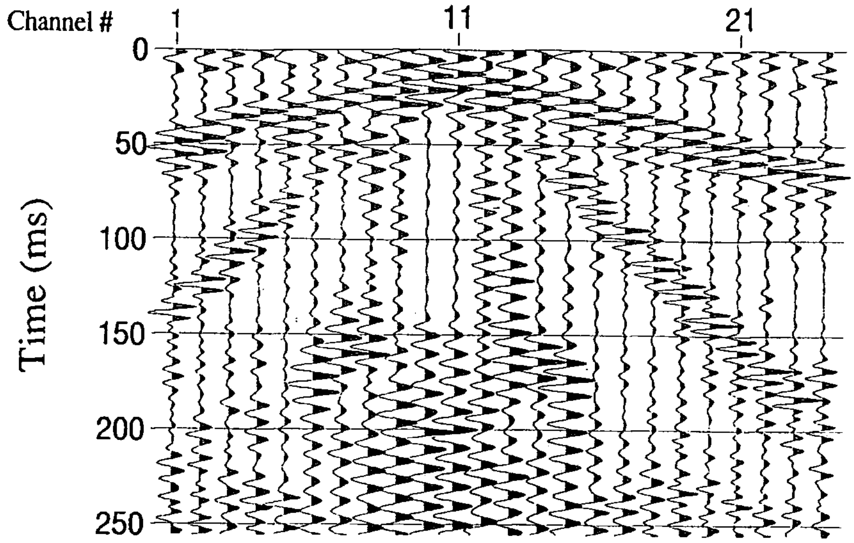

Fig 4.17. A shot record after applying a bandpass filter and matched filter: An AGC has been applied for display.

4.6.2 Statics

Field statics were calculated using the first breaks and Hagedoorn's plus-minus method. Except for the geophones closest to the source, the first arrivals were head waves refracted from the water table, within 2 m of the surface. It was decided to use this refracting horizon as the datum for static corrections. The first breaks were picked manually to an accuracy of one sample. The receiver statics were first obtained from the plus times. The shot statics were then calculated from the traveltimes, using the refractor velocity obtained from the minus-time graph, receiver statics and the shot-receiver distance. The statics for surveys H45/1, H45/4 and H45/7 calculated in this way are shown in Fig 4.18. The figure shows that the shot statics vary more rapidly along the profile than the receiver statics due to inconsistency in triggering.

To ensure that the receiver statics were free from triggering error, only those shots with difference in end to end time of less than 1 ms were used in calculating plus times. Hence, the maximum error in the combined static correction for each trace, including picking errors, is estimated to be 1 ms. An example of a traveltime graph of shots which could not be used to calculate the receiver statics is shown in Fig 4.19. The delay in the diagram is the difference in end to end traveltime between shots 17 and 37, which has been caused by triggering error, and in this case is about 4 ms.

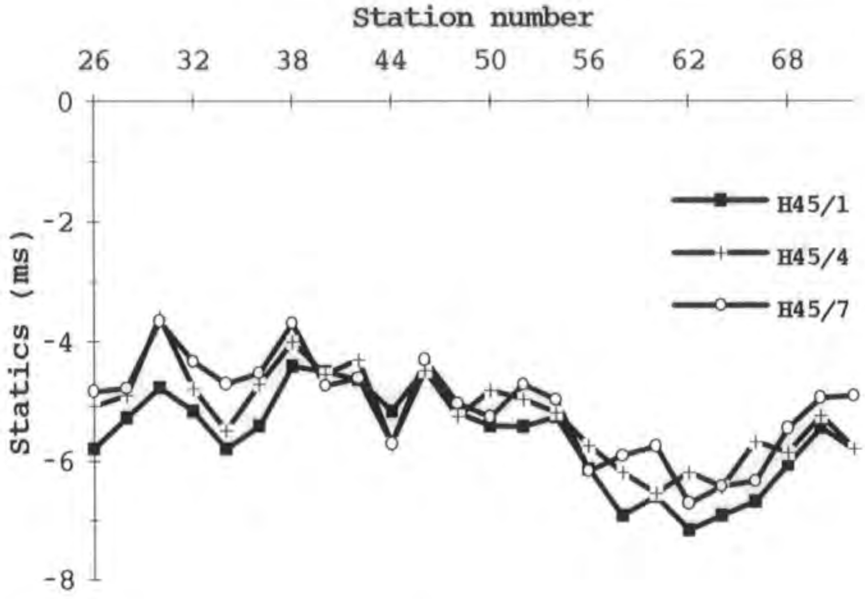

(a)

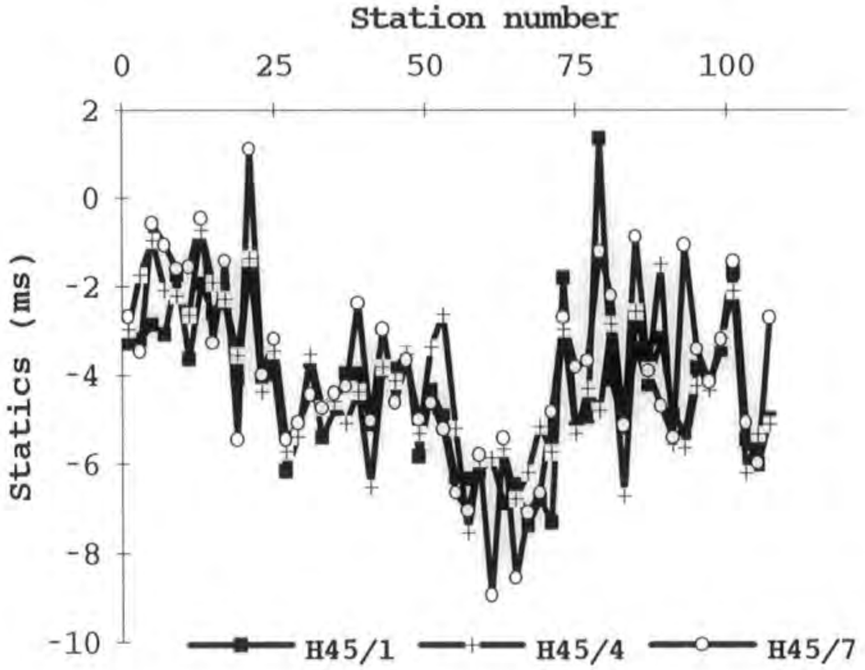

(b)

Fig 4 18. (a) Receiver and (b) shot statics for surveys H45/1, H45/4 and H45/7.

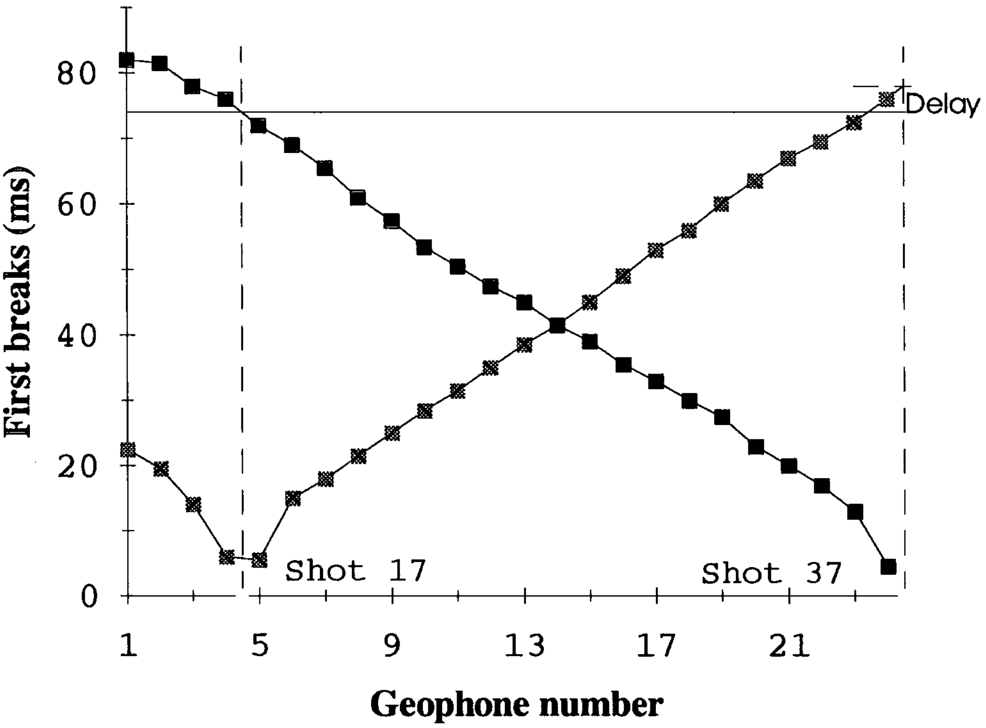

Fig 4.19. First breaks of shot records 17 and 37 of H45/1 showing the difference in end to end time between the two shots, which is identified as Delay on the upper right corner of the diagram.

Another approach for determining the statics was sought in which the picking of the first breaks and the method described above are performed only on the first surveys of each profile. Once the statics of the first survey have been applied, the statics of the subsequent surveys are then obtained by crosscorrelating the windows of the first arrivals of these surveys with their counterparts in the first survey. As long as the refractor velocity and the effective wavelets of the first arrivals are the same between surveys, the time shift required to obtain the maximum correlation is basically the total static of that trace. Although the refraction velocity between surveys was almost exactly the same, the wavelet of the first arrivals was found to vary significantly in some shot records due to the change in source and receiver coupling. Such change is illustrated in Fig 4.20. Consequently, this very easy method of calculating statics was not used in these surveys.

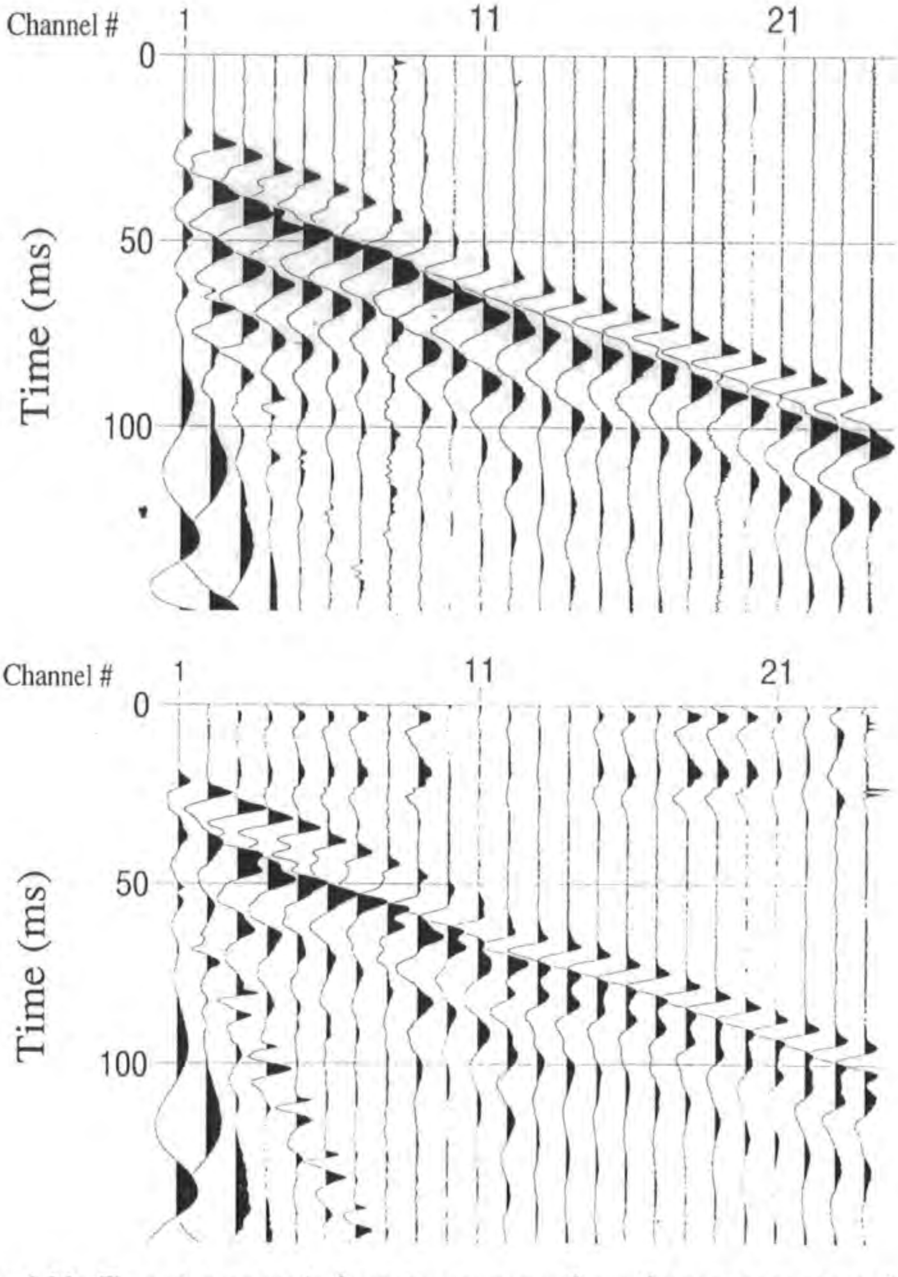

Fig 4.20. Two shot records from two surveys from the same source point showing the change in the shape of the wavelet of the first arrivals.

4.6.3 NMO correction and stack

A constant stacking velocity of 2000 m/s was used for NMO correction before the CMPs were stacked. The small value of stacking velocity to the depth of 150 m is due to the low interval velocity in a porous Bunter Sandstone, which constitutes most of the rockmass between the surface and the reflecting horizon. The maximum allowable NMO stretching was set at 30%.

4.6.4 Post stack processing

The stacked sections were processed using the scheme laid down in the preliminary survey. Spiking deconvolution was applied to the sections before being time migrated using an *f-k* migration algorithm. The final migrated sections for surveys H45/1 and H46/1 are shown in Fig 4.21. The CMP spacing is 2.5 m and the strong reflection, which can be traced easily across both sections, is from our target, the anhydrite layer. The description and interpretation of the results are presented in following chapters.

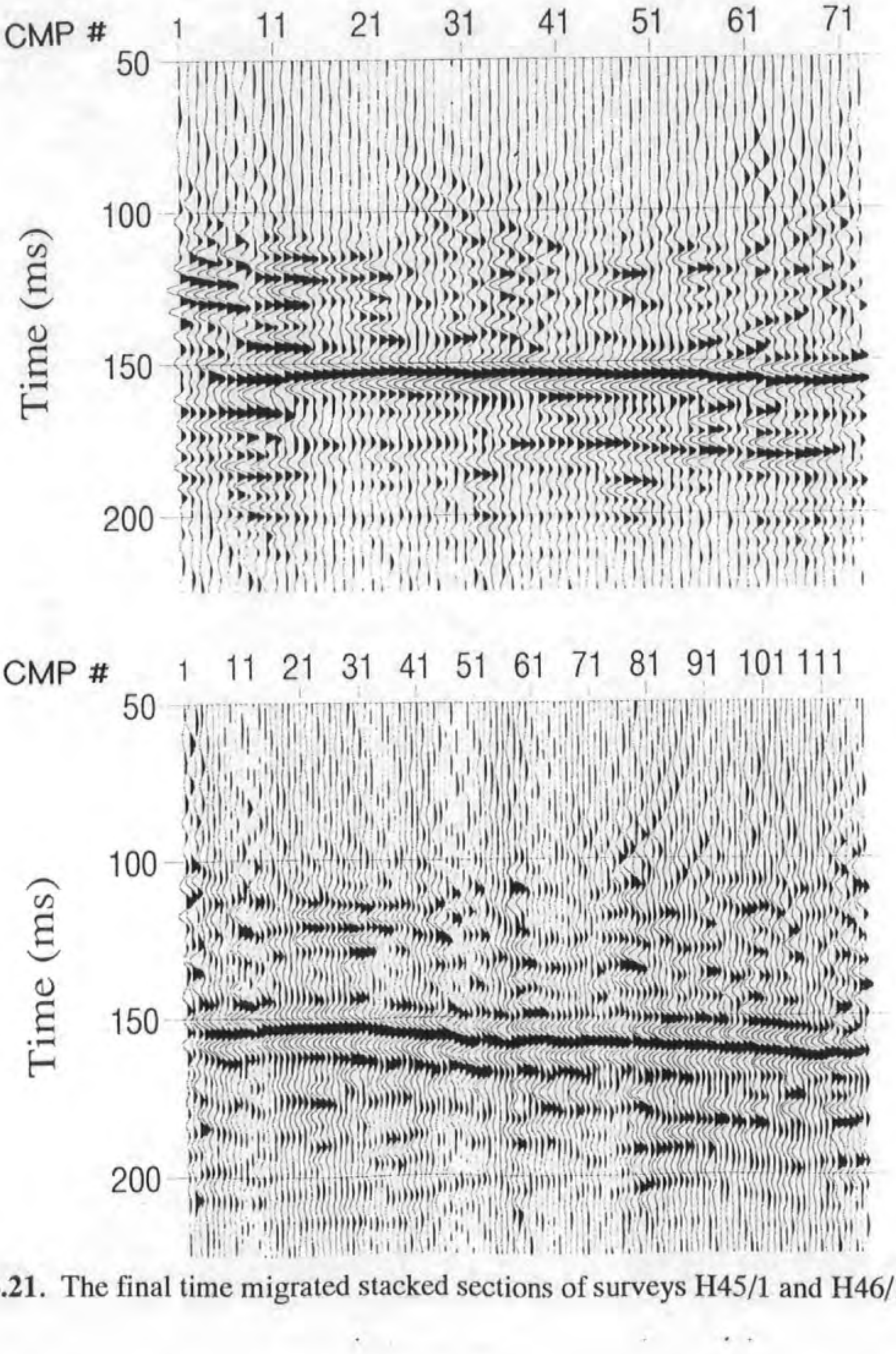

Fig 4.21. The final time migrated stacked sections of surveys H45/1 and H46/1.

4.7 Uses of coherent noise

Three different forms of coherent noise are identified in shot records (e.g. Fig 4.6), refracted arrivals, airwaves and ground roll. As described in § 4.6.2, the first arrivals, which are mostly refracted arrivals, were used to calculate the field statics. Here, attempts at using the other two forms of coherent noise are described.

4.7.1 Airwave

Since the airwave travels at almost constant velocity, its arrival time is expected to be approximately the same for all the traces in a common offset gather. The early or late arrival of the airwave in any trace in a gather may suggest that the shot of that particular trace had a triggering error or was positioned incorrectly. In this study, the airwave arrivals were used only as a rough guide in identifying the shots that had triggering error. As an example, Fig 4.22 illustrates how such shots can be identified. The figure shows the airwave arrivals in a 42.5 m common offset gather of survey H45/1. The arrivals correlate well across the gather except for shots 37 and 40. The statics of these shots as shown in Fig 4.18 were found to be much less than the statics of other shots in the survey. The shape of the wavelet of shot 37, which differs considerably from the rest, may be due to destructive interference of the airwave generated by individual hammer blows of the shot, which are stacked together. This may therefore suggest that the inconsistency in triggering takes place not only between shots but also between hammer blows.

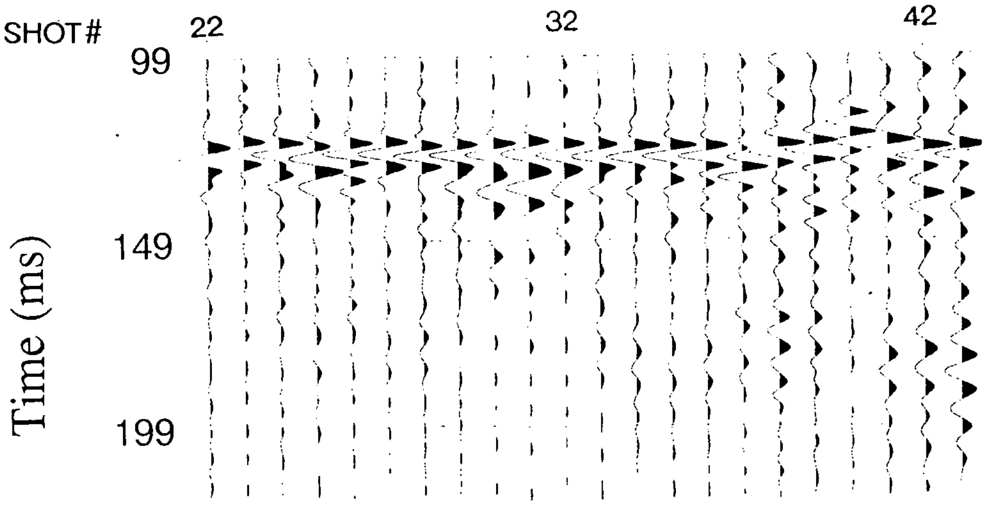

Fig. 4.22. A 42.5 m common offset gather of H45/1 showing the airwave arrivals.

The application of airwave arrivals to correlate shots from different surveys was not successful because of a significant change in the shape of the airwave wavelet between surveys. This may be due to the change in source coupling, since the ground at the source point was consistently compacted each time the profiles were surveyed.

4.7.2 Ground roll

To correlate shots from different surveys, attention was turned to another form of coherent noise, i.e. ground roll. The similarity in the shape of the ground roll in shot records of different surveys made the cross correlation possible. For a given shot position and offset, a perfect cross correlation is expected only if there is no triggering or positioning error, and the weathered layer conditions have stayed the same between surveys. However, if there is inconsistency in triggering, the time shift required to obtain a perfect correlation will be constant for all the geophones in the shot gather. With the assumptions that the weathered layer conditions have not changed significantly and that the positioning of the sources and geophones were perfect, ground roll in shot records of different surveys were cross correlated to find out if there is any inconsistency in triggering between surveys.

Figure 4.23 shows typical shot records of two different surveys obtained from the same shot point. Also shown in the figure is the time difference between ground roll traveltimes calculated by cross correlating the relevant traces. As the time difference calculated is not constant but varies along the gathers, this may suggest that the assumptions that the near surface ground conditions have not changed and/or the geophones and the sources were precisely positioned are not fulfilled. The time difference can also be seen by comparing the ground roll of two equal offset traces in one shot record. It is important to note that a mispositioning of a geophone or source by only a few centimetres can result in a significant change in ground roll travel times due to its low apparent velocity. Although special care was taken to ensure that the stations were positioned as accurately as possible, a 30 cm mispositioning could result in a 3 ms change in ground roll travel time. Therefore, the time difference observed could easily be accounted for by a small mispositioning of a station superimposed on a small change in ground conditions.

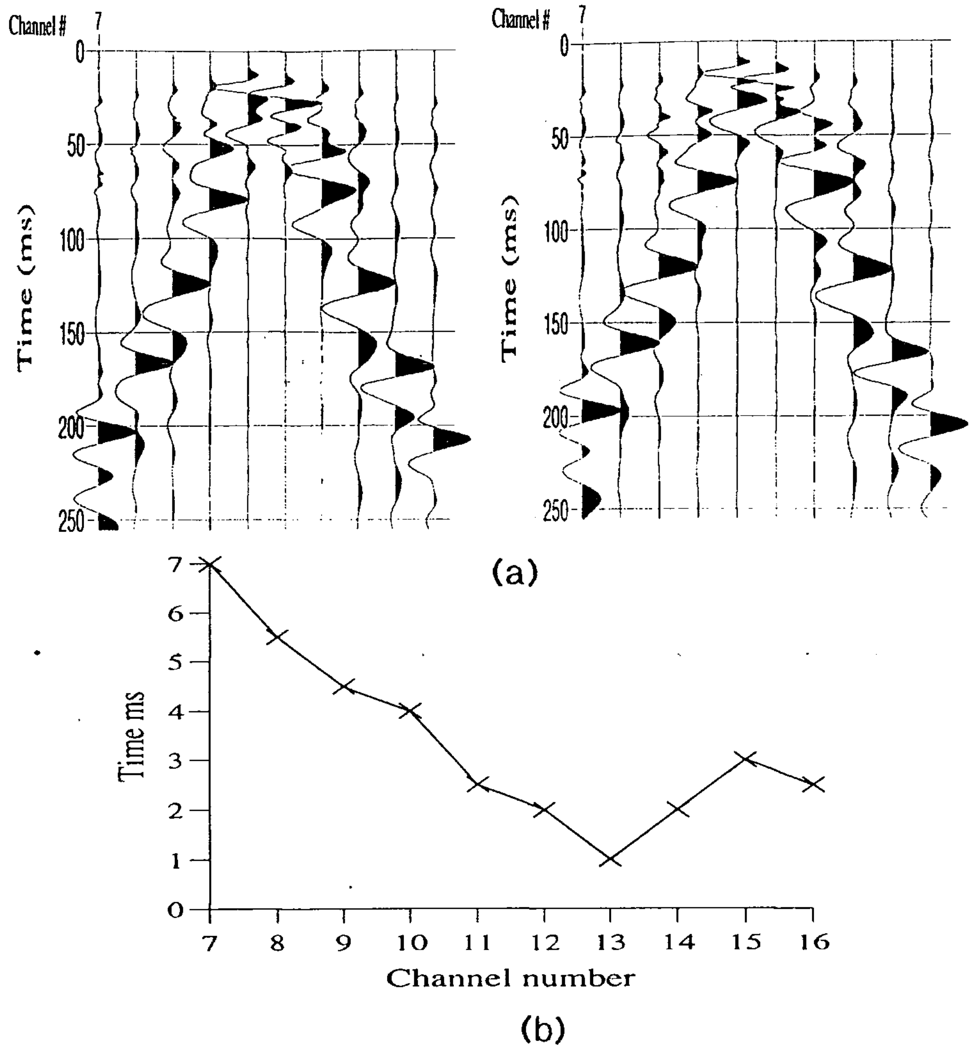

Fig 4.23. (a) Parts of shot records from surveys H46/1 and H46/11 obtained from the same source point showing the ground roll and (b) the result of cross-correlating the ground roll of the relevant traces of the two records.

The next logical step taken was to see if the change in ground condition could be determined by studying the change in the dispersion of the ground roll. It was noted in §3.1.2.3 that ground roll arrivals are Rayleigh waves and therefore in a non-homogeneous material they exhibit dispersion: their velocities vary with frequency. Dispersion of Rayleigh wave and other types of surface waves are often used to study the velocity structure of the crust and the upper mantle (e.g. Knopoff 1972). Usually the surface waves used in such studies are long period waves that are generated by earthquakes. However, although not common, higher frequency ground roll from exploration data have also been used to determine the properties of the upper crust (e.g. Al-Hussein *et al.* 1981).

Two different types of velocities are often used to describe a dispersed wave, phase velocity and group velocity. Phase velocity, $V = f/k$, is a velocity with which a particular phase, a crest or trough of the wavelet, propagates, while group velocity is the velocity with which the 'package' of wave energy at a particular frequency travels. For a non-dispersed signal, phase velocity is equal to group velocity. In this study only the dispersion of group velocity was considered.

Group velocity U is defined as

$$U = \frac{df}{dk} \quad \text{or} \quad U = \frac{d(Vk)}{dk} = V + k\frac{dV}{dk} \tag{4.8}$$

where V is the average phase velocity, and k and f are wavenumber and frequency, respectively. Equation (4.8) shows that group velocity can be obtained by calculating the slope of ground roll arrivals in an *f-k* spectrum plot. However, the ground roll in our data is severely aliased and there is strong interference from other arrivals, and therefore the slope in *f-k* spectrum cannot be determined easily. Thus the multiple-filter technique introduced by Dziewonski *et al.* (1969) was used instead. The technique involves applying narrow bandpass filters centred at different frequencies. The window function used in this analysis is the Gaussian function given as (Dziewonski *et al.* 1969),

$$H(f) = e^{-\alpha\left(\frac{f-f_n}{f_n}\right)^2} \tag{4.9}$$

where f_n is the centre frequency, α is given by

$$\alpha = \frac{ln(R)f_n^2}{(bandwidth/2)^2} \tag{4.10}$$

and R is the ratio of the amplitude at f_n to the amplitude at the cut off frequency. After filtering, the data are Hilbert transformed to obtain an envelope of the instantaneous amplitudes. The arrival times of the maximum amplitude of the envelope and the trace offset can be used to obtain group velocities as a function of frequency.

Examples of instantaneous amplitude envelopes calculated using the technique described above are shown in Fig 4.24. Traces used in this figure are at 17.5 m offset for surveys H46/1 and H46/11 (channel 8 in Fig 4.23). For comparison the maximum amplitudes of the envelopes of Fig 4.24(a) have been plotted as dots in Fig 4.24(b). The envelopes of the two traces correlate fairly well at low frequencies, but at high frequencies the envelopes of H46/11 trace seem to arrive earlier than those of H46/1. This may suggest that there is an increase in group velocities in the near surface ground between the two surveys. Since the discrepancy is mainly in the high frequency components, this may indicate that the effect is only for layers very close to the surface, a metre or less. However, the increase in velocity observed here was not consistent along the profile as can be seen in Fig 4.25. The traces analysed in Fig 4.25 are from the same surveys but at 12.5 m offset and the shot point is 10 m from that of the traces shown in Fig 4.24.

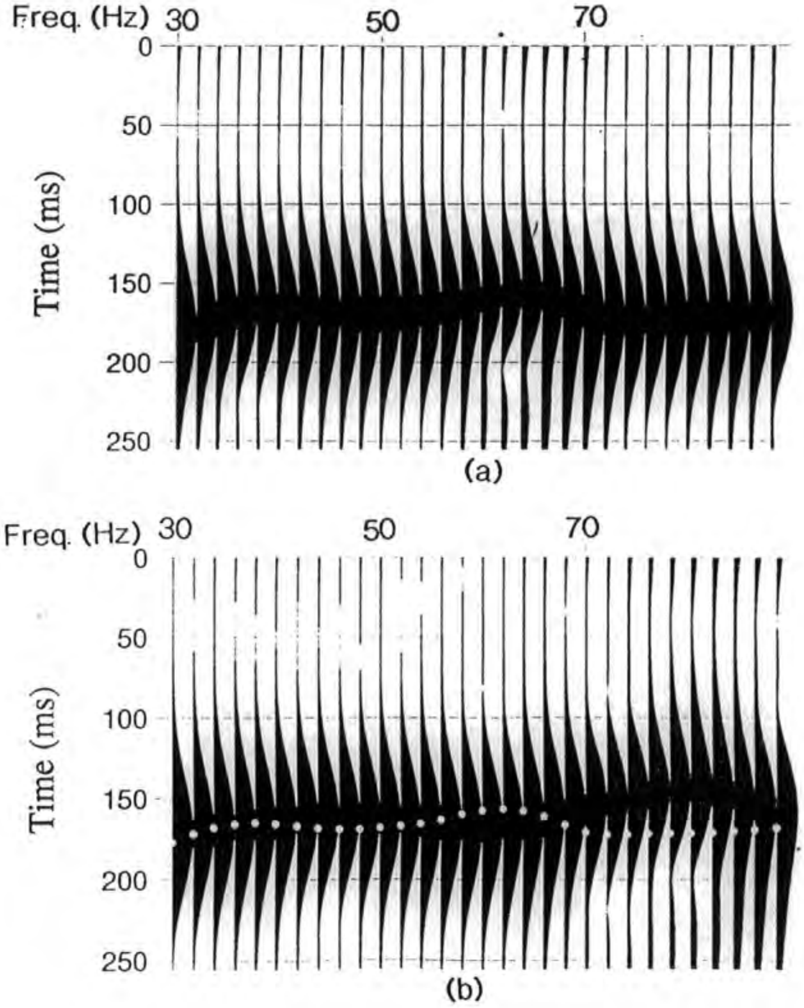

Fig 4.24. Instantaneous amplitude envelopes of the traces at 17.5 m offset of H46/1 (a) and H46/11 (b).

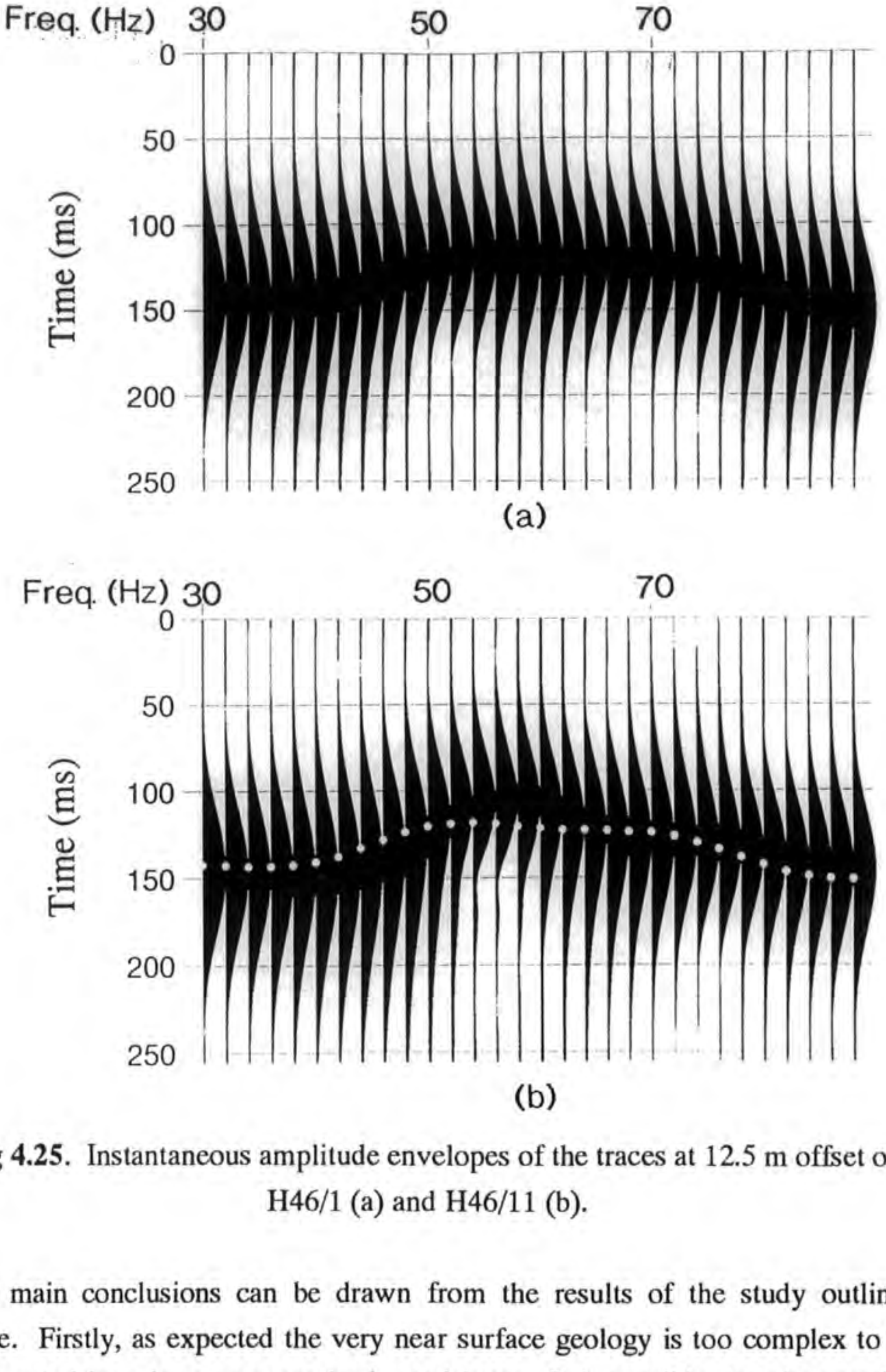

(a)

(b)

Fig 4.25. Instantaneous amplitude envelopes of the traces at 12.5 m offset of H46/1 (a) and H46/11 (b).

Two main conclusions can be drawn from the results of the study outlined above. Firstly, as expected the very near surface geology is too complex to be represented by a homogeneous horizontal layer. It is possible that the weather conditions and subsidence would affect the near surface ground differently along the profile. Secondly, it could be possible to use ground roll to study the structure of the base of the weathered layer, if there exists enough low frequency energy and the length of the spread is long enough to ensure that the arrivals of different frequencies could be separated easily .

Chapter 5

Results

5.1 Introduction

In this chapter, the seismic results obtained from Chapter 4 and subsidence results calculated using the empirical method described in Chapter 2 are presented. The analysis of subsidence induced stresses using the method outlined in Chapter 2 will also be presented in this chapter.

For each seismic profile, the changes in two-way traveltime, which will be referred to as 'differential two-way traveltimes', were calculated by subtracting the reflection times to the anhydrite on the first survey sections from the reflection times on the sections from the subsequent surveys. As the wavelet in the final migrated stacked sections was processed to zero phase, the two way traveltimes to the anhydrite were simply picked at the onset of the maximum amplitude of the wavelet. Alternatively, the differential traveltimes could be obtained by crosscorrelating the windows around the reflection of the first surveys with the subsequent surveys. This approach was used in some sections and the results were similar to those calculated from traveltimes.

The magnitudes of subsidence at the dates when the profiles were surveyed were obtained using empirical curves published by the NCB (see §2.5.2.1). The empirical graphs were used to find the expected subsidence at the anhydrite horizon and at the surface; the latter values were then subtracted from the former. Two different types of empirical curves were used: the final subsidence and the development curves. The final subsidence curves predict the total subsidence of a point after the mining has stopped, whilst the development curve gives the active subsidence as mining proceeds. The difference in subsidence between the surface and the anhydrite will be termed here as the 'differential subsidence'. This, however, must not be confused with horizontal differential subsidence, which is often used for calculating horizontal strain (NCB 1975).

The surface subsidence on profile H46 was also measured directly by levelling at the time of each seismic survey. Ideally, a fixed point, to which all the levelling measurements are referred, must be located as far away from the area affected by subsidence as possible. Due to access difficulties, however, the fixed point in this profile was taken at the gateway into the yard of Laburnum Farm, on Lordship Lane, which is located over panel H45 about 130 m from the profile. After all the levelling values had been tied to the fixed point, the surface subsidence was obtained by subtracting the values of the first surveys from those of the subsequent surveys.

The finite element method was used to calculate stresses induced by subsidence above panel H46. However, as calculations in the 2D finite element method are carried out using a plane strain assumption (i.e. the strain perpendicular to the profile is equal to zero), the method could not be used for the longitudinal profile over panel H45. The edges of panel H45 are so close to the seismic profile that the strain caused by them could not be neglected.

5.2 The profile over H45

5.2.1 Seismic results

The central part of the processed section (CMPs 10 to 70) from four surveys is shown in Fig. 5.1. CMPs 1 to 9 and 71 to 77 have been excluded from the interpretation due to their poor signal-to-noise ratio. The CMP interval is equal to 2.5 m and therefore the total length of the sections in Fig. 5.1 is 180 m. The figure shows that there is a progressive increase in the traveltime of the strong reflection event from the anhydrite (at 150-160 ms) as the coal face advances from left to right.

The differential traveltimes calculated from repeated surveys along this line are plotted in Fig. 5.2. The curves in Fig. 5.2b are polynomial fits to the differential traveltimes data points plotted in Fig. 5.2a. There is no significant increase in two-way traveltimes for surveys H45/2 and H45/3. In surveys H45/4, H45/5 and H45/6, there is a progressive increase starting on the left side of the profile. By the time of the survey H45/7, the panel extraction was almost complete, and the two-way traveltimes to the anhydrite had increased by almost 5.5 ms across the whole section.

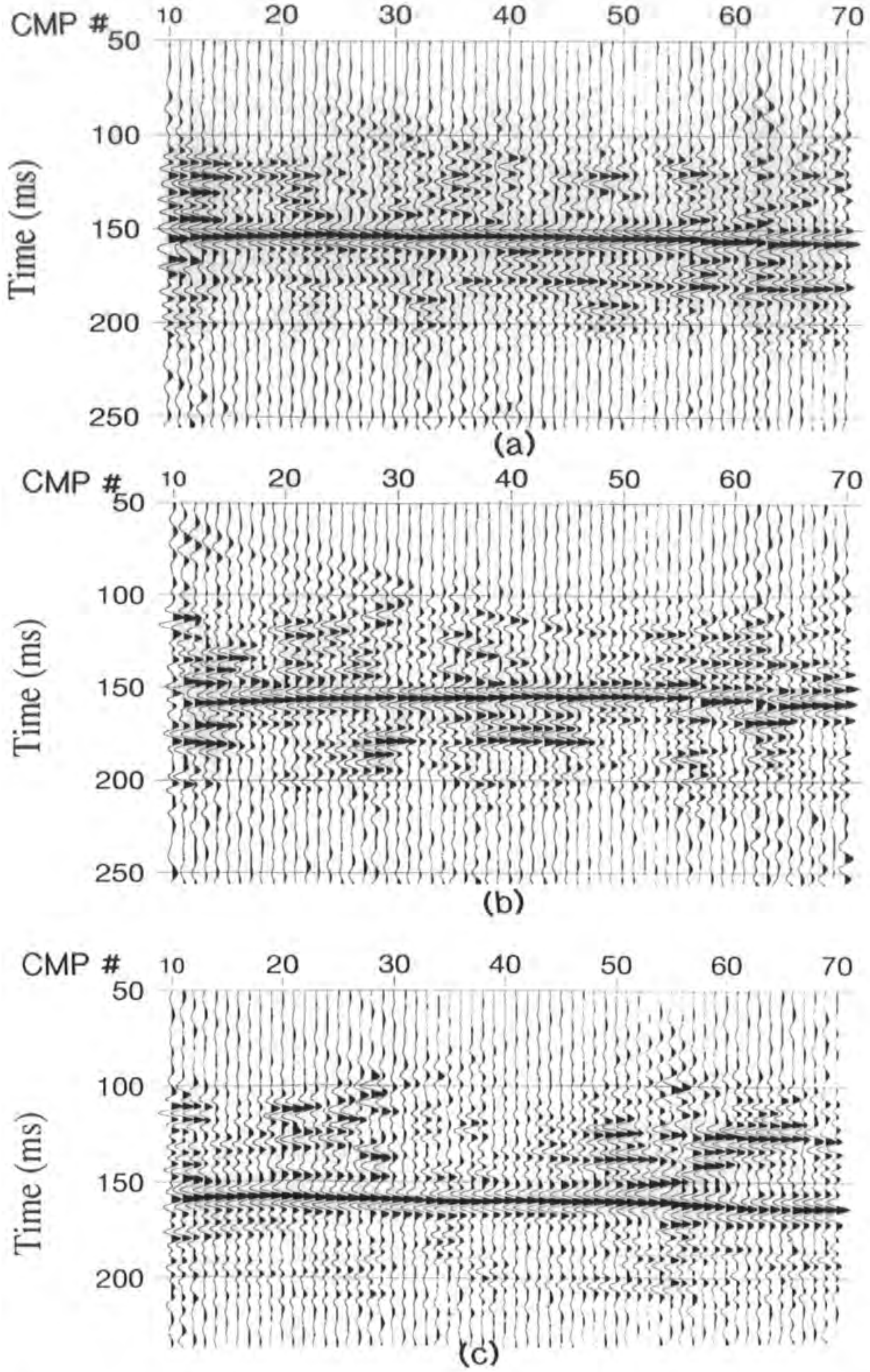

Fig. 5.1. Part of the final time migrated section from surveys (a) H45/1, (b) H45/5 and (c) H45/8. The trace spacing equal to 2.5 m and the direction of mining was from left to right.

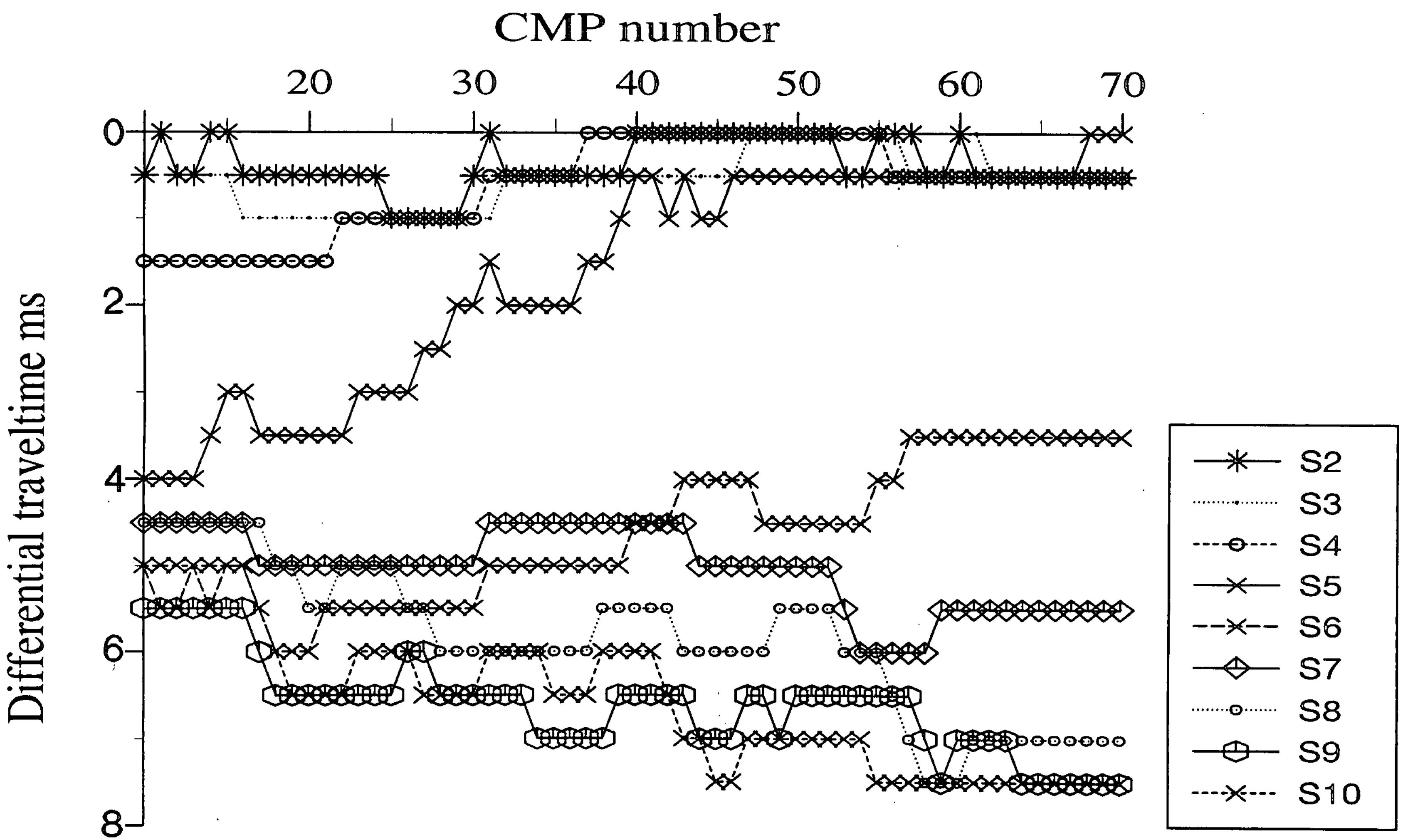

Fig 5.2a. Differential traveltimes calculated from the seismic results.

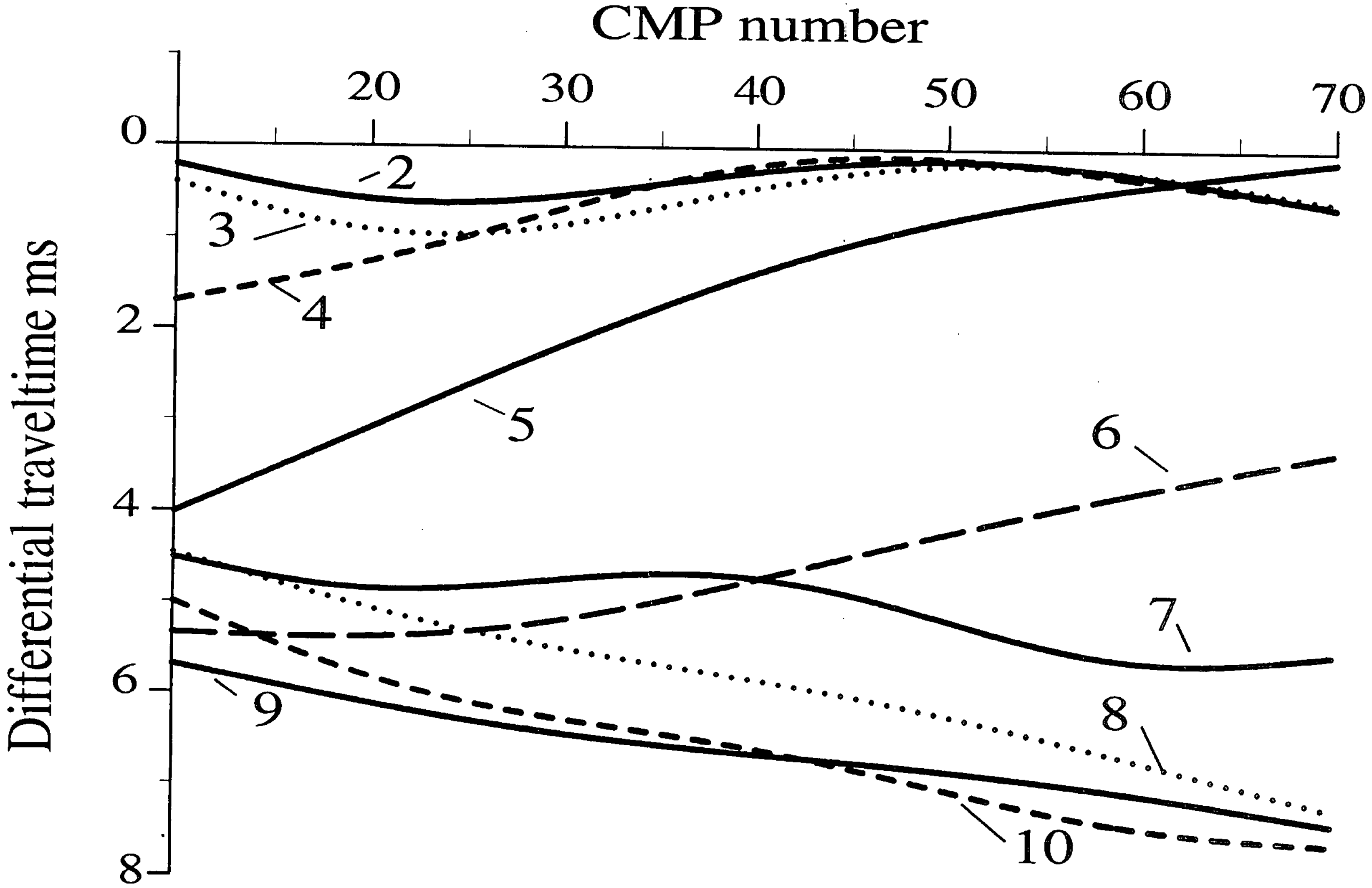

Fig 5.2b. Differential traveltimes calculated from the seismic results. The curves have been smoothed by polynomial fit.

5.2.2 Final differential subsidence

Since it is more convenient to use the NCB empirical curves to obtain subsidence along the profiles that run across the width of a panel, the width and the length of panel H45 were interchanged for calculation purposes. As an example, the parameters used in empirical curves to calculate the surface and the anhydrite subsidence for the survey H45/6, and the values obtained from them are shown in Table 5.1. The magnitudes of subsidence estimated are also plotted in Fig 5.3. It is important to note that the maximum subsidence given on the table is the maximum subsidence for the dimensions of the worked panel at the time of survey H45/6, which is less than the maximum subsidence when the whole panel had been completed (see §2.5.2.1).

Table 5.1 Parameters used to calculate the subsidence, and the subsidence values calculated for survey H45/6

	Surface	**Anhydrite**
Width	780 m	780 m
Depth	550 m	400 m
Advance	220 m	220 m
Seam thickness	2.6 m	2.6 m
Maximum subsidence	87 cm	132 cm

Distance from centre of panel m	**Surface subsidence cm**	**Distance from centre of panel m**	**Anhydrite subsidence cm**
775	0	670	0
506	4	474	7
446	9	430	13
391	17	390	26
358	26	366	40
336	35	350	53
314	44	334	66
292	52	318	80
270	61	302	92
242	70	282	107
198	78	250	119
154	83	218	125
8	87	58	132

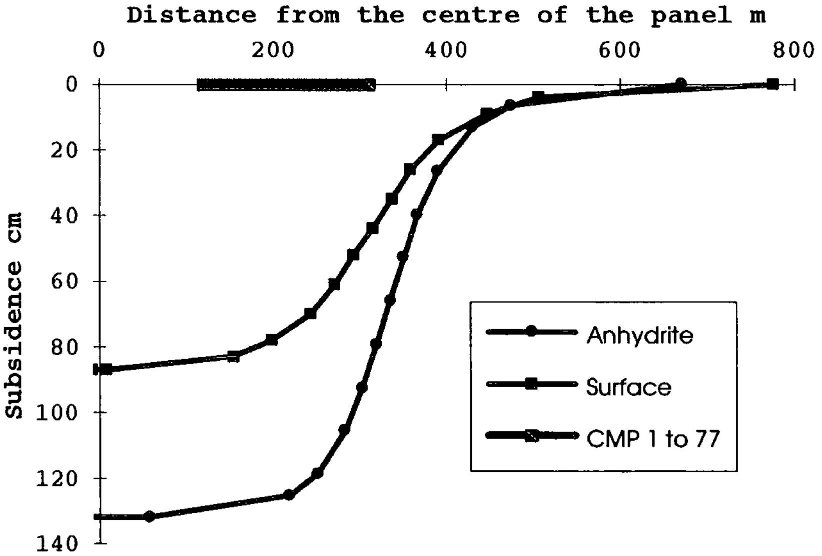

Fig 5.3. The subsidence at the ground surface and the anhydrite during the H45/6 survey. The positions of CMPs 1 to 77 are also shown on the x-axis.

The subsidence estimated using the final subsidence curves shows that the maximum possible subsidence at the anhydrite is about 132 cm and starts to occur when the length of the panel is just over 560 m and the face is 280 m from a given point on the profile. The curves also predict that the maximum possible subsidence at the surface is about 89 cm and occurs when the length of the panel is over 770 m and the face is more than 385 m from the observed point.

The final differential subsidence estimated for the panel dimensions at the times of surveys H45/2 to H45/10 are plotted against CMP position in Fig 5.4. There is a progressive increase in differential subsidence on the left side of the profile as the panel expands between face positions at the times of surveys H45/2 to H45/5. By the time of surveys H45/8 to H45/10, extraction had been completed and the differential subsidence had increased to an almost constant value of about 45 cm throughout the profile. However, the figure shows that there is a decrease in differential subsidence between the face positions at the times of surveys H45/6 and H45/7. This is because at the time of H45/6 the face had moved past the seismic profile by more than the critical distance for the anhydrite horizon. However, it was still within the critical distance for the surface so further face advance caused further subsidence at the surface but no more subsidence at the anhydrite, corresponding to a decrease in differential subsidence.

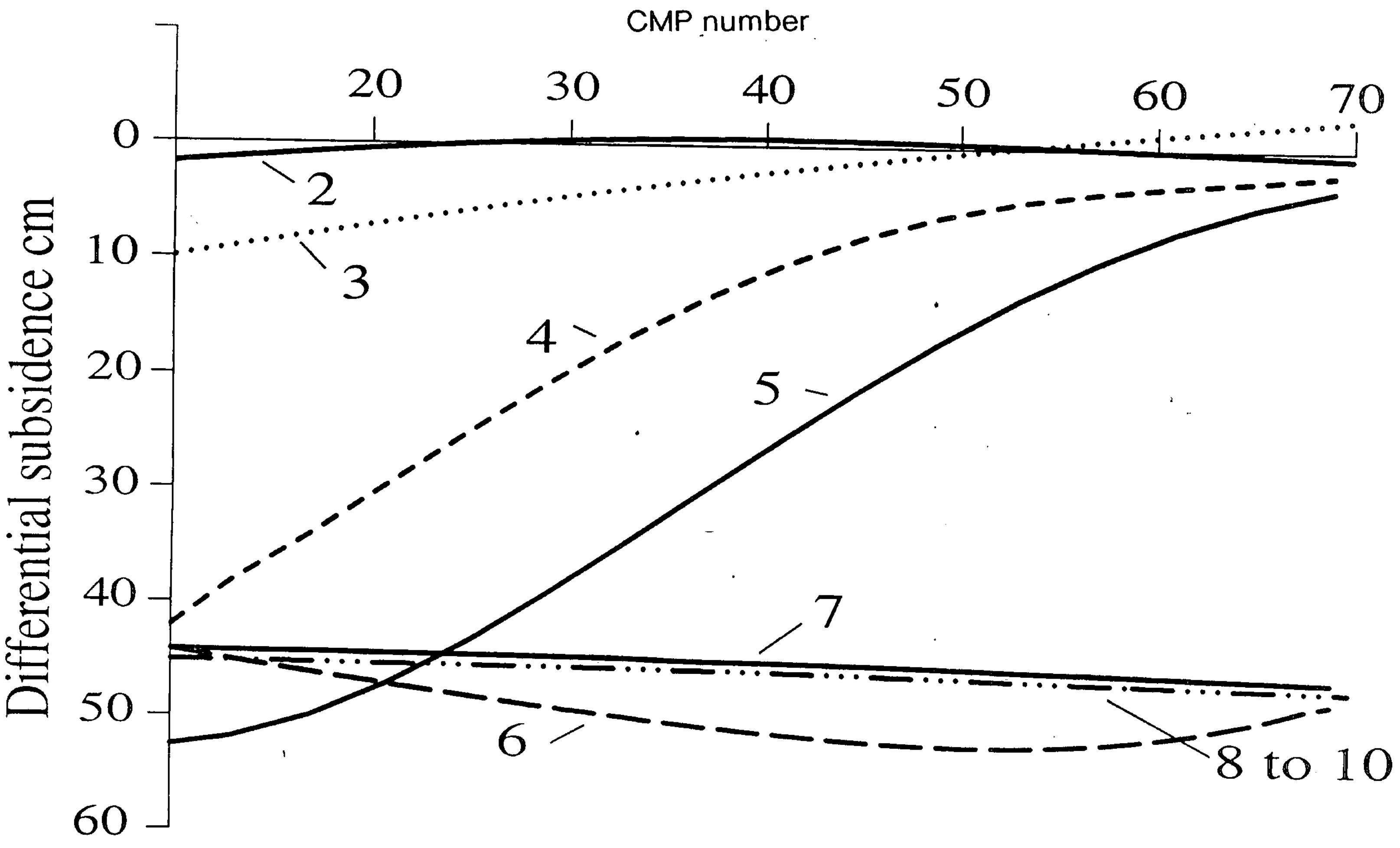

Fig 5.4. Differential subsidence calculated from the NCB final subsidence empirical curves for the H45 profile plotted against the CMP position.

5.2.3 Differential subsidence from the development curve

Using the final maximum possible subsidence at the surface and at the anhydrite horizon predicted using the final subsidence curves (§5.2.2), the development curve was used to estimate the active subsidence at the surface and at the anhydrite as a function of distance from the coal face. The two development curves were then subtracted to get the development differential subsidence for each coal face position when the profile was surveyed. The results are plotted as a function of CMP position in Fig 5.5. Since the mining had already been completed when surveys H45/8 to H45/10 were carried out, the values of the differential subsidence during these surveys are the same as in Fig 5.4.

The comparison between Fig 5.4 and Fig 5.5 shows clearly that for surveys H45/4 to H45/6 the differential subsidence calculated from the development curve lag behind the values calculated from the final subsidence curves. The maximum subsidence predicted by the development curve occurred between the H45/6 and H45/7 while the final curves predicted it to occur between H45/5 and H45/6. These observations were expected as the development curve predicts the active subsidence, whilst the final subsidence curves give the state of subsidence a long time after the excavation has been completed. (§2.5.2.1).

5.2.4 Correlation between the differential subsidence and traveltimes

Although the progressive increase in traveltime along the profile correlates well with the empirical calculations of the final differential subsidence (Fig 5.4), there is clear evidence of time dependence in the relationship. For example, the increased traveltimes for survey H45/5 match the total differential subsidence calculated for survey H45/4. The time dependence is also supported by a better correlation between the changes in traveltime and the differential subsidence calculated using the development curve (Fig 5.5). As noted in §2.5.2.1 the development curve takes the time factor into account.

Furthermore, if the results in Figs 5.2, 5.4 and 5.5, which were plotted against CMP position, are plotted against the distance from the coal face then a better comparison can be achieved, as shown in Fig 5.6. In Fig 5.6a the observed differential traveltimes for surveys H45/2 to H45/7 are plotted as scattered points and the curve is a polynomial fit of these points. Fig 5.6(b) shows that the differential traveltimes plot closer to the development curve than to the final subsidence curve.

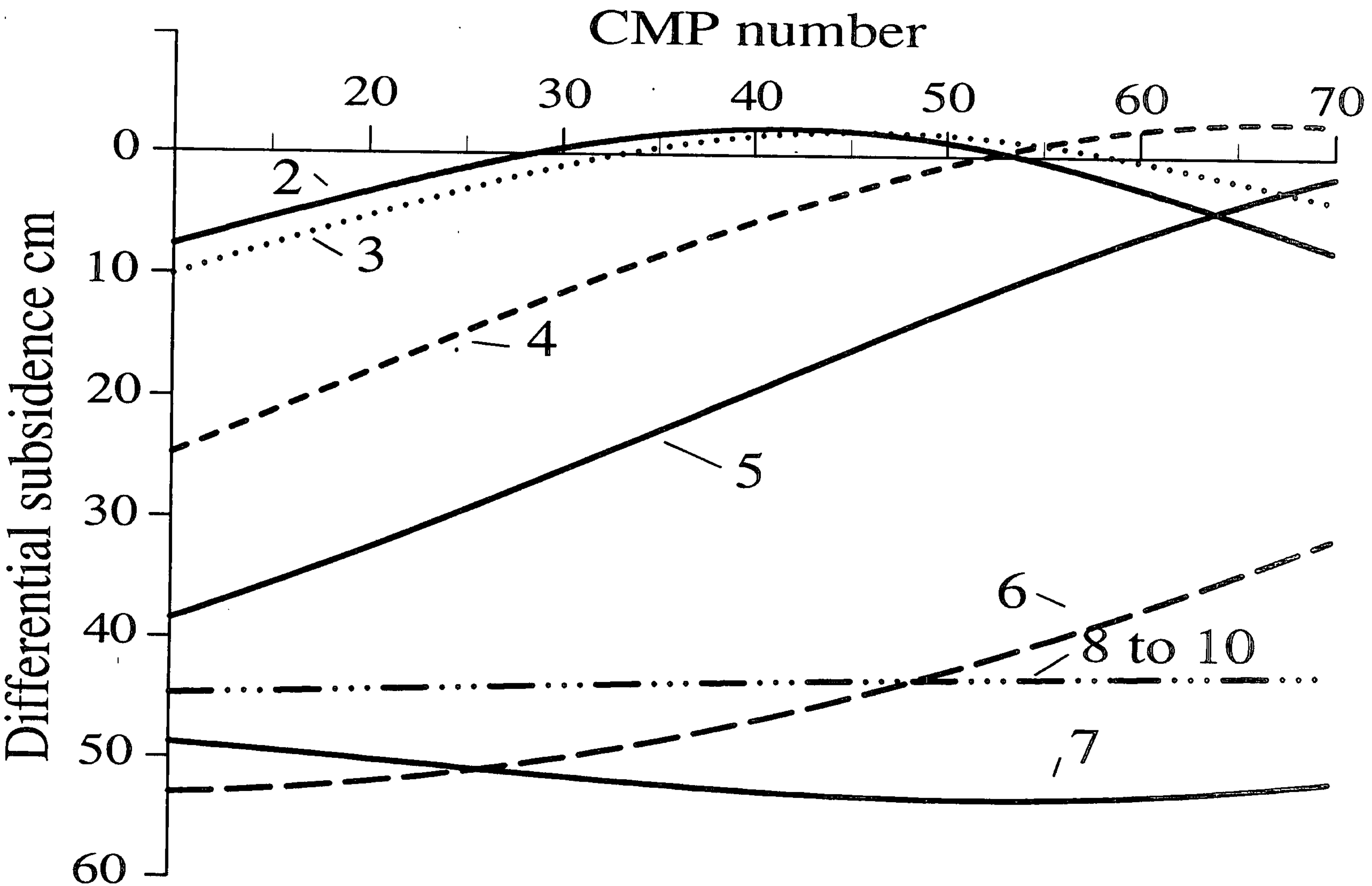

Fig 5.5. Differential subsidence vs. CMP number for the H45 profile, calculated from the development curve.

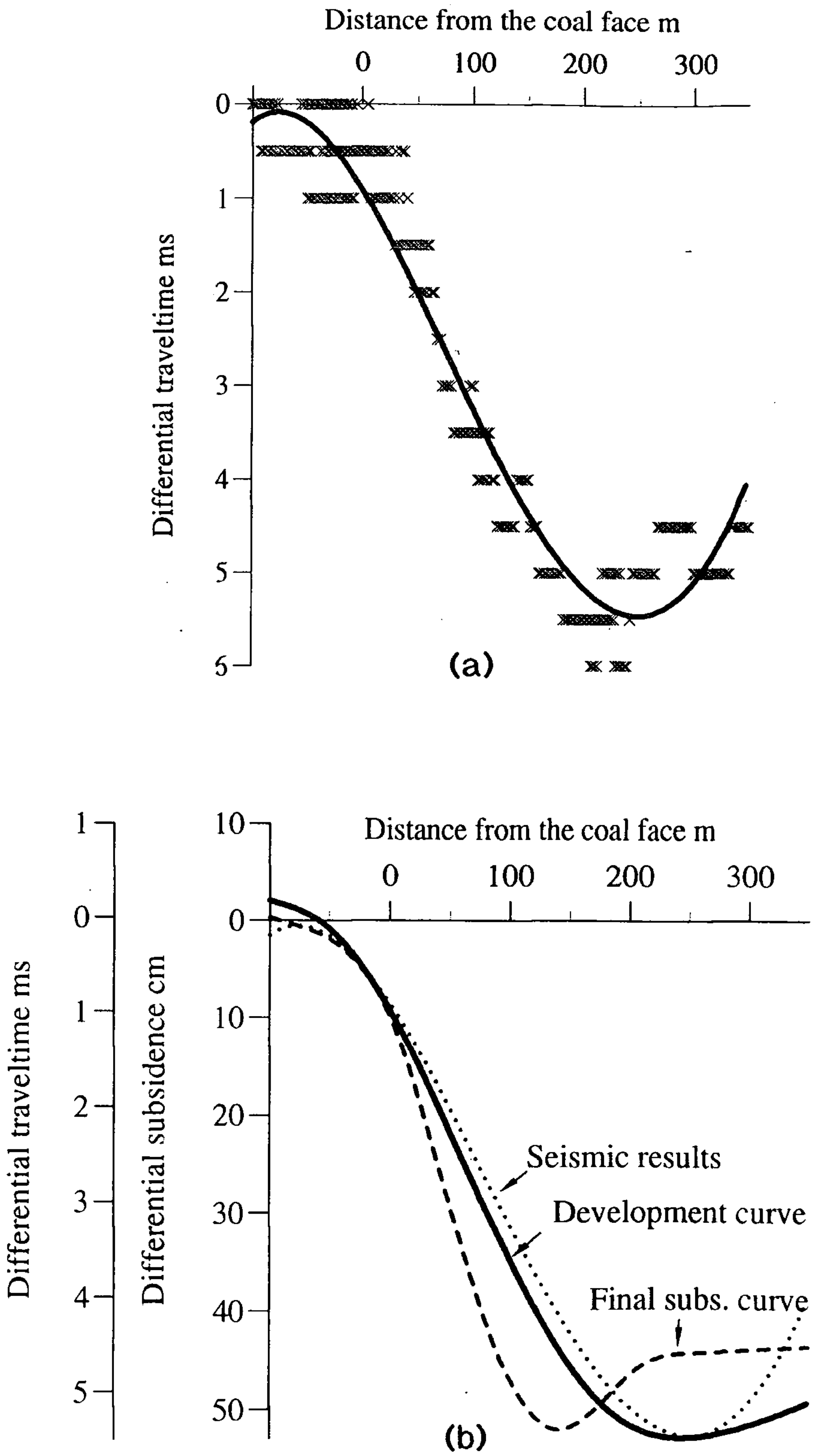

Fig 5.6. (a) Differential traveltimes obtained from the seismic sections on the H45 profile plotted against the distance from the coal face, and the polynomial fit of the data points. (b) The polynomial fit of the differential traveltimes, and the differential subsidence calculated from final and the development curves plotted against distance from the coal face.

5.3 The profile over H46

5.3.1 Seismic results

The final time migrated stack sections of some of the surveys from this profile, H46/1, H46/4 and H46/6, are shown in Fig 5.7. The sections show that the anhydrite layer is dipping towards the NE end of the profile at about 2° (using the average interval velocity of 2000 m/s). CMP 87 corresponds to the point at the middle of the panel and CMP 43 is vertically above the edge of the panel. Comparison of the sections in the figure shows that there is a progressive increase in two way traveltime above the panel on the right half of the sections.

The differential traveltimes calculated from time migrated sections of this profile are shown in Fig 5.8 with curves of polynomial fit. Due to the curves plotting close together, separate plots are given for curves 2-6 and 6-11 so that individual curves can be differentiated. It can be seen clearly in Fig 5.8 that there is a progressive increase in traveltimes as the coal face advances during the surveys H46/2 to H46/6. During the H46/7 to H46/11 surveys, however, the differential traveltimes are observed to decrease, especially towards the edge of the panel. The curves of the differential traveltimes for these last surveys are also tighter and, for surveys H46/8 to H45/11, have risen above zero over the edge of the panel. Values above the *x*-axis indicate a decrease in traveltime compared with the first survey.

5.3.2 Final differential subsidence

The NCB empirical curves were used to obtain the subsidence along the profile in the following manner. By interchanging the length and the width of the panel extracted at a given date, the subsidence at the centre of the panel was obtained as in H45. However, as in most cases the profile did not run across the centre of the panel, the distance between the profile and the centre of the panel was used to account for this effect. This gave the maximum subsidence at the centre of the profile and the rest of the subsidence values along the profile were obtained normally. Table 5.2 shows parameters used to obtain the subsidence during the H46/5 survey, and the subsidence values obtained are plotted in Fig 5.9. The differential subsidence calculated for all the surveys is plotted in Fig 5.10.

The subsidence values calculated using the procedure outlined above are those due to mining carried out in panel H46 alone. As shown in Fig 4.8, however, a part of the profile ran over panel H45 and therefore inevitably would have been affected by the subsidence due to extraction in this panel. However, since the subsidence was calculated relative to the ground and anhydrite levels during the H46/1 survey, the only effect would be the residual subsidence that had taken place after this survey was carried out. Although residual subsidence varies with time and space, its maximum value along the seismic profile during our surveys is expected to be of the order of only 5 cm.

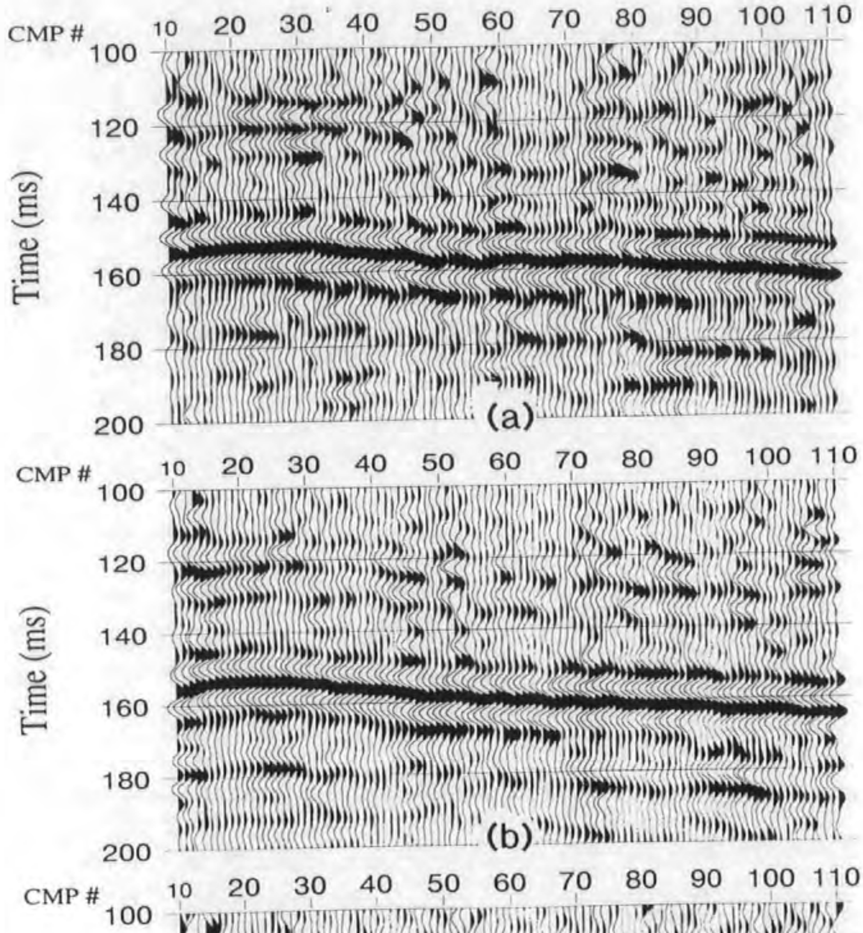

Fig 5.7. Time migrated section from surveys (a) H46/1, (b) H46/4 and (c) H46/6.

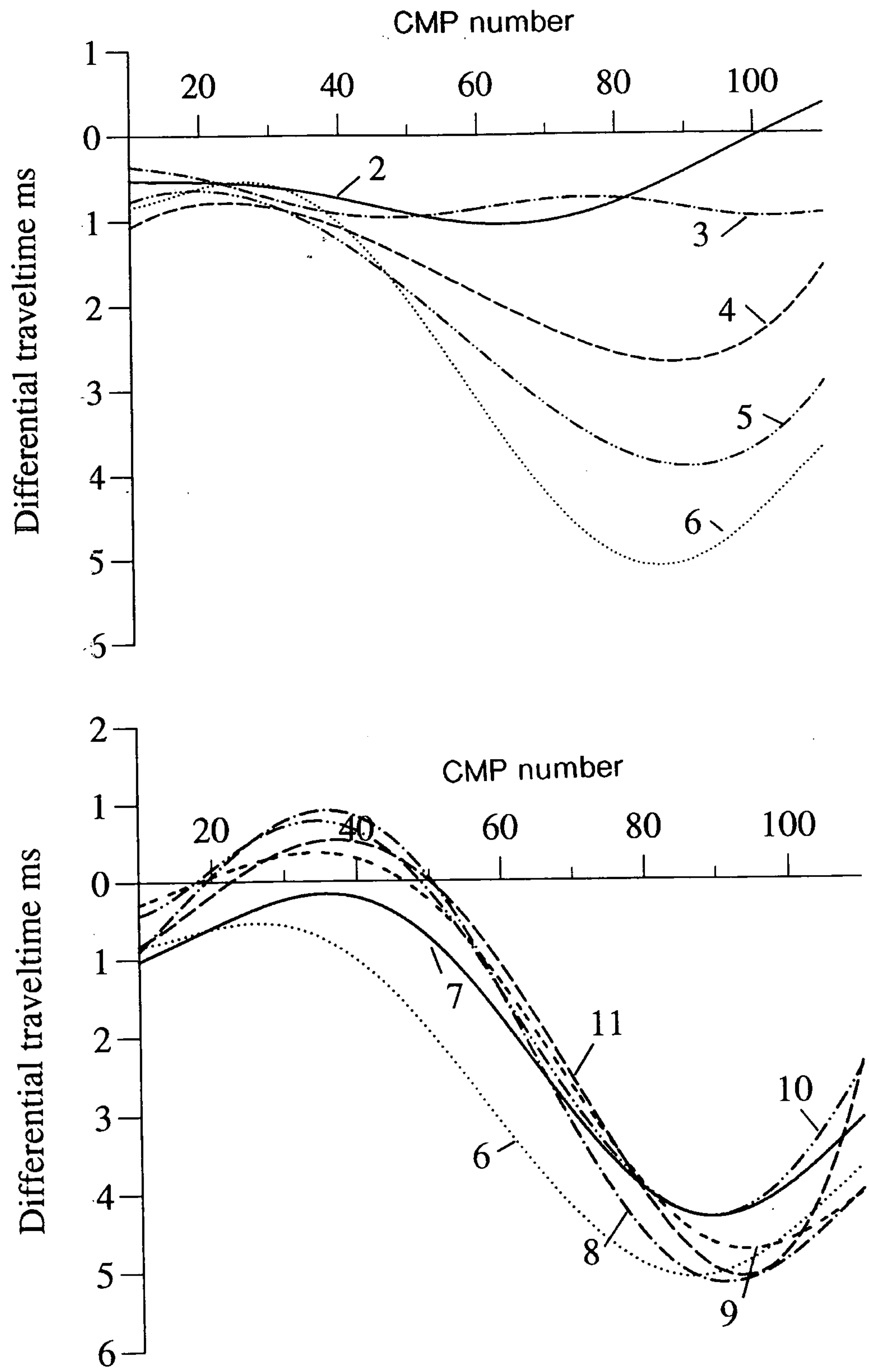

Fig 5.8. Differential traveltimes along the H46 profile calculated from the time migrated sections

Table 5.2. Parameters used to calculate subsidence and the values of maximum subsidence during the H46/5.

	Surface	**Anhydrite**
Width	760 m	760 m
Depth	550 m	400 m
Advance	220 m	220 m
Seam thickness	2.6 m	2.6 m
Maximum subsidence at the centre of the panel	88 cm	132 cm
Distance from the centre of the panel to the profile	198 m	198 m
Maximum subsidence at the centre of the profile	75 cm	125 cm

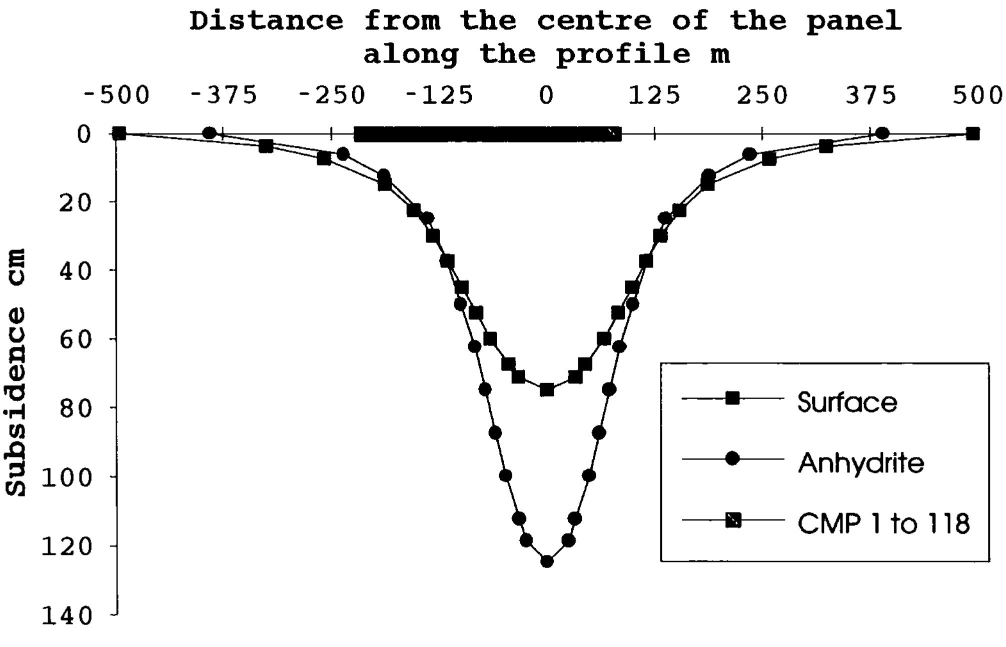

Fig 5.9. Subsidence at the surface and at the anhydrite during the H46/5 survey obtained from the final subsidence curves. The subsidence plotted is only due to mining of panel H46. The position of CMPs 1 to 118 are shown along the *x*-axis.

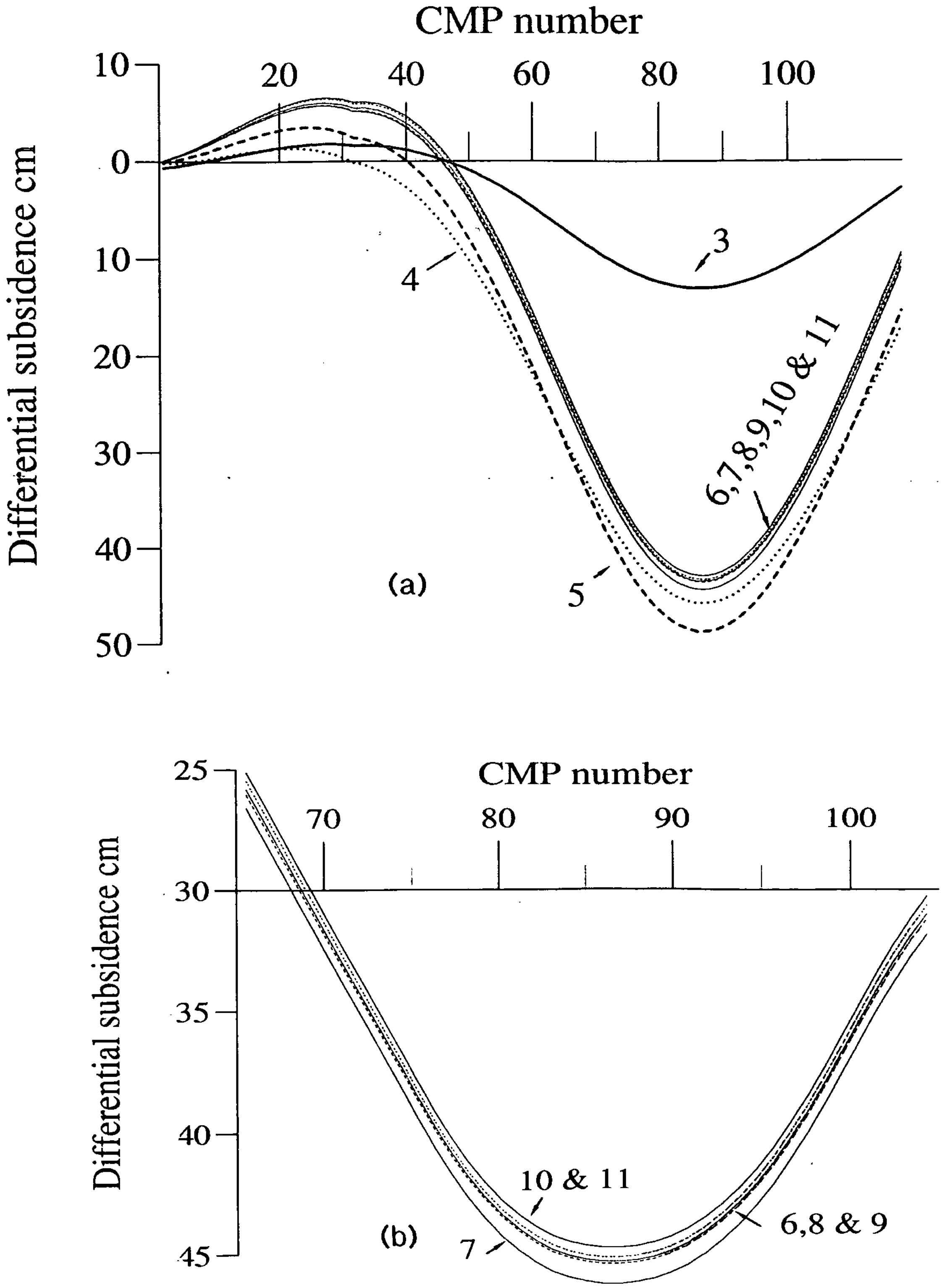

Fig 5.10. Final differential subsidence on the H46 profile calculated from the NCB empirical curves: (b) is a zoom for part of (a).

Figure 5.10 shows that over the panel, the final differential subsidence progressively increases with the extent of the worked panel at the times of surveys H46/3 to H46/5, but decreases as the panel dimensions increase further for face positions at the times of surveys H46/7 to H46/11. Over the unworked seam, the differential subsidence mainly decreases as the face position advances. Values plotted above the *x*-axis indicate that the surface has subsided more than the anhydrite.

5.3.3 Differential subsidence from the development curve

The NCB development curve and the maximum possible subsidence at the surface and at the anhydrite were used to obtain the active subsidence at the centre of the profile. The final subsidence empirical curves were then used to find the subsidence along the profile. The development differential subsidence obtained is shown in Fig 5.11. In this figure, the effect due to H45, as in Fig 5.10, was assumed negligible.

As in H45, the differential development subsidence plotted in Fig 5.11 lags behind the final differential subsidence in Fig 5.10. For example, the final curves show the maximum differential subsidence for the panel dimensions at the time of survey H46/5, whereas the maximum differential development subsidence is predicted at the time of survey H46/7.

5.3.4 Correlation between the differential subsidence and traveltimes

Over the panel, the increase in differential traveltimes during surveys H46/4 to H46/6 correlates well with the differential subsidence calculated from the development curve. Although the correlation is not so good in other surveys, the trend is generally the same between the two, e.g. the decrease in differential subsidence and traveltimes over the panel for surveys H46/8 to H46/11. There is also a good agreement at the edge of the panel. For surveys H46/8 to H46/11, the differential traveltimes and the final and development differential subsidence cross the *x*-axis around the same point, between CMPs 45 and 50,

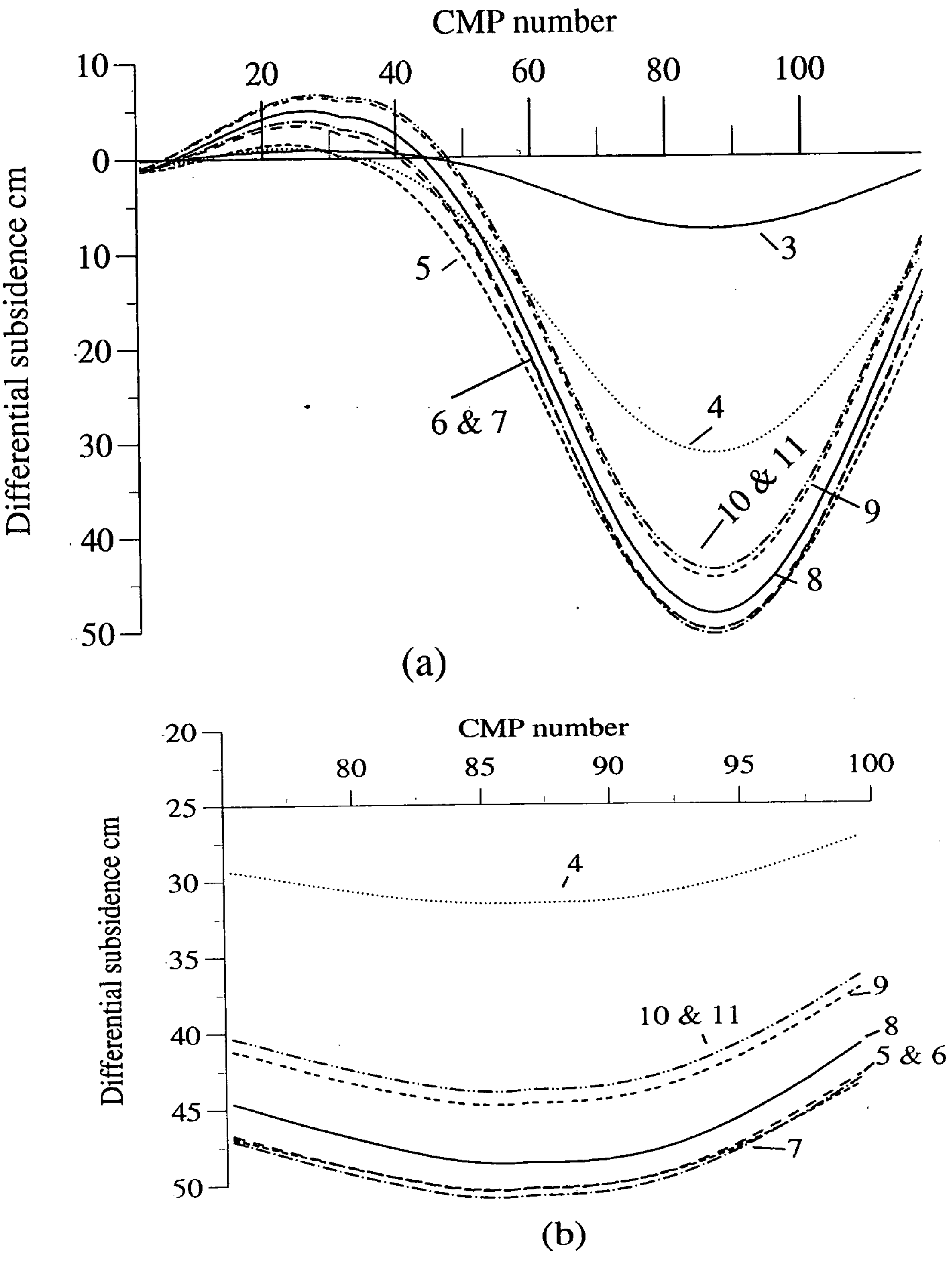

Fig 5.11. Differential subsidence on the H46 profile calculated from the development curve: (b) is a zoom for part of (a).

5.3.5. Subsidence induced stresses

The finite element method (FEM) was used to determine the state of the induced stresses after the mining was completed. A total of 210 elements were used in calculation. The stresses and displacements of the initial state were calculated using a Poisson's ratio of 0.25 to 0.3 for all the rocks, and Young's moduli of 1000, 2200, 10000 and 8000 MPa, for the near surface rockmass, Bunter Sandstone, Permian rocks and Coal Measures, respectively. The same rock properties were used for calculating the stresses and displacements after mining, except that for the rockmass close to the excavation the Poisson's ratio was reduced to 0 and the Young's modulus was quartered to simulate the plastic properties of the rocks close to the mining horizon.

Figure 5.12 shows the induced stresses and the surface subsidence calculated. Also shown in the figure is the surface subsidence profile obtained from the NCB empirical curves. Since the model is symmetrical about the centre of the panel, the figure shows only one half of it. The figure shows that the maximum subsidence calculated using the FEM is less than that predicted by empirical curves. The subsidence profile of the FEM is also wider than that predicted by empirical curves. This may be due to rocks not behaving like perfect elastic bodies as assumed by the FEM.

In Fig 5.12, the stresses are plotted as dashed lines for tensile and solid for compressive. As expected Fig 5.12c, which is a zoom for part of Fig 5.12b, shows that for the rockmass above the panel, the vertical induced stress is tensile over the panel and changes to compressive away from the edge of the panel. The maximum induced tensile stress at the centre of the panel and 75 m depth is about 1.23 MPa. The maximum induced vertical compressive stress over the unworked seam at the same depth is about 0.6 MPa.

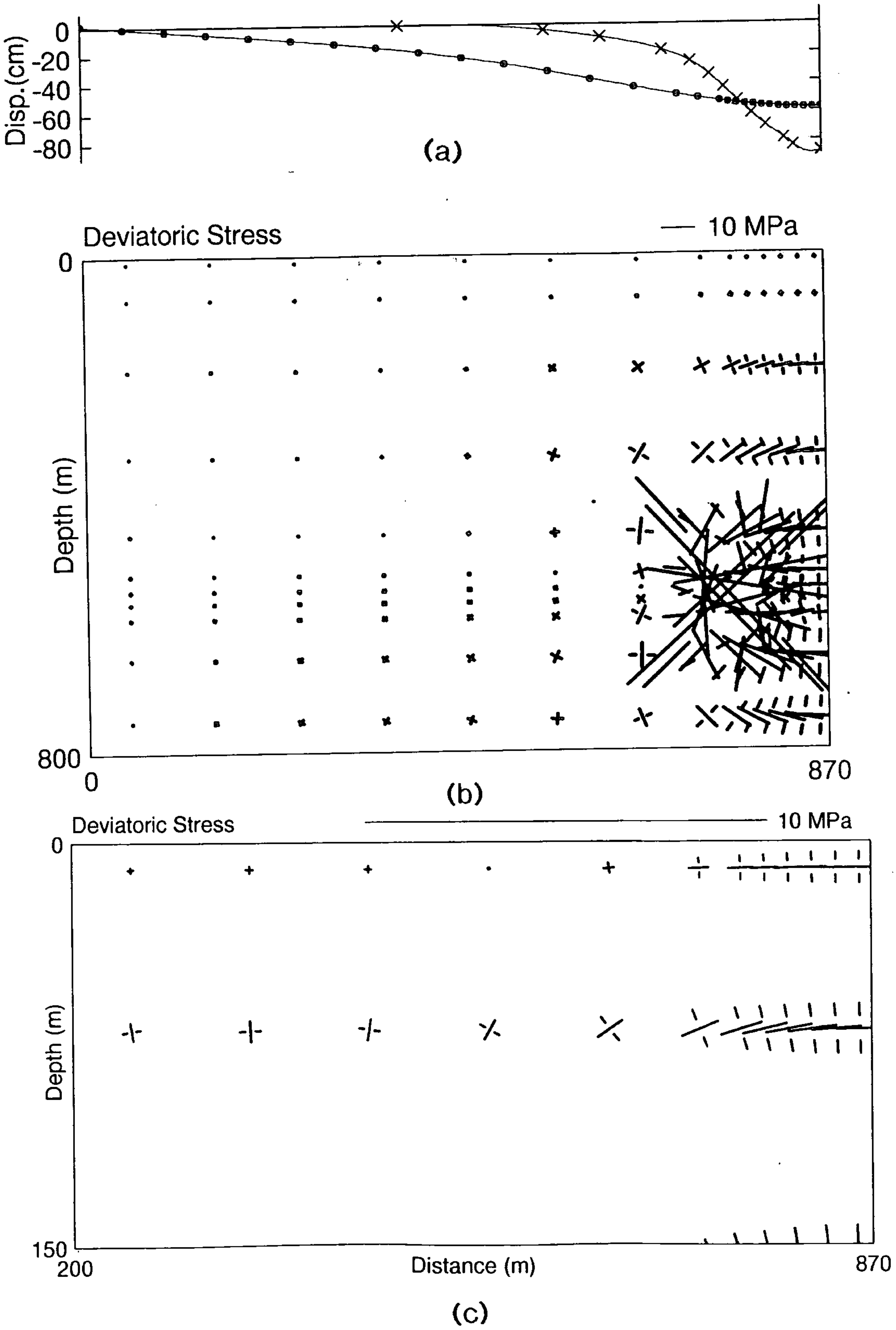

Fig 5.12. Stresses induced by subsidence and the surface subsidence calculated using finite element method: (c) is a zoom for part of (b).

5.3.6. Levelling results

The magnitudes of surface subsidence obtained from the levelling results during some of the surveys are plotted in Fig 5.13. Due to instrument or reading errors during surveys H46/8 and H46/9, the results of these surveys are not shown in the figure. Since it is not possible for the ground to rebound back, the decrease in subsidence observed between surveys 11 and 12 could be due to a small error between the surveys (see §6.4.1).

The maximum surface subsidence calculated from the levelling results is about 60 cm, whilst that obtained from the NCB empirical curves is 89 cm. The discrepancy, which is discussed in §6.3.1, is attributed to delayed subsidence. It is also apparent from Fig 5.13 that the subsidence profiles are not symmetrical about the centre of the panel (at about 240 m) as would have been predicted by NCB empirical curves from mining a single panel. The cause of the asymmetry is discussed in §6.3.1.

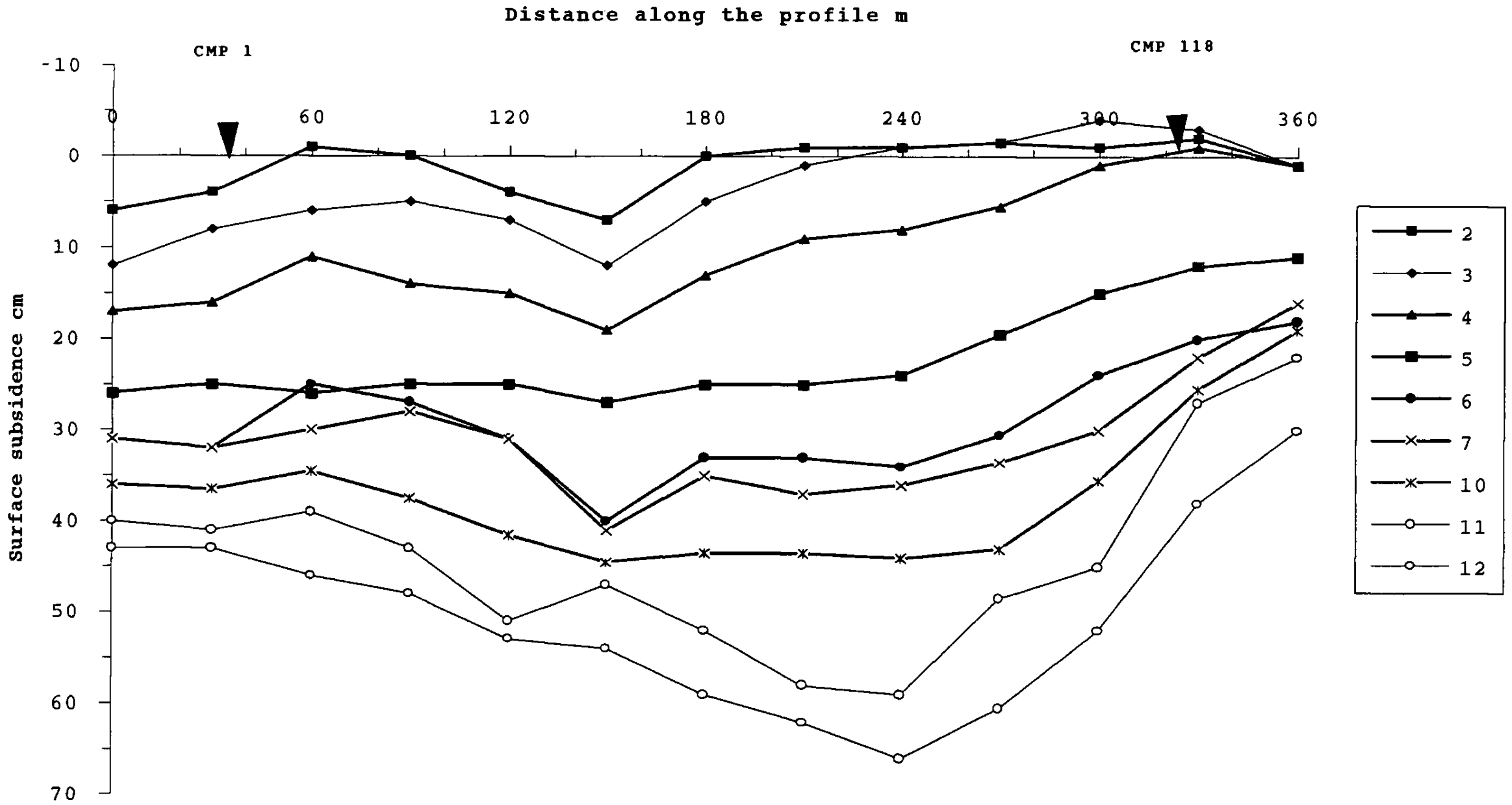

Fig 5.13. Surface subsidence along the seismic profile over panel H46 obtained from the levelling results. The positions of CMP 1 and CMP 118 are indicated by arrows on the *x*-axis.

Chapter 6

Interpretation and reliability of the results

6.1 Interpretation

6.1.1 Introduction

It was shown in §5.2.3 and §5.3.3 that along the seismic profiles, the maximum differential subsidence between the anhydrite and the surface calculated using the NCB empirical curves was about 50 cm. With a constant average interval velocity of 2000 m/s, this would cause a maximum increase in two-way traveltime of only about 0.5 ms. The two-way traveltime after mining, however, was found to increase by up to about 6 ms. This shows that the observed increase in the traveltime cannot principally be attributed to the increase in travel path (differential subsidence) for the reflected seismic signals; it must mainly be due to a change in seismic velocity through the overburden rockmass that accompanied subsidence.

The three main effects associated with subsidence discussed in chapter 2 (the change in relative level of the water table, change in porosity and the change in the state of stress), are all capable of causing the rockmass condition to alter and hence the velocity at which a seismic signal travels through it. Variations in the level of the water table could also be brought about by the seasonal changes. It was imperative, therefore, to interpret the data by examining these effects in terms of the observed changes in traveltime.

6.1.2 Change in the water table and water saturation

There are two different ways in which hydrological changes could affect the results of our surveys: a change in level of the near-surface water table, and a change in water saturation in the Bunter Sandstone aquifer.

As both base surveys, H45/1 and H46/1, were carried out during the wet seasons of the year, the drier conditions prevailing at the times of most of the subsequent surveys would have been associated with a drop in the near-surface water level in the Quaternary. Since this level was used as the datum for static corrections (see §4.6.2), the decrease in water level would have caused the reflection traveltimes on the processed sections collected during the summer months to decrease. Consequently, the changes in traveltime obtained from the sections corrected to that datum would have been underestimated. This is demonstrated in Fig 6.1. If the drop in the water level in Fig 6.1c was not taken into account, then the differential traveltime would be underestimated by time DT. However, the field statics did not increase between surveys and the water level in a pond near to profile H45 did not change noticeably. Taken together, these observations suggest that there was no significant seasonal variation in the level of the near-surface water table.

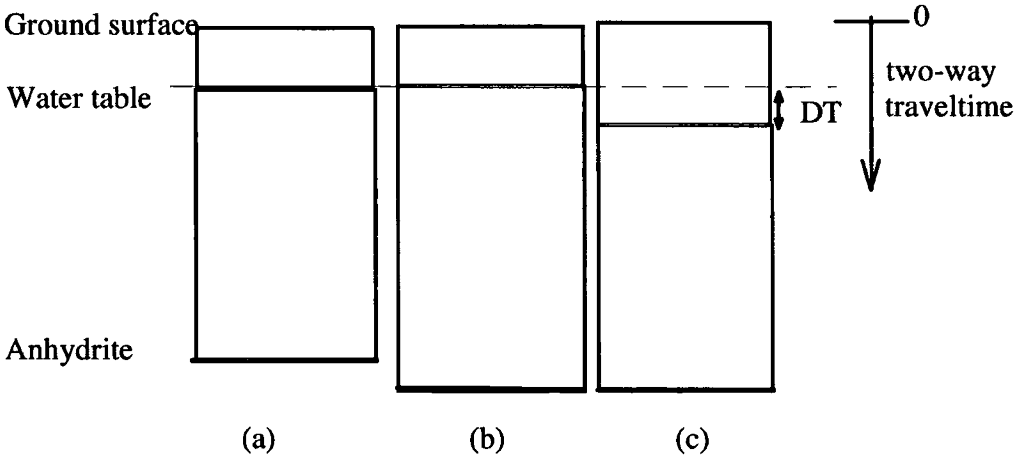

Fig. 6.1. Simple diagram illustrating the effect of change in the water table (the datum) on the reflected traveltime to the anhydrite: (a) before mining; (b) after mining without change in the water table; and (c) after mining with seasonal fall in the water table. Not drawn to scale.

A change in the near-surface water level could also have been caused by subsidence itself. As stated in §2.6, if the water flows freely in the weathered layer, i.e. there are no permeability barriers, then subsidence can cause the water table to rise relative to ground surface. If this had happened the datum for static corrections would have risen and caused the magnitude of the static corrections to decrease. Since there were no significant static changes in all the surveys over panel H45, it can be assumed that the water table did not change when the surveys over panel H45 were carried out. For H46, however, a decrease in magnitude of the static corrections for some surveys was noted. Figure 6.2 shows field receiver statics for surveys H46/1, H46/4, H46/8 and H46/9. Clearly, there is a decrease in the statics for surveys H46/8 and H46/9 (similar decrease was also observed in all surveys carried out after H46/6). If the magnitudes of the static corrections in these surveys had been underestimated, then the differential traveltimes observed in their sections would have been overestimated. However, the fact is that the differential traveltimes in these surveys actually decreased, so it is very unlikely that the magnitudes of the static corrections were underestimated.

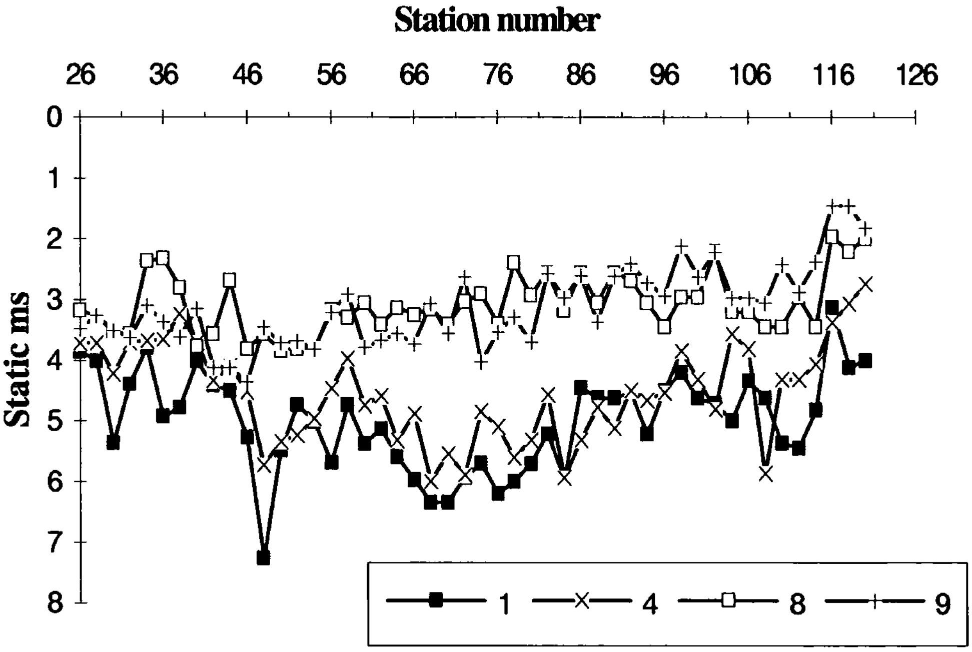

Fig 6.2. Receiver statics for surveys H46/1, H46/4, H468 and H46/9.

To determine whether the decrease in statics in these surveys was due to surface subsidence or was only due to change in velocity in the weathered layer, the first breaks at very short offsets would have to be analysed. Unfortunately, the average velocity of the weathered layer was found to be about 300 m/s, and therefore for traces with total statics of about 8 ms (receiver plus shot statics) the first arrivals at 2.5 m offset are headwaves and not direct arrivals.

It is apparent from the discussion above that the observed differential traveltimes could not have been caused by changes in the weathered layer. The increase in traveltimes is therefore attributed predominantly to the decrease in seismic velocity in the rockmass between the anhydrite and the ground surface. With an initial two-way traveltime to the anhydrite of 150 ms, the increase in traveltime of 6 ms represents a 4 % decrease in seismic velocity.

It was established in §4.2.2 that the Bunter Sandstone is very porous and an excellent aquifer. It is necessary, therefore, to consider whether the observed reduction in seismic velocity could have been due to a lowering of the water level in the Bunter Sandstone aquifer. Change in seismic velocity caused by variation in water saturation in a rock is a very well known phenomenon (e.g. Elliott and Wiley 1975; Gregory 1976; see also §1.2.2). Figure 6.3 shows the magnitude of velocity change that can be expected from changing water saturation in a sandstone of 30% porosity. A decrease in water saturation of only about 15% from full water saturation could result in a velocity decrease of about 33%. In fact, boreholes in the area monitored by the National Rivers Authority show that the Bunter was always fully saturated with water during the period of our surveys (K. Owen, personal communication).

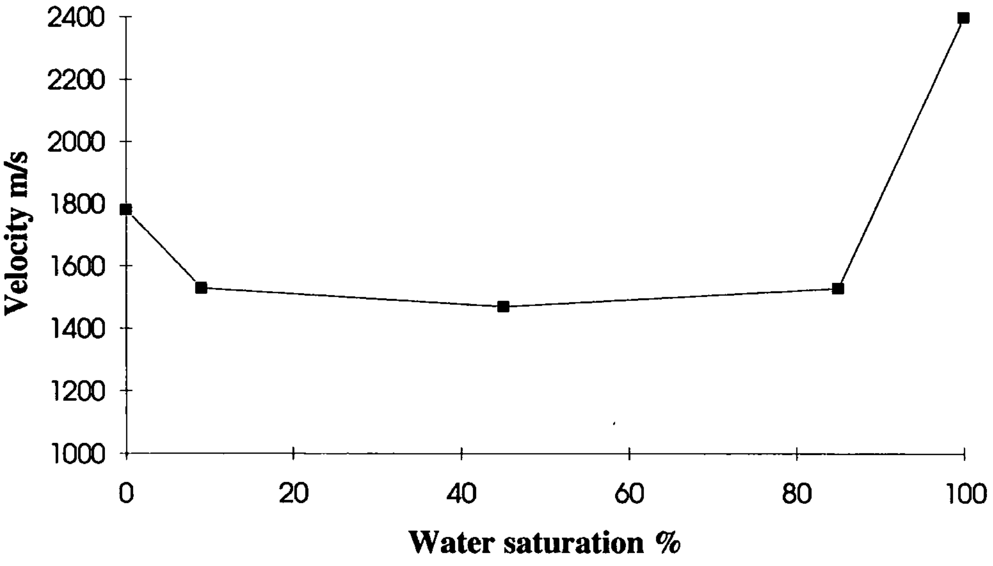

Fig 6.3. Velocity change caused by variation in the water saturation in a sandstone with the porosity of 30%. The values plotted are laboratory measurements reported by Elliot and Wiley (1975).

6.1.3 Change in porosity

The effect of porosity on velocity was discussed in §1.2.1. Subsidence increases porosity by creating Weber cavities and microcracks. Weber cavities (§2.3.1) are bed separations formed when a layer of a competent rock subsides by a lesser amount than an underlying layer of less competent rock. The existence of competent beds in the overburden has also been associated with unusually long delay in the completion of residual subsidence (Orchard and Allen 1975).

The levelling results over panel H46 showed a maximum surface subsidence of only 60 cm. The NCB empirical curves predicted a maximum surface subsidence of about 89 cm. Although the NCB curves are average measurements taken from about 200 different cases in British coalfields, the predicted subsidence is normally within about 10 % of the observed measurements. Further residual subsidence of at least 10 cm is therefore still expected to occur, having been delayed by the presence of competent rock in the overburden.

If the competent rock responsible for the delayed residual subsidence is located between the surface and the anhydrite, then its presence must also have affected the differential traveltime. The maximum and significant effect of the competent rock on the traveltime could occur only if the differential subsidence between the surface and the anhydrite is taken by the cavity and the cavity created is filled by air. In such circumstances most of the differential traveltime observed could be accounted for (differential two-way traveltime of about 4 ms can be caused by maximum differential subsidence of about 72 cm and velocity in the air of 330m/s). However, it is known from borehole records in this area that a thick competent homogeneous Lower Magnesian Limestone (Permian) overlies a fissured and, therefore, less competent limestone. After mining, some borehole electrical logging has detected a bed separation over the top of the fissured limestone, as shown in Fig 6.4 (Pyne and Randon 1986). Thus since the Lower Magnesian Limestone is underlying the anhydrite, even if the Weber cavities had occurred they would not have affected the differential traveltime between the surface and the anhydrite.

Microfractures or microcracks are small cracks that open along the planes of weakness. In sedimentary rocks these planes are mainly parallel to the bedding planes and along the grain contacts. By subjecting a sandstone of about 5% porosity to uniaxial compression parallel to the bedding, Sangha *et al.* (1974) showed that although microcracks were forming with orientations in all directions, those along the bedding planes were predominant. As the stress was increased, they also noted that most of the increase in total crack length was due to the new microcracks formed, rather than by any increase in the size of the existing ones.

In coal mining, the directions of maximum compressive and tensile stresses in most of the overburden rockmass are horizontal and vertical, respectively (Fig 5.12). This therefore causes microcracks to develop parallel to the bedding. If the total volume of the microcracks equals the dilatation caused by the differential subsidence, then we can use the Wyllie formula (equation (1.4)) to calculate the expected increase in traveltime. As the Bunter Sandstone was always fully saturated with water, the increase in traveltime due to the increase in porosity will be about 0.33 ms. The one-way traveltime from the surface to the anhydrite is 75 ms, so application of Wyllie formula gives a predicted decrease in velocity of 0.25 %. This is a much smaller effect than that observed (decrease of 4%). Clearly, Wyllie formula is not appropriate. The microcracks must cause an overall reduction in the elastic moduli of the rockmass.

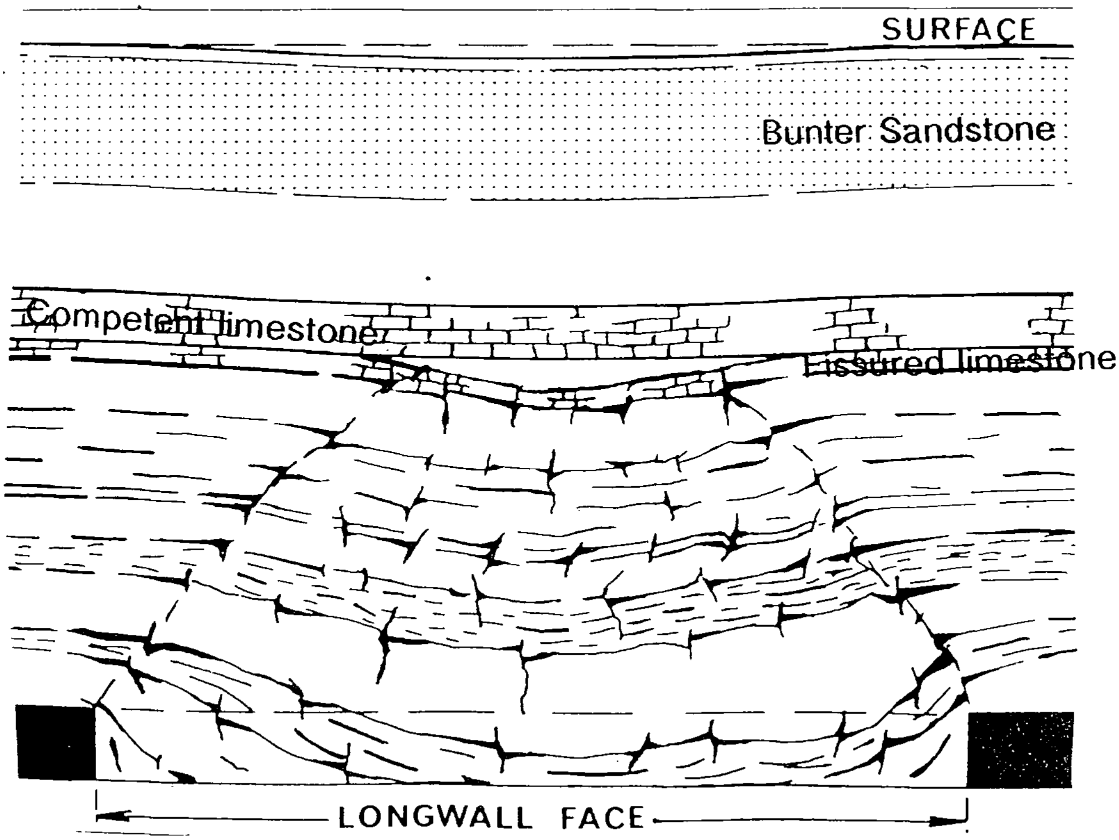

Fig 6.4. A diagram showing the Weber cavity between the competent and less competent limestone.

6.1.4 Change in stresses

The effect of stress on velocity is a very well documented phenomenon (e.g. King 1966; Domenico 1977; §1.2.3). The most obvious and noted effect of stress on seismic velocity is the increase in velocity with depth. However, since velocity is a function of effective stress (overburden pressure minus pore pressure, see §1.2.3), the rate at which the velocity increases with depth depends on the pore pressure condition in the sediments during and after burial. Under normal compaction conditions, as burial proceeds the pores between grains close and the pore fluid is squeezed out; hence the pore pressure increases along the hydrostatic gradient while overburden stress increases more rapidly at the lithostatic gradient (Mann and Mackenzie 1990). In this case the effective stress and the velocity increase with depth at the fastest rate possible. If the fluid is not allowed to escape, the pore pressure will build up above the hydrostatic and an overpressured zone will develop. In an overpressured zone, the effective stress and velocity are lower than in normally compacted rocks.

It was shown in §5.3.5 that subsidence induces stress changes in the overburden, and that the vertical induced stress is tensile over the panel and compressive over the unworked seam. The maximum tensile stress induced by mining for the rockmass above the anhydrite, as calculated from the finite element method, is about 1.2 MPa. Before mining, we can assume that the vertical effective stress is the overburden pressure minus the pore pressure due to the water column. This will be about 2 MPa at 150 m depth, reducing approximately linearly up to the surface. Before mining, therefore, the average effective stress for the rockmass above the anhydrite would be about 1 MPa. After mining, the effective stress induced by subsidence will cause the cracks to open parallel to the bedding planes such that the effective stress may drop almost to zero.

Although the effect of change in effective stress on velocity is a function of other physical parameters such as porosity, lithology and fluid type, at low overburden pressure the velocity is always highly stress-sensitive. Typical variation in velocity sensitivity with overburden pressure for dry sandstone is shown in Fig 6.5. For the overburden pressure in the rockmass studied here, Fig 6.5 suggests the change in velocity of up to nearly 60 m/s/MPa (with an initial velocity of 2000 m/s, this represents a change of 3%/MPa). The observed reduction in velocity of some 4% is, therefore, generally in accord with published laboratory data, although we are not aware of any specific measurements made on samples of Bunter Sandstone from this locality.

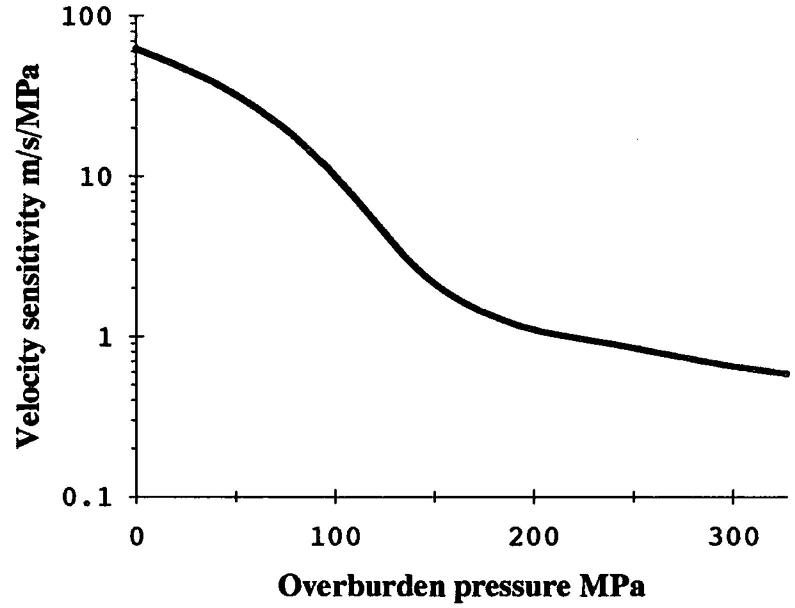

Fig 6.5. Variation of velocity sensitivity with overburden pressure for sandstone. Redrawn from Gladwin (1982).

In the petroleum industry, where a reduction in velocity may indicate overpressure, Eaton's method is often used to estimate the effective stress σ from the measured velocity V (Bowers 1994) by

$$\sigma = \sigma_{norm}\left[\frac{V}{V_{norm}}\right]^3 \qquad (6.1)$$

where σ_{norm} and V_{norm} are effective stress and velocity under normal pressure conditions. By assuming that the effective stress and velocity under normal pressure conditions are the values of effective stress and velocity before mining, equation (6.1) can be used to determine the change in effective stress necessary to cause the observed change in velocity after mining. Using the maximum change in velocity of 4 %, the maximum change in effective stress calculated is 0.115 MPa. However, Eaton's method has been shown to work well only in undercompacted conditions but underestimates pore pressure (and therefore overestimates effective stress) in cases where the overburden stress does not increase with the pore pressure (e.g. where the pore fluid has expanded) (Bowers 1994). Thus, it is likely that the effective stress has decreased more than the value predicted by Eaton's method.

Another empirical equation that relates effective stress to velocity is that given by Domenico (1977). For sandstone of 30% porosity, velocity V at effective stress σ is

$$V = A\sigma^{1/18} \tag{6.2}$$

where A is constant. Using an effective stress of 1 MPa and velocity of 2000 m/s, A equals to 2000. Thus, a change in velocity of 4% represents a change in the effective stress of about 0.5 MPa, which again is a reasonable value for the depth of our target.

6.2. Interpretation of H45 results

It was shown in §5.2.3 and Fig 5.5 that differential subsidence increased progressively across the whole profile as the coal face advanced during surveys H45/1 to H45/6, with the exception of the southeastern end of the profile where there were small increases in differential subsidence during H45/4 and between H45/5, H45/3 and H45/2 (the results are reproduced with smaller scale in Fig 6.6a). This implies that the tensile stress was also progressively increasing across the bulk of the profile. This is in agreement with the seismic results, which show almost similar trends (Fig 6.6b).

During survey H45/7, the differential subsidence decreased at the northwestern end of the profile, which suggests that the settlement of the rockmass above the anhydrite had started to take place at this end of the profile. The settlement indicates that the cracks and pores started to close and increase the effective stress. The seismic results also correlate with this, showing a corresponding decrease in traveltime. The seismic results for H45/8, H45/9 and H45/10 in Fig 6.6b have been combined to reduce any random errors (see 6.4.2), and the curve in the middle is the average of the three.

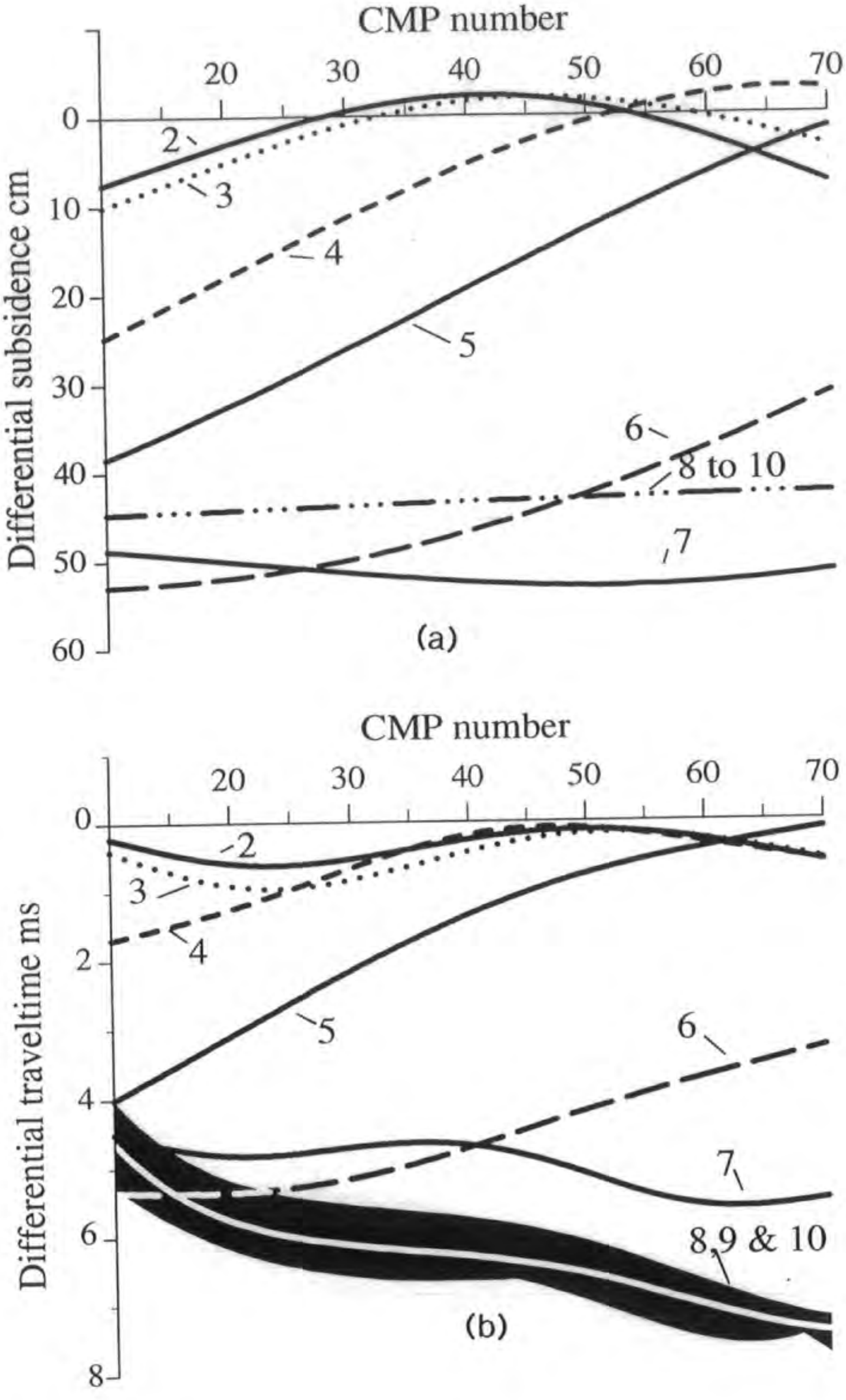

Fig 6.6. H45 results: (a) differential subsidence calculated from the development curve and (b) differential traveltime.

It is apparent from Fig 6.6 that there is a discrepancy in the trends between the differential subsidence and traveltimes between surveys H45/7 and H45/8 (i.e. after mining was completed). The differential subsidence decreased, whilst the differential traveltime increased, especially towards the end of the profile. This may be due to the delayed subsidence. It was suggested in §6.1.3 (see also 6.3.1) that some subsidence has been delayed due to the existence of a competent layer in the overburden. The empirical curves predicted that after H45/7 the anhydrite would have subsided to its maximum possible value and the only movement left would be the settlement of the overlying rockmass. However, due to the delayed subsidence, both the ground surface and the anhydrite, continued to subside. The fact that the differential traveltimes increased suggests that the anhydrite continued to subside faster than the overlying rockmass, so the differential subsidence increased too.

The relationship between the differential subsidence and traveltimes during surveys H45/2 to H45/7 is shown in Fig 6.7. Each data point in the figure is a differential traveltime from one CMP trace. The figure shows that the relationship is approximately linear from about 10 cm differential subsidence. However, even if differential traveltime varies linearly with differential subsidence, this does not necessarily imply that the differential traveltime is directly proportional to the effective stress. This is because the induced stress is not directly proportional to the differential subsidence (i.e. vertical strain), but is a function of strains in all directions (or two directions in the case of plane strain) and is governed by Hooke's law. Thus the significance of Fig. 6.7 is just to give a clear indication of the trend.

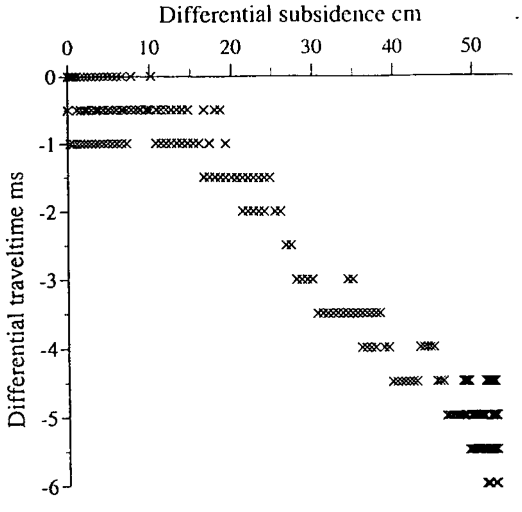

Fig 6.7. The relationship between the differential subsidence calculated from NCB development curve and the differential traveltime.

6.3. Interpretation of H46 results

6.3.1 Interpretation of subsidence results

A comparison between the surface subsidence measured during some of the surveys and that predicted from the NCB development empirical curve is shown in Fig 6.8. In both cases the datum used is the ground level during the H46/1 survey. The figure shows that the values of surface subsidence measured by levelling are not only asymmetrical, but also have smaller maximum magnitude compared with those obtained using the empirical curves. Surface subsidence in the area measured by NCB over a period of years has shown that the measured values tend to approach those predicted by empirical curves after 4 to 5 years. Thus the delayed subsidence may be attributed to the existence of a layer of competent rock in the overburden (see §6.1.3 and Fig 6.4). The asymmetry may partly be attributed to the residual subsidence of panel H45, and partly to a much longer time constant for the residual subsidence due to panel H46 over virgin ground (NE end of the profile) than over ground already weakened by subsidence due to H45 (SW end of profile).

Although only the surface subsidence was monitored, it is extremely likely that the discrepancy observed between the actual and predicted subsidence extended to the subsurface strata. However, the magnitudes of the discrepancy may vary between strata, dependent on their depths. It is not possible, therefore, to predict the differential subsidence using the empirically predicted anhydrite subsidence and the observed surface subsidence.

It is important to note that there have been no comparable published cases of repeated measurements of a subsidence profile similar to that obtained from levelling results in this study. According to NCB (1975), as long as the pillar left between two panels does not collapse, at a given time the subsidence profile over the two panels is the superposition of the subsidence due to individual panel. This, however, applies only if the two panels are extracted simultaneously, or if the ground surface over both panels has subsided to its final value. For the former, the subsidence is obtained by adding up the dynamic subsidence calculated from the development curve of each panel, whilst for the latter, the final subsidence curves are used.

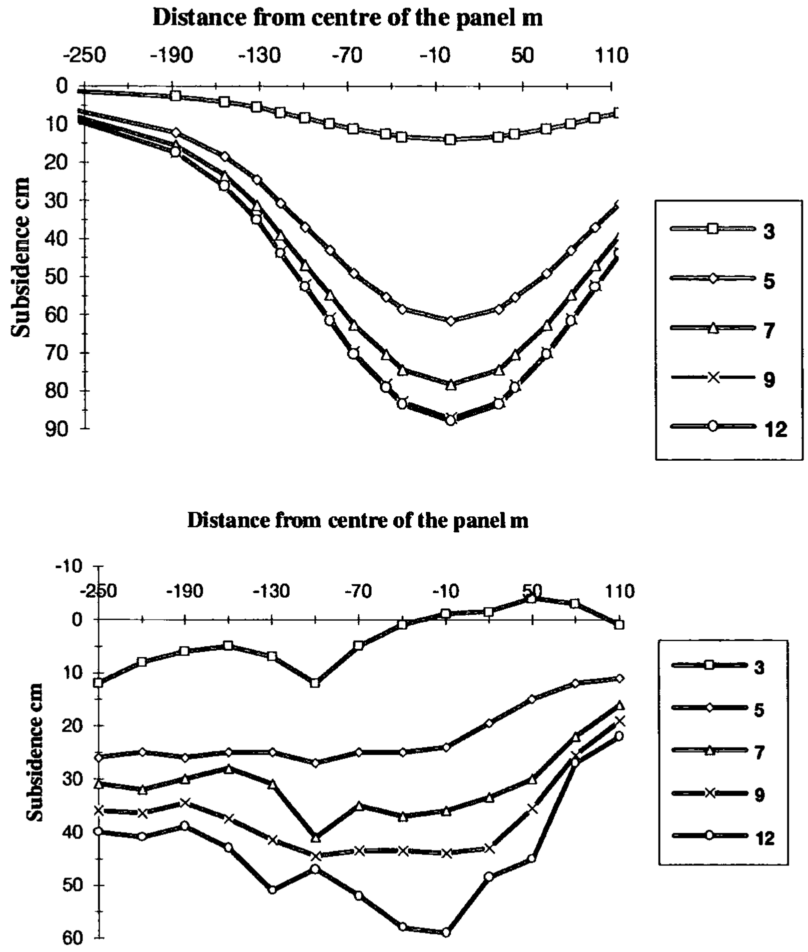

Fig 6.8. Surface subsidence obtained from NCB empirical curves (a) and from levelling results (b).

Figure 6.9 shows the locations of the two panels, and the surface subsidence during the H46/12 survey predicted from empirical curve and that measured by levelling. The subsidence predicted from the empirical curve is due to H46 alone (i.e. extraction in virgin ground). The subsidence profile has been plotted against the distance from the centre of panel H46.

Although the area affected by subsidence due to mining H45 extends across the whole of the panel H46, we can assume that the effect at the NE end of the profile is negligible. The observed subsidence values here, therefore, are mainly due H46 alone. Thus the surface subsidence due to H46 at point A, which is 110 m from the centre of the panel, is 25 cm. The empirical curve shows that the maximum subsidence predicted at this point is 45 cm, so the residual subsidence at point A is 20 cm. For point B, which is also at 110 m from the centre of the panel, the subsidence is about 40 cm, i.e. 15 cm more than at point A. There are two possible contributions making up this extra subsidence at B: delayed residual subsidence from panel H45 triggered by mining H46, and additional subsidence directly caused by H46 which occurred at B and not at A because the strata at B had already been weakened by subsidence due to H45.

The total subsidence at point B due to panel H45 is predicted to be 18 cm from the empirical curves. However, if we extrapolate NCB levelling results at this area, the subsidence at point B would have been only 14 cm before the mining of H46 had started, leaving a possible 4 cm of residual subsidence to be triggered on mining H46. Thus of the 40 cm subsidence measured at point B, perhaps only 36 cm was due to mining H46 and another 9 cm of delayed residual subsidence may yet occur.

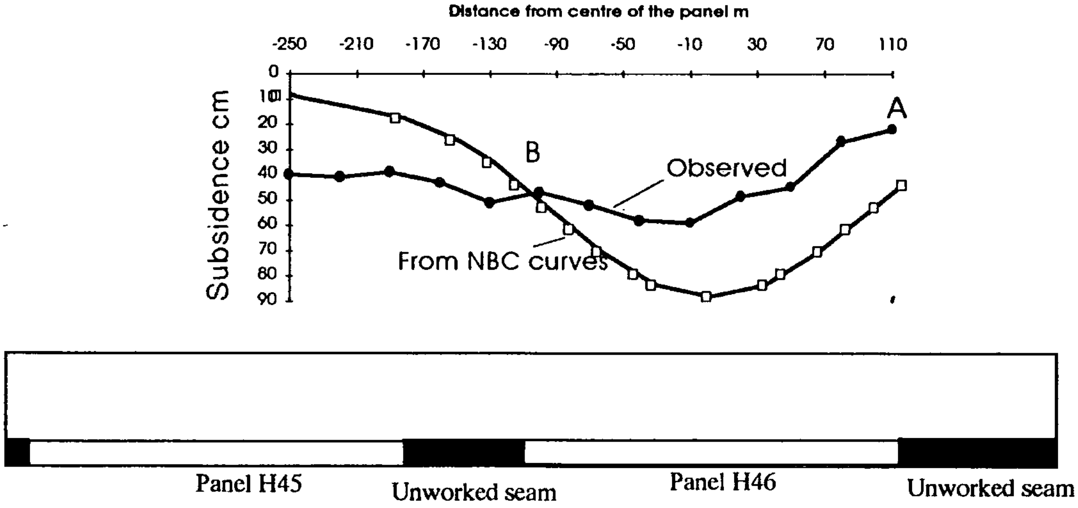

Fig 6.9. The positions of panels H45 and H46, and the surface subsidence calculated from the empirical curves and from the levelling results.

6.3.2. Interpretation of seismic results

The seismic results and the differential subsidence calculated from the development curve for the H46 surveys are reproduced in Fig 6.10. The differential traveltimes for surveys H46/8, 9. 10 and 11 have been combined and the dashed curve in the middle is the average of the four. The progressive increase in differential traveltimes from H46/2 to H46/6 can be seen in Fig 6.10b. This implies that the effective stress decreased progressively during this period.

The increase is mainly above the panel, without any significant change over the edge of the panel. These trends can also be traced in the differential subsidence curves in Fig 6.10a, except that the differential traveltime response seems to lag slightly behind the predictions of differential subsidence.

The decrease in differential traveltimes between H46/6 and the subsequent surveys (Fig 6.10d) indicates that there was an increase in effective stress after the H46/6 survey. Apart from H46/7, the differential traveltimes of all other surveys are practically the same. The decrease in differential traveltime following survey H46/6 is constant across much of the profile, but there is a small increase around CMPs 90-100. The centre of the panel is at about CMP 87. Figure 6.10c, however, shows that there is a decrease in differential subsidence across the whole profile. The differential traveltimes after H46/6, therefore, correlate well with the differential subsidence only near the edge of the panel and over the unworked seam towards panel H45.

The implication of the observed trend of differential traveltimes in Fig 6.10 on effective stress is as follows. When the H46/6 survey was carried out, the face had moved out of the critical distance for the anhydrite and therefore the active subsidence at the anhydrite horizon would have attained its maximum possible magnitude. Further advance of the face caused some further subsidence of the rockmass between the anhydrite and the ground surface, increasing the vertical effective stress by closing some of the cracks and pores. However, near the centre of the panel no significant reduction in differential traveltime was observed (Fig 6.10d), which suggests that the anhydrite continued to subside.

The trend of the decrease in differential traveltime along the profile noted above correlates fairly well with the observed surface subsidence expressed as a fraction of the expected final subsidence. At the centre of the panel (CMP 87), the NCB empirical curves predict the final surface subsidence of 88 cm. The measured maximum subsidence is only about 60 cm. Thus, at CMP 87 the observed subsidence is 68% of the final value, whilst close to panel H45 (around CMP 43), as noted in §6.3.1, the subsidence is 82% of the final value. The decrease in traveltime is also greater in CMP 43 than in CMP 87. However, more data in similar settings are required to show whether the correlation observed here is genuine.

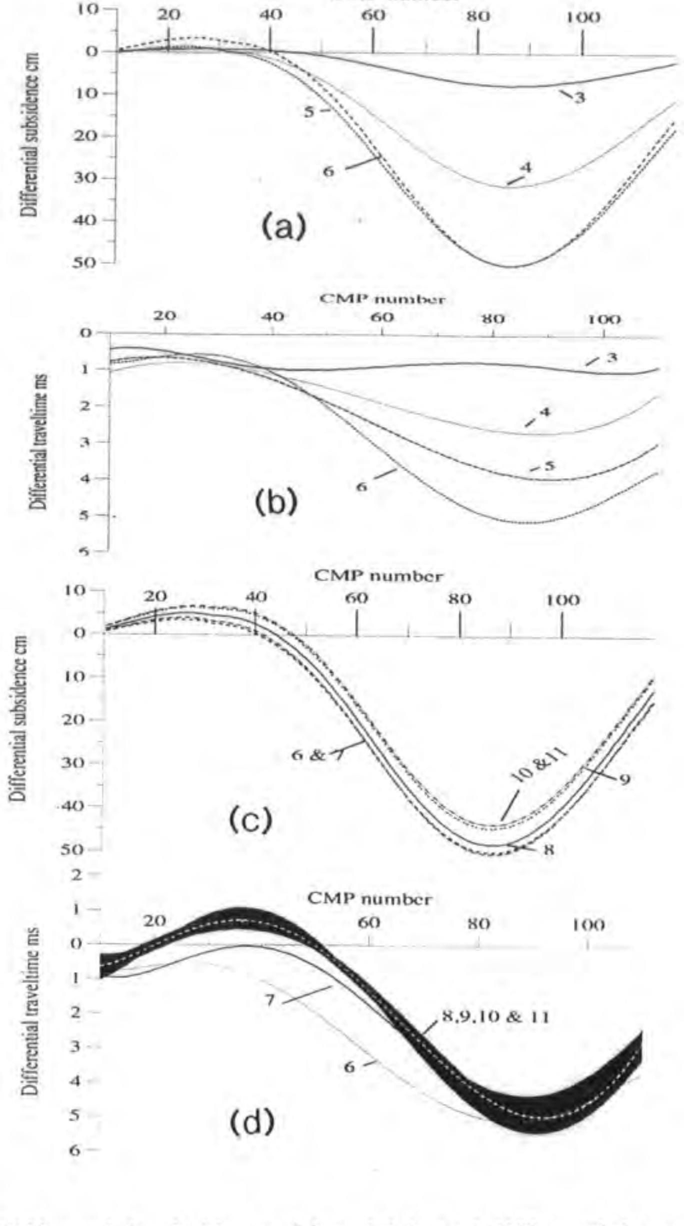

Fig 6.10. Differential subsidence (a) and (c), and differential traveltimes (b) and (d).

Since most of the near-offset traces were eliminated from the final processed stacked sections, the sharp lateral change in velocity could have caused the rays for long offsets to sample a wide range of velocity values. In order to test whether this had caused horizontal smoothing in our study, the GX2 ray tracing package was used to generate synthetic shot records from the models with velocities similar to those expected. The acquisition parameters used in the synthetic data were kept the same as those used in the real data.

Three models were used to represent the change in velocity along the profile (Fig 6.11a). The model of the base survey had a constant velocity of 2000 m/s along the panel. The second model represents a decrease in velocity of up to 4% over the panel, with no change over the unworked seam. In the last model the velocity over the panel was set the same as in the second model, but over the unworked seam the velocity was increased by up to 2 %. The results obtained from the processed synthetic data are shown in Fig 6.11b, and an example of a processed synthetic migrated stacked section is shown in Fig 6.12. The differential traveltimes obtained from the stacked synthetic sections reflect exactly the change in model velocities, and therefore no horizontal smoothing effect due to long offsets is observed.

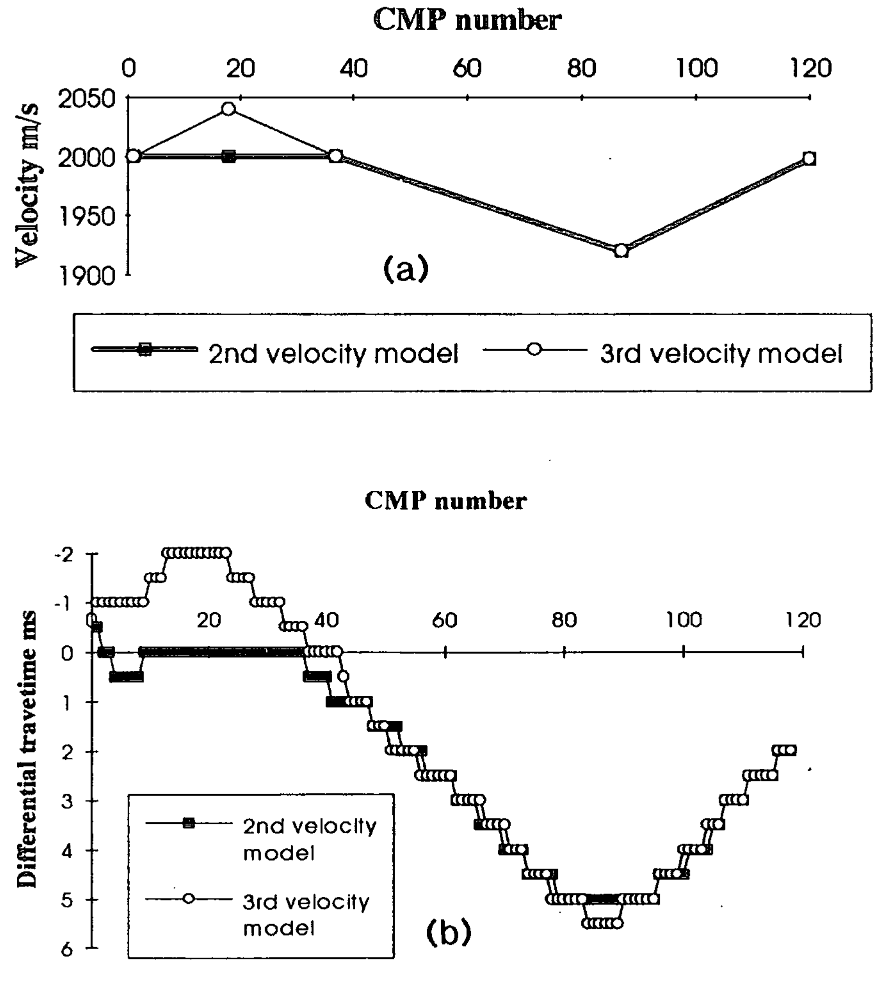

Fig 6.11. (a) Velocity models used in generating synthetic data, and (b) the differential traveltimes calculated from the synthetic stacked sections.

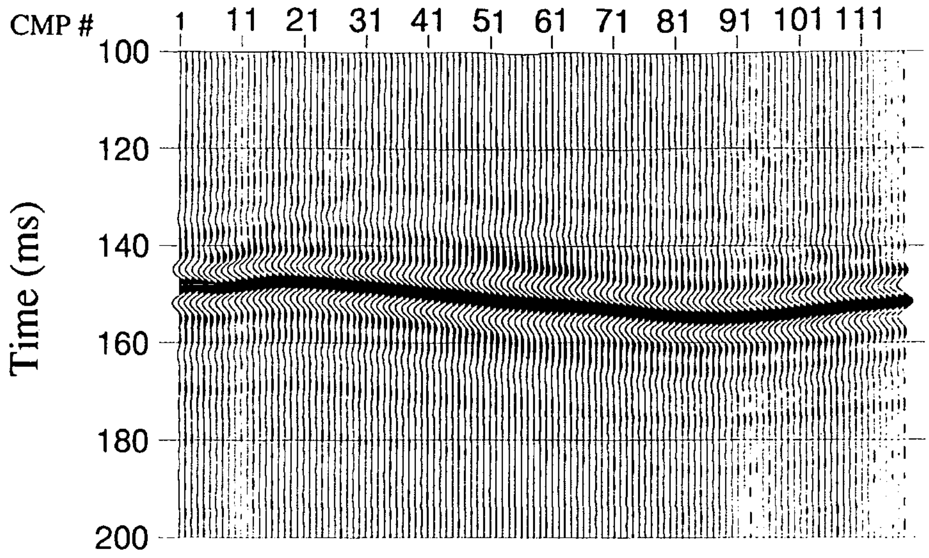

Fig 6.12. A synthetic processed stacked section.

6.4 Reliability of the results

6.4.1 Subsidence results

Levelling results Permanent survey markers were not used. The seismic line was simply pegged out using a tape measure, starting from the field boundary, on each occasion it was surveyed. Apart from subsidence, variations in station heights between surveys were caused by the height of grass, impressions left by tractor tyres along the profile and shifts in the positions of the wooden pegs relative to previous surveys. The effect was more apparent towards the north eastern end of the profile where the ground was soft and the grass was high. On the last survey, the height between the deepest and the highest point around a station at the NE end of the profile was found to be about 9 cm. The combined effects of the sources of error may perhaps amount to ± 5 cm standard deviation.

In contrast to the effect of local vertical displacement at the stations, which was essentially of short wavelength, any variations in the elevation of the base station would cause a dc shift to all the values along the profile. Since the base station was located at the edge of the panel H45, such variation caused by residual subsidence of H45 was possible; and if it had occurred the subsidence values along the profile would have been underestimated. Thus the levelling results give the minimum possible subsidence. However, the residual subsidence at the base station is expected to be no more than a few centimetres.

Subsidence from empirical curves It was noted in §2.5.2.1 that in most coal fields in the UK, the subsidence predicted by the NCB empirical curves are within ±10% of the actual values. Over panel H46, however, the maximum value of observed surface subsidence along the profile was more than 30% less than that calculated from the empirical curves. The difference was attributed mainly to the delayed subsidence.

If a comparable delay had also occurred over panel H45, would this mean that the differential subsidence calculated from the empirical curves is completely wrong? Fortunately, not: the amount of differential subsidence may have been overestimated but the actual shape of the profiles would be essentially the same. This is because, as noted in 6.1.3, the possible cause of the delay is the thick limestone bed in the Lower Magnesian Limestone (underneath the studied anhydrite), and therefore both the anhydrite and the overlying rockmass will be affected equally.

6.4.2 Seismic results

Sources of errors in the seismic results presented in this study are mispositioning of geophone and source stations and the field statics analysis.

Although the source point positions were easily identified from the impressions left by the rubber plate driven into the ground by the hammer blows, the geophone positions could have been misplaced by up to a few tens of centimetres. A maximum depth of the impressions at the source points, which were progressively deepened each time the profiles were surveyed, can be estimated to be about 0.15 m, whilst mispositioning of geophones could result in errors of 0.3 m in source-receiver distances.

Errors associated with field statics are results of errors in picking first arrivals, inconsistency in triggering (see §4.6.2) and those due to mispositioning of source and geophones as described above. The errors in picking first arrivals and inconsistency in triggering add to a maximum of ±1 ms. By taking the velocity in the weathered layer as 300 m/s and the refractor velocity of 1500 m/s, the maximum errors due to mispositioning of sources (vertically) and of geophones (horizontally) is 0.5 ms and 0.2 ms, respectively. However, as a number of source records were involved in calculating the field statics, these estimates for individual errors are possibly much higher than the actual errors.

If we assume that the maximum static error in a trace is ±1 ms and that a minimum number of traces in a CMP gather is 5, then the maximum error in stacked trace is ± 0.5 ms (due to reduction by a factor $\sqrt{n}$ where n=5). Since the differential traveltimes were calculated by subtracting arrival times in two stacked sections, the maximum error in the final differential traveltime is ± 1 ms. Even by including an error of ±0.5 ms in picking reflection arrivaltimes, it is obvious that most of the differential traveltimes observed are caused by change in the actual reflected traveltimes. Furthermore, by combining differential traveltimes of three or four surveys, which were carried out close together or were carried out when most of the subsidence had taken place, the error can be reduced by a further factor of $\sqrt{3}$ or 2.

Chapter 7

Conclusions and suggestions for further work

7.1 Conclusions

The results of the study presented here link laboratory experiments, which are numerous, to observations on the in situ rockmass. Such observations are scarce.

Time-lapse shallow surface reflection surveys over two coal longwall panels have been used to monitor changes in seismic velocity induced by subsidence. The results showed that the reflected traveltime to an anhydrite bed at 150 m depth, due to extraction of a coal seam at a depth of 550 m, increased by about 4% overall as mining proceeded. The magnitude of the change must principally be accounted for by a decrease in seismic velocity in the Bunter Sandstone, which constitutes most of the rockmass between the surface and the anhydrite.

The observed decrease in velocity is interpreted as being due to change in the vertical effective pressure in the Bunter Sandstone. The change in stress is induced by differential subsidence, which represents vertical extension over the panel and compression over the unworked seam. When subjected to vertical tension, the effect of subsidence on the overlying rock mass is to allow cracks to open parallel to the bedding planes. The pore pressure is hydrostatic and does not change, so the vertical effective stress is reduced.

Other causes of change in seismic velocity were considered and found to be insignificant. Such causes included the direct effect of the increase in travelpath from the datum to the anhydrite due to differential subsidence, and possible changes in the ground water level in the drift and the permanent water level in the Bunter Sandstone.

For the seismic line over panel H45, the observed differential traveltimes correlated well with differential subsidence calculated from NCB empirical curves. The closely linear relationship between the differential traveltimes and differential subsidence calculated from the subsidence development curve indicates that the change in stress, like the subsidence, is a function of both time and position of the coal face.

The differential subsidence and traveltime over panel H46 showed a good correlation only for some surveys. The poor correlation observed in other surveys was attributed to the asymmetric subsidence behaviour along this transverse profile due to prior mining of panel H45.

Surface subsidence obtained from levelling results over panel H46 suggests that at least 20 cm of delayed residual subsidence has yet to occur above the NE side of the panel due to the presence of a thick limestone bed in Middle Permian.

The effect of subsidence on seismic velocities is not merely a matter of peripheral interest to subsidence engineers. It has commonly been observed, both by British Coal and by oil companies prospecting for hydrocarbons in Carboniferous strata, that seismic reflection data are of poor quality where longwall mining has taken place. It may be that this is due to the lateral variations in velocity caused by subsidence in the beds overlying the coal seams, rather than scattering from voids left at the worked horizons. We can expect that similar reductions in seismic velocities will take place over producing hydrocarbon fields following primary recovery. For time-lapse seismic reflection surveys monitoring fluid contacts, this may not prove to be a problem because the reflection from the fluid contact will be located relative to interfaces between different rock types. However, careful interpreters will want to be aware of the phenomenon because it may cause laterally varying velocity `push down` over producing fields, and mis-ties between surveys acquired at different times.

In mining and site engineering, the relationship between the change in effective stress and change in seismic velocity could be used to provide valuable information about the condition of the subsurface. Once the velocity-stress sensitivity of a rock at a particular overburden pressure has been established, the change in stress could be determined by monitoring the velocity. Thus there are various possible applications in mining or engineering where velocity monitoring may replace, or supplement, conventional strain measurements (Goulty 1993).

7.2 Further work

In order to be able to quantify the relationship between the differential subsidence and velocity, more profiles have to be surveyed over different panels. The profiles would have be oriented in different directions relative to the panels.

Further studies by surveyors are also called for to examine the effect of mining successive panels on subsidence. Such studies must involve monitoring surface subsidence at regular intervals over a period of years, and if feasible the subsurface subsidence as well. The conclusion in the Subsidence Engineers' Handbook is that final subsidence profiles due to multiple workings, whose effects overlap at the surface, can be found by simple superposition. However, our observations at Wistow indicate that residual subsidence may have a much shorter duration in ground previously affected by subsidence; conversely its occurrence may be substantially delayed in previously unworked ground. Although this does not contradict the idea of superposition, our results (together with others e.g. Orchard and Allen (1975)) just emphasise that there is a lot we don't know about time dependence in mining subsidence, especially residual subsidence.

References

Afrouz, A. and Harvey, J.M. 1974. Rheology of rocks within the soft to medium strength range. *Int. J. Rock Mech. Min. Sci. & Geomech. Abstr.* **11**, 181-290.

Al-Husseini, M.I., Glover, J.B. and Barley, J. 1981. Dispersion patterns of the ground roll in eastern Saudi Arabia. *Geophysics* **46**, 121-137.

Anstey, N.A. 1986. Whatever happened to ground roll? *The Leading Edge* **5**, 40-45.

Banthia, B.S, King, M.S. and Fatt, I. 1965. Ultrasonic shear-wave velocities in rocks subjected to simulated overburden pressure and internal pore pressure. *Geophysics* **30**, 117-121.

Bell, D.W. and Shirley, D.J. 1980. Temperature variation of the acoustical properties of laboratory sediments. *Journal of Acoustical Society of America* **68** 227-231.

Berry, D.S. 1960. An elastic treatment of ground movement due to mining-1. isotropic ground. *J. Mech. Phys. Solids* **8**, 280-292.

Berry, D.S. 1963a. An elastic treatment of ground movement due to mining-Corrigendum. *J. Mech. Phys. Solids* **11**, 373

Berry, D.S. 1963b. Ground movement considered as an elastic phenomenon. *Mining Engineer* **123**, 28-41

Berry, D.S. 1964. The ground considered as transversely isotropic material. *Int. J. Rock Mech. Min. Sci. & Geomech. Abstr.* **1**, 159-167.

Berry, D.S. and Sales, T.W. 1961. An elastic treatment of ground movement due to mining-II. transversely isotropic ground. *J. Mech. Phys. Solids* **9**, 52-62

Berry, D.S. and Sales, T.W. 1962. An elastic treatment of ground movement due to mining-III. three dimensional problem, transversely isotropic ground. *J. Mech. Phys. Solids.* **10**, 73-83.

Biot, M.A. 1956a. Theory of propagation of elastic waves in fluid-saturated porous solid. I. Low-frequency range. *J. Acoustic Soc. Am.* **28**, 178-179.

Biot, M.A. 1956b. Theory of propagation of elastic waves in fluid-saturated porous solid. II. Higher-frequency range. *J. Acoustic Soc. Am.* **28**, 179-191.

Blincikoff , H.J. and Zverev, A.I. 1976. Filtering in the time and frequency domains. A Wiley-Interscience Publication. New York.

Bowers, G.L. 1994. Pressure estimation from velocity data: Accounting for overpressure mechanism besides undercompaction. *IADC/SPE drilling conference* SPE **27488,** 515-530.

Brandt, H. 1955. A study of the speed of sound in porous granular media. *Journal of Applied Mechanics* **22** 479-486.

Bredewout, J.W. and Goulty, N.R. 1986. Some shallow seismic reflections. *First Breaks* **4**, 15-23.

Brown, A. R., Wright, R.M., Burkart, K.D., Abriel, W.L., and McBeath, R.G. !986. Tuning effects, lithological effects and depositional effects in seismic response of gas reservoirs. *Geophysical Prospecting* **34**, 623-647.

Brown, R.J.S. and Korringa, J. 1975. On the dependence of the elastic properties of a porous rock on the compressibility of the pore fluid. *Geophysics* **40**, 608-616

Brown, E.T. and Hoek, E. 1978. Trends in relationships between the measured in situ stresses and depth. *Int. J. Rock Mech. Min. Sci. & Geomech. Abstr.* **15**, 211-215.

Bulau, J.R, Tittmann, B.R., Abdel-Gawad, M. and Salvado, C. 1984. Role of aqueous fluids in the internal friction in rock. *Journal of Geophysical Research* **89**, 4207-4212.

Burland, J.B. and Moore, J.F.A. 1974. The measurements of ground displacement around deep excavations. In *Field Instrumentation In Geotechnical Engineering*. Butterworth. 70-84.

Burns, D.R, Cheng, C.H. and Wilkens, R.H. 1990. Sandstone pore aspect ratio spectra from direct observations and velocity inversion. *Int. J. Rock Mech. Min.Sci. & Geomech. Abstr.* **27(4)**, 315-323.

Cheng, C.H and Toksoz, M.N. 1979. Inversion of seismic velocities for the pore aspect ratio spectrum of a rock. *Journal of Geophysical Research* **84**, 7534-7543.

Christensen, N.I. and Wang, H.F. 1985. The influence of pore pressure and confining pressure on dynamic elastic properties of Beria sandstone. *Geophysics* **50**, 207-213.

Collins, B.J. 1978. Measurement and analysis of residual mining subsidence movements. In *Large Ground Movements And Structures* (ed. J.D. Geddes). Pentech Press London. 3-29.

Corden, C.H.H. and King, H.J. 1965. A field study of the development of surface subsidence. *Int. J. Rock Mech. Min. Sci. & Geomech. Abstr.* **2**, 43-55.

Dahl, H.D. and Choi, D.S. 1973. Some case studies of mine subsidence and its mathematical modelling. *Proc. 15th Symp. Rock Mech.* Custer State Park, SD. 1-22.

Davies, K., Barker, R.D. and King, R.F. 1992. Application of shallow reflection techniques in hydrogeology. *Quarterly Journal of Engineering Geology* **25**, 207-216.

Desai, C.S. and Abel, J.F. 1972. Introduction to the finite element method. Van Nostrand Reinhold Company, New York.

Diering, J.A.C. 1982. Mining simulation of tabular excavations using finite elements. *Proceedings Of The Fourth International Conference On Numerical Methods in Geomechanics* **2**, 545-550.

Domenico, S.N. 1974. Effects of water saturation of sand reservoirs encased in shales. *Geophysics* **29**, 759-769.

Domenico, S.N. 1977. Elastic properties of unconsolidated sand reservoirs. *Geophysics* **41**, 882-894.

Domenico, S.N. 1984. Rock lithology and porosity determination from shear compressional wave velocities. *Geophysics* **49**, 1188-1195.

Douglas, T. 1991. Seismic reflection profiles from Skye and Selby. Unpublished MSc dissertation, University of Durham.

Dziewonski, A.M., Bloch, S. and Landisman, M. 1969. A technique for the analysis of transient seismic signals. *Bulletin of the Seismology Society of America* **59**, 427-444.

Elliot, S.E. and Wiley, B.F. 1975. Compressional velocities of partially saturated, unconsolidated sands. *Geophysics* **40**, 949-954.

Fairbairn, C.M., Holt, J.M. and Padget, N.J. 1986. Case histories of the use of surface seismics in the UK coal mining industry. In *Coal Geophysics* (ed. D.J. Buchanan and L.J. Jackson). 188-203. Society of Exploration Geophysicists.

Findlay, M.J. 1991. Cross-hole seismic reflection surveying in Coal Measures. Unpublished PhD dissertation, University of Durham.

Franklin, J.A. 1977. The monitoring of structures in rock. *Int. J. Rock Mech. Min. Sci. & Geomech. Abstr.* **14**, 163-192.

Gardner, G.H.F, Wyllie, M.R.J. and Droschak, D.M. 1965. Hysteresis in velocity-pressure characteristics of rocks. *Geophysics* **30**, 111-116.

Gassmann, F. 1951. Elastic waves though a packing of spheres. *Geophysics* **16**, 673-685.

Gay, N.C. 1975. In-situ measurements in Southern Africa. *Tectonophysics* **29**, 447-459.

Geertsma, J. 1961. Velocity-log interpretation. The effect of rock bulk compressibility. *Soc. Petr. Eng.* **1**, 235-248.

Gladwin, M.T. 1982. Ultrasonic stress monitoring in underground mining. I*nt. J. Rock Mech. Min. Sci. & Geomech. Abstr.* **19**, 221-228

Gochioco, L.M. and Cotten, S. 1989. Locating faults in underground coal mines using high-resolution seismic reflection techniques. *Geophysics* **54**, 1521-1527.

Goodman, R.E. 1980. Introduction to rock mechanics. John Wiley & Sons, New York.

Goulty, N.R. 1993. Controlled-source tomography for mining and engineering applications. In *seismic tomography: theory and practice* (ed. H.M. Iyer and K. Hirahara). 797-813. Chapman & Hall London.

Goulty, N.R. 1994. Discussion. *Quarterly Journal of Engineering Geology* **27**, 383-384.

Goulty, N.R. and Al-Rawahy, S.Y.S. 1995. Some remarks concerning the time-dependence of subsidence due to longwall coal mining. *Quarterly Journal of Engineering Geology* in press.

Goulty, N. R. and Ziolkowski, A. 1985. Seismic reflection surveys applied to problems in coal mining: example from Bilsthorpe colliery, UK. **in** *Proceedings of the 9th International Congress on Carboniferous Stratigraphy and Geology* **4**, 689-694. Southern Illinois University Press.

Greaves, R.J. and Fulp, T.J. 1987. Three-dimensional seismic monitoring of an enhanced oil recovery process. *Geophysics* **52**, 1175-1187.

Gregory, A.R. 1976. Fluid saturation effects on dynamic elastic properties of sedimentary rocks. *Geophysics* **41**, 895-921

Greiner, G. 1975. In-situ measurements in Southwest Germany. *Tectonophysics* **29**, 265-274.

Hackett, P. 1959. An elastic analysis of rock movements caused by mining. *Transactions of The Institution of Mining Engineers* **118**, 421-435.

Haimson, B.C 1978. The hydrofracturing stress measuring method and recent field results. *Int. J. Rock Mech. Min. Sci. & Geomech. Abstr.* **15**, 167-178.

Hamilton, E.L. 1971. Elastic properties of marine sediments. *Journal of Geophysical Research* **76(2)**, 576-604.

Han, D., Nur, A. and Morgan, F.D. 1986. Effects of porosity and clay content on wave velocities in sandstones *Geophysics* **51**, 2093-2107.

Hatton, L., Worthington, M.H. and Makin, J. 1986. Seismic data processing. Blackwell Scientific Publications, London.

Haws, E.T., Lippard, D.C. Tabb, R. and Burland, J.B. 1974. Foundation instrumentation for the National Westminster tower. In *Field Instrumentation In Geotechnical Engineering*. Butterworth. 180-193.

Hicks, W.G and Berry, J.E. 1956. Fluid saturation of rocks from velocity logs. *Geophysics* **21**, 739-754.

Hill, I.A. 1992. Field techniques and instrumentation in shallow seismic reflection. *Quarterly Journal of Engineering Geology* **25**, 183-190.

Hoek, E. and Brown, E.T. 1980. Underground excavations in rock. The institution of mining and metallurgy. London.

Holla, L. and Buizen, M. 1991. The ground movement, strata fracturing and changes in permeability due to deep longwall mining. *Int. J. Rock Mech. Min. Sci. & Geomech. Abstr.* **28**, 207-217.

Hunter, J.A., Pullan, S.E., Burns, R.A., Gagne, R.M. and Good, R.C. 1984. Shallow seismic reflection mapping of the overburden bedrock interface with the engineering seismograph-some simple techniques. *Geophysics* **49**, 1381-1385.

Ito, H. and Sasajima, S. 1987. A ten year creep experiment on small rock specimen. *Int. J. Rock Mech. Min. Sci. & Geomech. Abstr.* **24**, 113-121.

Jarosz, A., Karmis, M. and Stroka, A. 1990. Subsidence development with time-experiences from longwall operations in Appalachian coalfield. *International Journal of Mining and Geological Engineering* **8**,261-273.

Jaeger, J.C. and Cook, N.G.W. 1969. Fundamentals of rock mechanics. Methuen & Co Ltd London.

Justice, J.H., Mathisen, M.E., Vassiliou, A.A., Shiao, I., Alameddine, B.R. and Guinzy, N.J. 1993. Crosswell seismic tomography in improved oil recovery, *First Break* **11,** 229-239.

Justice, J.H., Vassilou, A.A., Singh, S., Logel, J.D., Hansen, P.A., Hall, B.R., Hutt, P.R., and Solanki, J.J. 1989. Acoustic tomography for monitoring enhanced oil recovery. *The Leading Edge* **8**, 12-19.

King, M.S. 1966. Wave velocities in rocks as a function of changes in overburden pressure and pore fluid saturant. *Geophysics* **31**, 50-73.

King, H.J., Whittaker, B.N. and Shadbolt, C.H. 1975. Effects of mining subsidence on surface structures. In *Minerals and the Environment* (ed. M.J. Jones). Institution of Mining and Metallurgy, London. 617-642.

Knapp, R.W. and Steeples, D.W. 1986a. High-resolution common-depth-point seismic reflection profiling: Instrumentation. *Geophysics* **51**, 276-282.

Knapp, R.W. and Steeples, D.W. 1986b. High-resolution common-depth-point seismic reflection profiling: Field acquisition parameter design. *Geophysics* **51**, 283-294.

Knopoff, L. 1972. Observation and inversion of surface wave dispersion. *Tectonophysics* **13**, 497-519.

Kormendi, A., Bodoky, T., Hermann, L., Dianiska, L. and Kalman, T. 1986. Seismic measurements for safety in mines. *Geophysical Prospecting* **34**, 1022-1037.

Kowallies, B., Jones, L.E.A. and Wang, H.F. 1984. Velocity -porosity-clay content: systematics of poorly consolidated sandstones. *Journal of Gephysical Research* **89**, 10355-10364.

Kragh, J.E. 1990. Borehole seismic methods for opencast coal exploration. Unpublished PhD dissertation, University of Durham.

Kratzsch, H. 1983. Mining subsidence engineering. Springer-Verlag, Berlin.

Kuster, G.T and Toksoz, M.N. 1974(a) Velocity and attenuation of seismic waves in two-phase media: Part I—theoretical formulations. *Geophysics* **39**, 587-606.

Kuster, G.T and Toksoz, M.N. 1974(b) Velocity and attenuation of seismic waves in two-phase media: Part II—experimental results. *Geophysics* **39**, 607-616.

Lee, A.J. 1966. The effect of faulting on mining subsidence. *Mining Engineer* **125**, 735-745.

Legget, M. 1992. Crosshole seismic processing of physical model and Coal Measures data. Unpublished PhD dissertation, University of Durham.

Macrides, C.G., Kanasewich, E.R. and Bharatha, S. 1988. Multiborehole seismic imaging in steam injection heavy oil recovery projects. *Geophysics* **53**, 65-75.

Mann, D.M. and Mackenzie, A.S. 1990. Prediction of pore fluid pressures in sedimentary basins. *Marine and Petroleum Geology* 55-70.

Marr, J.E. 1975. The application of the zone area system to the prediction of mining subsidence. *Mining Engineer* **135**, 53-62.

Mather, J.D., Gray, D.A. and Jenkins, D.G. 1969. The use of tracers to investigate the relationship between mining subsidence and groundwater occurrence at Aberfan, South Wales. *Journal of Hydrology* **9**,136-154.

Mathews, L. 1992. 3-D seismic monitoring of in-situ thermal process: Athabasca Canada. *Reservoir Geophysics*, R. Sheriff (ed.) 301-308. Society of Exploration Geophysicists, Tulsa.

McCann, D.M., Andrew, E.W. and McCann, E.M. 1985. Seismic sources for shallow reflection surveying. *Geophysical Prospecting* **33**, 943-953.

Meekes, J.A.C., Scheffers, B.C. and Ridder, J. 1990. Optimization of high-resolution seismic reflection parameters for hydrogeological investigations in The Netherlands. *First Break* **8**, 263-270.

Miller, R.D., Pullan, S.E., Waldner, J.S. and Haeni, F.P. 1986. Field comparison of shallow seismic sources. *Geophysics* **51**, 2067-2092.

Miller, R.D., Steeples, D.W. and Brannan, M. 1989. Mapping a bedrock surface under alluvium with shallow seismic reflections. *Geophysics* **54**, 1528-1534

Miller, R.D., Saenz, V. and Huggins, R.J. 1992. Feasibility of CDP seismic reflection to image structures in a 220-m depth, 3-m thick coal zone near Palau, Coahuila, Mexico. *Geophysics* **57**, 1373-1380.

Murphy III, W.F. 1982. Effects of partial water saturation on attenuation in Massilon sandstone and Vycor porous glass. *Journal of Acoustical Society of America* **71**, 1458-1468.

Murphy III, W.F. 1984 Acoustic measures of partial gas saturation in tight sandstones. *Geophysics* **89**, 11549-11559.

Murphy III, W.F, Winkler, K. and Kleinberg, R. 1984. Frame modulus reduction in sedimentary rocks - The effect of adsorption on grain contacts. *Gephys. Res. Lett.* **11**, 805-808.

Muskhelishvili, N.I. 1953. Some basic problems of the mathematical theory of elasticity. Nordhoff, Groningen.

National Coal Board 1975. Subsidence Engineers' Handbook. National Coal Board, London.

Obert, L. and Duvall, W.I. 1967. Rock mechanics and the design of structures in rock. John Wiley & Sons, New York.

Orchard, R.J. and Allen, W.S. 1975. Time-dependence in mining subsidence. In *Minerals and the Environment*, (ed. M.J. Jones). Institution of Mining and Metallurgy, London. 643-659.

Pickett, G.R. 1963. Acoustic character logs of and their application in formation evaluation. *Journal of petroleum technology* 659-667.

Pietsch, K and Šlusarczyk, R. 1992. The application of high-resolution seismics in Polish coal mining. *Geophysics* **57**, 171-180.

Pullan, S.E. and MacAulay, H.A. 1987. An in-hole shotgun source for engineering seismic surveys. *Geophysics* **52**, 985-996

Pyne, R. and Randon, D.V. 1986. Surface environmental aspects of the Selby Coalfield. *Mining Engineer* **146**, 77-84.

Ranalli, G. 1975. Geotectonic relevance of rock-stress determinations. *Tectonophysics* **29**, 49-58.

Roberts, A. 1981. Applied geotechnology. Pergamon press, Oxford.

Rowbotham, P. 1993. Advances in crosshole seismic reflection processing. Unpublished PhD dissertation, University of Durham.

Saatçilar, R. and Canitez, N. 1988. A method of ground-roll elimination. *Geophysics* **53**, 894-902.

Salamon, M.D.G. 1968. Two-dimensional treatment of problems arising from mining tabular deposits in isotropic or transversely isotropic ground. *Int. J. Rock Mech. Min. Sci. & Geomech. Abstr.* **5**, 159-185.

Salamon, M.D.G. 1974. Rock mechanics of underground excavations. In *advances in rock mechanics, Proceedings 3rd Congress of the International Society of Rock mechanics, Denver* **1(b)** 951-1099.

Salem, J., Panet, M. and Guenot, A. 1987. Closure analysis in deep tunnel. *Int. J. Rock Mech. Min. Sci. & Geomech. Abstr.* **24**, 145-154.

Sangha, C.M, Talbot, C.J. and Dhir, R.K. 1974. Microfracturing of a sandstone in uniaxial compression. *Int. J. Rock Mech. Min. Sci. & Geomech. Abstr.* **11**, 107-113.

Sauer, G. and Sharma, B. 1977. A system for stress measurement in construction in rock. In *Field Measurements in Rock Mechanics* (ed. K. Kovari). Balkema, Rotterdam. **1**,317-329.

Shu, D.M. and Bhattacharyya, A.K. 1990. Relationship between sub-surface and surface subsidence - a theoretical model. *Mining Sciences and Technology* **11**, 307-319.

Shumway. G. 1958. Sound velocity vs. temperature in water-saturated sediments *Geophysics* **23**, 494-505.

Singh, S. 1986. Reflection-window mapping of shallow bedrock. *Geophysical Prospecting* **34**, 492-507.

Spathis, A.T, Blair, D.P. and Grant, J.R. 1985. Seismic pulse assessment of changing rock mass conditions induced by mining. *Int. J. Rock Mech. Min. Sci. & Geomech. Abstr.* **22**, 303-312.

Steeples, D.W., Knapp, R.W. and McElwee, C.D. 1986. Seismic reflection investigations of sinkholes beneath interstate highway 70 in Kansas. *Geophysics* **51**, 295-301.

Timur, A. 1977. Temperature dependence of compressional and shear wave velocities in rocks. *Geophysics* **42**, 950-956.

Toksoz, M.N, Cheng, C.H. and Timur, A. 1976. Velocities of seismic waves in porous rocks. *Geophysics* **41**, 621-645.

Tosaya, C. and Nur, A. 1982. Effects of diagenesis and clays on compressional velocities in rocks. *Geophysics Research Letters* **9**, 5-8.

Urick, R.J. 1947. A sound velocity method for determining the compressibility of finely divided substances. *Journal of Applied Physics* **18**, 983-987.

Wang, Z. and Nur, A. 1988. Seismic velocities in tar sands: The basis for in-situ recovery monitoring. *Proc. of the 4th Internat. Conf. on Heavy Crude and Tar Sands* **4**, 601-611.

Wardell, K. 1954. Some observations on the relationship between time and mining subsidence. *Transactions of the Institution of Mining Engineers* 113, 471-483.

Wilson, A.H. 1981. Stress and stability in coal ribsides and pillars. In *Proc. 1st Ann. Conf. on Ground Control in Mining.* West Virginia University (ed. S.S. Peng). 1-12.

Wood, A.B. 1941. Textbook of Sound. G. Bell and Sons, London.

Wyllie, M.R.J., Gregory, A.R. and Gardner, G.H.F. 1958. An experimental investigation of factors affecting elastic wave velocities in porous media. *Geophysics* **23**, 459-493.

Wyllie, M.R.J., Gregory, A.R. and Gardner, L.W. 1956. Elastic wave velocities in heterogeneous and porous media. *Geophysics* **21**, 41-70.

Yale, D.P. 1985. Recent advances in rock physics. *Geophysics* **50**, 2480-2491.

Yao, X.L. and Reddish D.J. 1994a. Analysis of residual subsidence movements in the UK coalfields. *Quarterly Journal of Engineering Geology* **27**(**1**), 15-23.

Yao, X.L. and Reddish D.J. 1994b. Reply. *Quarterly Journal of Engineering Geology* **27**, 384-385.

Zienkiewicz, O.C. 1977. The finite element method. McGraw Hill, New York.

Ziolkowski, A. 1979. Seismic profiling for coal on land. In *Developments in Geophysical Exploration Methods v1* (ed. A.A. Fitch). Applied Science Publishers LTD. Essex England.

Ziolkowski, A. and Lerwill, W.E. 1979. A simple approach to high resolution seismic profiling for coal. *Geophysical Prospecting* **27**, 360-393.

Zoback, M.L. 1992. First- and second-order patterns of stress in the lithosphere: The world stress map project. *Journal of Geophysical Research* **97(B8)**, 11,703-728.

Appendix 1

Assumptions

1) The depth to the excavation is infinite. The method still valid if $8 \leq H/a$, where H is the mining depth and a is the half span of the excavation (Salamon 1974).
2) The panel is so wide that the strain across the panel is zero.
3) The ground is homogeneous, isotropic and behaves in a linear elastic manner.
4) The premining stress condition is lithostatic.
5) The excavation is horizontal..

Strain components of an isotropic elastic body under plane strain conditions, i.e. one of its normal strain components equal to zero, are given by

$$\begin{aligned} \varepsilon_{xx} &= \frac{(1-\upsilon^2)}{E}(\sigma_{xx} - \frac{\upsilon}{(1-\upsilon)}\sigma_{yy}) \\ \varepsilon_{yy} &= \frac{(1-\upsilon^2)}{E}(\sigma_{yy} - \frac{\upsilon}{(1-\upsilon)}\sigma_{xx}) \\ \gamma_{xy} &= \frac{1}{G}(\sigma_{xy}) = \frac{2(1+\upsilon)}{E}\sigma_{xy} \end{aligned} \tag{1}$$

where υ is Poisson's ratio, σ is stress, γ is shear strain, ε is normal strain, G is the modulus of rigidity and E is the Young's Modulus. The strain compatibility equation in two dimensions is

$$\frac{\partial^2 \varepsilon_{xx}}{\partial y^2} + \frac{\partial^2 \varepsilon_{yy}}{\partial x^2} = \frac{\partial^2 \gamma_{xy}}{\partial x \partial y}. \tag{2}$$

Substituting (1) in (2) gives

$$\frac{(1-\upsilon^2)}{E}\left(\frac{\partial^2 \sigma_{xx}}{\partial y^2} - \frac{\upsilon}{(1-\upsilon)}\frac{\partial^2 \sigma_{yy}}{\partial y^2} + \frac{\partial^2 \sigma_{yy}}{\partial x^2} - \frac{\upsilon}{(1-\upsilon)}\frac{\partial^2 \sigma_{xx}}{\partial x^2}\right) = \frac{2(1-\upsilon^2)}{E}\frac{\partial^2 \sigma_{xy}}{\partial x \partial y}. \tag{3}$$

Also for zero body forces, the differential equations of equilibrium in two dimensions are

$$\frac{\partial \sigma_{xx}}{\partial x} + \frac{\partial \sigma_{xy}}{\partial y} = 0, \quad \frac{\partial \sigma_{yy}}{\partial y} + \frac{\partial \sigma_{xy}}{\partial x} = 0. \tag{4}$$

Differentiating the first part of (4) with respect to x and the second with respect to y yields

$$\frac{\partial^2 \sigma_{xx}}{\partial x^2} = \frac{\partial^2 \sigma_{yy}}{\partial y^2} = -\frac{\partial^2 \sigma_{xy}}{\partial y \partial x}. \tag{5}$$

Equation (3) can be simplified by using equation (5) to get

$$\frac{\partial^2\sigma_{xx}}{\partial x^2}+\frac{\partial^2\sigma_{yy}}{\partial y^2}+\frac{\partial^2\sigma_{xx}}{\partial y^2}+\frac{\partial^2\sigma_{yy}}{\partial x^2}=\left(\frac{\partial^2}{\partial x^2}+\frac{\partial^2}{\partial y^2}\right)(\sigma_{xx}+\sigma_{yy})=0. \qquad (6)$$

Equation (6) shows that the sum of the normal stresses in two dimensions satisfy the Laplace's equation. If *U(x,y)* is a function such that

$$\frac{\partial^2 U}{\partial y^2}=\sigma_{xx},\ \frac{\partial^2 U}{\partial x^2}=\sigma_{yy},\ \frac{\partial^2 U}{\partial y\partial x}=\sigma_{xy}, \qquad (7)$$

then equation (6) can be written as

$$\nabla^4 U=0 \qquad \text{where} \qquad \nabla^2=\frac{\partial^2}{\partial x^2}+\frac{\partial^2}{\partial y^2}. \qquad (8)$$

The function *U(x,y)* is known as Airy's stress function and equation (8) is called biharmonic equation.

One of the methods of solving the biharmonic equation is that of using complex functions outlined by Muskhelishvili (1953) and Jaeger and Cook (1969). If $z=x+iy$, then $U(z)$ can be expressed in terms of two functions of z, $\phi(z)$ and $\chi(z)$ in the form of

$$U(z)=R(\bar{z}\phi(z)+\chi(z))=\frac{1}{2}\left(\bar{z}\phi(z)+\overline{z\phi(z)}+\chi(z)+\overline{\chi(z)}\right) \qquad (9)$$

where R is the real part of the function, and bar over a function indicates a complex conjugate. Stresses may be obtained by successive differentiation of (9) and integration can be used to determine the strain components:

$$\sigma_{xx}+\sigma_{yy}=2(\phi'(z)+\overline{\phi'(z)})=4R(\phi'(z)) \qquad (10)$$

$$\sigma_{yy}-\sigma_{xx}+2i\sigma_{xy}=2(\bar{z}\phi''(z)+\psi'(z)) \qquad \text{where } \psi(z)=\chi(z) \qquad (11)$$

$$2G(u+iv)=(3-4\nu)\phi(z)-\overline{z\phi'(z)}-\overline{\psi(z)}. \qquad (12)$$

To solve a particular problem, suitable forms of the function $\phi(z)$ and $\psi(z)$ are first selected. A number of these functions have been formulated by Jaeger and Cook (1969) and most of them involve z or z^{-1}. For example, for a circular hole in a medium subjected to a uniaxial stress p_1 at infinity, the potential functions take the form of

$$\phi(z)=\frac{1}{4}p_1(z+\frac{A}{z}) \qquad \psi(z)=-\frac{1}{2}p_1(z+\frac{B}{z}+\frac{C}{z^2}) \qquad (13)$$

where A, B and C are constants and can be evaluated by taking appropriate boundary conditions.

Berry (1960) and Salamon (1968, 1974) adopted the solutions used in cracks by Muskhelishvili (1953) to model the stresses and displacement field induced by tabular mining in an isotropic medium at infinite depth. For a *non closure condition*, no contact between the floor and the roof of the excavation, the complex potential functions are given by

$$\phi(z)=\frac{1}{4}p(z-\sqrt{z^2-a^2}) \quad \psi(z)=\phi(z)-z\phi'(z) \tag{14}$$

where a is the half length of the of the excavation and $-p$ is the initial stress at the mining horizon. From (14), therefore,

$$\begin{aligned}
\phi'(z)&=\frac{p}{2}\left(1-\frac{z}{\sqrt{z^2-a^2}}\right)\\
\phi''(z)&=\frac{p}{2}\left(\frac{z^2}{\sqrt{z^2-a^2}^3}-\frac{1}{\sqrt{z^2-a^2}}\right)\\
\psi(z)&=\frac{p}{2}\left(z-\sqrt{z^2-a^2}\right)-z\left(1-\frac{z}{\sqrt{z^2-a^2}}\right)\\
\psi'(z)&=\frac{p}{2}\left(\frac{z}{\sqrt{z^2-a^2}}-\frac{z^3}{\sqrt{z^2-a^2}^3}\right)
\end{aligned} \tag{15}$$

The stresses are then given by

$$\sigma_{xx}+\sigma_{yy}=2pR\left(1-\frac{(x+iy)}{\sqrt{(x+iy)^2-a^2}}\right) \tag{16}$$

$$\sigma_{yy}-\sigma_{xx}+2\sigma_{xy}=p((x-iy)-(x+iy))\left(\frac{(x+iy)^2}{\sqrt{(x+iy)^2-a^2}^3}-\frac{1}{\sqrt{(x+iy)^2-a^2}}\right).$$

Solving (16) at the mining horizon, y=0, gives the stresses along the x-axis in the interval x>a as

$$\sigma_{yy}=\sigma_{xx}=p\left(1-\frac{x}{\sqrt{x^2-a^2}}\right). \tag{17}$$

The stresses vertically above the centre of the panel are given by solving equation (16) with x=0:

$$\sigma_{yy}=p\left(1-\frac{|y^3|}{\sqrt{y^2-a^2}^3}\right) \tag{18}$$

$$\sigma_{xx} = p\left(1 - \frac{y(2a^2 + y^2)}{\sqrt{y^2 + a^2}}\right). \tag{19}$$

If the depth to the mining horizon and the initial stress at this level are H and q, respectively, and the negative y-axis is towards the surface then total stresses can be calculated from stresses in equation (17) and (20) to give

$$\sigma_{xx} = \sigma_{yy} = -q + \frac{qx}{\sqrt{x^2 - a^2}} + q = \frac{qx}{\sqrt{x^2 - a^2}} \tag{20}$$

and vertically above the centre of the panel:

$$\sigma_{yy} = -q + \frac{q\left|y^3\right|}{\sqrt{y^2 + a^2}^3} + \frac{qh}{H} = \frac{qy}{H} + \frac{q\left|y^3\right|}{\sqrt{y^2 + a^2}^3} \tag{21}$$

$$\sigma_{xx} = -q + \frac{q|y|(2a^2 + y^2)}{\sqrt{a^2 + y^2}^3} + \frac{qh}{H} = \frac{qy}{H} + \frac{q|y|(2a^2 + y^2)}{\sqrt{a^2 + y^2}^3} \tag{22}$$

where h is the depth below the surface and therefore $h=H+y$. Equations (20), (21) and (22) are given in chapter 2 as equations (2.13) and 2.15).

The displacement field is obtained by solving equation (12) using the relationship (14). The convergence Δv is given by

$$\Delta v = \frac{-2p(1-\upsilon)}{G}\sqrt{a^2 - x^2}. \tag{23}$$

For the *partial closure state* the potential functions are given by

$$\begin{aligned}
\phi'(z) &= \frac{p}{2}\left(1 - \sqrt{\frac{z^2 - b^2}{z^2 - a^2}}\right) \\
\phi''(z) &= -\frac{p}{2}\left(\frac{z\sqrt{z^2 - b^2}}{\sqrt{z^2 - a^2}^3} - \frac{z}{\sqrt{(z^2 - b^2)(z^2 - a^2)}}\right) \\
\psi'(z) &= -z\phi''(z) = \frac{p}{2}\left(-\frac{z^2\sqrt{z^2 - b^2}}{\sqrt{z^2 - a^2}^3} + \frac{z^2}{\sqrt{(z^2 - b^2)(z^2 - a^2)}}\right)
\end{aligned} \tag{24}$$

where b is the half length of the contact zone at y=0. By substituting (24) into (10) and (11), the stresses at the mining horizon at interval $|x| \le b$ are

$$\sigma_{xx} = \sigma_{yy} = p\left(1 - \sqrt{\frac{b^2 - x^2}{a^2 - x^2}}\right), \tag{25}$$

and the stresses vertically above the centre of the panel are given by

$$\sigma_{yy} = p\left(1 - \left(\frac{y^4 + 2y^2b^2 + a^2b^2}{\sqrt{y^2+a^2}^3\sqrt{y^2+b^2}}\right)\right)$$

$$\sigma_{xx} = p\left(1 - \left(\frac{y^4 + 2y^2a^2 + a^2b^2}{\sqrt{y^2+a^2}^3\sqrt{y^2+b^2}}\right)\right) \qquad (26)$$

For complete closure, *b*=*a*, ϕ(z) is

$$\phi(z) = \frac{Gt}{4\pi(1-\upsilon)}\log\left(\frac{z+a}{z-a}\right), \qquad (27)$$

and thus using (10), (11), (12) and (27) stresses are

$$\sigma_{xx} = \sigma_{yy} = \frac{Gat}{\pi(1-\upsilon)(a^2-x^2)} \text{ at mining horizon,} \qquad (28)$$

and $\sigma_{yy} = \dfrac{Gta(a^2+2y^2)}{\pi(1-\upsilon)(a^2+y^2)^2}$ and $\sigma_{xx} = \dfrac{Gta^3}{\pi(1-\upsilon)(a^2+y^2)^2}$ vertically above the centre of the panel. (29)

Appendix 2

The final time migrated sections for surveys H45/1 to H45/10 and H46/1 to H46/11.

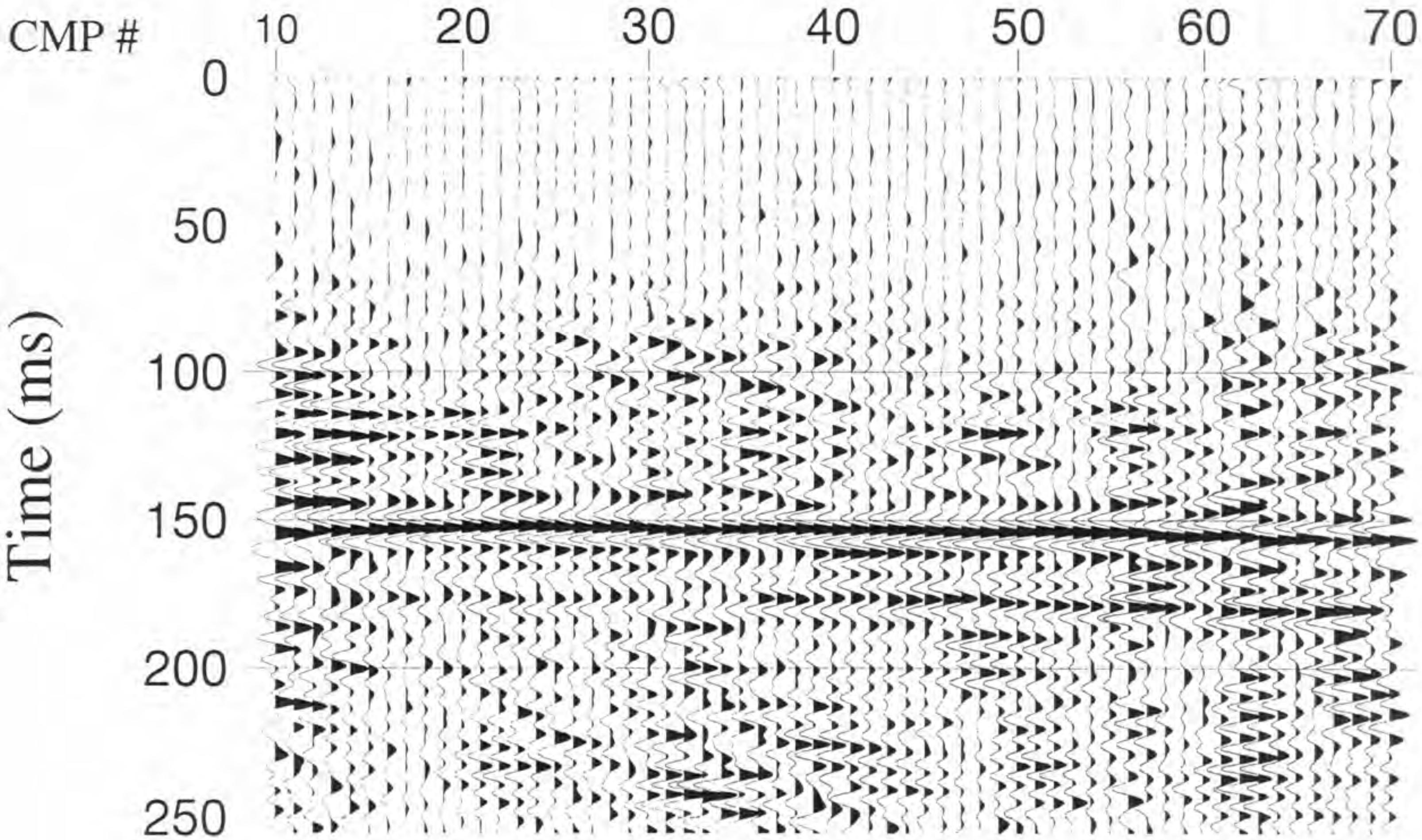

H45/1

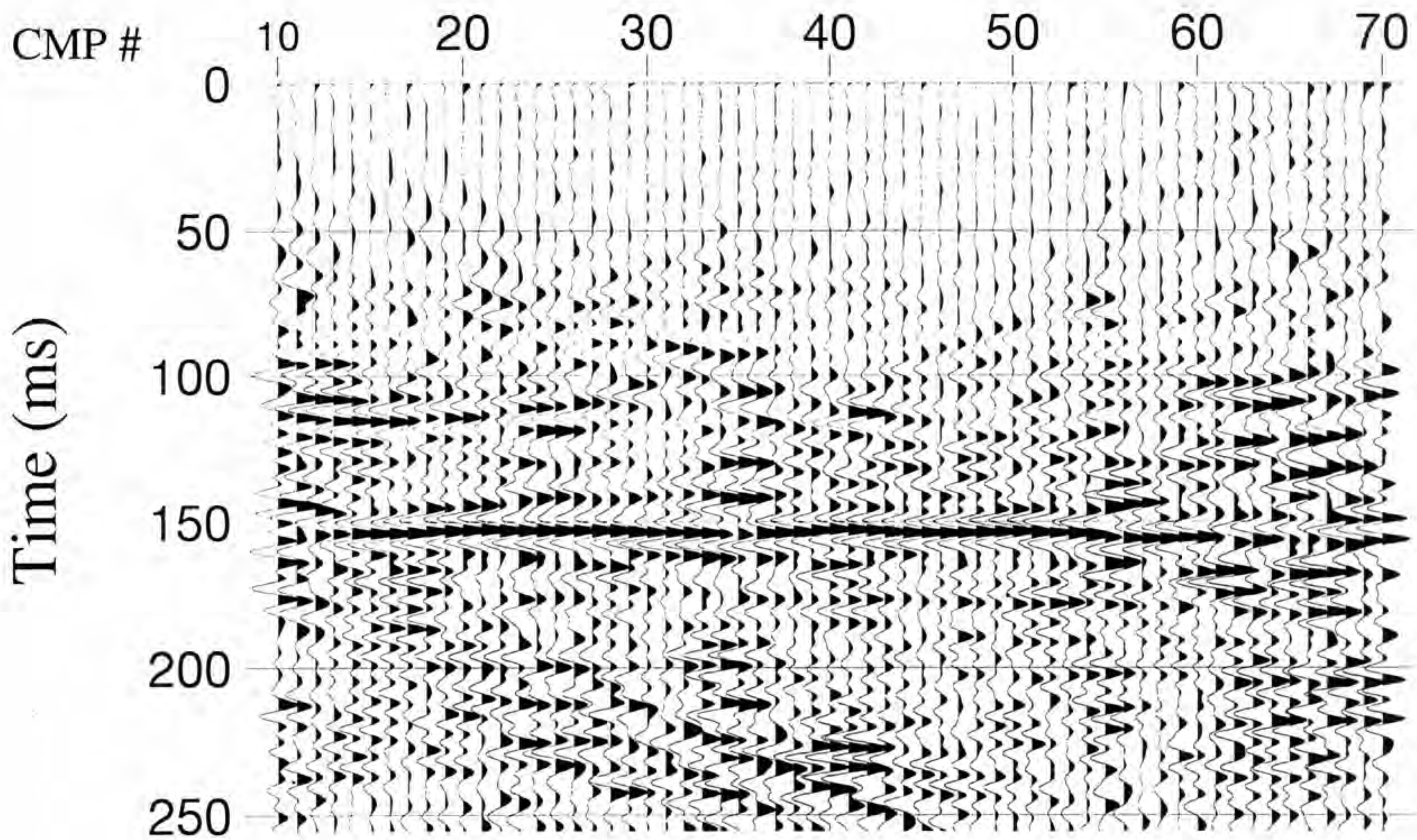

H45/2

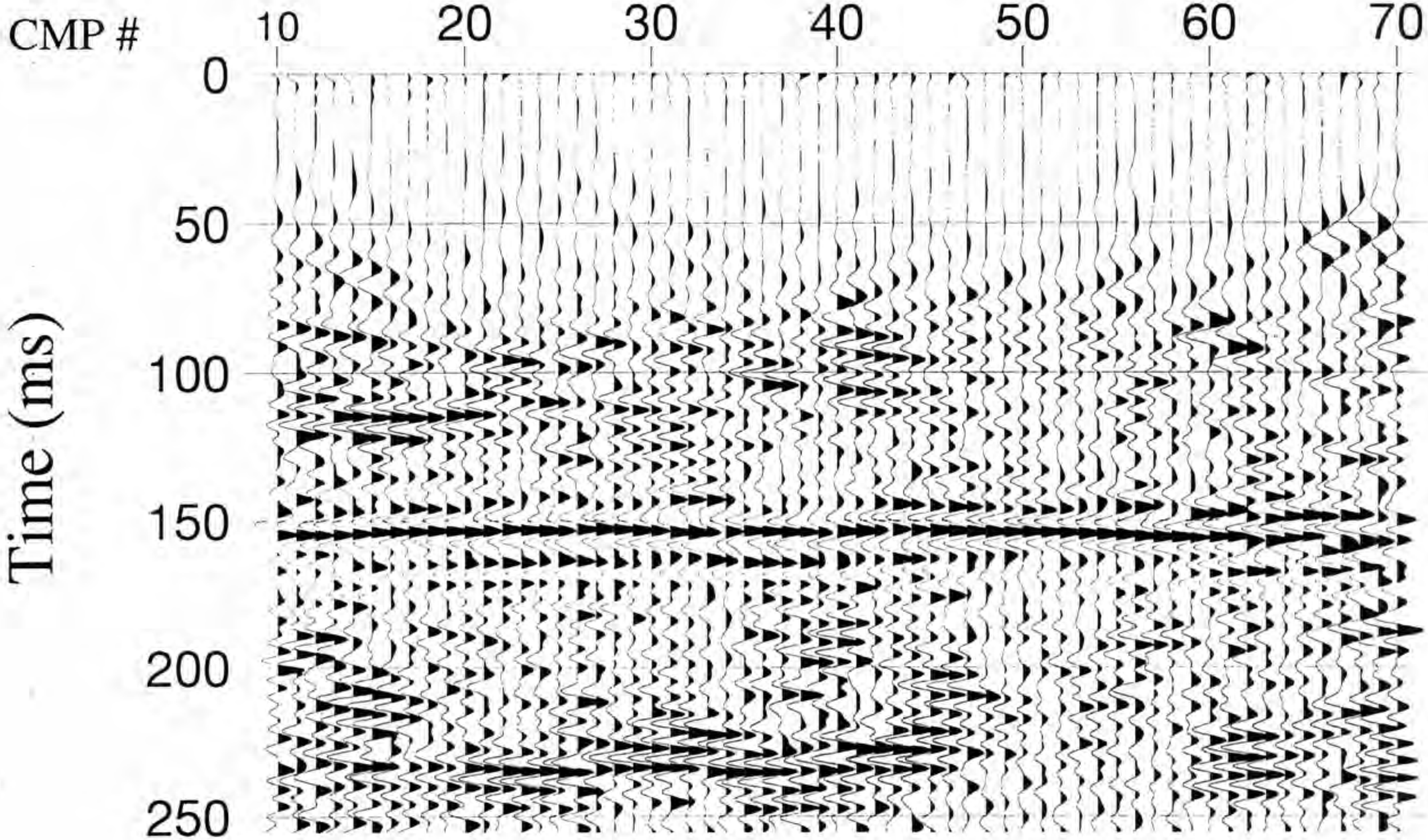

H45/3

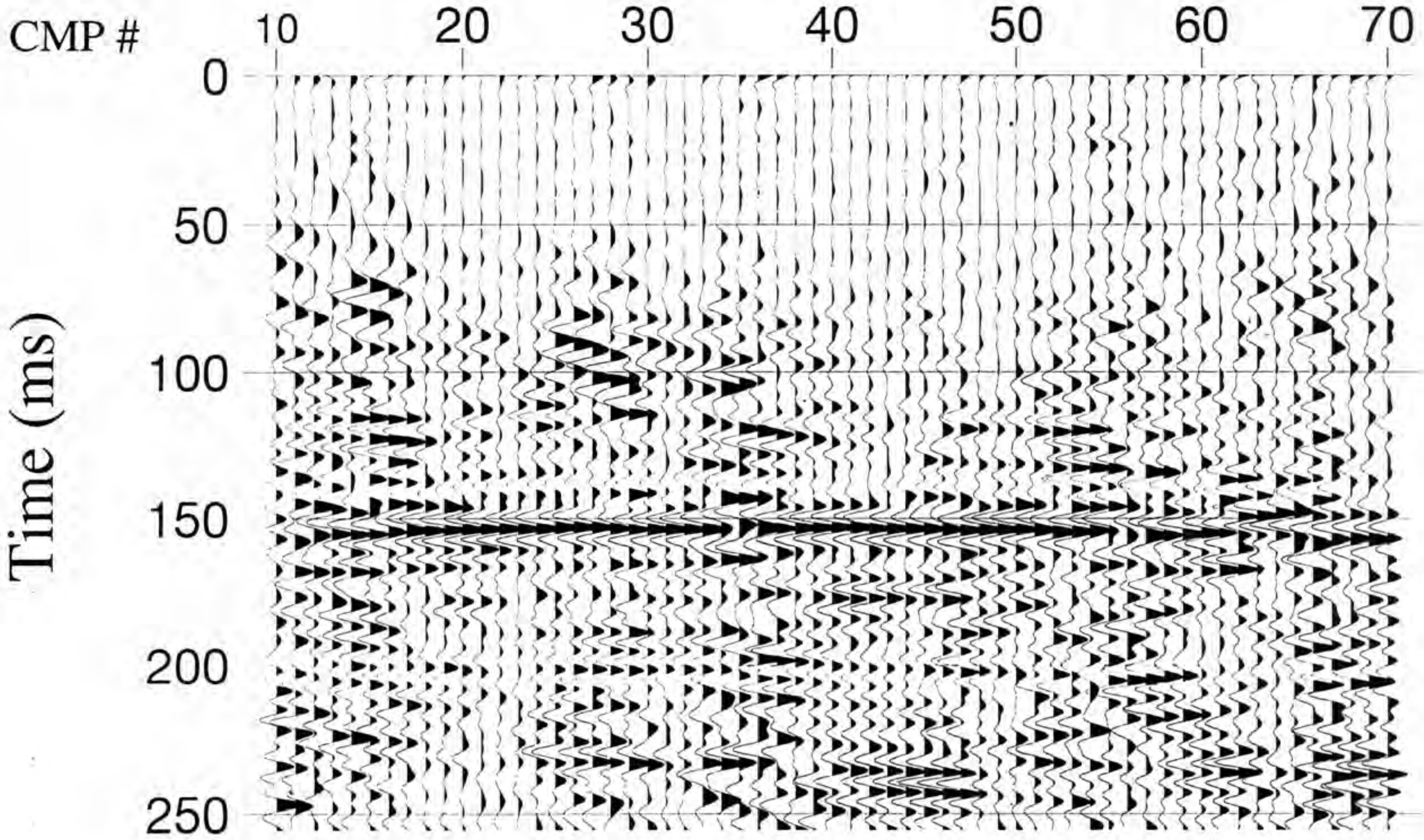

H45/4

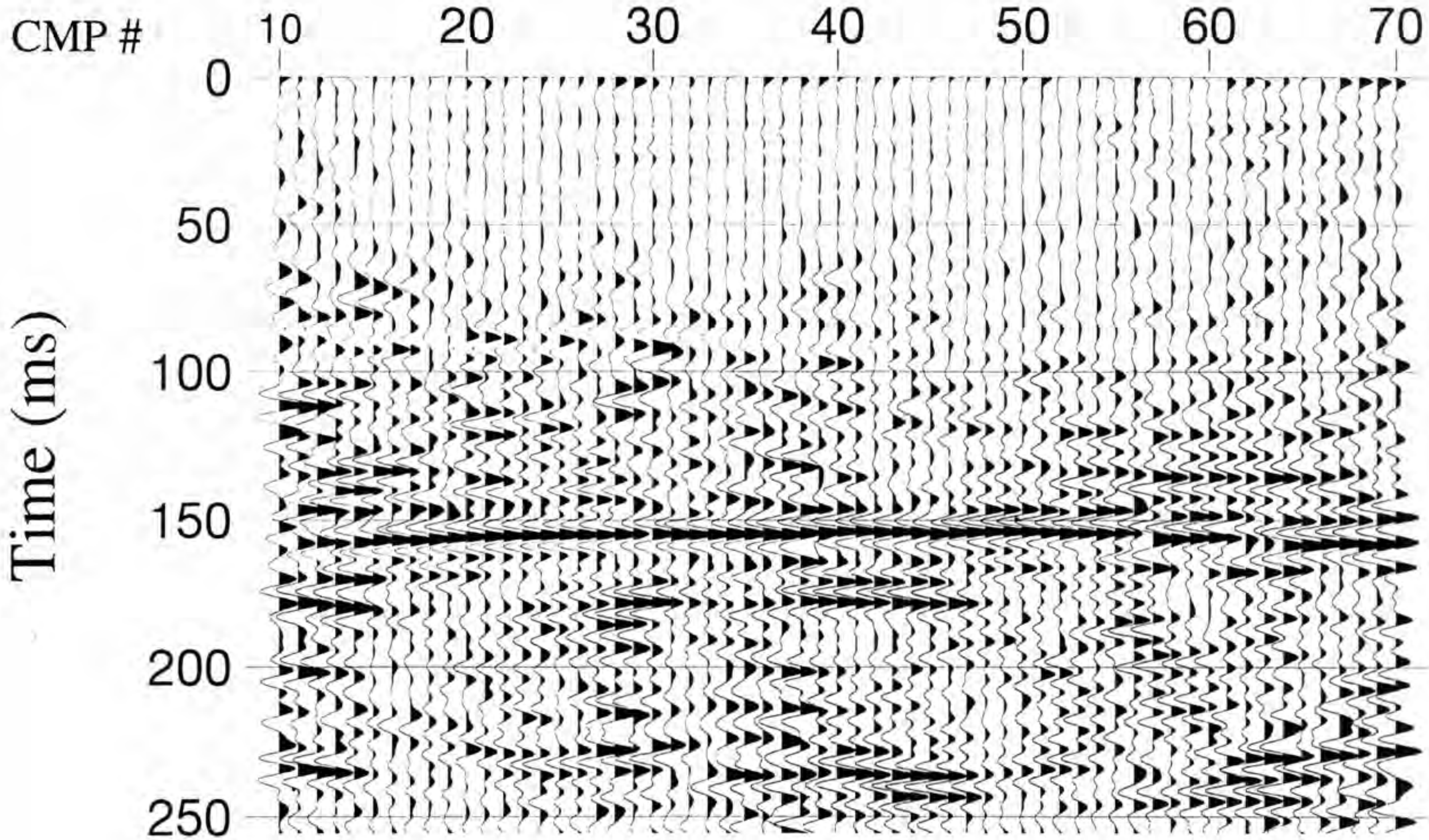

H45/5

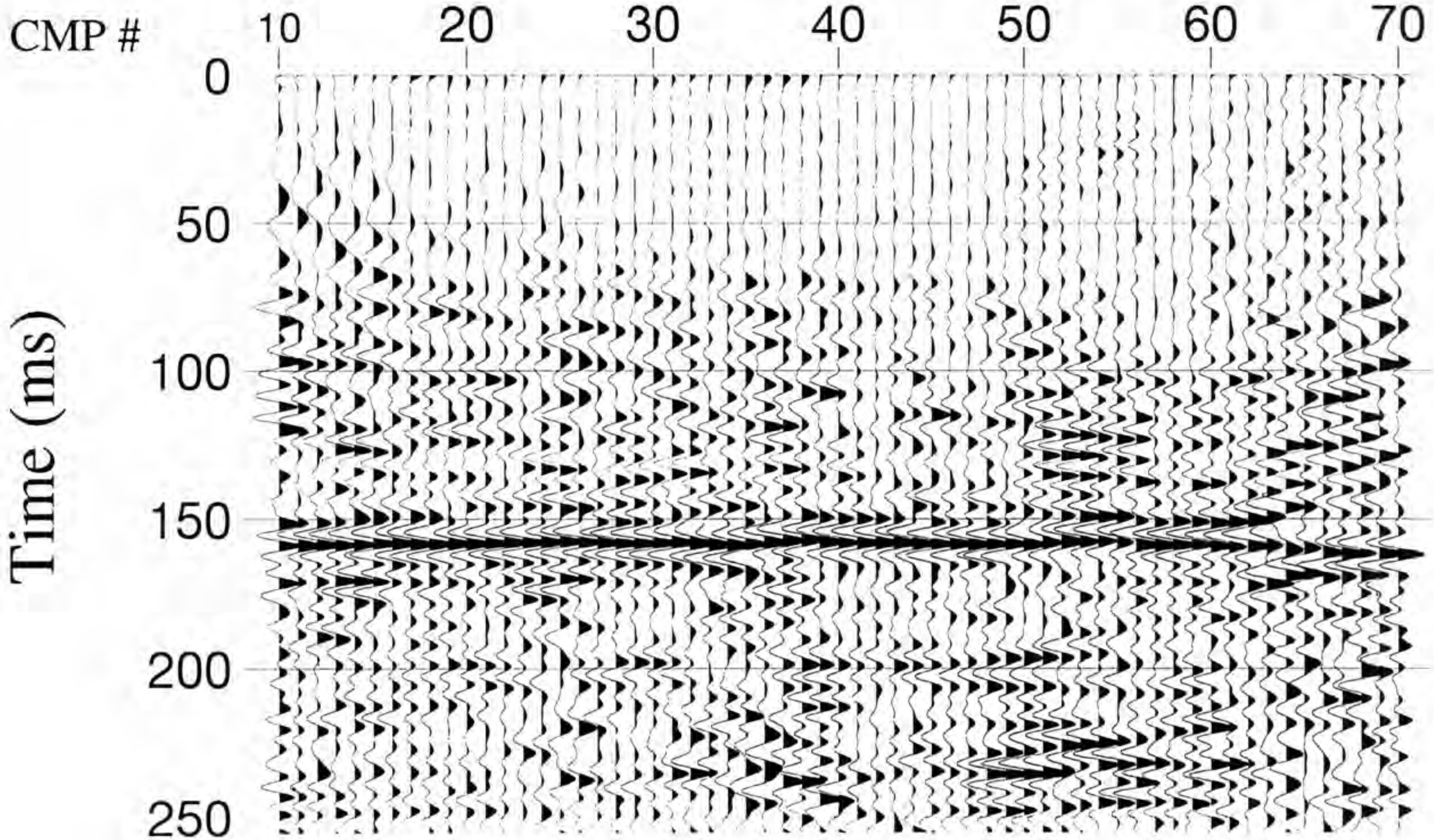

H45/6

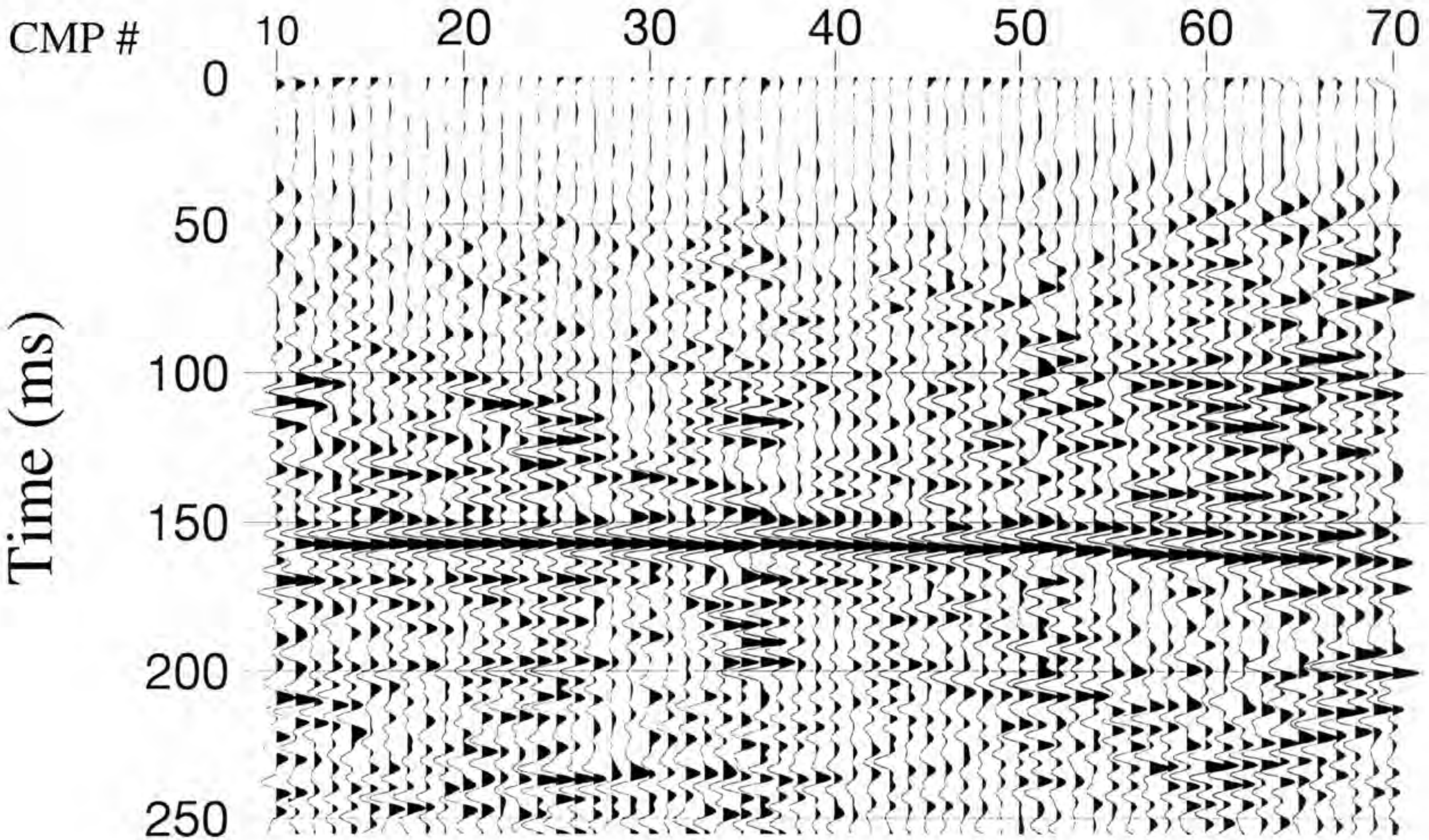

H45/7

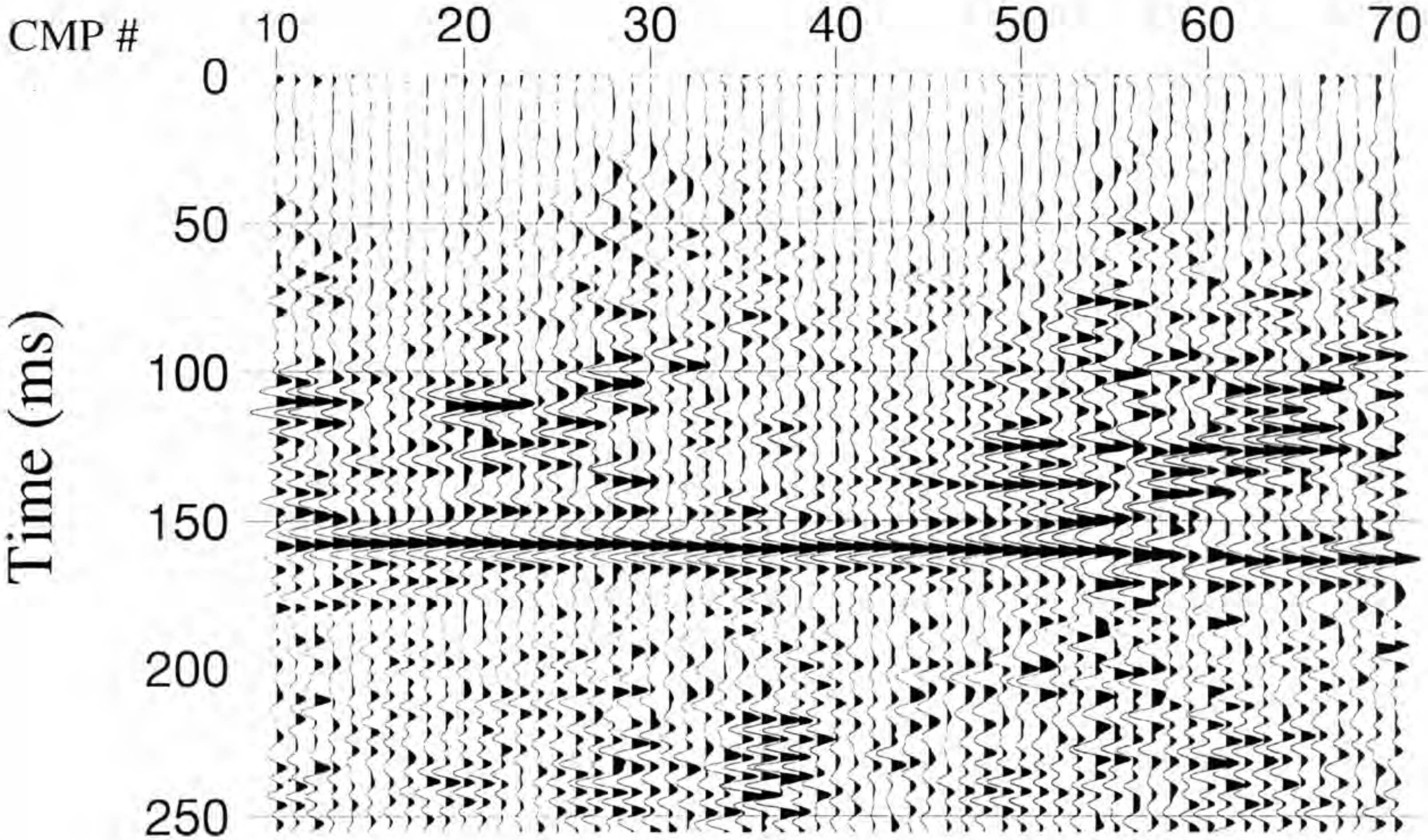

H45/8

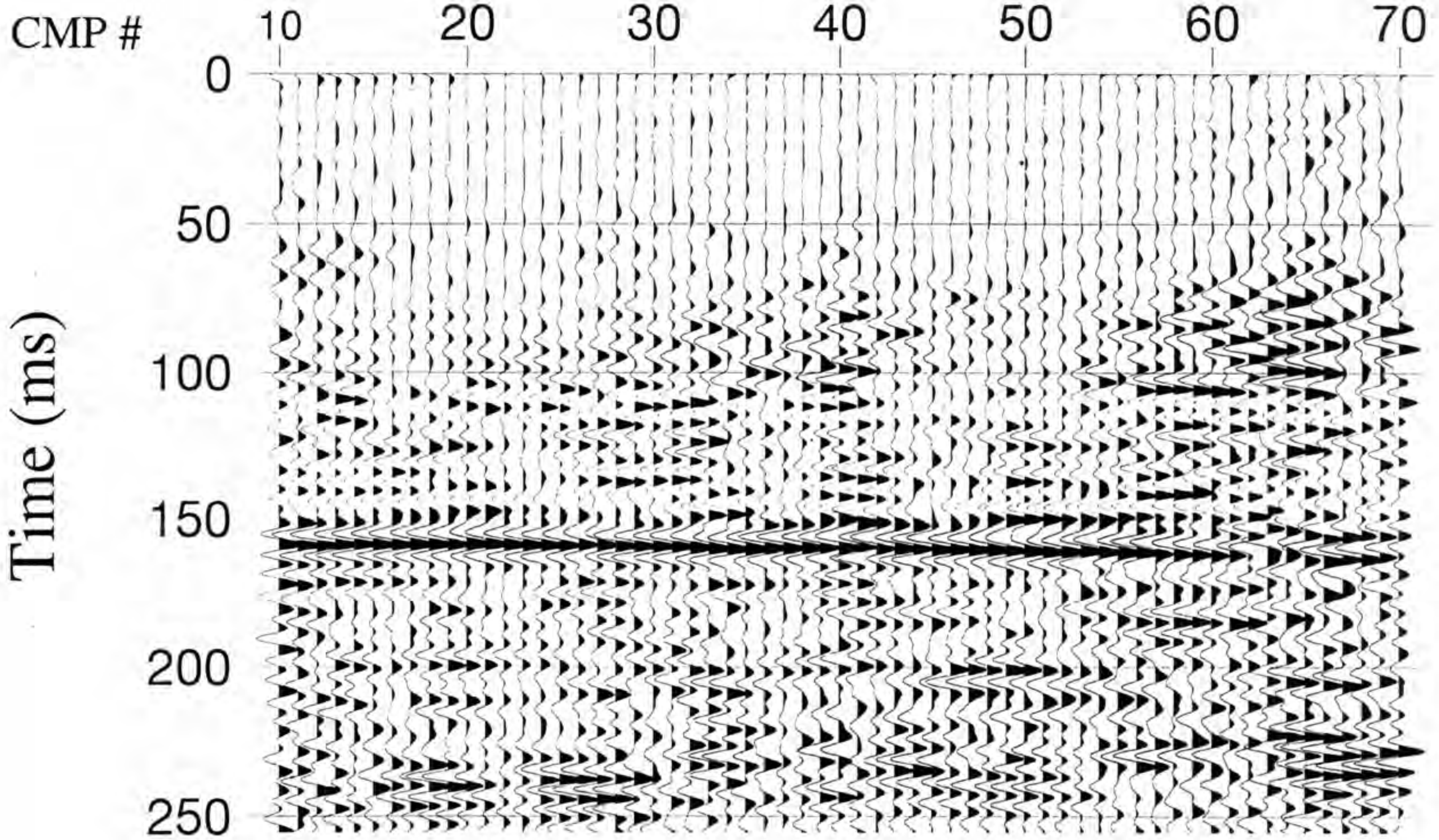

H45/9

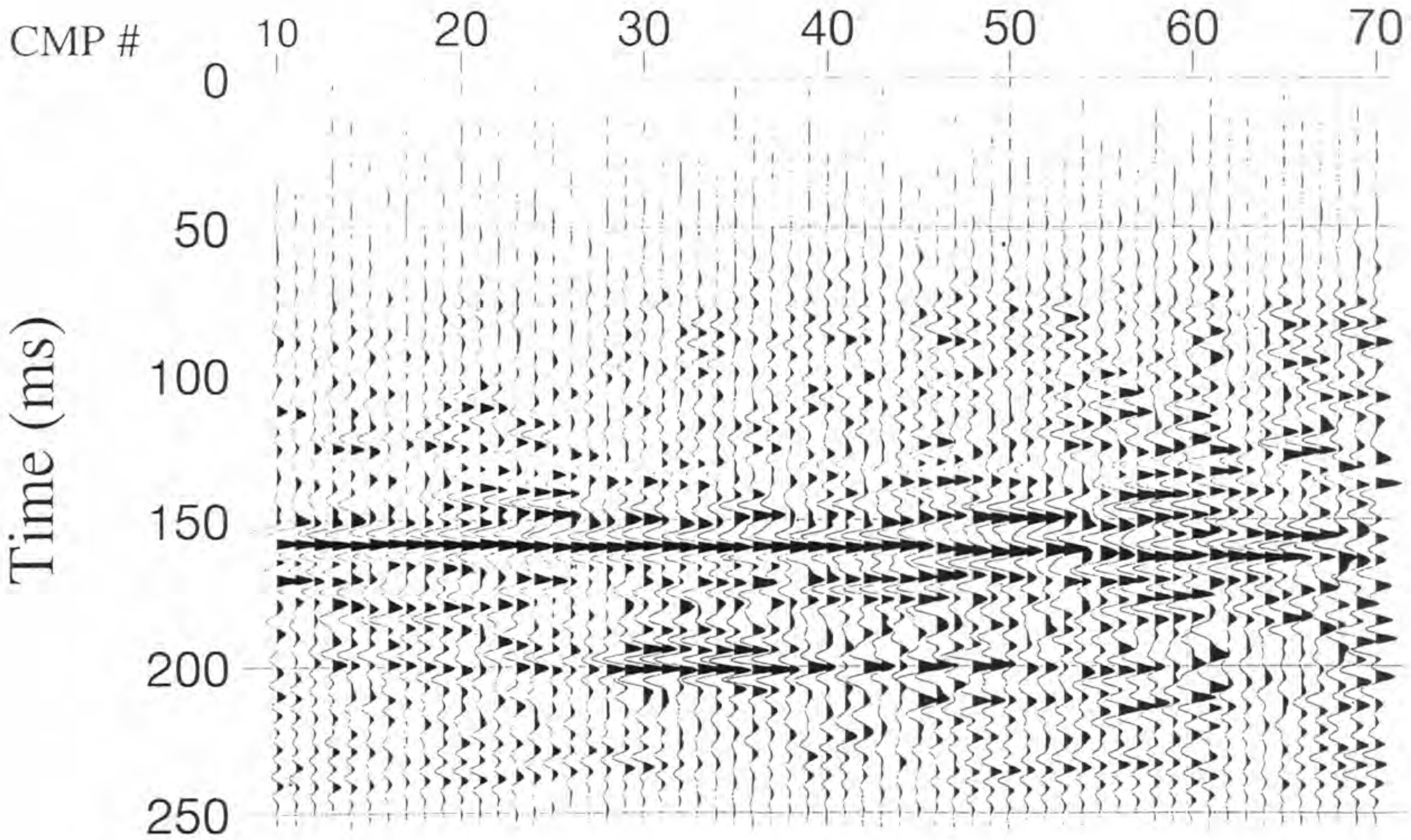

H45/10

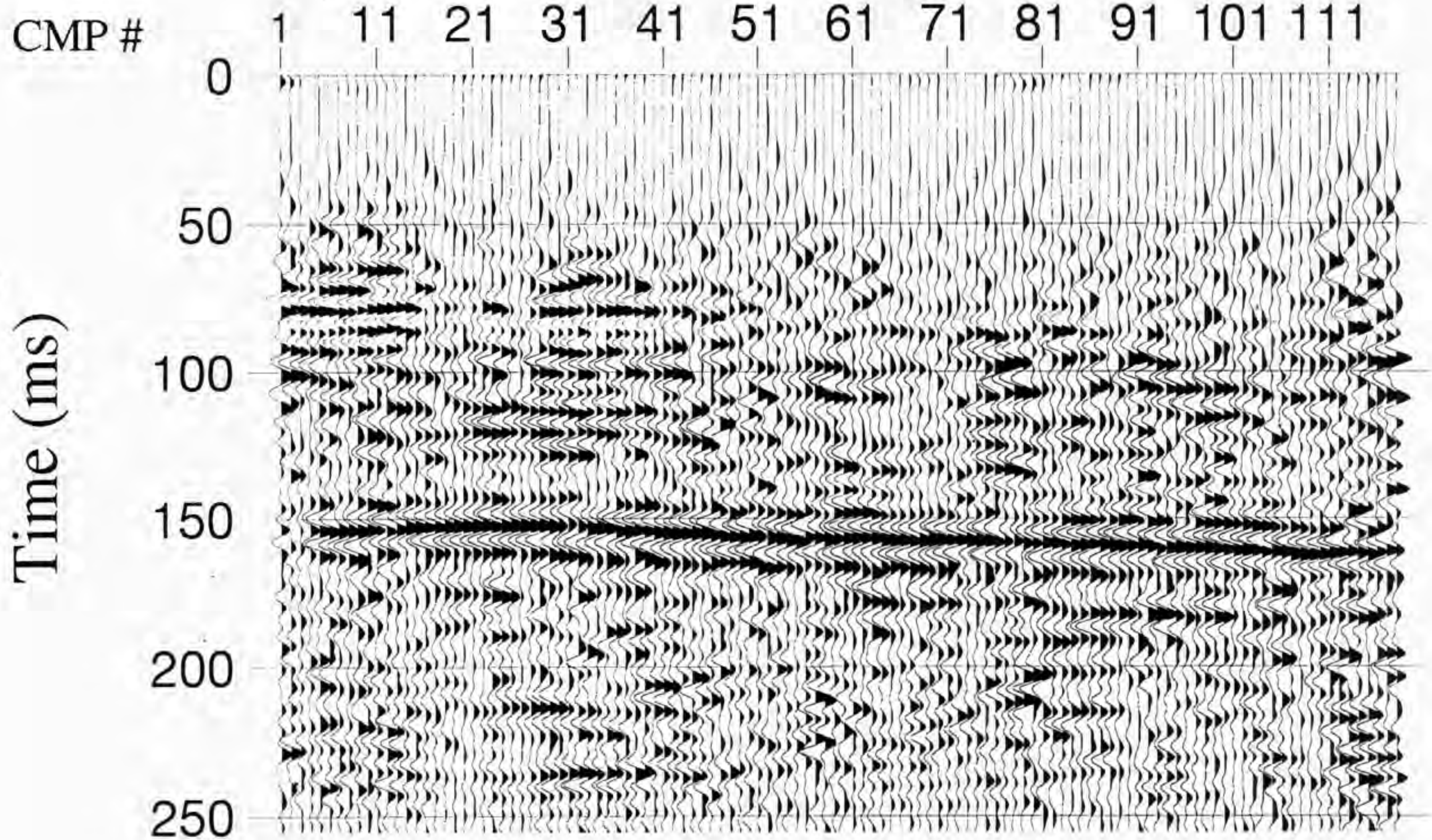

H46/1

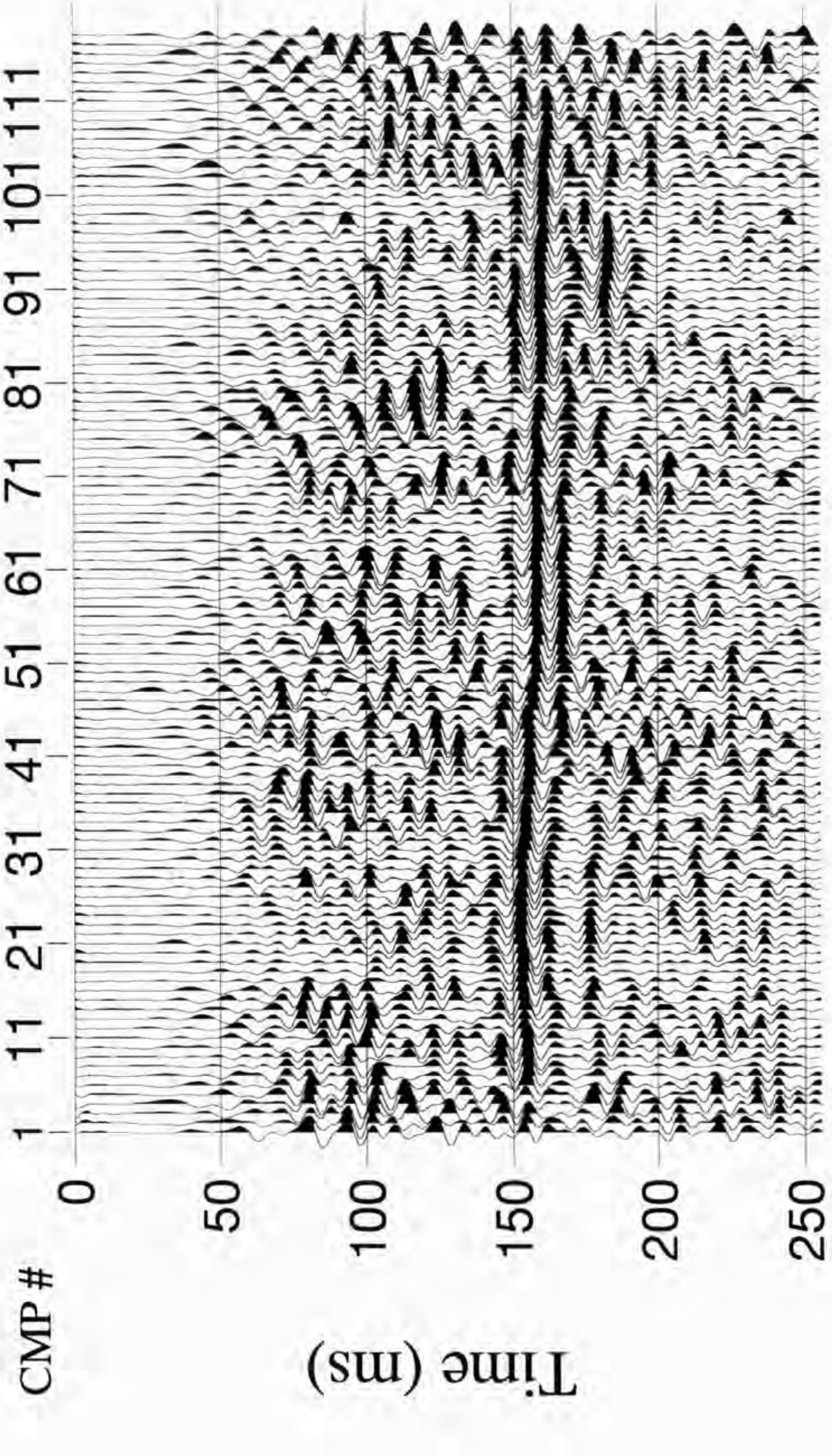

H46/2

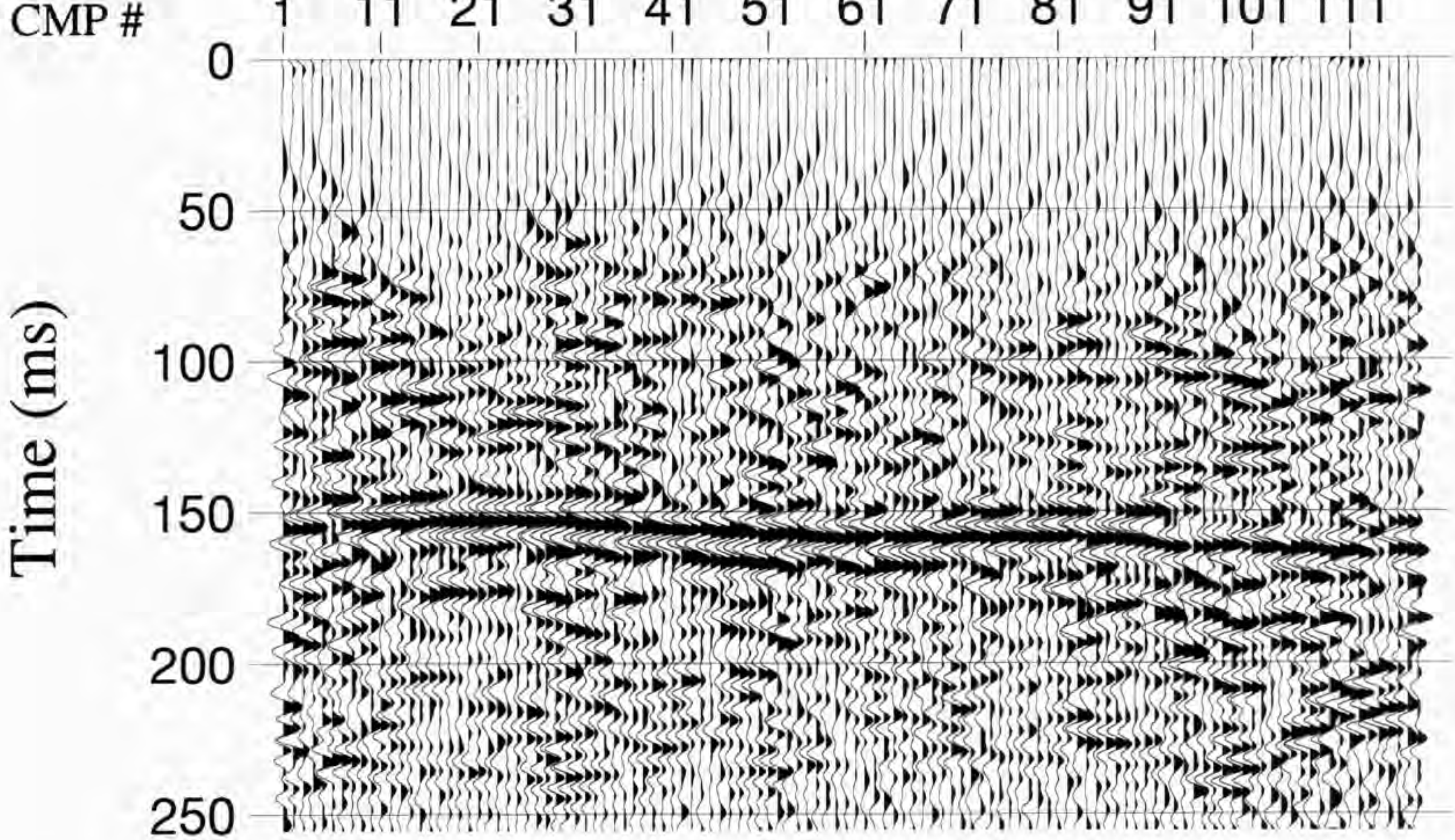

H46/3

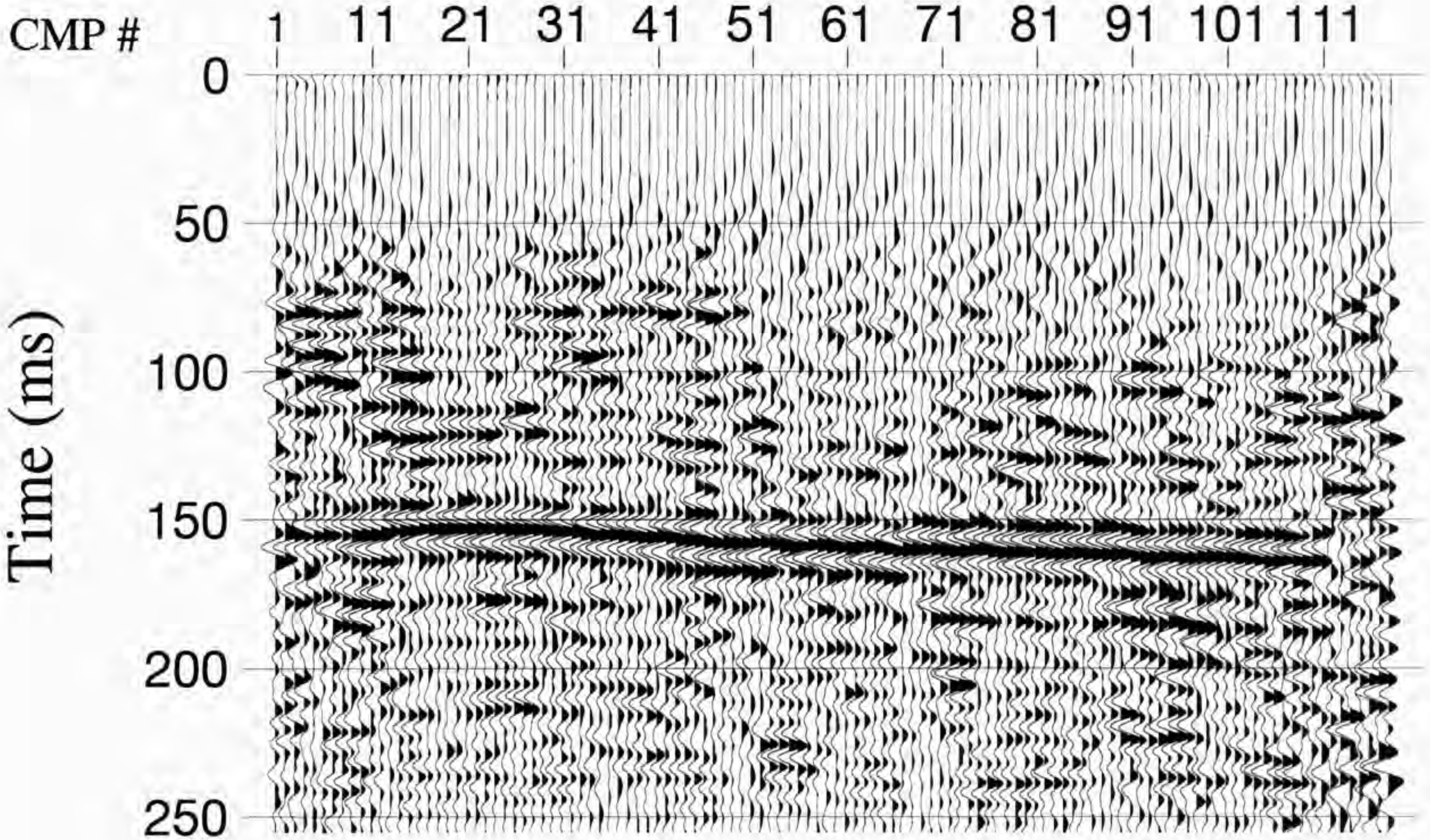

H46/4

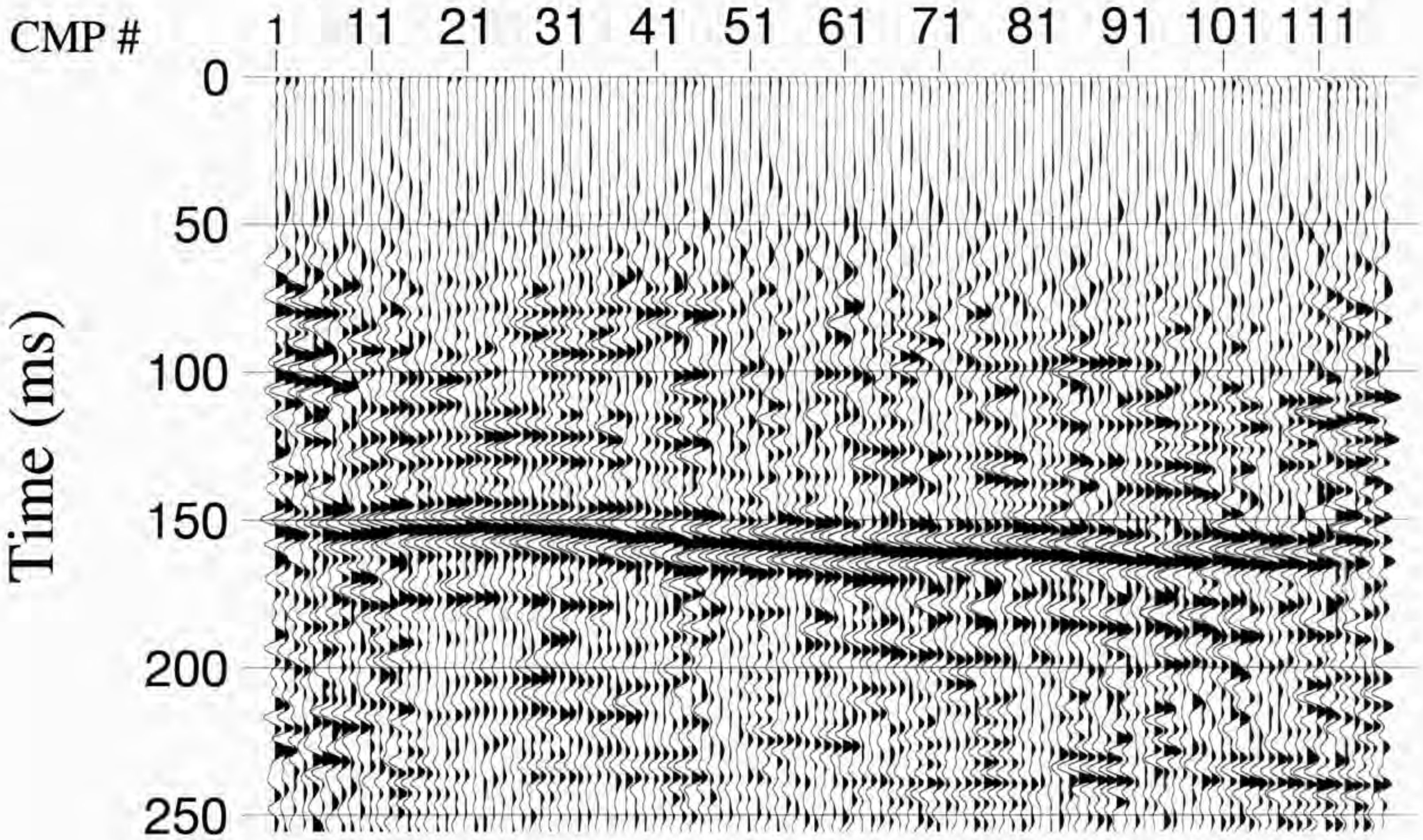

H46/5

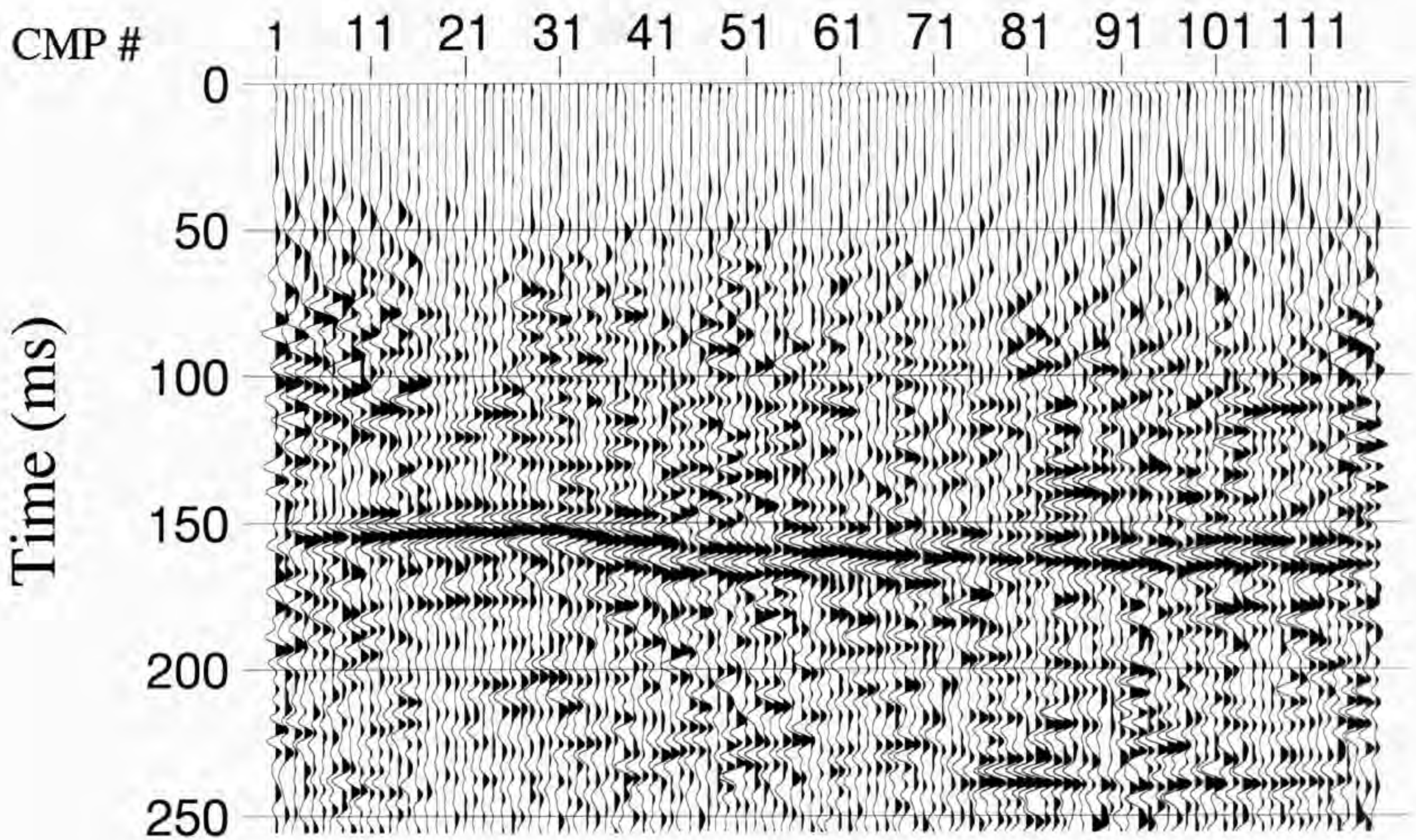

H46/6

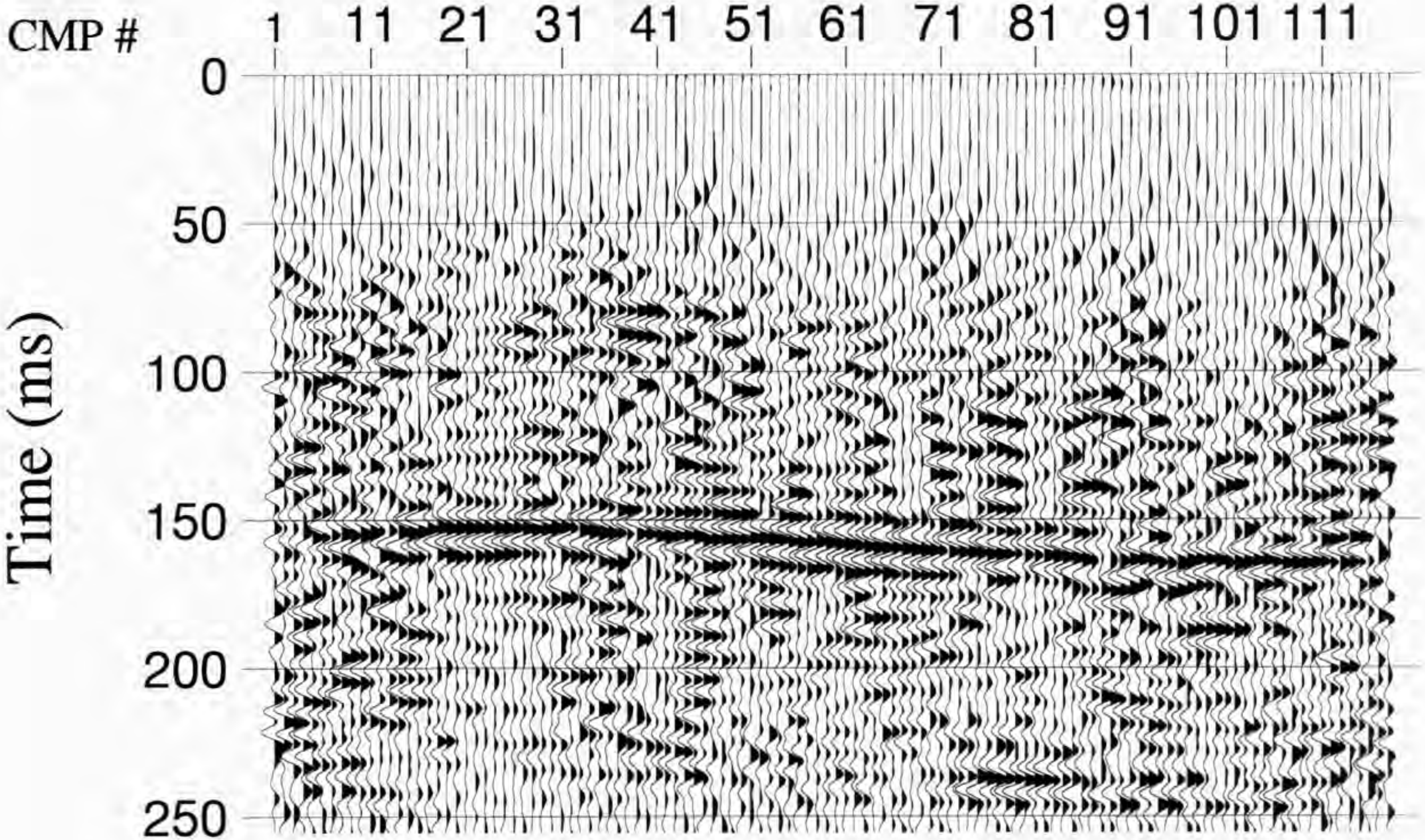

H46/7

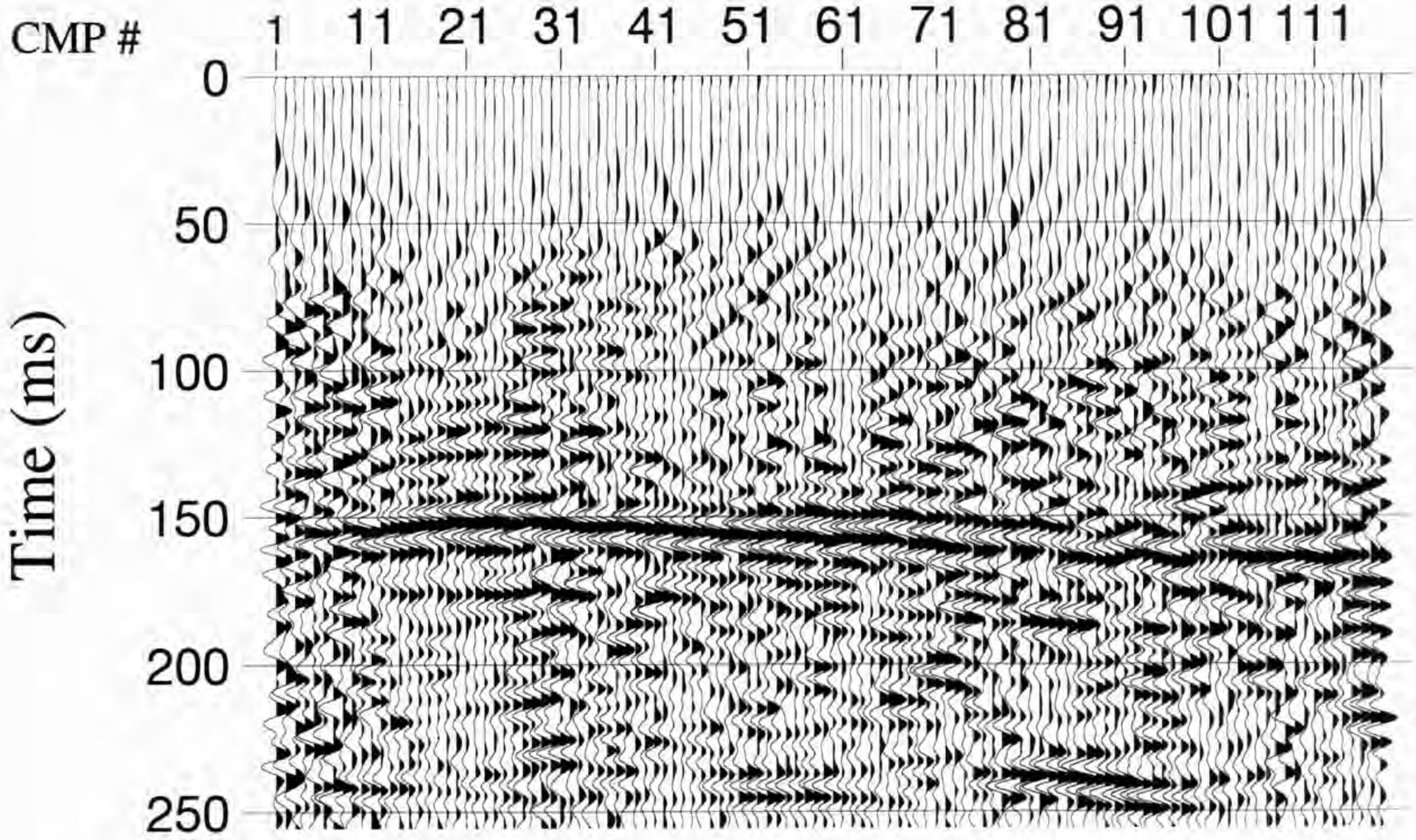

H46/8

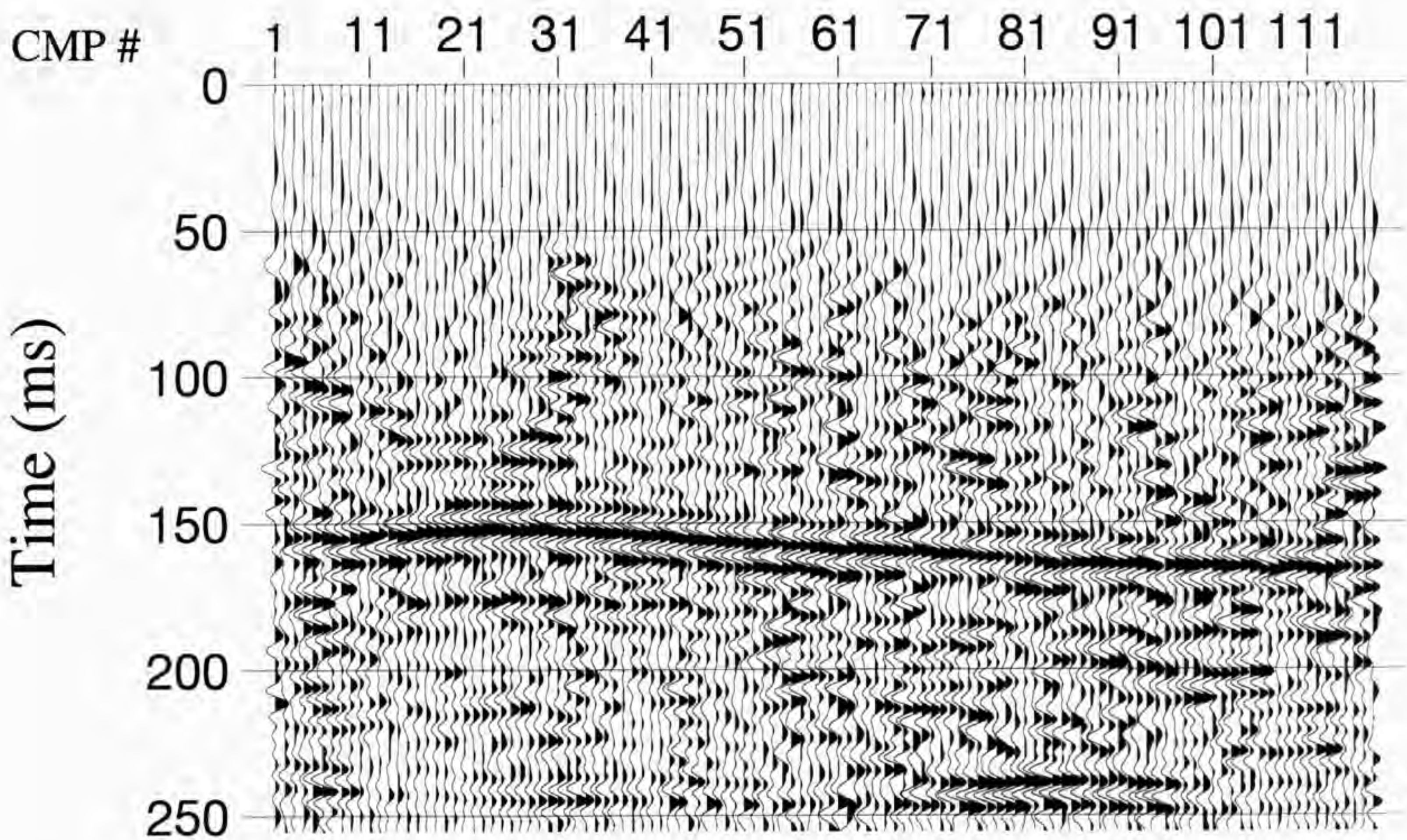

H46/9

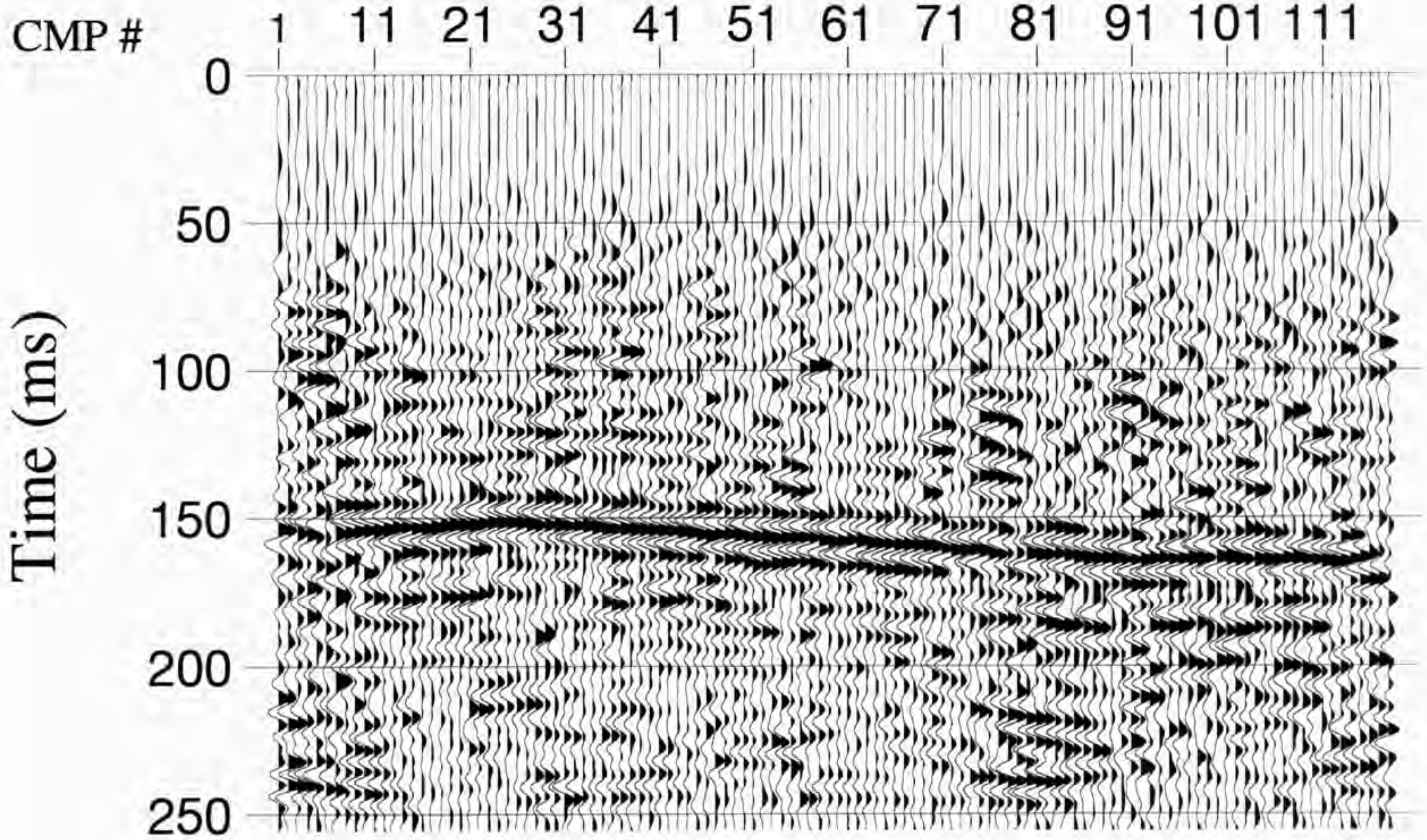

H46/10

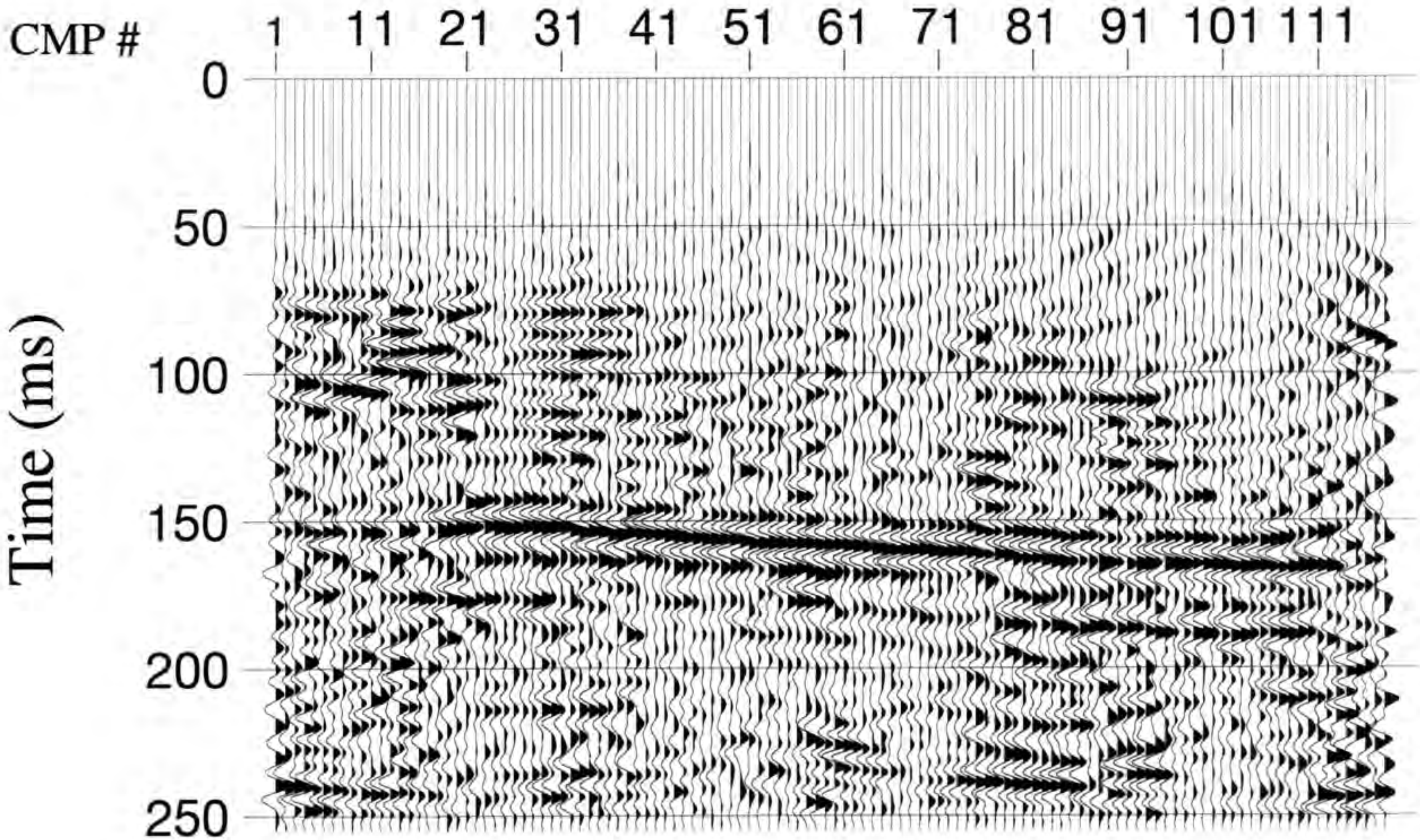

H46/11